UNIVERSITÀ DEGLI STUDI DI TRIESTE

XXXIV CICLO DEL DOTTORATO DI RICERCA IN

"Scienze della Terra, Fluidodinamica e Matematica.
Interazioni e Metodiche"

Surface deformation analysis in Northeast Italy by using PS-InSAR and GNSS data

Settore scientifico-disciplinare: GEO/03 Geologia Strutturale

DOTTORANDA

Giulia AREGGI

COORDINATORE

Prof. Stefano MASET

SUPERVISORE DI TESI

Prof. Lorenzo BONINI

CO-SUPERVISORE DI TESI

Dr. Giuseppe PEZZO

ANNO ACCADEMICO 2020/2021

To my Dad

“Oltre ogni ostacolo”

ABSTRACT

In the present study, we employed MT-InSAR data together with the measurements provided by GNSS stations 1) to estimate the interseismic deformation over the satellites' observation period, 2) to detect and analyze the main deformation patterns, and 3) to correlate the signals to the active tectonic structures in Northeastern Italy.

Geodetic data play a significant role in environmental monitoring and hazard studies. Indeed, these techniques detect and monitor several natural and anthropogenic phenomena by observing the deformation patterns over large areas and estimating their rates with high accuracy. Among different applications, satellite-based geodetic data are extremely useful for detecting and measuring surface displacements during the different phases of the earthquake cycle. In particular, in the last decades, many studies focused on estimating and analyzing the interseismic deformation to evaluate the behavior of the roots of the faults below the locking depth. Considering that the surface displacement during the interseismic period is related to the aseismic slip of the deeper portion of a fault, it is possible to define the geometry and the kinematics of the tectonic structures together with their seismogenic potentials by running an inversion under the assumptions of an elastic dislocation model (e.g., Okada, 1985).

Northeast Italy is characterized by the presence of the Southeastern Alps and the External Dinarides in the northern and the northeastern sector and by the Venetian-Friulian plain and the Adriatic coasts in the southern area. The study region is tectonically active, as testified by instrumental and historic seismicity (Anselmi *et al.*, 2011; Danesi *et al.*, 2015; Bressan *et al.*, 2016; Rovida *et al.*, 2020) despite the low deformation rates of ~1.5-3 mm/yr (Battaglia *et al.*, 2004; D'Agostino *et al.*, 2005; Bechtold *et al.*, 2009; Cheloni *et al.*, 2014; Serpelloni *et al.,* 2016). The active seismogenic faults are connected to the N-S convergence between the Adriatic and Eurasian plates (e.g., Battaglia *et al.*, 2004). Indeed, the convergence is accommodated mainly by NE-SW and N-S south-verging thrusts and by NW-SE-trending sub-parallel, dextral strike-slip faults, which belong to the Southeastern Alps and the External Dinarides, respectively (e.g., Castellarin and Cantelli, 2000; D'Agostino *et al.*, 2005; Bechtold *et al.*, 2009; Serpelloni *et al.*, 2016). These tectonic structures result from three main compressional phases starting from the Cenozoic, which also involved the development of foreland basins (i.e., Venetian-Friulian Plain).

In the study area, GNSS and MT-InSAR methods have been exploited primarily for estimating the deformation rate in the study areas caused by different geological phenomena. Regarding tectonics, geodetic data have been employed for seismic hazard purposes to evaluate the potential of the seismogenic sources (e.g., D'Agostino *et al*., 2005; Vrabec *et al.*, 2006; Bechtold et al., 2009; Cheloni *et al.*, 2014; Moulin *et al.*, 2016; Serpelloni *et al.*, 2016; Anderlini *et al.*, 2020). However, geodetic data have also been used to estimate the post-glacial isostatic rebound (Stocchi *et al.*, 2005), the non-tectonic non-seasonal ground deformations related to hydrologic flux in karstic areas in

response to rainfall and groundwater flow (Devoti *et al.*, 2015; Serpelloni *et al.*, 2018), and the active subsidence located on the Venetian-Friulian plain and along the coasts due to natural (i.e., consolidation of Quaternary sediments) and anthropogenic causes (i.e., groundwater and gas pumping, consolidation due to surface loading)(Carbognin *et al.*, 2009; Tosi *et al.*, 2010, 2013; Bock *et al.*, 2012; Da Lio and Tosi, 2018; Farolfi *et al.*, 2019a).

In the present study, we applied the Persistent Scatterers Interferometric (PSI) method to Sentinel-1 SAR images acquired along the ascending and descending orbit tracks between 2015 and 2019. PSI is one of the Multi-Temporal InSAR (MT-InSAR) approaches, which focuses on extracting pixels dominated by bright and temporally stable scatterers (Persistent Scatterers – PSs) from a single master-stack of differential interferograms (Ferretti *et al.*, 2001). Specifically, we used the Stanford Method for Persistent Scatterers (StaMPS) by Hooper *et al.* (2007, 2012). The method has been developed to obtain good results in different areas (urban and non-urban) characterized by variable deformation rates by preserving the accuracy and spatial resolution (Hooper *et al.*, 2007; Crosetto *et al.*, 2016). The approach exploits the amplitude and the phase information to discriminate in a probabilistic way the PSs candidates during amplitude dispersion and phase noise analysis. After the phase unwrapping and applying spatial-temporal filters, the final products consist of mean ground velocity maps and related time series.

After the data downloading and the Reference images' selection, we formed a stack of differential interferograms and coregistered images through the SNAP-STAMPS integration for Sentinel-1 Persistent Scatterer Interferometry processing (*snap2stamps)* (Foumelis *et al.*, 2018), by using the outcome as input for StaMPS processing. After analyzing the amplitude and the phase noises, the potential PSs were selected, and then their phases were corrected by removing residual topographic contributions. Then, the data were unwrapped to recover the unambiguous phase from the wrapped phase and obtain a unique deformation plane by testing different parameters, such as the Goldstein filter window size. Finally, after estimating the spatially-correlated errors related to the Reference image, we tested different approaches for removing the atmospheric phase component. In particular, we applied a temporal high pass filter and spatial low pass filter of 90 days and 400 meters.

We also applied additional post-processing operations to improve the data quality further. Considering potential atmospheric residuals correlated to the topography, we removed PSs, whose height was higher than 1000 meters with respect to a reference point we fixed on a stable plain area. Similarly, we also removed PSs having a difference in velocity higher than 1 mm/yr between the two tests ran with different Goldstein filter parameters (window size 32x32 and 64x64 pixels). Finally, we excluded the PSs with low coherence (< 0.6) and areas characterized by potential unwrapping and processing errors. We then obtained mean ground velocity maps along both the orbit tracks, showing the surface displacements with respect to the satellite along its Line-Of-Sight direction (LOS).

We then integrated and calibrated the SAR measurements with the GNSS data in the study area, obtained by processing data from continuous stations belonging to several public and private

networks in an Adria-fixed reference frame in the 2000-2020 interval (Serpelloni *et al.* 2006, 2013, 2018). After their projection along LOS, we also calculated the mean ground velocities of all the PSs located within a search radius from each GNSS station, and we calculated the standard deviation associated with the average velocity. We proposed four criteria (the temporal coverage of InSAR-GNSS data, the GNSS data continuity, the minimum number of PSs around each site, and the related spatial variability) to select the GNSS data for calibration. After that, we ran 32 tests we obtained using different Goldstein filter parameters, search radius, and calibration models for both orbit tracks. Based on statistics, we selected the best solution.

The LOS mean ground velocity maps on ascending and descending tracks have been used to decompose along the east-west and vertical components using a regular grid with 100x100 meters spacing. Compared with GNSS data, we observed a good agreement in both geometries.

The resulting E-W velocity map shows a general eastward ground motion that increases northeastward by reaching ~1-2 mm/yr. The Venetian-Friulian plain is characterized by a positive signal, especially in the northern sector. A westward deformation can be observed in the Dolomites area, with average values of 1-2 mm/yr. The northern Friuli, the Austrian region, and the eastern Slovenian sector show E-ward velocities at rates of ~1-2 mm/yr, whereas the southeastern sector of the study area presents rates of 0.5-1 mm/yr. Finally, the area east of Udine, across the Italian-Slovenian border, is moving westward with rates of 0.5-1 mm/yr.

Regarding the vertical velocities, the subsidence affects the Venetian-Friulian plain and the coasts, especially between the Venetian and the Grado-Marano Lagoon, with negative rates of 0.5-2 mm/yr. The vertical velocity increases northward across the Alpine belt. We estimate an uplift of ~1-2 mm/yr in the northwestern sector of the study area, between the Dolomites and the Carnic Alps. Moving eastward, we observe positive vertical rates higher than 2 mm/yr in the northeastern Friuli and southern Austria, decreasing southward and eastward. Finally, we observe subsidence of ~ -1 mm/yr affecting the Slovenian area west of Ljubliana and the Austrian region, whereas the southeastern sector is characterized by positive vertical displacement of 0.5-1 mm/yr. The detected deformation patterns and the estimated rates agree with the measurements provided by previous geodetic studies. Nevertheless, some differences can be observed, such as the presence of a westward displacement of the area close to Udine or the lower subsidence rates measured in the southern region.

To better analyze the signals induced by active tectonics, we traced three velocity profiles across the SSE-verging thrusts in the western area, the S-verging and strike-slip faulting in the central sector, and the NW-SE-trending strikes slip faults in the eastern sector. We also correlated the geodetic data with a geological section and seismicity.

For the westernmost NNW-SSE-trending section crossing the alpine thrusts (Dolomites) to the north and the Venetian plain to the south, we observe a significant positive velocity gradient of 1 mm/yr. Considering the presence of seismicity and thrusts, we suggest that the tectonic signal might be

attributed to the aseismic motion of the root of the Bassano Valdobbiadene thrust. We also ran an inversion using the Geodetic Bayesian Inversion Software (GBIS) developed by Bagnardi and Hooper (2018). Based on the inversion of geodetic data and the definition of the source parameters under the assumption of Okada (1985), we confirmed our hypothesis and defined the parameters of the fault. Considering the velocity signals and the GNSS misfit between the observed and modeled data, we also suggest a secondary contribution related to the activity of the Montello thrust.

A visible uplift characterizes the second velocity profile across the Alpine and Dinaric systems, reaching values up to 2 mm/yr around Tarvisio. We also observe an eastward movement of the northern region (north of Udine) and a westward motion of the plain. Similar trends can be roughly observed in GNSS data but with slower rates. Considering the velocity gradients, the seismicity, and the geological setting of the study area, we observe that the velocity pattern corresponds with the main tectonic structures, even if it is impossible to distinguish the contribution of every single fault clearly. Finally, the westward signal detected on the Friulian plain (around Udine) might be related to transcurrent and transpressive tectonic structures.

Regarding the eastern sector of the study area, the profile crosses the dextral NW-SE sub-parallel Dinaric faults. We note an uplift of about 1 mm/yr between the Raša and Idrija faults and an eastward motion with a change in trend around the Predjama fault (0.5 and 1 mm/yr). The seismicity here is localized on the transition between the basement and the carbonates units (10-15 km deep). The velocity gradients are related to the activity of these Dinaric structures. We suggest that some segments of the Predjama fault might move aseismically. Despite the lower density of GNSS and SAR data, the geodetic measurements roughly agree.

Alongside tectonic aspects, from the analysis of the mean ground velocity maps, we also find evidence of non-tectonic signals, such as the subsidence along the coasts and on the Venetian-Friulian plain. In particular, we observe that the significant subsidence measured on the northern Venice Lagoon corresponds to the transition between the Friuli platform and the Belluno-Northern Adriatic basin, with rates up to 2-3 mm/yr. Conversely, the eastern coasts present lower subsidence rates (> -1 mm/yr). In general, our study reveals significant deformation signals at a regional scale by confirming the correlation between subsidence and the geological setting of the study area. We finally report some examples showing subsidence in human activities and slope instabilities.

1. INTRODUCTION

Geodetic data play a significant role in environmental monitoring and hazard studies, as these techniques enable the detection and the monitoring of several natural and anthropogenic phenomena through the observation of the deformation patterns over large areas and the estimation of their relative rates with high accuracy. Global Navigations Satellite Systems (GNSS) represent one of these geodetic techniques, providing high-accurate punctual daily 3D surface displacement and velocity information referred to a receiver on the ground (Li, 2021). On the other hand, MT-InSAR approaches enable information about the displacement of stable and reflective scatterers on the ground by using a stack of differential interferometric SAR images with good data accuracy and high spatial coverage. These methods have been exploited mainly in several investigations all over the world. Specifically, in response to active tectonics, geodetic data can be used to model interseismic deformation. That approach has been successfully employed in several studies in the Himalaya-Tibet region (Grandin *et al.*, 2012; Pezzo *et al.*, 2012; Karimzadeh *et al.*, 2013; Liu *et al.*, 2018), California (Fialko, 2006; Tong *et al.*, 2013; Chaussard et al., 2016), Anatolia (Wright *et al.,* 2001; Walters *et al.*, 2011; Hussain *et al.*, 2016; Weiss *et al.*, 2020), and in Italy (Cheloni *et al.*, 2014; Pezzo *et al.*, 2015, 2020b; Serpelloni *et al.*, 2016; Anderlini *et al.*, 2020). Other studies can also be mentioned related to the other natural and anthropogenic phenomena, such as subsidence (Teatini *et al.*, 2005; Tosi *et al.*, 2010, 2013; Osmanoğlu *et al.*, 2011; Da Lio and Tosi, 2018; Del Soldato *et al.*, 2018; Polcari *et al.*, 2018; Farolfi *et al.*, 2019a, 2019b; Floris *et al.*, 2019), landslides and slope instabilities (Žibret *et al.*, 2012; Komac *et al.*, 2015; Notti *et al.*, 2015; Aslan *et al.*, 2020), sinkholes (Busetti *et al.*, 2020), volcanic processes (Hooper *et al.,* 2007; Pezzo *et al.,* 2020a; Beccaro *et al.*, 2021), monitoring of infrastructures, reservoirs and mining activities (Perski *et al.* 2009; Klemm *et al.*, 2010; Ab Latip *et al.*, 2015; Gama *et al.*, 2020).

In the last few years, the development and extensive use of new satellites and new algorithms have made it possible to detect tectonic, gravitative, hydrogeological, and anthropogenic signals, even with low deformation rates.

Northeast Italy is characterized by the presence of the Southeastern Alps and the External Dinarides in the northern and northeastern sectors. At the same time, the foreland, covered by the Venetian-Friulian plain, dominates the southern area. The study region is tectonically active, as testified by instrumental and historic seismicity (Anselmi *et al.*, 2011; Danesi *et al.*, 2015; Bressan *et al.*, 2016; Rovida *et al.*, 2020) despite the low deformation rates. The active faults are connected to the N-S convergence among the Adriatic and Eurasian plates (e.g., Battaglia *et al.*, 2004). This convergence is accommodated mainly by thrusting in the Southeastern Alps and strike-slip faulting in the External Dinarides area (e.g., Castellarin and Cantelli, 2000; D'Agostino *et al.*, 2005; Bechtold *et al.*, 2009; Serpelloni *et al.*, 2016).

The Venetian-Friulian plain and the coastal areas are affected by active subsidence caused by natural (i.e., consolidation of Quaternary sediments) and anthropogenic causes (i.e., groundwater and gas pumping, consolidation due to surface loads)(Carbognin *et al.*, 2009; Tosi *et al.*, 2010). In combination with sea-level rise and global climate changes, the subsidence in the area causes an increase in the flooding hazard, damages to infrastructures and cultural heritage, and adverse effects on natural environments, e.g., in the lagoon areas (Carbognin et al., 2009).

In the study area, both geodetic approaches have mainly been exploited in several studies to estimate the displacement rate in the study areas caused by different geological phenomena. Regarding tectonics, geodetic data (GNSS and MT-InSAR data) have been employed for seismic hazard purposes to evaluate the potential of the seismogenic sources in the area by inverting the obtained velocity field. Many studies have estimated a ~1.5-3 mm/yr convergence rate caused by the Adria-Eurasia plates collision, based on GNSS data analysis (Battaglia *et al*., 2004; D'Agostino *et al.*, 2005; Bechtold *et al.*, 2009; Cheloni *et al.*, 2014; Serpelloni *et al.,* 2016). Other studies focused on the definition of the geometrical and kinematic behaviors of the active faults and their seismogenic potential (e.g., D'Agostino *et al.*, 2005; Vrabec *et al.*, 2006; Bechtold *et al.*, 2009; Cheloni *et al.,* 2014; Moulin *et al.*, 2016; Serpelloni *et al*., 2016; Anderlini *et al*., 2020). Rossi *et al.* (2016, 2018, 2021) have evidenced transient deformations propagating in the region and interpreted them due to pore pressure variations in response to the tectonic stresses.

Furthermore, other processes have been studied using geodetic data. Stocchi *et al.* (2005) have estimated the post-glacial isostatic rebound contribution in the vertical velocity field along the Alpine arc, which amounted to ~ 1/3 of the measured vertical rates. Devoti *et al.* (2015) and Serpelloni *et al.* (2018) have revealed horizontal non-tectonic and non-seasonal ground deformation dealing with the hydrologic flux in karstic areas in response to rainfall and groundwater flow. Finally, several studies have been carried out on the Venetian-Friulian plain and coasts by estimating and analyzing the subsidence rates (Tosi *et al.*, 2010, 2013; Bock *et al.*, 2012; Serpelloni *et al.*, 2013; Da Lio and Tosi, 2018; Farolfi *et al.*, 2019a; Vecchio *et al.*, 2019).

In the present study, we employed MT-InSAR data together with the measurements provided by GNSS stations 1) to estimate the interseismic deformation over the satellites' observation period, 2) to detect and analyze the main deformation patterns, and 3) to correlate the signals to the active tectonic structures in Northeast Italy. We applied the Persistent Scatterers Interferometric (PSI) method to Sentinel-1 SAR images, integrated with GNSS data for calibration. The resulting mean ground velocity maps enable the observation of the deformation patterns, the definition of the trends across the mountain belt and on the coastal and plain areas, the estimation of the related rates, and the improvement of the knowledge of the ground effects due to tectonic and other geological phenomena in the last few years.

1.1. Earthquake cycle

According to plate-tectonics theory, tectonic deformations occur in response to the interaction between the rigid lithosphere and the lower viscoelastic asthenosphere. In this contest, the resulting deformations, due to the cyclical accumulation and release of strain, can be accompanied by seismic activity, mainly distributed along the plate boundaries (convergent and divergent margins) or located within the plates (intraplate earthquakes) (e.g., Le Pichon *et al.*, 2013).

Reid (1910), for the first time, proposed the theory of "elastic rebound" considering a relationship between the surface displacements detected by geodetic data (i.e., triangulation surveys) and the earthquake movements (i.e., coseismic displacement) that occurred along the San Andreas fault during the 1906 San Francisco event. The following studies then led to the development of this theory by introducing the concept of seismic or earthquake cycle to better explain the correlation between tectonic deformations and earthquakes.

The cycle describes the different phases related to the occurrence of an earthquake based on the cyclic accumulation (interseismic phase) and consequent release of the elastic strain energy (coseismic and post-seismic phase) along an active fault (e.g., Avouac, 2015). During the interseismic period, the seismogenic fault is locked above the so-called locking depth, enabling the accumulation of strain due to active tectonics. Conversely, below the locking depth, the deeper portion of the fault can slip aseismically (interseismic creep) without causing a seismic event. During the coseismic period, because of the slip of the seismogenic fault, the accumulated strain is released in terms of seismic waves, generating a seismic event (Segall, 2010). However, during the following period (post-seismic), postseismic deformations (i.e., postseismic relaxation, after slip, aftershocks, transient slip on nearby faults) can occur due to the stress changes caused by the earthquakes in a variable time scale (hours to decades) (Thatcher, 1983; Bürgmann *et al.*, 2000).

The aseismic (i.e., interseismic and post-seismic phases) and seismic (coseismic phase) slip of a fault located within the lithospheric layer induces a surface displacement, which can be detected and measured by using satellite-based geodetic data (Avouac, 2015). Based on the surface displacement measurements, many studies have been conducted to define a kinematic model to describe the tectonic deformations and the earthquake cycle in different tectonic settings together with the fault parameters, such as the slip rates and the locking depth.

Given a strike-slip fault, Savage and Burford (1973) proposed a 2D elastic buried dislocation model to observe the distribution of shear strain and strike-slip on the Earth's surface during the interseismic period. In particular, they focused on two configurations, as shown in Figure 1.1. In the first model, the deeper portion of the fault, below the so-called locking depth, slips during the interseismic period. In contrast, the upper part (i.e., the seismogenic fault), which is locked, accumulates strain, as observed in the central plot in Figure 1.1. On the other hand, different behaviors can be observed

when a fault slips (creep) continuously or at slow rates without generating large earthquakes, storing little to no strain energy (e.g., Thatcher, 1979; Fig. 1.1).

The model was also improved by Savage and Prescott (1978) by adding a viscoelastic layer (asthenosphere) below the upper rigid and elastic plate (lithosphere) for a better evaluation of the displacements during the earthquake cycle.

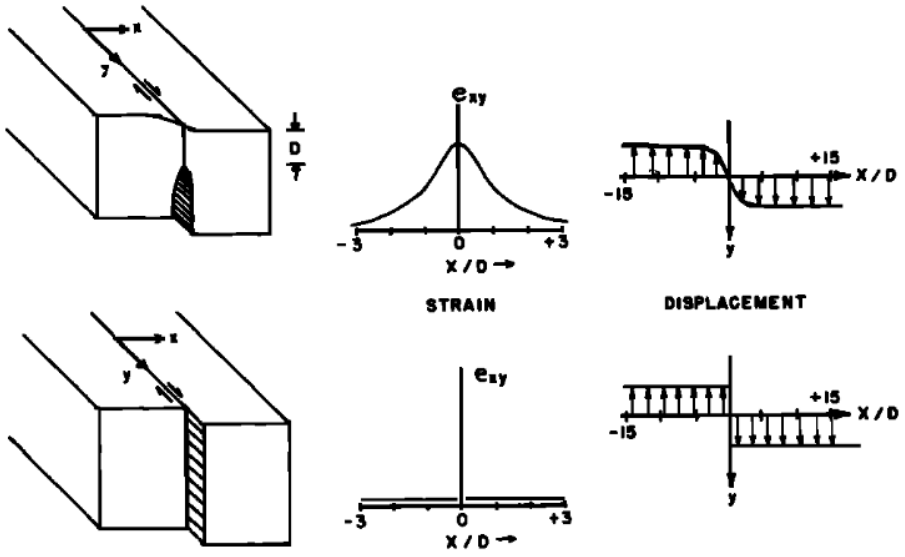

Figure 1.1. 2D dislocation fault model for a strike-slip fault. The two graphs show the distribution of shear strain and strike slip detected on the ground by assuming a rigid block model. Bottom: rigid fault model where the slip is uniform with depth. Top: the fault slips below the locking depth (D), whereas the upper portion is locked. In this case, there is an accumulation of strain, as observed in the central plot. (From Savage and Burford, 1973).

Considering the dislocation model for a strike-slip fault, the strike-slip displacement (u) across the fault during the coseismic and interseismic period can be estimated by applying the following formulae:

$$u_{cos} = \left(\frac{s}{\pi}\right) \tan^{-1}\left(\frac{D_1}{x}\right) \tag{1.1}$$

$$u_{int} = \left(\frac{s}{\pi}\right) \tan^{-1}\left(\frac{x}{D_2}\right) \tag{1.2}$$

with s as the strike-slip rate, x as the horizontal perpendicular distance from the fault trace, and D_1 and D_2 as the depth of the base of the coseismic rupture and the locking depth (Segall, 2010). Figure 1.2 shows the displacement and strain as a function of the increasing distance from the fault trace for both scenarios.

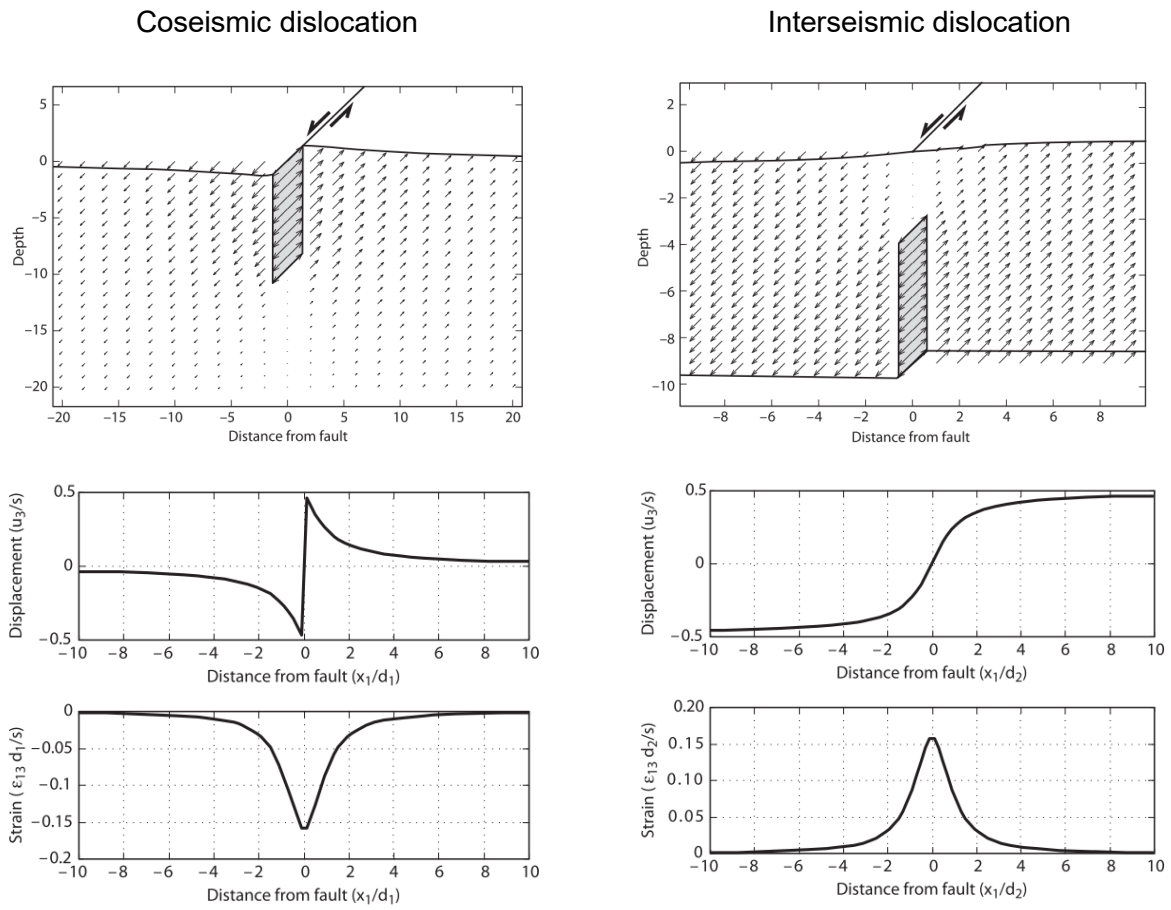

Figure 1.2. Dislocation model of a strike-slip fault. On the left: Coseismic displacement. The dislocation model slips from the surface to depth D_1, and the distribution of the displacement and strain can be observed in the followed plots with respect to the distance from the fault trace. On the right: Interseismic displacement. The model is locked until depth D_2, while the lower portion of the fault is left free to slip. The plots show the displacement and the strain as a function of the distance from the fault trace. (From Segall, 2010).

Other studies, such as Savage (1983), Cattin and Avouac (2000), and Vergne *et al*. (2001), described a 2D model to represent the accumulation and release of strain due to subduction, intracontinental, and continental thrusts, respectively. Okada (1985) also proposed a dislocation theory under the assumptions of a finite rectangular fault embedded in an elastic, homogeneous, and isotropic half-space. Several studies have successfully employed the fault model to determine the source parameters of seismogenic faults starting from the surface displacement.

As explained, the occurrence of an earthquake and the consequent release of energy (i.e., the coseismic phase) is followed by a post-seismic and interseismic period. A transient deformation can be present in the former because of the stress changes that may occur after the seismic event. The latter represents a phase where a steady deformation characterized by low rates can be measured over a long period. During this interval, the seismogenic fault, namely the portion of the fault able to produce earthquakes, is locked and accumulates strain because of the active tectonic stresses. Conversely, the deeper segments below the locking depth can slip aseismically without generating

strong earthquakes. Considering the relationship between the magnitude of an earthquake and the dimensions of the seismogenic fault (e.g., Wells and Coopersmith, 1994), the detection and determination of the locking and the creeping fault segments are essential for the estimation of the seismogenic potentials of the active faults and the seismic hazard assessment.
Therefore, long geodetic time series are required to obtain the interseismic velocity field of the study area and then estimate the slip distribution along the faults. Among all the approaches, over the last decades, satellite-based geodetic methods, such as GNSS and InSAR, have been used, given the data quality (high accuracy, high resolution, low uncertainties) and the data availability (global coverage, low-cost data). The following section will discuss these two geodetic methods for estimating ground displacements.

1.2. Active tectonics and geodesy

Geodetic data have been exploited mainly for several geological and geophysical investigations to detect, identify and measure the surface processes worldwide. For active tectonics studies, geodetic data provide measurements of surface deformations to correlate them with active structures and to improve the knowledge of ongoing processes.
In the past, tectonic deformations were investigated by using ground-based methods, such as triangulation, trilateration, and leveling. However, in the last 30 years, space geodesy replaced the terrestrial methods by providing precise measurements with a high spatial and temporal resolution, global coverage, and temporal data continuity. Moreover, the reduction in costs and time (i.e., installation of instruments, maintenance, weather-dependent acquisitions, data availability) promoted the use of satellite-based methods (e.g., Bürgmann and Thatcher, 2013).
In the following sections, we will describe two satellite-based methods, namely GNSS and InSAR data, and their integration. We will also report some of their applications in active tectonics.

1.2.1. GNSS data

The Global Navigation Satellite System is a geodetic toll based on the use of a constellation of satellites and a receiver on the ground. GNSS includes several networks, such as the USA's *NAVSTAR Global Positioning System* (GPS), the European *Galileo*, the Russian *Global'naya Navigatsionnaya Sputnikovaya Sistema* (GLONASS), and the Chinese's *BeiDou* system.
The method provides 3D position and time data referred to a station on the Earth's surface in every weather condition, with high precision and accuracy.
The principle of GNSS is based on the measurements of the satellite-receiver distances, namely *pseudoranges*. Given the precise position of each satellite through the ephemerides, the receiver's

position can be determined by measuring three satellite-receiver ranges. However, since the GNSS signals are only transmitted by the satellite (i.e., one-way ranging technique) and the receiver clock is not synchronized with the satellite clock, a fourth measurement (i.e., time) is required for the estimation of the position of the receiver itself (e.g., Seeber, 2003). For this reason, the receiver must receive the information provided by a minimum of four visible satellites to ensure the GNSS tracking (Fig. 1.3).

The electromagnetic signal, generated by the atomic oscillator located on the satellite, is characterized by a frequency f0 = 10.23 MHz, corresponding to radio waves in L-band. Specifically, it is divided into three main components (e.g., Seeber, 2003):

1) the carriers (L1 and L2), whose frequency is a multiple of the fundamental frequency f0;
2) the codes (C/A, P, and M) that modulate the carries with a pseudorandom noise (PRN) constituted by a sequence of +1/-1 values to determine the travel time of the signal;
3) the message, containing several data, such as the ephemerids of the satellite, its status, and the satellite clock information.

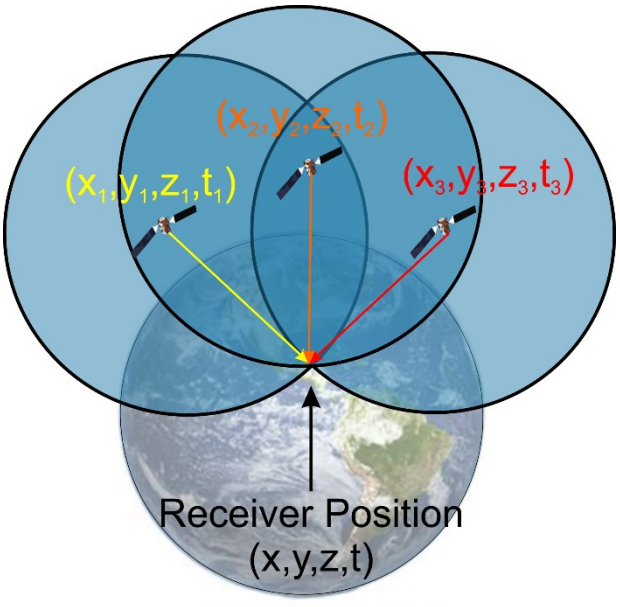

Figure 1.3. Configuration of GNSS method. Satellites-receiver configuration for the estimation of the location of the receiver on the ground. The minimum number of satellites required for localization is four. (Modified from Seeber, 2003).

The main advantages of GNSS data are the high temporal resolution, the data precision and millimetric accuracy, and the capability of data acquisition in every weather condition (e.g., Seeber, 2003). Furthermore, the temporal continuity of the data and the three-dimensional displacement measurements provided by continuous GNSS stations enable the estimation and monitoring of the geological and geophysical processes over longer time intervals. In this case, GNSS receivers are located on a stable monument on a permanent site instead of occasional GNSS receivers, which are employed for temporary surveys (i.e., annual or semi-annual period).

On the other hand, GNSS data are characterized by a lower spatial density, which depends on the number of installed receivers. The measurements are also affected by errors related to the orbits, the atmospheric layers, and the receiver characteristics.

1.2.1.1. GNSS Configuration

The GNSS method is constituted by:

1. *space segment,*
2. *control Segment,*
3. *user segment*.

The s*pace segment* represents the constellation of satellites around the Earth. For the Global Position System (GPS), the constellation is composed of 30 satellites located in six equally-spaced orbital planes (www.gps.gov). The satellites have an orbital inclination of 55 degrees, an orbital height of about 20,200 km, and an orbital period of 12 hours of sidereal time (e.g., Seeber, 2003). In each satellite, an atomic clock, a radio transceiver, computers, a power supply, a propulsion system, and other auxiliary equipment are present (e.g., Hofmann-Wellenhof *et al.*, 2008).
The radio signal is transmitted to the user's receiver to enable the measurement of the *pseudorange* and other information, like the satellite position and the error of the satellite clock.
The Control Segment is responsible for the continuous monitoring and control of the satellites and their positions, the determination of the GNSS System time, the prediction of the satellite ephemerides and clock parameters, and the upload of data messages (Seeber, 2003; Hoofmann-Wellenhof *et al.*, 2008). In the control segment, a master control station (MCS) for the coordination of the system, monitoring stations (MS), and ground antennas (GA) for communication with the satellites are present.
Finally, the user segment is constituted by the instruments (i.e., receiver and antennas) required for detecting the transmitted signal, the software for data processing, storage, and a power supply. They are subdivided into several categories based on applications, such as civilians and military.

1.2.1.2. GNSS Principles

The aim of GNSS is the definition of the location of a user based on the measurements of the distances between the satellites and the user's receiver. In this case, the radio signal is transmitted by the satellite's antenna at a given time. Then, after the propagation through the atmospheric layers, the same signal is detected by the receiver. Considering the satellite's precise position and the signal's propagation velocity, it is possible to extract the satellite-receiver distance given the

difference in time between the receiver and the satellite clocks. The distance is called *pseudorange* (*r*) and can be expressed as:

$$r = (t_2 - t_1) * \mathrm{c} \tag{1.3}$$

with t_1 and t_2 as the satellite and receiver clock time and *c* as the speed of light.
Since each *pseudorange* defines a sphere in space, the use of three satellites enables to determine the user's location.
However, because of the slight difference in synchronization between the two clocks, an offset may be introduced in the estimation of the distance, which should be corrected to obtain the precise range measurement (*R*)

$$R = r + c\delta \tag{1.4}$$

with *δ* as the clock error.
Thus, by using at least four satellites, the three spatial coordinates and the clock error are estimated (Fig. 1.3), and then the location of the user's receiver can be defined.
The high (millimetric) accuracy of the GNSS data is achieved by applying additional post-processing operations to remove errors within the signal.
Indeed, the GNSS measurements can be affected by several error sources.
For example, the slight differences between the satellite's position along the orbit and the precise ephemerides caused by the influence of the moon's and the sun's gravitational forces induce orbital or ephemerides errors.
Even the discrepancies and inaccuracies of the satellite and receiver clocks may introduce an error, affecting the GNSS signal.
The atmospheric layers, such as the ionosphere and the troposphere, may cause some delays during the propagation of the electromagnetic signal due to the presence of ions (ionosphere) and water vapor (troposphere).
The presence of obstacles (e.g., tall buildings and trees) may yield a "bounce" of the signal, introducing a delay in the signal and potentially increasing the range.
The receiver noise can be related to the monumentation, and the phase center variation (e.g., Seeber *et al.*, 2003), whereas other errors, may be introduced because of the processing and the employed instruments.

1.2.2. InSAR data

1.2.2.1. SAR acquisitions

Thanks to Radar (*RAdio Detection And Ranging*) (e.g., Skolnik, 2009) instruments located on satellites, the Synthetic Aperture Radar (SAR) technique enables the acquisition of 2D images for the detection and the localization of targets on the Earth's surface. Based on the phase combination of all the backscattered echoes of a target, it is possible to simulate a virtual large antenna array, increasing the resolution along the azimuth direction with respect to the Real Aperture Radar (Chan and Koo, 2008; Maître, 2008; Fig. 1.4).

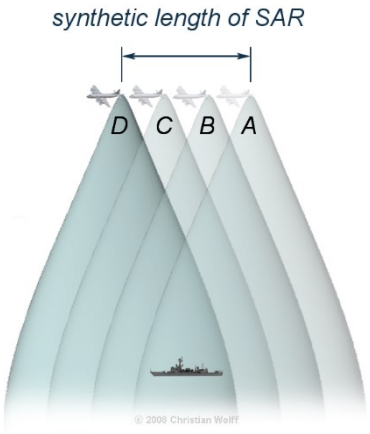

Figure 1.4. Synthetic Aperture Radar. The length of the SAR antenna is measured between the two points A–D, where the beam begins and finishes illuminating the target. The length of the synthetic antenna is longer than the real antenna length, increasing the spatial resolution. (Source: Christian Wolff, http://www.radartutorial.eu/20.airborne/pic/sar_principle.print.png)

According to its definition, the Radar Systems recognize (*Detect*) the characteristics of the targets on the ground and measure their distance (*Range*) with respect to the radar sensor. The radar antenna, the instruments, and the equipment are located on a platform (e.g., a satellite), which moves along the *Azimuth* direction. The radar antenna generates an electromagnetic signal (i.e., microwaves) which is transmitted in the perpendicular direction (*Range*) with respect to the satellite flight track, along the so-called Line-Of-Sight (LOS) direction. As shown in Figure 1.5, the radar beam with a given *Look Angle*, measured from the SAR sensor's projection, illuminates an area on the ground called *Swath.* The portion of the swath area close to the satellite is called *near range,* whereas the *far range* zones are located farthest from the *Nadir* or the intersection point between the ground and the projection of the SAR sensor. The *incidence angle*, measured between the radar beam and the perpendicular line of the Earth's surface, increases from near to the far field. The distance between the SAR sensor and the target, along the LOS direction, is called *Slant-range,* whereas its horizontal projection is called *Ground range*.

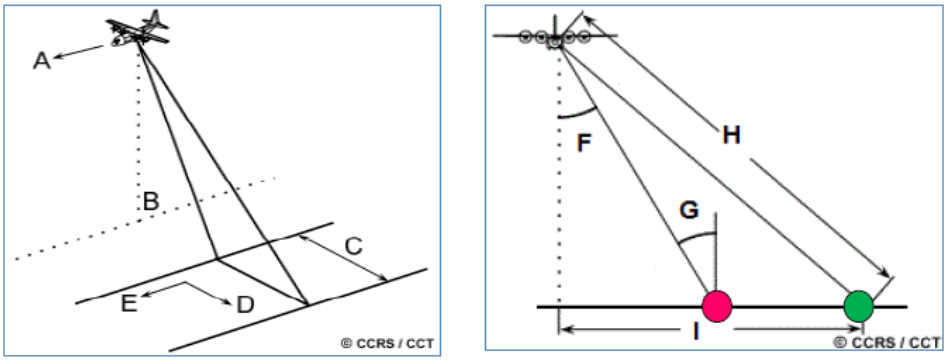

Figure 1.5. Radar Geometric View. A: Flight direction of the platform; B: Nadir point or the intersection point between the Earth's surface and the vertical projection of the SAR sensor; C: Swath or the area on the ground illuminated by the radar beam; D and E: Range and Azimuth directions; F: Look angle or the angle between the projection of the SAR sensor and the radar beam; G: Incident Angle or the angle measured between the radar beam and the normal of the ground surface; H: Slant Range Distance, measured along the LOS of the satellite; I: Ground Range Distance, or the horizontal projection of the Slant Range Distance. The pink point refers to the Near Range, while the green one to the Far Range zone. (Source: Canada Centre of Remote Sensing).

The emitted signal propagates through the atmosphere, where potential delays and other physical phenomena can occur due to the interaction between the beam and the different layers. However, due to longer wavelengths, the microwave beam is less affected by the atmosphere-radiation interactions compared to other electromagnetic signals, which are characterized by shorter wavelengths.

When microwaves reach the ground, three physical phenomena can occur in response to the target-beam interaction: absorption, transmission, and the reflection of the signal. In the case of diffuse reflection, where the radiations are reflected uniformly in all directions, the SAR receiver detects a part of the backscattered signals after the target interaction. On the other hand, the radiations are partly or entirely lost due to the medium absorption, the transmitted radiation through the medium, or the re-orientation of the signal in a unique direction (i.e., specular reflection).

When the receiver detects and processes the backscattered signals, a 2D SAR image of several pixels is generated. Each pixel, representing a ground area of 10-20 meters, contains the amplitude and the phase values of the targets detected by the radar sensor.

In the radar image, the amplitude measures the reflectivity of the targets or the amount of backscattered radiations detected by the SAR sensor (Massonnet and Feigl, 1998). The amplitude is related to several mechanisms which can increase or decrease the amount of backscattered energy, such as the characteristics of the targets, the orientation of the features, and the presence of vegetation (Blom and Elachi, 1981).

The phase depends on the rotation, change in position, and dielectric proprieties of the target on the ground. Furthermore, the phase is also correlated with the range. In the SAR image, the phase appears noisy, characterized by random values in a range of 0° and 360° without providing

meaningful information (Massonnet and Feigl, 1998). Nevertheless, the measurements of the ground displacements that occurred in a given observation period can be computed based on the phase difference between two SAR images. For that reason, we have to introduce SAR Interferometry.

1.2.2.2. SAR Interferometry (InSAR)

The SAR Interferometry or InSAR is a technique based on the measurement of the phase difference between two SAR images acquired from different geometrical views at different times in order to estimate the terrain elevation or the ground displacement with respect to the satellite (Bamler and Hartl, 1998; Goldstein and Werner, 1998; Bürgmann *et al.,* 2000). By exploiting the phase difference between the first and the second acquisition, an interferogram can be generated, showing the changes in dielectric proprieties or the surface motion of a target in terms of fringes or fraction of wavelength (Goldstein *et al.,* 1988; Massonnet and Feigl, 1998; Bürgmann *et al.*, 2000).
Compared to other geodetic approaches, InSAR data present a high spatial resolution, good data accuracy, and global data coverage (Bamler and Hartl, 1998; Goldstein and Werner, 1998; Bürgmann *et al.,* 2000). Conversely, the main limitation is the 1D displacement measurements, expressing a relative movement toward or away from the satellite along its Line-Of-Sight direction. Other disadvantages are the lower temporal resolution, which depends on the revisit time of the satellite, and the decorrelation due to the change in dielectric proprieties of the targets on the ground (e.g., Seeber, 2003).
The slant range or the target-satellite distance along the LOS direction can be estimated using the look angle and the satellite altitude. However, using a single sensor is not sufficient to determine the target's location without any additional information, such as the terrain elevation. Indeed, several points on the ground may be characterized by the same slant-range value, as observed in Figure 1.6 A.

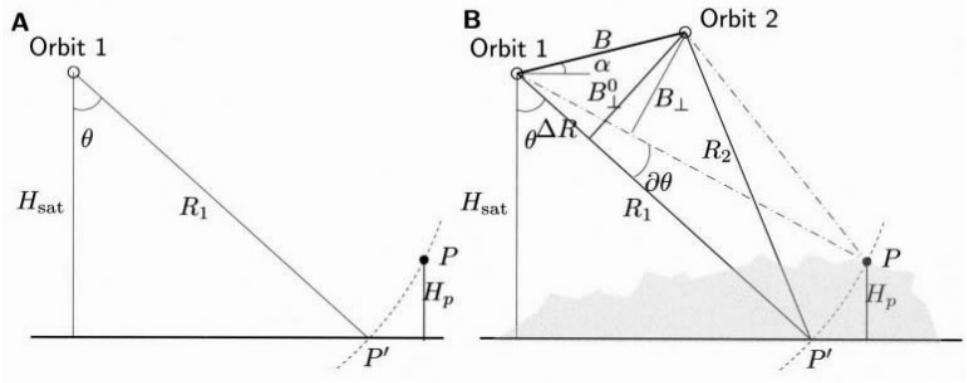

Figure 1.6. Interferometric Configuration. A: Single-Pass configuration with single SAR satellite. The points P and P' cannot be distinguished because their distance from the satellite (range R1) is the same. However, they have different height values (0 for P'; Hp for P). The slant range (R1) can be calculated as a function of the look angle (θ) and the altitude (H_{sat}). B: Repeat-pass Configuration. The distance between two SAR antennas mounted on the same platform

is called baseline (B). The difference in look angle δθ can be determined from the interferometric phase. Given the altitude (H_{sat}) and the range, the height of the point P (H_p) is then measured (From Hanssen, 2001).

Hence, to overcome this limit, two SAR antennas are required to observe the targets on the Earth's surface from different points of view, given the assumption of parallel tracks (Bamler and Hartl, 1998; Hanssen, 2001; Fig. 1.6B). In this case, two configurations can be adopted (Bamler and Hartl, 1998):

1. The single-pass interferometry is generally used for estimating terrain elevation and generating products such as the Digital Elevation Model (DEM). On the satellite platform, two SAR antennas operate at the same time. The distance between the SAR antennas, called Perpendicular or Normal Baseline, is hundreds of meters.
2. The repeat-pass interferometry consists of using a single SAR antenna on a platform that acquires images from a slightly different point of view at different times. This configuration, usually employed for estimating the surface displacements, requires a small Perpendicular Baseline (< 100 meters).

The main aim of tectonic investigations is the estimation of the displacement on the Earth's surface. For that reason, a repeat-pass configuration is required to obtain interferometric products. In the next section, we will describe Differential Interferometry (DInSAR), a technique exploited for these purposes.

1.2.2.3. Differential SAR Interferometry (DInSAR)

The ground deformation due to natural and anthropogenic phenomena can be observed and detected using the Differential Interferometry method applied to SAR images (DInSAR). Based on the measure of the signal phase changes between two satellite images acquired with the same geometry at different times, the DInSAR method provides a high spatial resolution outcome with good data accuracy. The method is based on the measurement of the phase differences between two acquisitions to estimate the ground displacement with respect to the satellite along its Line-Of-Sight (Goldstein *et al.,* 1988; Massonnet and Feigl, 1998; Bamler and Hartl, 1998; Bürgmann *et al.*, 2000; Rosen *et al.*, 2000; Hanssen, 2001).
Considering the repeat-pass configuration, the first (*Master* or *Reference*) and the second image (*Secondary* image) should be ideally acquired under the same viewing geometry. For that reason, the perpendicular baseline, namely the distance between the satellite position during the first and second pass, should be as small as possible to minimize the decorrelation effects (Massonnet and Feigl, 1998; Hanssen, 2001). Furthermore, a short time interval between the acquisitions (i.e., temporal baseline) should be preferred to isolate only the signal derived by the surface displacement.

Hence, since the feasibility of DInSAR strongly depends on the coherence or the similarity between the two radar images, both baselines should be chosen as small as possible.

Once obtained the SAR pair, the signal derived from the first acquisition is combined with the second SAR image. Specifically, every Reference image pixel is multiplied by the corresponding pixel in the coregistered Secondary image (Massonnet and Feigl, 1998; Hanssen, 2001) to obtain the Interferometric Amplitude and the Interferometric Phase.

The Interferometric Phase ($\Delta\phi_{int}$) represents the phase difference between the two complex SAR images, which corresponds to the ground motion that occurred between the two acquisitions with respect to the satellite (Fig. 1.7) and can be written as:

$$\Delta\phi_{int} = \frac{4\pi}{\lambda}\Delta R \tag{1.5}$$

Where λ is the SAR wavelength, which depends on the characteristics of the satellite, and ΔR is the shift in the slant range direction.

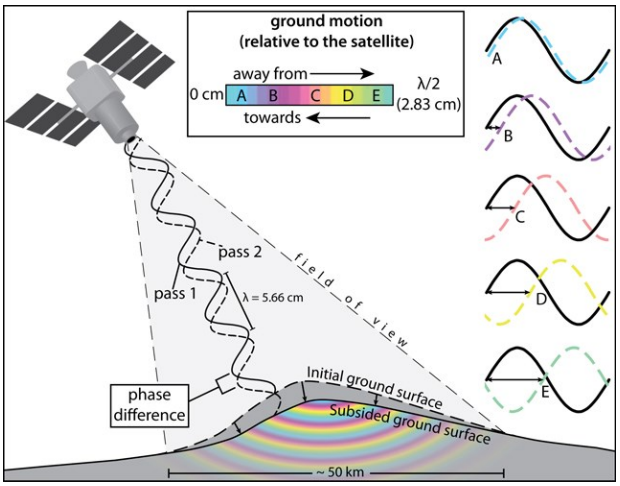

Figure 1.7. InSAR Configuration. The first pass of the satellite collects an image of the surface along LOS (solid waves). After a given period of time, the satellite acquires another image of the same area (dashed waves) from the same (or nearly) viewing geometry. Comparing the phases of the two complex backscattered signals makes it possible to estimate the surface displacement during the two acquisitions. In the case of ground motion, the second phase is not aligned with the first one, as shown in the figure. The phase difference between the two satellite acquisitions, expressed in terms of colored fringes, is converted into a surface displacement with respect to the satellite along its LOS, showing a movement toward or away from the satellite itself. A phase fringe corresponds to half of the wavelength, which is 28 mm in the case of C-band SAR sensors. (Source: www.volcano.si.edu)

The interferometric phase (ϕ_{int}) is the sum of several contributions related to displacement, topography, atmospheric propagation, orbital trajectories, and noise (e.g., scattering, thermal noise) (Massonnet and Feigl, 1998).

$$\phi_{int} = \phi_{topo} + \phi_{atmo} + \phi_{orb} + \phi_{noise} + \frac{4\pi}{\lambda}\Delta R \quad (1.6)$$

The topographic phase contribution (ϕ_{topo}) is related to the different acquisition geometry, which involves the generation of fringes that mimic the local topography (Massonnet and Feigl, 1998). The phase contribution related to the atmosphere (ϕ_{atmo}) deals with the presence of the ionosphere and the troposphere, which can affect the measurements of the radar-target distance by adding some delays during the propagation of the electromagnetic signal.

Shifts and inaccuracies in orbital trajectories (ϕ_{orb}) during the SAR acquisitions may also affect the interferometric phase by adding orbital fringes. Finally, other contributions (ϕ_{noise}) dealing with the radar instruments or changes of the scatterers on the ground may generate extra phase fringes.

Based on these considerations, the way to isolate the phase contribution related to the surface displacement is to estimate and remove the other contributions.

The topographic fringes strictly depend on the perpendicular baseline values, implying an increase in topographic phase contribution in the case of a large spatial baseline. Since the viewing geometry of the satellite during the first acquisition is slightly different from the second pass, a given number of fringes correlated with the topography may be present. For that reason, using a Digital Elevation Model (DEM), a Synthetic Interferogram can be estimated and removed from the original interferogram to remove the topographic phase (Rosen *et al.*, 2000). Further operations, such as the use of filters, are then applied to minimize the effects of the other extra phase contributions (e.g., atmospheric effects, orbit trajectory inaccuracies, and noises).

The resulting Differential Interferogram (DInSAR) will express, in terms of fringes, the occurred phase shift along the satellite LOS.

Each fringe defines a phase shift of 2π radians corresponding to half of the SAR wavelength. In case of C-band satellite, each fringe corresponds to 28 mm of displacement (Bürgmann *et al.*, 2000). At this stage, the InSAR interferogram presents several fringes corresponding to multiple half wavelengths. The “wrapped” interferogram should then be " unwrapped " to obtain a unique phase ramp without discontinuities. The operation is performed by integrating all the fringes from an arbitrary reference point (Massonnet and Feigl, 1998; Dudczyk and Kawalec, 2014). Finally, after the phase-to-displacement conversion and the geocoding step, a LOS surface displacement map is obtained.

Since the satellites can acquire the SAR images along the ascending (from South to North) and descending (from North to South) orbit tracks (Fig. 1.8), two LOS datasets may be combined to extract the displacement field along the east-west and vertical directions (see Section 2.2.2).

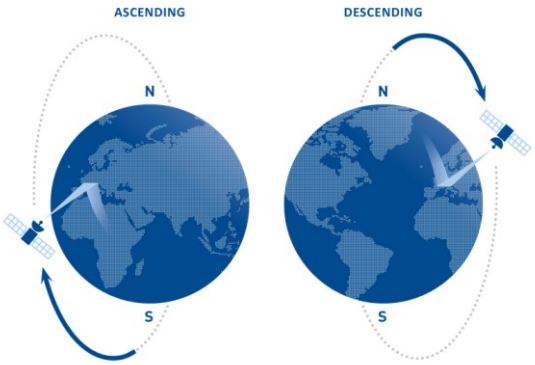

Figure 1.8. SAR satellite acquisition. The satellites acquire SAR images along the descending (from North to South) and the ascending (from South to North) orbit track. (Source: www.site.tre-altamira.com)

Based on the acquisition of the two radar images before and after the event, the method has been successfully applied to study several phenomena, such as the coseismic and post-seismic deformation (Massonnet *et al.*, 1993; Stramondo *et al.*, 1999; Wright *et al.*, 2003; Ryder *et al.*, 2007; Delouis *et al.*, 2010; Pezzo *et al.*, 2013; Ozawa *et al.*, 2016; Cheloni *et al.*, 2017).

However, the classic DInSAR method cannot be suitable for monitoring purposes and detecting changes related to slow phenomena over longer temporal intervals. Indeed, the approach presents some limitations dealing with the temporal and geometrical decorrelation and the effects of the atmospheric contribution. Temporal decorrelation increases with a large temporal baseline, preventing the detection of stable points, especially in vegetated and non-coherent areas. Similarly, spatial decorrelation related to the perpendicular baseline and the superimposed atmospheric contribution (atmospheric phase screen - APS), due to the tropospheric and ionospheric layers, may reduce the estimation of the deformation (Goldstein, 1995; Zebker *et al.,* 1997; Hanssen, 2001; Bechor and Zebker, 2006).

Hence, to overcome the limits of classic differential interferometry, a different approach must be introduced: Multi-Temporal Interferometry.

1.2.2.4. Multi-Temporal Interferometry (MT-InSAR): PSI and SBAS

Multi-Temporal Interferometry (MT-InSAR) estimates millimetric surface displacements over large areas during a given observation period by identifying targets extracted from a SAR image stack.

Persistent Scatterers Interferometry (PSI) and Small Baseline Subset (SBAS) represent two of these MT-InSAR approaches that have been developed and used to generate mean ground velocity maps.

The first method was proposed by Ferretti *et al.* (2001), focusing on the extraction of pixels dominated by bright and temporally stable scatterers (Persistent Scatterers –PSs) (Fig. 1.9B). Based on the original PSInSAR™ algorithm, the potential PSs can be extracted from a single master-stack

of differential interferograms and then selected if their phase variable can be compared to a priori linear deformation model.

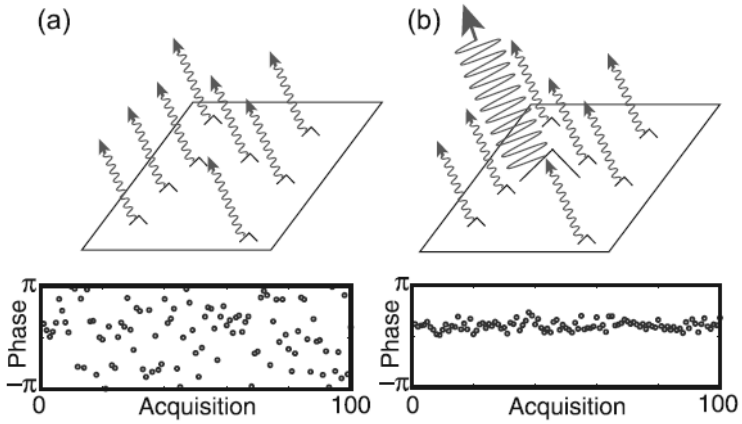

Figure 1.9. Comparison between Distributed and Persistent Scatterers. A) The DS pixel is characterized by the sum of the backscattered signals generated by several small objects on the ground, while the PS pixel (B) is mainly dominated by the presence of one bright object. On the bottom, the resulting plot shows higher phase stability in PS than DS pixels during the observation period. (From Hooper *et al.,* 2007)

The main advantages of this approach are good coherence despite large baselines of interferograms, low geometrical decorrelation despite large baselines, and millimetric precision for detecting surface displacements (Ferretti *et al.,* 2001; Crosetto *et al.,* 2016). The robustness of the method and the ability to detect high reliable scattering structures make it a valuable approach that can be applied to urban areas with high population density (Ferretti *et al.*, 2001). Conversely, the method is not so stable in case of application in non-urban areas, where the density of man-made structures is low, and if the deformation is not linear and not known a priori (Hooper *et al.*, 2007; Crosetto *et al.*, 2009; Virk *et al.*, 2018).

On the other hand, the SBAS method, based on a combination of a large number of interferograms characterized by small temporal and geometrical baselines and their related inversion, aims to identify distributed scatterers with homogeneous characteristics (Berardino *et al.*, 2002; Lanari *et al.*, 2004; Fig. 1.9A). In this case, the detected pixels are characterized by the presence of several scattering objects, whereas, for PSI, the pixels are mainly dominated by a single, stable, and high coherent scatterer (Fig. 1.9). The different approach of SBAS determines a higher spatial coverage, especially in rural and non-urban areas, with respect to the lower spatial density provided by PSI. On the other hand, in PSI methods, no constraints in temporal/spatial baselines are required with respect to the SBAS approach (Lanari *et al.*, 2004). In addition, in several SBAS algorithms, the data are characterized by a lower resolution due to the application of multilooking filters to reduce the decorrelation noise (Berardino *et al.*, 2002).

In the last 20 years, many techniques, algorithms, and software have been developed and employed in different studies, like PSInSAR™ (Ferretti *et a*l., 2001), Small BAseline Subset (SBAS) technique (Berardino *et al.*, 2002), Coherent Pixels Technique (CPT) (Mora *et al.*, 2003; Blanco-Sanchez et

al., 2008), Interferometric Point Target Analysis (IPTA) (Werner *et al*., 2003), SqueeSAR™ (Ferretti *et al.,* 2011), Stanford Method for Persistent Scatterers (StaMPS) (Hooper *et al*. 2007, 2012). To summarize, Table 1.1 lists the different MT-InSAR methods and their relative characteristics based on baseline configuration, pixel selection criterion, and deformation model.

Method reference	Baseline configuration	Pixel selection criterion	Deformation model
Ferretti et al., 2000, 2001	Single Master	Amplitude dispersion	Linear deformation in time
Berardino et al., *2002*	Small baselines	Coherence	Spatial smoothness
Mora et al., 2003	Small baselines	Coherence	Linear deformation in time
Schmidt and Bürgmann, 2003	Small baselines	Coherence	Spatial and temporal smoothness
Werner et al., 2003	Single master	Amplitude dispersion and spectral phase diversity	Linear Deformation in time
Duro et al., 2003; Crosetto et al., 2008	Small baselines	Amplitude dispersion, coherence, spectral coherence	Linear deformation in time
Kampes, 2006	Single master	Amplitude dispersion and signal to clutter ratio	Different types of deformation models
Hooper et al., 2004	Single master	Amplitude and phase criterion	Spatial smoothness
Crosetto et al., *2005*	Small baselines	Coherence	Stepwise linear function in time
Costantini et al., *2008*	Single master	Amplitude dispersion	Spatial smoothness
López-Quiroz et al., 2009	Small baselines	Coherence	Deformation model in time
Ferretti et al., *2011*	Single master after triangulation	Statistical homogeneity test	Linear deformation in time
Perissin and Wang, 2012	Target-dependent interferogram subset	Quasi-PS approach	Different types of deformation models
Hetland et al., 2012	Small baselines	Coherence	Different types of deformation models

Van Leijen, 2014	Single master	Amplitude dispersion	Different types of deformation models
Goel and Adam, 2014	Small baselines	Statistical homogeneity test	Linear deformation in time
Lv et al., 2014	Single master	Statistical heterogeneity test	Linear deformation in time
Devanthéry et al., 2014	Small baselines	Amplitude dispersion and Cousin PS	Spatial smoothness

Table 1.1. Comparison of different MT-InSAR approaches. From Crosetto *et al.,* 2016.

1.2.3. GNSS-InSAR integration

As explained in the previous Sections (1.2.1 and 1.2.2), GNSS and InSAR methods present several strengths and weaknesses, as synthesized in Table 1.2.

	Continuous GNSS	**DInSAR**
Strengths	High temporal density	High spatial density
	3-D positioning	Remotely sensed
	mm-accuracy	No monumentation necessary
Weaknesses	Limited spatial density	Limited temporal density
	Stable monumentation	1-D scalar measurement
	Siting difficulties	Image decorrelation

Table 1.2. Comparison between GNSS and InSAR methods. (From Seeber, 2003)

Since the two methods appear complementary, the combination of the two geodetic techniques should overcome the limitations of the single method and improve the final surface measurements. Hence, many studies proposed different approaches to combine and integrate these two methods. For example, GNSS data have been used for InSAR and MTInSAR calibration, for InSAR and MTInSAR comparison and validation, and for the estimation and the correction of the atmospheric effects due to ionospheric and tropospheric delays in MTInSAR processing (Del Soldato *et al.*, 2021). Because InSAR-MTInSAR measurements are relative and potentially residual errors (i.e., atmospheric and orbital contributions) may be present in the datasets, GNSS data can be integrated by computing a calibration. The calibration allows estimating a 2-D surface and a relative offset to correct the misfits between the two geodetic datasets.

The method consists of the calculation of scatterers' velocities (or displacement) around each GNSS site. Since GNSS sites and scatterers are not usually located in the same spot, a median value of the scatterers' velocities (displacements) can be calculated by considering the nearby pixels at a given distance from each GNSS site. In some cases, the radius is fixed (e.g., Feng *et al.*, 2012; Farolfi *et al.*, 2019a), whereas in others, the number of scatterers is fixed, and the radius is variable (e.g., Henriquet *et al.*, 2022). Once the median InSAR values are obtained, and after the projection along LOS of GNSS data, the differences between InSAR and GNSS velocities (or displacements) are minimized by estimating a 2-D surface and a related offset through the application of a weighted least squares method. Specifically, the estimated bidimensional surface can be planar (i.e., linear calibration model) for short strips acquisitions (i.e., 1-2 frames)(Feng *et al.*, 2012) or quadratic (e.g., Lohman and Simons, 2005; Biggs *et al.*, 2007).

After the calibration, the outcome is evaluated, and the standard deviation of the residuals can also be used to define the accuracy of the InSAR measurements (e.g., Chaussard *et al.*, 2016). A following comparison between the geodetic datasets can help observe and discuss the potential discrepancies between GNSS and SAR data after the calibration.

1.2.4. Applications

Regarding active tectonic investigations, satellite-based geodesy has been exploited in order to detect the deformation patterns, measure the surface displacement and rates, and correlate them with the faults and tectonic structures in the study area. As explained in the previous chapters, surface displacements represent the visible, detectable, and measurable effects in response to the subsurface processes related to the so-called earthquake cycle (see Section 1.1).

Regarding the co-seismic and post-seismic displacements, geodetic data allow the measurement of the surface displacement provoked by the occurrence of a mainshock and related aftershocks.

GNSS data were used for the first time to detect the coseismic displacement that occurred in October 1989 for the Mw 7.1 Loma Prieta earthquake in San Francisco (California). The strike-slip event caused a rupture of 37 km along the strike of the San Andreas fault at a depth of 5 to 17.5 km. Based on the geodetic data, the resulting modeled dextral strike-slip and the reverse slip were estimated with values of 1.6 m and 1.2 m, respectively (Lisowski *et al.*, 1990).

A few years later, InSAR data were tested for the first time in another event in California: the 1992 Landers earthquake. The Mw 7.3 strike-slip event, followed by another seismic event (Mw 6.2), caused a coseismic displacement, which was estimated to be up to 50 cm of range change due to the horizontal and vertical motion thanks to ERS satellite (Massonnet *et al.*, 1993; Zebker and Rosen, 1994; Fig. 1.10).

Since the Landers earthquake, many studies have been conducted using InSAR data and integrating InSAR and GNSS measurements to estimate the near and far-field displacements. In addition, the

data have also been used to model the fault source and define the geometrical and kinematic parameters.

Here, we report some co-seismic and post-seismic studies focused on seismic events in California (Wdowinski *et al.*, 1997; Barbot *et al.* 2008, 2009; Zeng and Shen, 2014; Shen and Liu, 2020), in Mexico (Gonzalez-Ortega *et al.*, 2014; Rollins *et al.,* 2015; Wen *et al.*, 2021), in Chile (Delouis *et al.,* 2010), in the Himalaya-Tibet region (Ryder *et al.*, 2007), in the Anatolian region (Vajedian *et al.*, 2018; Yang *et al.*, 2019), in Japan (Feng *et al.*, 2012; Iinuma *et al.*, 2011; Moya *et al.*, 2017), and in Italy (Stramondo *et al.*, 1999; Giuliani *et al.*, 2007; Anzidei *et al.*, 2009; Atzori *et al.*, 2009; Serpelloni *et al.*, 2012; Pezzo *et al.*, 2013; Cheloni *et al.*, 2017).

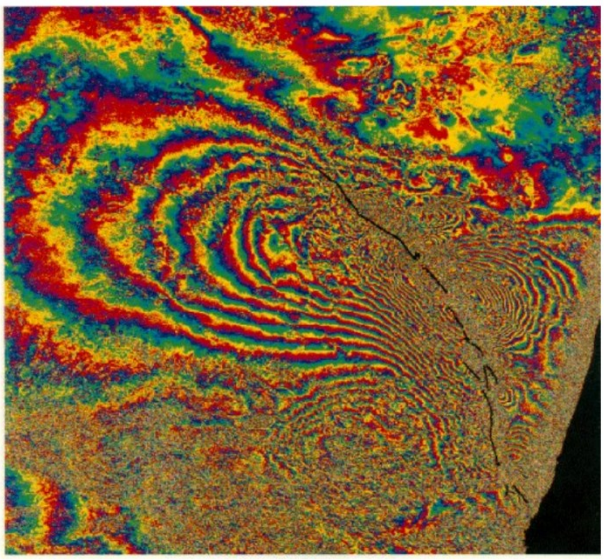

Figure 1.10. Coseismic interferogram of Landers earthquake. Each fringe corresponds to 28 mm of range change. The black lines indicate the fault surface ruptures. (From Massonnet *et al.*, 1993).

In the most active tectonics areas in the world, some investigations focused on the estimation of interseismic deformation by using geodetic data. Several studies have been carried out in the Himalaya-Tibet region (Grandin *et al.*, 2012; Liu *et al.*, 2018), California (Wang *et al.*, 2003; Fialko, 2006; Tong *et al.,* 2013; Chaussard *et al.*, 2016), and Anatolia (Wright *et al.*, 2001; Walters *et al.*, 2011; Wang and Wright, 2012; Karimzadeh *et al.*, 2013; Hussain *et al.*, 2016; Weiss *et al.*, 2020). In these regions, the InSAR-GNSS combined approach has provided valuable information about the deformation patterns in the study area. The geometry and the kinematics of the deeper portion of the active faults have also been extracted using the geodetic data as input for the modeling. Among these parameters, the estimation of the aseismic slip rate and the locking depth helped define the seismogenic potential of the investigated tectonic structures. In addition, further investigations have been carried out for seismic hazard purposes, like interseismic coupling.

In Italy, the most active tectonic areas have been investigated with geodetic data.

For example, some studies focused on the estimation of the velocity and strain-rate fields in central Italy (i.e., northern Adria and the central Apennines) in light of the seismic sequences of L'Aquila (2009), Emilia (2012), and Amatrice (2016-2017). Galvani *et al*. (2012) and Pezzo *et al*. (2015, 2020b) analyzed the velocity and strain-rate fields derived from GPS only and InSAR-GPS combination to detect the velocity gradients, extract the fault source parameters through modeling, and discuss the seismic potential of the structures in the study area.

Despite the low convergence rates, many studies have been conducted in Northeastern Italy, across the Southeastern Alps and the External Dinaric system. For example, in D'Agostino *et al.* (2005), the continuous GPS (cGPS) measurements and the use of dislocation models allowed the determination of the geometry and the kinematic parameters of the tectonic structures by comparing the results with the seismicity. Based on GPS data, Bechtold *et al.* (2009) focused more on the interaction between the Alpine and Dinaric systems by running an inversion with a 3-D kinematic model to better estimate the indenter tectonics and the oblique Adria-Eurasia collision in the study area. Cheloni *et al*. (2014) and Serpelloni *et al*. (2016) exploited the dense network of cGPS to estimate the velocity and strain-rate fields across the Southeastern Alps. Based on these measurements, they also extracted the geometry and the kinematic parameters of the tectonic structures by running some inversions, computed the interseismic coupling to discriminate the seismic and aseismic areas, and finally discussed the seismic potential and the earthquake recurrence. Even Barba *et al*. (2013) worked on the seismic potential using GPS and leveling data, focusing more on the Montello thrust. Regarding the same area, the recent work of Anderlini *et al.* (2020) employed GPS, InSAR, and leveling data to estimate the interseismic surface displacement rates and correlated the detected gradients to the active tectonic structures through a model inversion.

The success of these investigations, the improvements of the geodetic methods, and the increasing data availability further promoted the applications of these techniques in tectonics studies, even in areas characterized by low deformation rates, such as Northeastern Italy.

1.3. Geological setting

Northeastern Italy is a complex region characterized by the interaction of two orogenic belts: the Southeastern Alps and the External Dinarides, located in the northern and northeastern sectors of the study area. The foreland basin of these orogens is the Venetian-Friulian plain located in the southern part of the region (Fig. 1.11A).

In the study area, the lithostratigraphic sequence consists of a Paleozoic crystalline basement, covered by a thick succession of carbonate rocks due to the deposition in basin and platform environments during the Mesozoic (Nicolich *et al.*, 2004; Fantoni and Franciosi, 2010; Masetti *et al.*, 2012). Tertiary terrigenous layers (i.e., flysch and clastic deposits) related to the erosion of the Alpine-Dinaric chain and the deposition of Quaternary sediments in shallow-marine and non-marine

(alluvial deposits) environments complete the sequence (Mellere *et al.*, 2000; Nicolich *et al.*, 2004; Fantoni and Franciosi, 2010; Toscani *et al.*, 2016; Fig. 1.11C).

Northeastern Italy is subjected to an active convergent regime due to the Adria-Eurasia continent-continent collision with estimated rates of ~1.5-3 mm/yr (Battaglia *et al.,* 2004; D'Agostino *et al.*, 2005; Bechtold *et al.*, 2009; Cheloni *et al.*, 2014; Serpelloni *et al.,* 2016). The N-S convergence is accommodated by thrusting and faulting in the Southeastern Alps and the External Dinarides. These orogens derive from the superposition of three main tectonic phases from the Late-Cretaceous- to the present day (Fig. 1.11A).

During the Mesozoic, the region was affected by an extensional phase, which influenced the evolution of carbonate platforms and a basin. In particular, from the Triassic to the Cretaceous, two thick carbonate platforms, i.e., the Trento Platform in the western sector and the Friuli Platform to the east, have been developed (Nicolich *et al.*, 2004; Masetti *et al.*, 2012). The Trento platform is characterized by Early Jurassic shallow-water sedimentary layers and condensed pelagic units, which were deposited after a subsequent drowning phase (Bosellini *et al.*, 1981; Masetti *et al.*, 2012). On the other hand, the Friuli Platform is characterized by thick shallow-water carbonate units from the Jurassic to the Cretaceous (Masetti *et al.*, 2012).

The two carbonate platforms were divided by the Belluno-Northern Adriatic basin, developed during the Early Jurassic rifting and filled by carbonate sediments from the adjacent platforms, mainly from the Friuli platform, through gravity-flow processes (i.e., debris flows, turbidites) (Bosellini *et al.*, 1981; Nicolich *et al.*, 2004; Masetti *et al.*, 2012). Finally, during Paleogene, a small and shallow basin was formed in the northern part of the Friuli platform (Placer *et al.,* 2010; Fig. 1.11B).

From the Cenozoic, three main compressional phases occurred in the area, involving the formation and development of the Alpine and Dinaric chains.

The first compressional event occurred from Cretaceous to Late Eocene, generating the NW–SE-trending External Dinarides thrust system (e.g., Doglioni and Bosellini, 1987; Castellarin and Cantelli, 2000). In particular, in the northeast sector of the Friuli Platform, a new accommodation space was created, and the basin was then filled by turbiditic sequences (Flysch) derived from the erosion of the Dinaric chain (Nicolich *et al.*, 2004; Toscani *et al.*, 2016).

From Serravallian to Messinian, the second phase (Alpine phase) was the principal responsible for the formation and development of the Alpine chain, especially the Southern Alps (Doglioni and Bosellini, 1987; Bressan *et al.*, 2003). Indeed, an intense compression NNW-SSE-oriented caused the partial reactivation and the counterclockwise rotation of the Dinaric thrusts and the subsequent generation of ENE-SWS south-verging thrusts and folds (Castellarin and Cantelli, 2000; Bressan *et al.*, 2016). Finally, from the Late Messinian to the present day (Neo-alpine phase), new southeast-verging thrust-and-fold- systems developed in the central-eastern sector of the Southern Alps due to the rotation of the maximum stress axis northward (Doglioni and Bosellini, 1987; Castellarin and Cantelli, 2000). Meanwhile, major strike-slip faults developed in the eastern sector, some of them

partially reusing pre-existing thrusts (Vrabec and Fodor, 2006). These two tectonic phases substantially impacted the deposition of thick sedimentary layers in the foreland basin covering the Venetian-Friulian plain due to the intense erosion of the Southern Alps (Nicolich *et al.*, 2004; Toscani *et al.*, 2016). The sedimentary succession, controlled by the Cenozoic tectonic phases and the successive eustatic sea-level changes, was deposited in shallow-marine and non-marine (Quaternary alluvial deposits) environments (Mellere *et al.*, 2000; Toscani *et al.*, 2016).

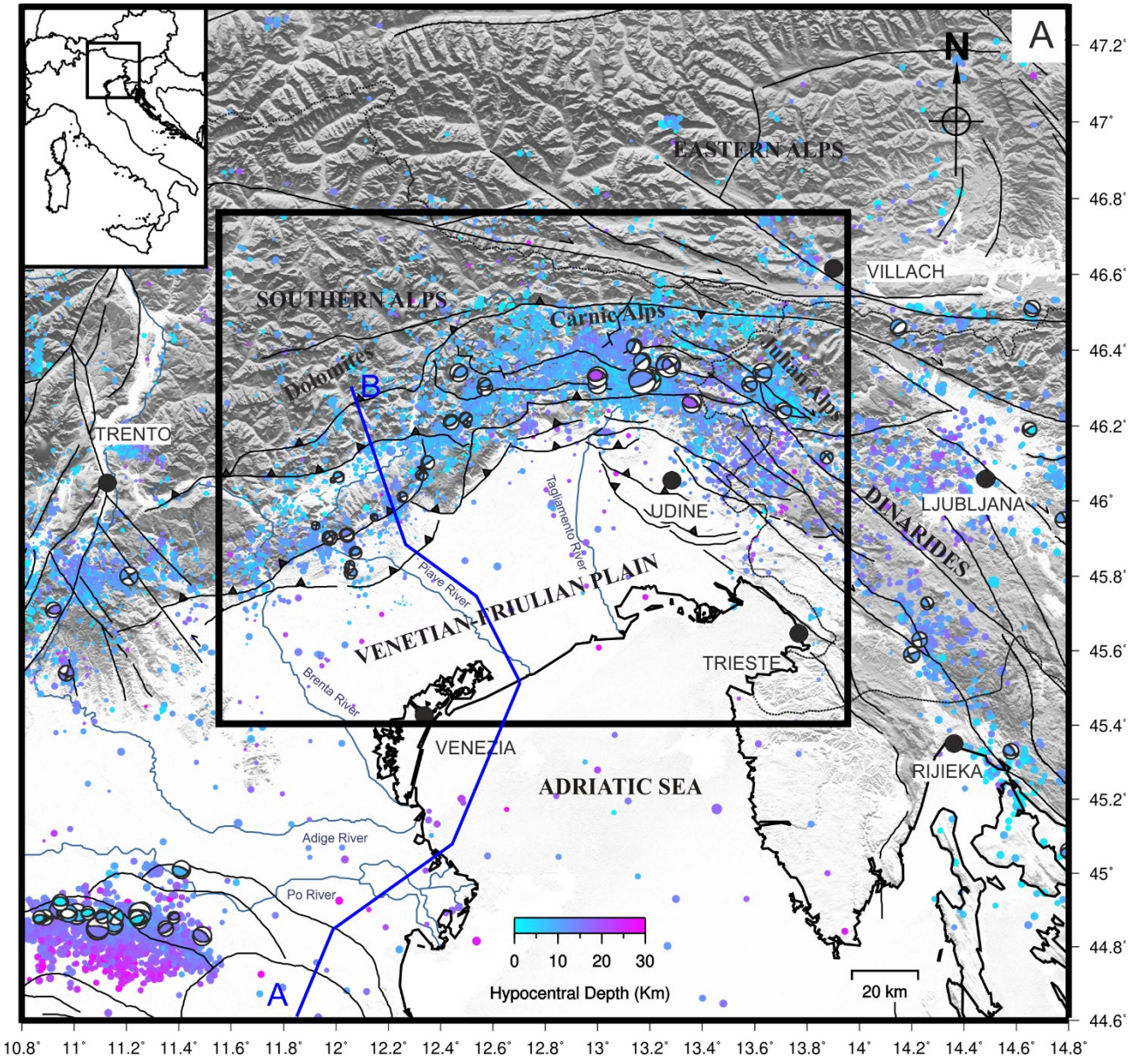

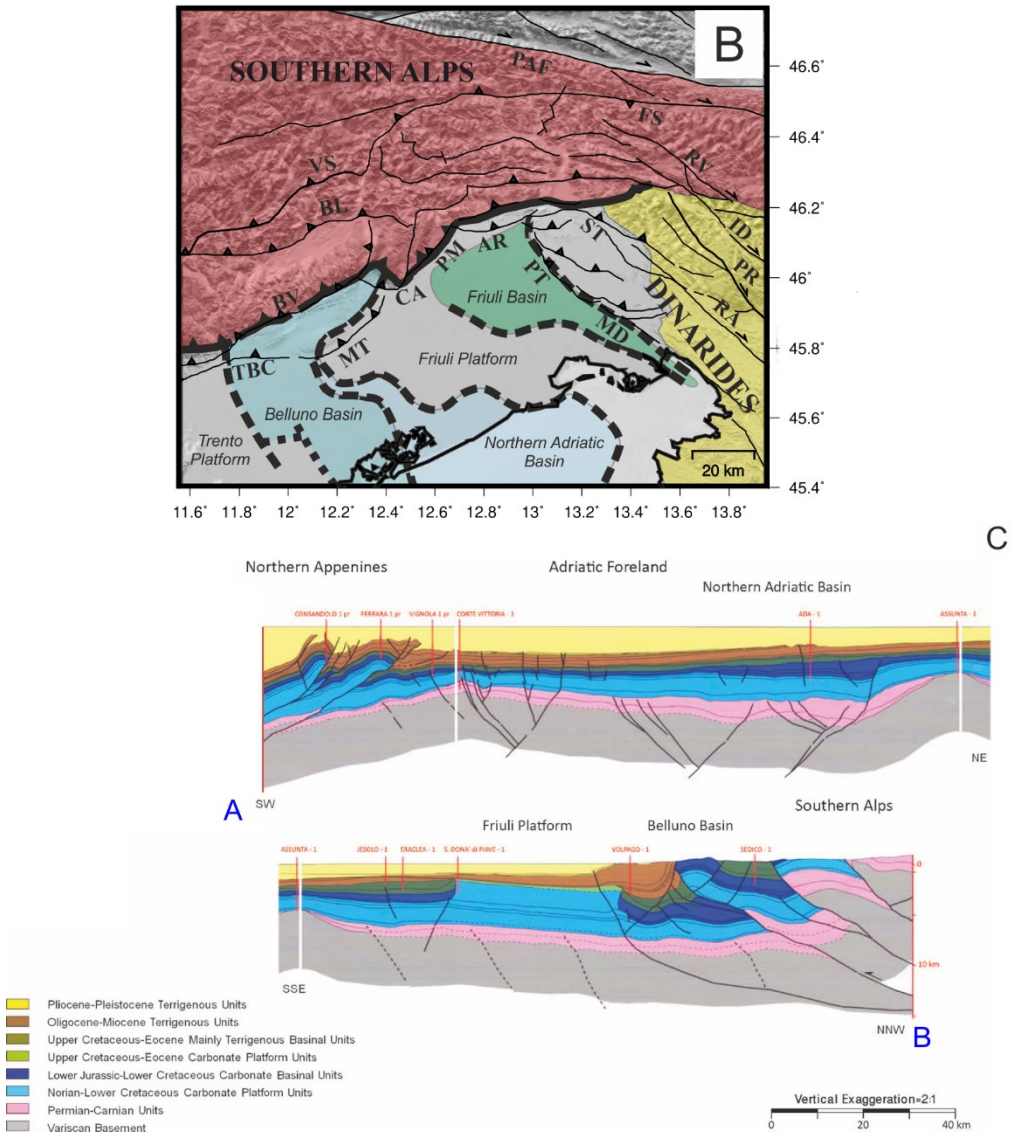

Figure 1.11. Seismotectonic map of the study area. A) The map shows the seismicity and tectonics of the region. The blue-purple circles represent the instrumental seismicity for the 2000-2017 time span provided by OGS bulletins (http://www.crs.inogs.it/bollettino/RSFVG) with focal mechanisms (from Anselmi *et al.*, 2011; Danesi *et al.*, 2015; Serpelloni *et al.*, 2016). The blue line indicates the trace of the profile. B) The map shows the main tectonic structures (black lines) belonging to the Southern Alps (red area) and the Dinarides (yellow area). The dashed black lines indicate the borders of the Trento and Friuli platforms (grey areas), which are separated from the Belluno–Northern Adriatic (light blue areas) and the Friulian Basin (green area). (AR: Arba-Ragogna thrust; BL: Belluno thrust; BV: Bassano-Valdobbiadene thrust; CA: Cansiglio thrust; FS: Fella-Sava line; ID: Idrija fault; MD: Medea thrust; MT: Montello thrust; PAF: Periadriatic fault; PM: Polcenigo-Maniago thrust; PR: Predjama fault; PT: Pozzuolo thrust; RA: Raša fault; RV: Ravne Fault; ST: Susans-Tricesimo thrust; TBC: Thiene-Bassano-Cornuda thrusts; VS: Valsugana thrust). C) Geologic section through the Southeastern Alps and the Adriatic foreland. The white column represents the junction of the seismic lines (Modified from Fantoni and Franciosi, 2008).

As a result of these tectonic phases, the present-day tectonic setting of the western area (i.e., Dolomites, Fig. 1.11A) is mainly dominated by the presence of ENE-trending, southeast-verging thrusts and folds, such as the Valsugana thrust, the Belluno thrust, the Bassano-Valdobbiadene

thrust in the inner sectors, and the external thrust front including, from west to east, Thiene-Bassano-Cornuda, Montello, Cansiglio, Polcenigo-Maniago and Arba-Ragogna thrusts (Galadini *et al.*, 2005; Burrato *et al.*, 2008; Fig. 1.11B). Along the front, the seismic activity is low and mainly concentrated in the north, with a predominant hypocentral depth of ~10 km (Bressan *et al.,* 2003). However, based on historical seismicity and geological evidence, many of these structures can be considered potentially seismogenic and capable of generating moderate/strong earthquakes (Galadini *et al.,* 2005; Burrato *et al.*, 2008). East of Belluno, high-angle dipping faults are present due to the Neoalpine reactivation of paleofaults in a transpressive sinistral regime. Even in this case, the seismic activity is low (Bressan *et al.,* 2003).

In the central sector, where the interaction of the Alpine (the Carnic and the Julian Alps; Fig. 1.11A) and Dinaric systems is most active, the south-verging thrust-and-fold system tends to be mainly E-W-oriented, as, for example, the Periadriatic thrust and the Susans-Tricesimo line (Galadini *et al.,* 2005; Burrato *et al.*, 2008; Bressan *et al.*, 2018). However, several reactivated NW-SE-oriented structures can be observed in the area (Merlini *et al.*, 2002). Based on the instrumental and historical catalogs, the seismicity is moderate and characterized by a hypocentral depth of 7-12 km (Burrato *et al.*, 2008). Here, the destructive 1976 Friuli sequence hit the area near Gemona with a mainshock of Mw 6.4 and several aftershocks of Mw > 5 (Aoudia *et al.*, 2000; Carulli and Slejko, 2005). According to literature, the events were caused by the activity of thrusts and blind tectonic structures, such as the Susans-Tricesimo thrust, revealing the great seismogenic potentials of the faults involved in the area (Poli *et al.*, 2002; Galadini *et al.*, 2005; Poli and Zanferrari, 2018). Moving northward, high-angle east-west thrusts and backthrusts dominate the region, characterized by low seismic activity. Here, transcurrent and extensional faults are also present.

The eastern sector presents NW-SE-oriented, sub-vertical, dextral strike-slip faults belonging to the External Dinaric system, such as the Raša, Predjama, Idrija, and Ravne faults (Burrato *et al.*, 2008; Bechtold *et al.*, 2009; Moulin *et al.*, 2016; Atanackov *et al.*, 2021). The seismicity is mainly focused on the junction between the Southeastern Alps and Dinarides, as testified by the 1998 Bovec-Krn earthquake (Mw 5.6) and the recent 2004 Mw 5.2 Bovec event that occurred on the Ravne fault (Bajc *et al.*, 2001; Bressan *et al.,* 2003; Kastelic *et al.*, 2008).

The Dinaric system is today interrupted along the Fella-Sava fault, a transpressional fault located in the northeastern sector, which accommodates a large part of the right-lateral motion between the Eastern Southern Alps and the Eastern Alps (Serpelloni *et al.,* 2016).

Finally, the Friulian plain is characterized by the presence of south-verging thrusts, especially around Udine, like the Udine-Buttrio and Medea thrusts, buried by the thick Quaternary sediment cover (Burrato *et al.*, 2008; Viscolani *et al.*, 2020). Despite the low seismic activity, based on geological evidence, the tectonic structures are potentially capable of generating earthquakes (Galadini *et al.*, 2005; Burrato *et al.*, 2008).

2. METHOD

2.1. InSAR Data

2.1.1. Sentinel-1 Data

The European Spatial Agency developed several Sentinel missions within the Copernicus program. The Sentinel-1 mission consists of two near-polar orbiting satellites, which acquire C-band radar images with medium-high resolution in every weather condition, day and night. The purpose of Sentinel-1 is the data acquisition and monitoring of oceans, land surface, and cryosphere (Malenovský *et al.*, 2012).

The satellite orbit is sun-synchronous, near-polar, and circular, with an inclination of 98.18 degrees, an orbital height of 693 km, and a repeat cycle of 12 days. The Sentinel-1A/B satellites, launched on 3 April 2014 and 25 April 2016, respectively, share the same orbit with 180° of orbital phasing difference, moving within an orbital Earth fixed "tube" of 50m radius and providing a 6-days images acquisition (Torres *et al.*, 2012). Such configuration enables the data acquisition along the ascending (from South to North) and descending (from North to South) orbit tracks.

Sentinel-1 is equipped with a C-band SAR instrument (5.405 GHz) supporting a dual-polarization, a right-looking active phased array antenna for scanning elevation and azimuth, and a data storage (Torres *et al.,* 2012). The images can be acquired in four modes, which are Stripmap (SM), Interferometric Wide swath (IW), Extra-Wide swath (EW), and Wave mode (WV) (Fig. 2.1). The table reports the different characteristics.

Mode	**Swath**	**Spatial Resolution (range and azimuth)**
Strip Map Mode	80 km	5x5 m
Interferometric Wide Swath	250 km	5x20 m
Extra-Wide Swath Mode	400 km	25x100 m
Wave-Mode	20 km	5x20 m

Table 2.1. Sentinel-1 acquisition mode. The table reports the characteristics of the acquisition modes in terms of swath width and spatial resolution.

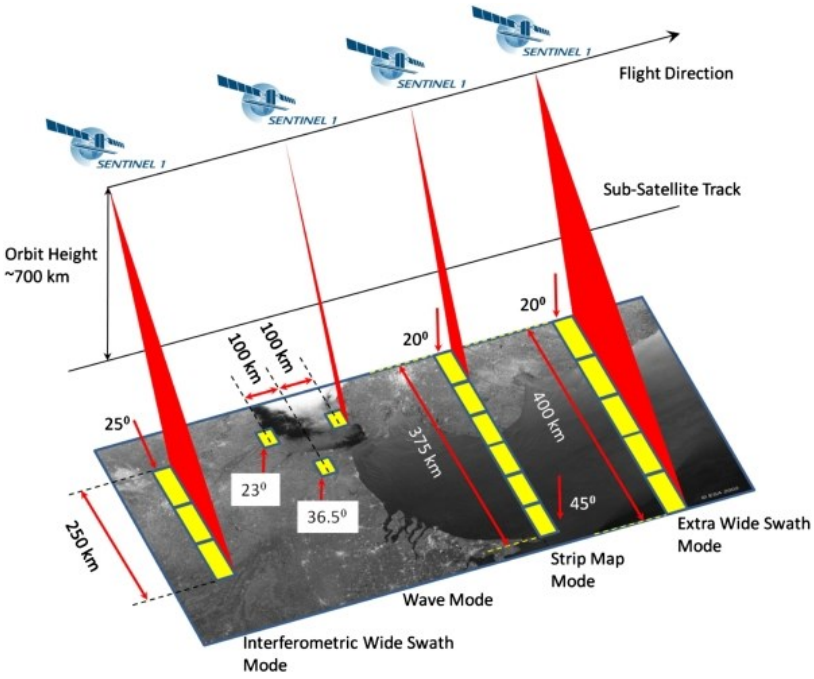

Figure 2.1. Sentinel-1 acquisition mode (From https://sentinels.copernicus.eu/web/sentinel/user-guides/sentinel-1-sar/acquisition-modes).

Among others, the TOPSAR (*Terrain Observation with Progressive Scans SAR*) Interferometric Wide swath mode enables the acquisition of three sub-swaths with a larger swath width and a higher spatial resolution (De Zan and Guarnieri, 2006). The mode is commonly used for high-resolution large-swath interferometric investigations (De Zan and Guarnieri, 2006).

2.1.2. Persistent Scatterers Interferometric (PSI) processing

2.1.2.1. PreProcessing: SNAP2StaMPS Workflow

In the present study, we applied the PSI approach by using the Stanford Method for Persistent Scatterers (StaMPS) by Hooper *et al.* (2007, 2012). The method has been developed in order to obtain good results in different areas (urban and non-urban) characterized by variable deformation rates by preserving the accuracy and spatial resolution (Hooper *et al*., 2007; Crosetto *et al*., 2016). The approach exploits the amplitude and the phase information to discriminate in a probabilistic way the PSs candidates through the amplitude dispersion and phase noise analysis. After the phase unwrapping and the application of spatial-temporal filters, mean ground velocity maps and related time series can be extracted.

To further improve the outcome, the SBAS approach has also been implemented in StaMPS, enabling the PSI-only, SBAS-only, or PSI-SBAS combination modes (Hooper *et al.,* 2012). Here we

used the PSI configuration by following the workflow steps (Fig. 2.2) and using free and open-source software.

The former is known as SNAP-STAMPS integration for Sentinel-1 Persistent Scatterer Interferometry processing (*snap2stamps*) (Foumelis *et al.,* 2018), and it consists of python scripts and XML files provided by the Sentinel Application Platform (SNAP), a software developed for the European Space Agency (ESA) by the Array Systems Computing under GPL license.

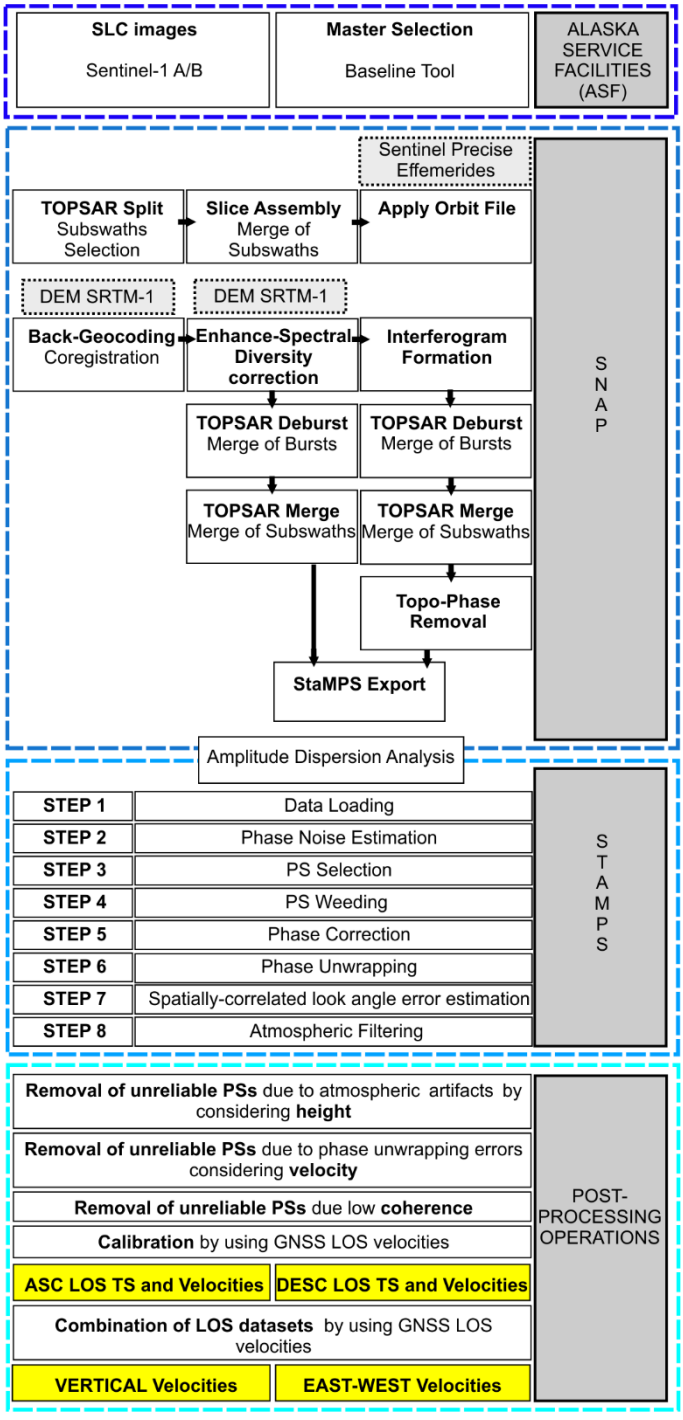

Figure 2.2. Workflow for PSI processing. The final products, highlighted in yellow, are mean velocity maps showing the surface movements along the satellite LOS and along the east-west and vertical directions.

For PSI processing, we used the Matlab-based StaMPS software (Hooper *et al.,* 2007, 2012). Finally, for post-processing operations, we used Matlab and the Generic Mapping Tool (GMT) version 6 (Wessel *et al.,* 2019).

The entire processing was composed of three main parts: the preprocessing based on *snap2stamps*, the PSI processing with *StaMPS* software, and the post-processing operations.

Before starting the processing, we gathered the data covering the area of interest, and we selected the Reference image.

The area of interest is a region of approximately 300,000 km^2, covering Friuli Venezia Giulia, northeastern Veneto, and the western sector of Croatia, Slovenia, and Austria. We downloaded the Single-Complex Look (SLC) images acquired by C-band Sentinel 1A-B in ascending (track N° 44) and descending orbit (N° track 95), spanning late March 2015 to December 2019 (Fig. 2.3). The images (216 for ascending and 227 for descending orbits) were provided by the Alaska Satellite Facility (ASF; https://search.asf.alaska.edu/).

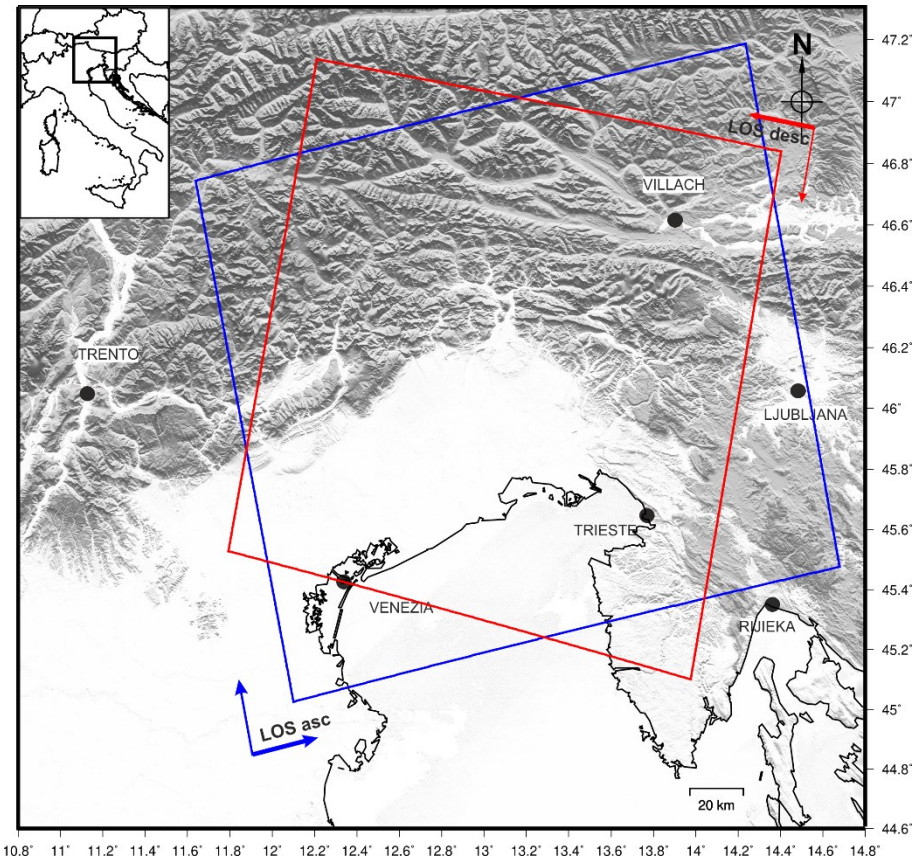

Figure 2.3. SAR data. The data are acquired along the ascending (blue rectangle) and descending (red rectangle) orbit tracks, covering the area of interest.

We then proceeded with the selection of the Reference image. Considering the perpendicular and the temporal baselines of SAR images, the Reference image should be chosen at the barycenter of the baseline plot in order to reduce the impact of geometrical and temporal decorrelation (Ferretti *et al.*, 2001). For that reason, we chose the Reference images on 7th August 2017 and 11th August 2017 for the ascending and descending datasets, respectively (Fig. 2.4).

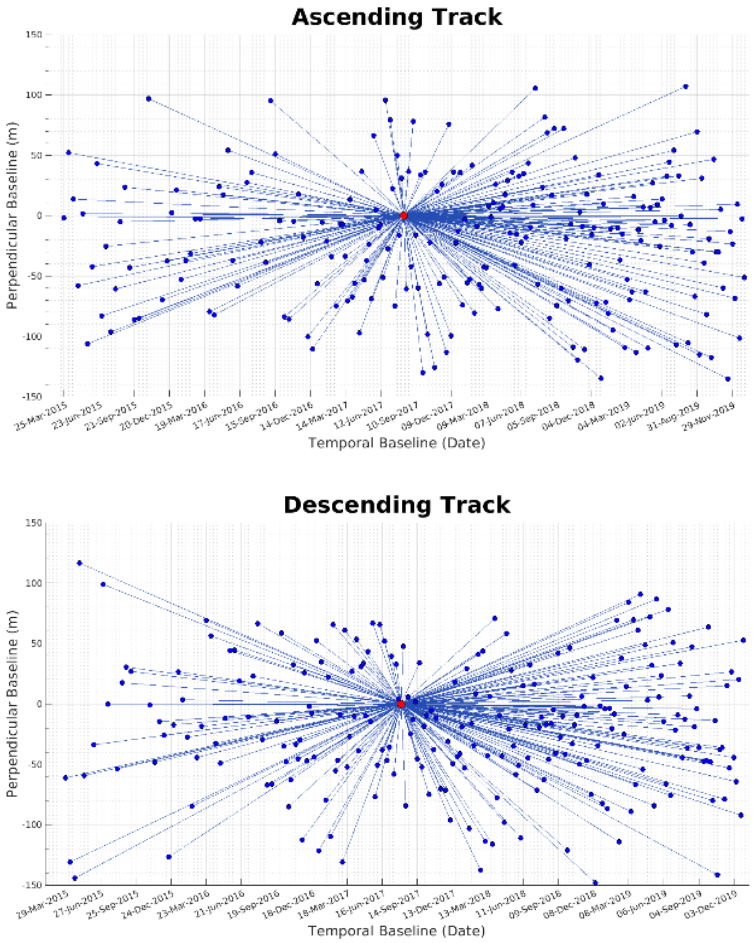

Figure 2.4. Baseline plots. The baseline plots show the combinations of SAR images with the Reference image based on temporal (data acquisition) and spatial (geometric characteristics) baselines for the ascending (top) and the descending (bottom) datasets.

We started with the initial phases of *snap2stamps* by launching the XML files through python scripts. After the initial preparation, the secondary images were split into subswaths and bursts covering the study area to enhance the computational performances (*TOPSAR Splitting)*. Considering the area of interest, we modified the original XML file to enable the multi-subswaths processing (Fig. 2.5-2.6). The *Slice Assembly* step was applied to merge the sub-swaths along the same orbit track to cover the region of interest entirely. Then, thanks to the satellite position and velocity position provided by the precise orbit ephemerides automatically downloaded by SNAP during *Apply Orbit File* step, the satellite orbit vectors were refined (https://qc.sentinel1.eo.esa.int).

The same operations (*TOPSAR Split – Slice Assembly - Apply Orbit File)* were also performed on the Reference image.

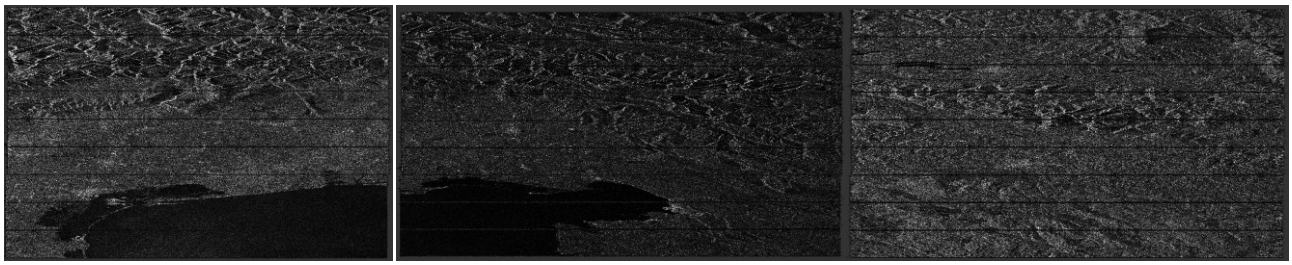

Figure 2.5. TOPSAR Splitting for the ascending dataset. Each SAR image has been divided vertically and horizontally into smaller areas, namely subswaths and bursts, respectively.

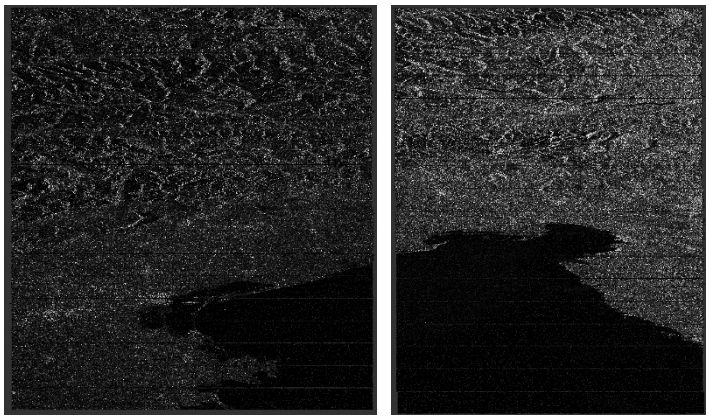

Figure 2.6. TOPSAR Splitting for the descending dataset. Each SAR image has been divided vertically and horizontally into smaller areas, namely subswaths and bursts, respectively.

The next step consisted of generating a stack of coregistered images and a stack of differential interferograms. For the second outcome, we proceeded with *Back-Geocoding, Enhanced Spectral Diversity correction, Interferogram Formation, TOPSAR Deburst, TOPSAR Merge, and Topographic Phase Removal* steps, whereas, for the first case, we applied the same processing chain by avoiding the generation of interferograms and the removal of topographic phase.

During *Back-Geocoding* step, each SAR pair was properly co-registered thanks to the vector orbits information and the use of a Digital Elevation Model (DEM) provided by SRTM arcsec-1 with a resolution of 30 m. Considering the shifts and the distortions due to different viewing geometries, starting times, and distances of observations, several corrections were required to geometrically superpose the common bursts and subswaths in every SAR pair (Massonnet and Feigl, 1998; Hein, 2004). The operation was divided into coarse and fine coregistration to achieve a high-accuracy alignment and correct the along and across-track shifts by applying cross-correlation techniques (Hanssen, 2001; Hein, 2004).

However, since some azimuthal misalignment of bursts could be present, *Enhanced Spectral Diversity correction* must be applied to improve the coregistration accuracy. By exploiting the burst-overlapping region containing pixels that have been observed by different squint angles, azimuth

and range corrections can be estimated to minimize the phase discontinuities across the bursts (Prats-Iraola *et al.*, 2010).

After the corrections, the complex interferograms were generated (*Interferogram Formation*) relying on the amplitude and phase information provided by each SAR pair. Every pixel of the Reference image was multiplied with the corresponding complex pixel in the coregistered secondary image for the generation of the complex interferogram:

$$y_1 y_2 *= |y_1||y_2| \exp(j\Phi_1 - \Phi_2) \tag{2.1}$$

with y_1 as the complex signal of the Reference, y_2* the complex conjugate signal of the Secondary image, $|y1|$ $|y2|$ as the Interferometric Amplitude and $\Phi_1 - \Phi_2$ as the Interferometric Phase (Massonnet and Feigl, 1998; Hanssen, 2001; Hein, 2004). In each resulting interferogram, the LOS displacements measured between the two acquisitions were expressed as phase differences (Interferometric Phase) in terms of colored fringes.

Once the interferograms were obtained, the flat-earth phase was estimated and removed using a polynomial refinement based on the orbital data and DEM information. Indeed, because of the curvature of the surface, the phase generated by an ideally flat Earth must be substracted (Bamler and Hartl, 1998; Bürgmann *et al*., 2000).

TOPSAR Deburst and *Merge* were then applied to remove the discontinuities between the bursts and the sub-swaths along the azimuth and range directions.

At this point, during the *Topographic Phase Removal*, the topographic phase contributions related to the elevation of the terrain of the study area were estimated and removed. According to the equation showing the height of ambiguity or the shift in altitude required for the generation of one topographic fringe,

$$h_a = \frac{\lambda R \sin\theta}{2B_\perp} \tag{2.2}$$

with λ as wavelength and θ as incidence angle, we observe that an increase in perpendicular baseline ($B_\perp$) implies a decrease in the height of ambiguity and a consequent increase in topographic fringes (Bamler and Hartl, 1998; Massonnet and Feigl, 1998; Bürgmann *et al.*, 2000). Thus, a small perpendicular baseline value should be preferred to minimize the effects of the topographic fringes in the interferograms.

Based on DEM, precise orbits data, and timing information, a synthetic interferogram containing the topographic information was generated and then subtracted to isolate the displacement signal (Massonnet *et al.*, 1993; Massonnet and Feigl, 1998; Hanssen, 2001).

Finally, the stacks of differential interferograms and coregistered images were generated and then evaluated before exporting the data in a proper format required by the Matlab-based StaMPS software (Hooper *et al.*, 2012).

Before the PSI processing, we made a preliminary selection of the potential PS candidates by using the Amplitude Dispersion Analysis (DA)

$$DA = \frac{\sigma_A}{\mu_A} \tag{2.3}$$

with σ_A and μ_A as the standard deviation and the mean of the amplitude of the pixels (Ferretti *et al.*, 2001). The parameter DA allows the discrimination of the potential PSs characterized by phase stability relying on amplitude information (Ferretti *et al.*, 2001; Hooper *et al.*, 2007). Specifically, higher phase stability of PS candidates correlates with a lower amplitude dispersion in the SAR images. In this case, assuming the value suggested for PSI by Hooper *et al.* (2004), we set the DA at 0.4.

During this step, we also divided the area of interest into 3x3 patches with an overlap of 50 pixels to improve the following computational operations.

2.1.2.2. StaMPS Processing

We proceeded with the StaMPS software by Hooper *et al.* (2012) (Fig. 2.2).

After the data loading (#1), the phase noise was estimated for each pixel in every interferogram (#2) and then used for the selection of potential PS candidates (#3).

The wrapped phase for each *xth* pixel of each *ith* interferogram can be expressed as the sum of several contributions as written in the following expression:

$$\psi_{x,i} = W\{\phi_{D,x,i} + \phi_{A,x,i} + \phi_{S,x,i} + \phi_{\theta,x,i} + \phi_{N,x,i}\} \tag{2.4}$$

with $\phi_{D,x,i}$ as the phase shift due to the Line-Of-Sight displacement of the pixel during the acquisitions, $\phi_{A,x,i}$ as the phase contributions related to the atmospheric delays, $\phi_{S,x,i}$ as the phase component due to the satellite orbit inaccuracies, $\phi_{\theta,x,i}$ as the phase related to the look angle error (i.e., DEM), $\phi_{N,x,i}$ as the phase noise term due to scattering, thermal noise, errors in co-registration, and W{:} as wrapping operator (Hooper *et al.*, 2007).

Assuming the spatial correlation of the first three terms and the partial correlation of the fourth term, the phase contributions can be estimated and then subtracted using an iterative approach, as explained in Hooper *et al.* (2004, 2007). At the end of the phase analysis, for each pixel was defined the temporal coherence as a measure of its phase noise. Using amplitude dispersion index and

temporal coherence, the PS candidates were selected based on their phase noise characteristics and then on the contributions of their neighboring pixels (#4).

The phase of the remaining pixels was corrected by considering the spatially-uncorrelated DEM errors. After the correction, the patches were merged and resampled with a sampling of 100x100 meters for computational purposes (#5).

During step #6, the 3D phase unwrapping was performed using the algorithm described by Hooper and Zebker (2007), aiming to recover the unambiguous phase from the wrapped phase. In particular, the operation was computed using the statistical-cost, network-flow phase-unwrapping algorithm (SNAPHU) by Chen and Zebker (2002), implemented in StaMPS.

The data have been resampled in a grid with a 100-meter spacing (*unwrap_grid_size*) and filtered in time by defining a window of 180 days (*unwrap_time_win*) to determine the probability of phase jump for each pair of adjacent pixels in each interferogram.

The adaptive Goldstein filter was also applied to enhance the signal-to-noise ratio (Goldstein and Werner, 1998). Hence, each interferogram was divided into overlapping patches where the Fast Fourier Transform (FFT) was computed. The final formula of the filter $Z_{(U,V)}$ is

$$Z_{(U,V)} = \left|\hat{S}_{(U,V)}\right|^{\alpha} \tag{2.5}$$

with $\left|\hat{S}_{(U,V)}\right|$ as the smoothed Power Spectrum and α as the strength of the filter (Goldstein and Werner, 1998). Since the alpha value depends on the correlation, the filter will be more effective in incoherent areas, implying noise reduction, especially in the decorrelated zones (Hanssen, 2001). In the present work, we tried different values for the filter's window size (*unwrap_gold_n_win*) (32x32 and 64x64 pixels) to compare and evaluate the results, namely 100_32 and 100_64 datasets.

After the phase unwrapping, the spatially-correlated DEM (i.e., inaccuracies of the DEM itself) errors and the atmospheric and orbital contributions of the Reference image were estimated by applied specific filters (#7).

We finally defined a reference area within a radius of 500 meters from a reference point (Long. 12.84° E; Lat. 45.95° N) on a stable area because of the relative measurements.

At this point, the LOS mean ground velocity has been extracted based on the linear estimation of the respective time series, obtained by converting the unwrapping phase (rad) into displacement (mm). We also removed the spatially-correlated DEM error (SCLA – spatially-correlated look angle error) and the orbital ramp estimated during step #7 in StaMPS.

Finally, we obtained two mean ground velocity maps for both tracks, showing the deformation in LOS and with respect to the reference point itself.

Among the several phase contributions (Formula 2.4), the phase delays due to the propagation of the radar signals through the atmosphere represent one of the most critical limitations in the interferometric data (Zebker *et al.,* 1997*;* Hanssen, 2001).

The atmospheric delay can be distinguished into an ionospheric and a tropospheric component. The former is related to the content in free electrons, which affects more the auroral zones and the longer wavelength radar signals, such as L-band SAR sensors, causing azimuth distortions and shifts (e.g., Gray *et al.,* 2000). Considering the study area (midlatitudes) and the use of C-band SAR data, the ionospheric effects are small or even negligible (Liang *et al.,* 2019).

The troposphere can provoke signal delays due to the stratified (hydrostatic component) and the turbulent (wet component) atmospheric contributions (Hanssen, 2001).

The stratified delay depends on the vertical changes in reflectivity of the atmospheric layers, and it is correlated with the topography (Massonnet and Feigl, 1998; Hanssen, 2001). Conversely, the turbulent delay mainly depends on the variation of the water vapor, which may cause heterogeneity within the layers (Goldstein, 1995; Hanssen, 2001).

Many authors proposed several methods for estimating and removing the atmospheric phase contributions to correct the SAR data and extract the deformation signals.

Since the atmospheric contributions can be considered correlated in space but uncorrelated in time, the application of temporal high pass filter and low pass filter in space can enhance the final results by removing these effects (Ferretti *et al.*, 2000; Ferretti *et al.*, 2001; Berardino *et al.*, 2002; Ab Latip *et al.*, 2015). Considering that the tropospheric contributions are significant on a length scale between a few km to tens of km (Hooper *et al.*, 2012) and therefore a smaller length scale (< 2km) is not so sensitive to larger-scale tropospheric signals (Lin *et al.*, 2010), we set the low-pass filter in space at 400 meters. Regarding the temporal window, since the atmospheric (i.e., troposphere) components can be considered uncorrelated in time (e.g., Hooper *et al.,* 2007), we chose a high-pass filter of 90 days to preserve the potential seasonal contributions and better compare the results with GNSS time series in future works. Thus, in the present study, we set the temporal filter at 90 days (*scn_time_win* = 45 days) and the spatial filter (*scn_wavelength) at* 400 meters, and we ran Step #8 in StaMPS (Hooper *et al.*, 2007).

However, we also tested a second approach, which consisted of applying the Toolbox for Reducing Atmospheric InSAR Noise (TRAIN) tool by estimating a linear atmospheric correction (Bekaert *et al.,* 2015). Indeed, because of the correlation between the phase delay due to the tropospheric component and the topographic height, a linear correction can be computed and removed from all the interferograms under the assumption of a uniform troposphere.

We evaluated the best solution by calculating the standard deviation's maximum, mean, and median values extracted from the mean ground velocities. We chose the approach that minimized these statistical values.

Nevertheless, it should be noted that atmospheric correction is one of the most crucial and challenging operations for improving the SAR measurements since the phase shifts related to the atmospheric contributions, especially the tropospheric components, affect the signal meaningfully. For that reason, many methods have been proposed, applied, and compared during the last years (i.e., spatial-temporal filters, weather models, spectrometer measurements, interferometric phase-based approaches, and GNSS observations). However, it must be said that no universal approach can be applied to every condition in every region worldwide (Ding *et al.*, 2008; Bekaert *et al.*, 2015). Thus, in the present study, we chose a method by comparing two different approaches, but we also applied additional post-processing operations to mitigate the atmospheric contributions of the datasets.

2.1.2.3. Post-Processing

As shown in Figure 2.2, we performed additional operations to improve the final results.
As previously explained, the atmospheric contributions strongly affect the interferometric signal, but they can be estimated and removed by applying different methods (Bekaert *et al.*, 2015).
We adopted a more conservative approach by removing the PSs based on topographic height with respect to the reference point we chose on a stable plain area (see Section 2.1.2.2). In the plain areas, the atmospheric contributions deal mainly with the lateral variations of water vapor within the layers (Hanssen, 2001). As regards the areas characterized by strong topography, an additional contribution related to the correlation between the atmosphere and the topographic height must be considered (Delacourt *et al.*, 1998; Hanssen, 2001; Doin *et al.*, 2009).
Although spatial and temporal filters can mitigate the turbulent atmospheric delays, which are considered spatially correlated and temporally uncorrelated (Ferretti *et al.*, 2001; Berardino *et al.*, 2002; Hooper *et al.*, 2007), this method might not be so effective in the case of temporally correlated stratified tropospheric contributions (Doin *et al.*, 2009).
Hence, considering the topography of the study area and the potential correlation with the atmospheric layers, we removed the PSs whose difference in height with respect to the reference point was higher than 1000 meters (Doin *et al.*, 2009).
Another step was performed by exploiting the two datasets obtained after step #6 of StaMPS processing (see Section 2.1.2.2). The application of the Goldstein filter with different window sizes involved the generation of two datasets for each track velocity (100_64 and 100_32). Since we observed some significant changes in velocities, mainly localized in the northern sector of the study area, we removed the PSs having a difference in velocity higher than a given threshold to exclude unreliable pixels. Considering the estimated rates in the study area of ~1.5-3 mm/yr (D'Agostino *et al.*, 2005; Bechtold *et al.*, 2009; Serpelloni *et al.*, 2016), we fixed the threshold at 1 mm/yr.

Finally, we excluded pixels having lower coherence (< 0.6) and, for the ascending datasets, we also masked out an area characterized by spatially-correlated PSs, having a significant velocity difference (mean values up to 5 mm/yr) compared to the adjacent persistent scatterers. These PSs might be potentially affected by errors during the processing, so they should not be considered in successive operations.

2.2. InSAR-GNSS Integration

2.2.1. Calibration

InSAR measurements are relative both in time (w.r.t. the first image of the data stack) and in space (w.r.t. to the selected spatial reference), and large-scale deformation gradients measured with this technique may be affected by residual atmospheric propagation effects and orbital uncertainties (Hooper *et al.,* 2012). Hence, we integrated and calibrated SAR measurements with the GNSS data in the study area.

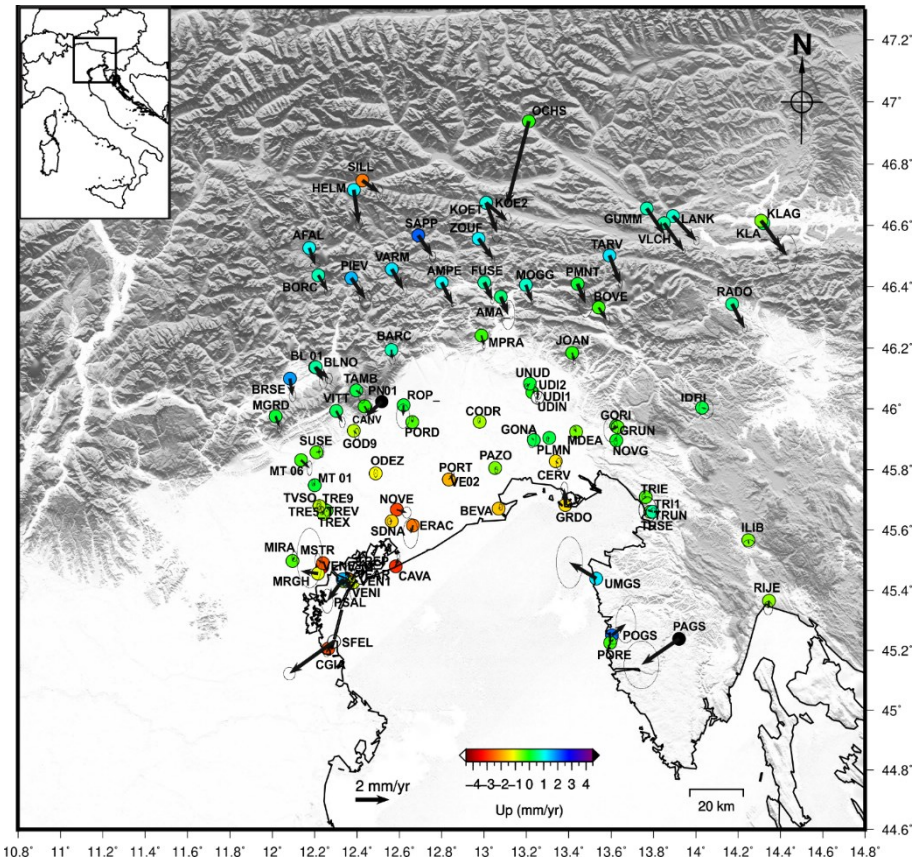

Figure 2.7. GNSS data. The arrows show the horizontal velocities in an Adria-fixed reference frame, considering the rotation pole from Serpelloni *et al.* (2016). The colored points indicate the vertical velocity according to the color scale.

The GNSS velocities used in this work have been obtained by processing data from continuous stations belonging to several public and private networks, following the approach described in Serpelloni *et al.* (2006, 2013, 2018). They are part of a Euro-Mediterranean geodetic solution (e.g., Devoti *et al.*, 2017) using the GAMIT/GLOBK (Herring *et al.*, 2015) and QOCA software (http://qoca.jpl.nasa.gov). Starting from the displacement time-series in the 2000-2020 time span, realized in the IGb14 reference frame (https://lists.igs.org/pipermail/igsmail/2020/007917.html), linear velocities, seasonal signals, and eventual instrumental offsets for sites with a minimum observational period of 4.5 years, to minimize possible biases in the linear trend estimation due to seasonal signals (Blewitt and Lavallée, 2002) and non-seasonal hydrological deformation signals have been estimated (Serpelloni *et al.,* 2018). The processing and further post-processing operations have followed three-step procedures described in detail in Serpelloni *et al.* (2006, 2013, 2016, 2018). The horizontal velocities shown in Figure 2.7 are referred to an Adria-fixed reference frame, considering the rotation pole from Serpelloni *et al.* (2016).

In the present work, the GNSS velocities were processed and kindly provided by the researchers of the Istituto Nazionale di Geofisica e Vulcanologia (INGV).

For each GNSS station, the 3D velocity vector has been projected along the ascending and descending LOS directions (Fig. 2.8). We also calculated the mean ground velocities of all the PSs located within a search radius from each GNSS station and the related standard deviation. Finally, we compared the resulting velocities of PSs with LOS projected GNSS velocities.

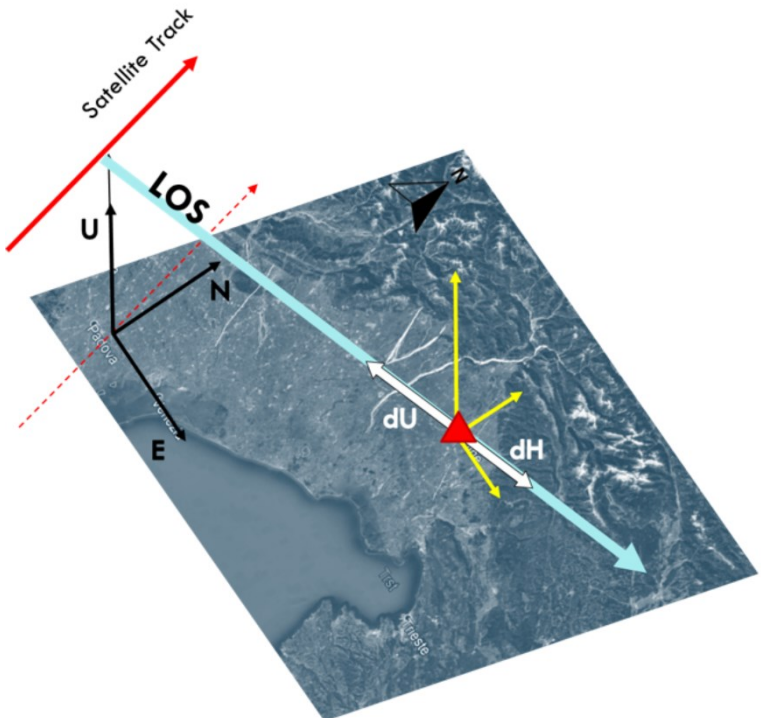

Figure 2.8. Projection along LOS of the GNSS 3D velocity vector.

For the calibration of SAR measurements, we selected the GNSS stations relying on the following criteria:

1. InSAR-GNSS temporal coverage overlapping
2. GNSS data continuity
3. InSAR-GNSS spatial colocation
4. Low spatial variability underlying deformation field

Concerning criterion #1, we considered the SAR observation interval (2015-2019) as the reference period, thus excluding GNSS stations whose data acquisitions terminated before 2015. Similarly, for condition #2, within the same temporal interval, we also defined a minimum period of 2.5 yr by excluding the GNSS stations having shorter time series to compare better SAR and GNSS data in the 2015-2019 reference period.

We ran different tests by varying the radius value, namely 200, 400, 600, and 800 meters. We then counted the number of the detected PSs and calculated the standard deviation of their ground velocity values. To ensure a minimum number of PSs around each GNSS station, we assumed as a threshold the minimum PS number below which 10% of the values fall (criterion #3). Moreover, regarding the standard deviation of the ground velocities of all persistent scatterers, we fixed the threshold at 1 mm/yr to limit the spatial variability (criterion #4). Hence, relying on these conditions, we excluded the GNSS stations having few PSs and high spatial variability in PSs velocities by considering all the radii (see tables in Appendix A and B).

Finally, we obtained 47 GNSS stations for the LOS datasets distributed in the study area.

Once selected, we exploited the GNSS velocities to perform a calibration, allowing the estimation of an offset due to the different reference frames between InSAR and GNSS and for image-wide trends due to orbital uncertainties and atmospheric propagation (e.g., Gabriel *et al.*, 1989; Zebker and Rosen, 1994).

For that reason, we estimated a planar (Feng *et al.,* 2012) and quadratic ramp (Lohman and Simons, 2005; Biggs *et al.*, 2007) by fitting the InSAR-GNSS velocity differences in a least-squares sense.

The processing settings described in Section 2.1.2.2, namely two processing runs using different Goldstein filter parameters (window sizes of 32x32 and 64x64 pixels, respectively), and the different GNSS-calibration settings, namely different search radii (200, 400, 600, and 800 meters) and calibration error models (linear and quadratic), yielded 16 other calibrated deformation products for each track. Finally, we determined the best solution after a statistical comparison with GNSS data.

2.2.2. Decomposition

Since the measurements referred to the satellite LOS directions, we combined the resulting calibrated velocity maps to obtain the region's vertical and horizontal (east-west) velocity maps. After defining a 100x100 m regular grid, we calculated the mean velocity of PSs for each cell in both datasets (Δd_{asc} and Δd_{desc}). We also extracted the values of the local incidence angle (θ) (positive from the vertical), and the azimuth of the satellite heading vector (φ) (positive clockwise from the North) (Fig. 2.9).

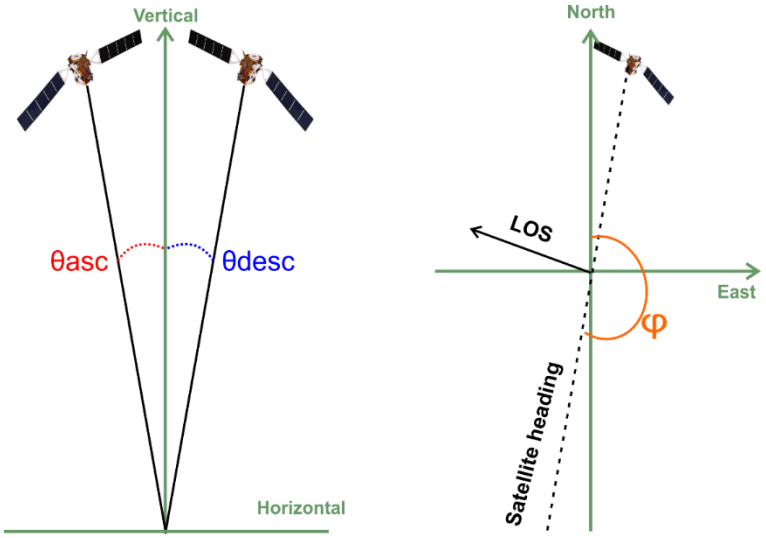

Figure 2.9. SAR acquisition geometry: the incidence (θ) and the satellite heading angle (φ).

For each grid node characterized by both LOS velocity values, we applied the following formula (Mehrabi *et al.*, 2019) to extract the vertical and the east-west velocity components:

$$\begin{pmatrix} \Delta d_{asc} \\ \Delta d_{desc} \end{pmatrix} = \begin{pmatrix} -\cos\varphi_{asc}\sin\theta_{asc} & \sin\varphi_{asc}\sin\theta_{asc} & \cos\theta_{asc} \\ -\cos\varphi_{desc}\sin\theta_{desc} & \sin\varphi_{desc}\sin\theta_{desc} & \cos\theta_{desc} \end{pmatrix} \begin{pmatrix} \Delta_E \\ \Delta_U \end{pmatrix} \quad (2.6)$$

Considering the lower sensitivity of near-polar satellites, the small contribution along the North direction can be neglected.

We finally compared the InSAR-GNSS velocity after the decomposition.

2.2.3. Velocity Profiles

Once we obtained the vertical and east-west maps, we traced some velocity profiles to better analyze the signals in the study area. Thus, we used GMT to select 40km-wide profiles perpendicular to the main tectonic structures in the area. Together with SAR data, we also plotted the GNSS velocities (East and Up components). We then added the seismic data provided by OGS bulletins (period: 2000-2017; http://www.crs.inogs.it/bollettino/RSFVG) and a geological section containing stratigraphic and tectonic information.

2.3. Modeling

2.3.1. Geodetic Bayesian Inversion Software (GBIS)

We performed an inversion relying on a two-dimensional model to extract geometrical and kinematic parameters referred to the active tectonic structures in the study area. Based on the velocity profiles, we ran a test where the tectonic signal was present and associated with the motion of the deeper portion of a single fault below a given depth. This was the case with the Alpine system in the western sector of the study area (Dolomites).

In the present study, we exploited the potential of the open-source Geodetic Bayesian Inversion Software (GBIS) developed by Bagnardi and Hooper (2018). Based on the inversion of geodetic data, the software uses the Bayesian approach to obtain the parameters' posterior probability density functions (PDFs) by exploiting the Markov-chain Monte Carlo and the Metropolis-Hastings algorithm (e.g., Hastings, 1970). Among the analytical forward models used in GBIS to model the magmatic and seismogenic sources with different geometry, we used the one proposed by Okada (1985), relying on the dislocation with a uniform slip along a rectangular plane within an elastic, homogenous, and isotropic half-space.

Many authors used GBIS to model the volcanic and coseismic displacements using Differential SAR Interferometry (DInSAR) (Vajedian *et al.*, 2018; Yang *et al.*, 2019; Galetto *et al.*, 2020; Wen *et al.*, 2021). However, given the interest in interseismic deformation in the present study, we made some adjustments to obtain information about the aseismic slip rate due to the motion of the deeper portion of the fault located below the locking depth.

Firstly, we modified the input data using the LOS calibrated SAR velocities (mm/yr) instead of the displacement expressed as wrapped phase (rad). Similarly, we used the North, East, and Up GNSS velocities (mm/yr).

In GBIS, the estimation of the errors in the SAR datasets is performed by estimating a variance-covariance matrix, considering the presence of spatially-correlated errors (i.e., residual topographic errors, atmospheric contributions) within the SAR dataset. Among the approaches, semivariograms can be exploited to compute the spatial variability of the geodetic data based on their spatial separations (e.g., Curran, 1988): specifically, the higher the distance between two data points, the higher their value difference will be.

Thus, after removing a linear ramp from the data, the experimental semi-variogram, and the fitted parameters can be computed to estimate the data errors (Bagnardi and Hooper, 2018).

As regards the GNSS data, assuming no spatial correlation of the errors between stations, the standard deviations of each displacement component, namely the North, East, and Up components, are used to estimate the data variance at each site.

In this case, considering the adopted strategies during the processing and post-processing, such as the application of filters and the calibration, we assumed that no extra spatially-correlated contributions should be present in the dataset, except for the displacement signals. Therefore, as done for GNSS data, we used the standard deviations of the estimated LOS velocities to estimate the data errors for each PS.

The third modification concerns the SAR data subsampling. Data sampling is a fundamental step in improving the computational efficiency of the inversion. However, this operation should not only reduce the number of data points but also preserve the information required for the inversion.

Among the approaches, the method used in GBIS is an adaptive quadtree sampling (gradient-based method; Decriem *et al.*, 2010), which divides the area into smaller regular polygons relying on phase variance and assigns the mean data values at the centroid of each polygon. Thus, the adopted approach enables to sample more the areas characterized by high variances, such as deforming areas, than the areas with lower variance (i.e., non-deforming areas) (Bagnardi and Hooper, 2018).

In the present work, we applied the method presented in Anderlini *et al.* (2020), successfully employed in a region characterized by low displacement signals. The area is divided into smaller rectangles until the number of pixels in each polygon is smaller than a threshold n_{crit}. Then, the coordinates and median velocity are computed and assigned to every single polygon together with the incidence angle, the heading angle, and the standard velocity deviation.

The critical number of pixels is calculated by applying these formulae:

$$n_{crit} = \frac{T_p}{div_{lon} * div_{lat}} \tag{2.7}$$

$$\frac{N_p}{R} = (div_{lon} * div_{lat})^2 \tag{2.8}$$

with T_p as the initial number of SAR pixels, div_{lon} and div_{lat} as the longitude and latitude division, N_p as the number of final points after the sampling, and R as the percentage of area covered by original SAR data with respect to the initial rectangle, which can vary from 20% to 45% (Anderlini *et al.*, 2020).

2.3.2. Input preparation: InSAR data, GNSS data, and source parameters

Before the inversion, we selected some 40km-wide profiles perpendicular to the main tectonic structures for the ascending and descending SAR datasets. We undersampled to reduce the density of pixels and improve the computational performance as previously reported. We exported the outcome (longitude, latitude, median velocity, standard deviation, incidence, and heading angles) and used it as input for the inversion.

Concerning GNSS data, we used the geographic coordinates, the East, North, and Up velocities, and their standard deviations as input.

Given the presence of three geodetic datasets, we also assigned a weight to each dataset. Initially, the software allows attributing a weight (1-10) to the GNSS data with respect to the SAR data. However, considering the different acquisitions, we decided to fix the weight of GNSS data (1) and independently vary the weight of the two SAR datasets.

In particular, we tried a different approach by defining the weight of each LOS dataset based on the difference in direction between the LOS and the median GNSS horizontal velocity direction.

Since the SAR data measure the velocity along the satellite LOS (1D) direction, orthogonally with respect to the satellite trajectory, the sensitivity of SAR measurements strongly depends on the orientation of the ground motion vector. In light of these considerations, north-south displacements are less detectable than the east-west deformations due to the near-polar orbit of the satellites and the geometry viewing (Fig. 2.10). For that reason, we suggest that the contributions of LOS datasets may vary in function of the median displacement rate direction. A similar hypothesis was developed by Dumont *et al.* (2021), which revealed that the LOS measurements acquired from ascending and descending orbits might lead to differences in data magnitude, potentially affecting the inversion.

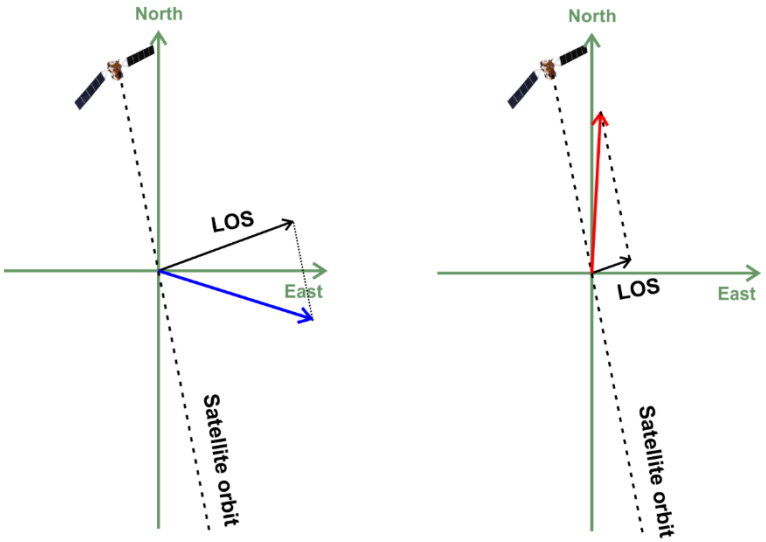

Figure 2.10. Ground displacement and SAR data. The figure shows the acquisition of SAR data along the Line-Of-Sight for the ascending dataset. Left: the blue arrow represents the ground displacement with a prevailing eastward component, while the black arrow indicates the projection along the LOS direction. Right: the red arrow indicates the direction of the ground displacement, mainly northward. In this case, the observed LOS signal is lower due to the different direction of the ground motion vector.

Hence, by exploiting the presence of a 3D velocity vector provided by the GNSS stations, we extracted the main direction of the ground motion, and we then estimated the weight of SAR datasets based on the difference in direction between the displacement rate and the LOS. Under these

assumptions, the weight of a SAR dataset increases when the LOS direction is aligned with the velocity vector. Conversely, the weight decreases if the LOS direction is nearly perpendicular to the main velocity direction.

Finally, we defined the region of interest and a point for the local reference system used during the inversion. We used as a fault model a dipping rectangular plane characterized by uniform slip under the assumptions of Okada (1985). Specifically, we defined the source model by setting nine parameters: the length and the width of the rectangular fault plane, the coordinates of the edge mid-point (X-, Y-center, and depth), the dip angle, the strike and the slip rates, divided into dip- and strike-slip components (Fig. 2.11).

We ran several tests and finally evaluated the results based on the WRSS of the geodetic datasets and the residual maps for InSAR (ascending and descending) and GNSS data.

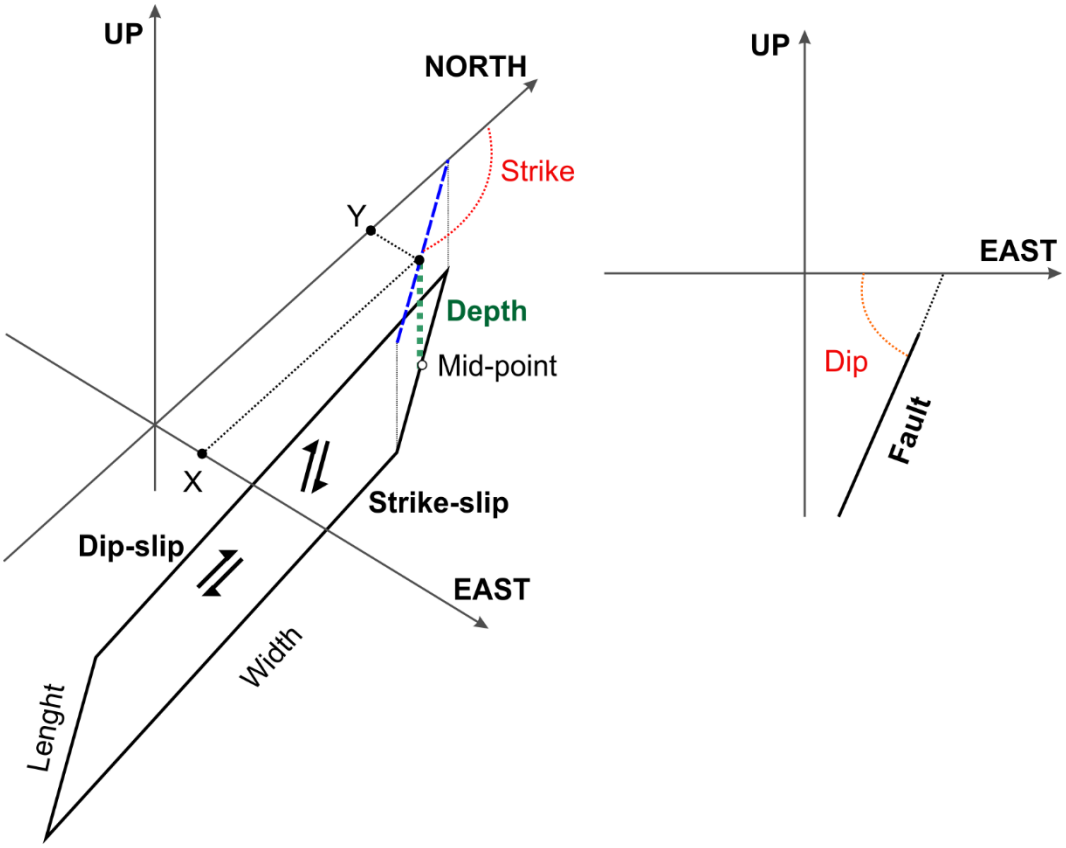

Figure 2.11. Source parameters for dipping rectangular fault model.

3. RESULTS

3.1. LOS Velocity maps and removal of DEM errors and orbital ramps

While preparing the differential interferograms and coregistered images with *snap2stamps*, we tested the *Enhanced Spectral Diversity correction* tool. As observed in Figure 3.1 A-B, the operation effectively improved the data quality by estimating the azimuthal shift and removing the phase jumps. Indeed, in Figure 3.1A, we can observe the presence of velocity jumps due to the misregistration of the bursts along the azimuth direction, subsequently corrected by applying the ESD step (Fig. 3.1B). After the phase corrections and the generation of the stacks of InSAR data, we exported the results for the PSI processing with StaMPS. Following the processing workflow (Fig. 2.2), we extracted the PS candidates based on amplitude and phase analysis for each patch, as explained in Section 2.1.2.2.

During step #5, the phase of the PSs was corrected, and then the patches were merged and resampled (see Section 2.1.2. for further details). Figure 3.2 shows an example of the resulting wrapped interferograms where the phase differences (rad) are represented as several colored fringes. Indeed, each fringe indicates a phase shift along the satellite LOS for both orbit tracks.

Before the phase unwrapping (step #6), the interferograms were also filtered using the Goldstein filter. We obtained two different datasets by setting the filter window size at 64 and 32 pixels, as observed in Figures 3.3 and 3.4, respectively. No significant differences can be observed at this processing stage by comparing the resulting products. However, we used both datasets in the following steps.

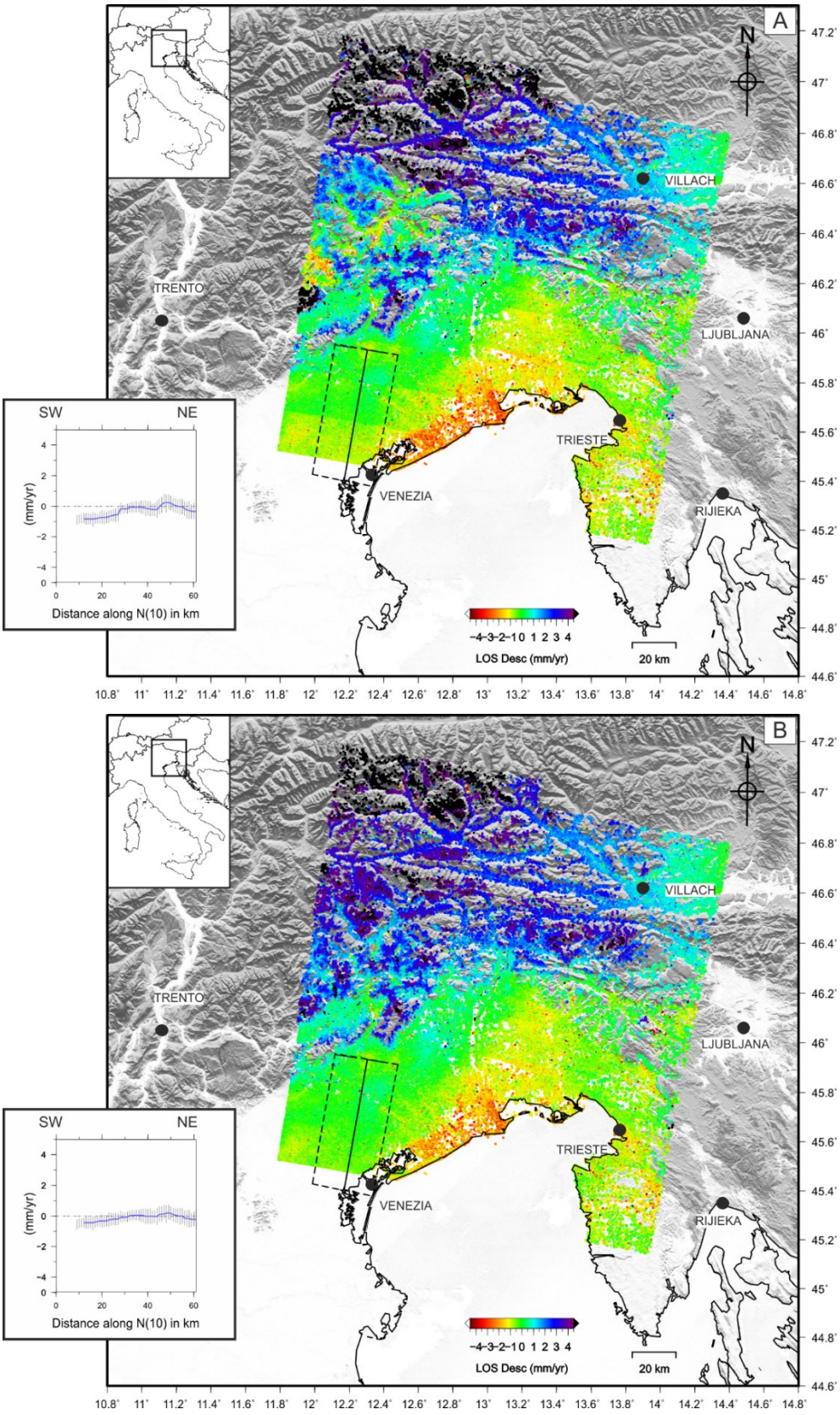

Figure 3.1. Enhanced Spectral Diversity Correction (ESD). A) On the descending LOS velocity dataset, several velocity jumps may be observed, corresponding to the burst misalignments due to the missing ESD correction. On the other hand, after the correction, the velocity field presents no discontinuities (B).

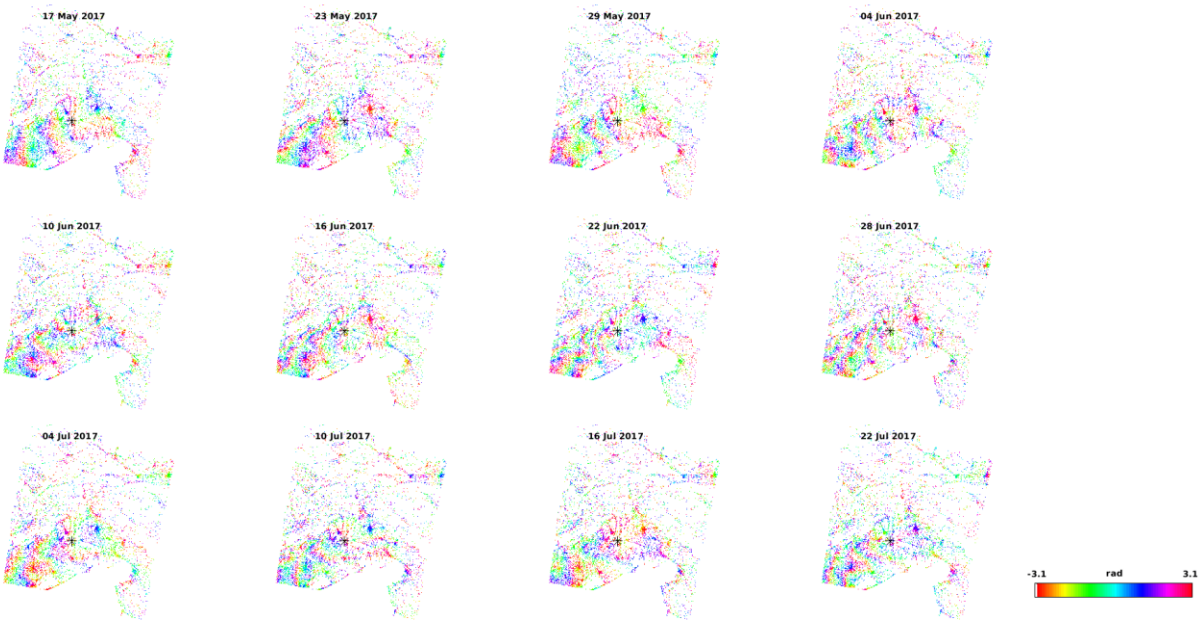

Figure 3.2. Example of wrapped interferograms for the descending dataset. The colored fringes express in radians the phase differences with respect to the Reference image.

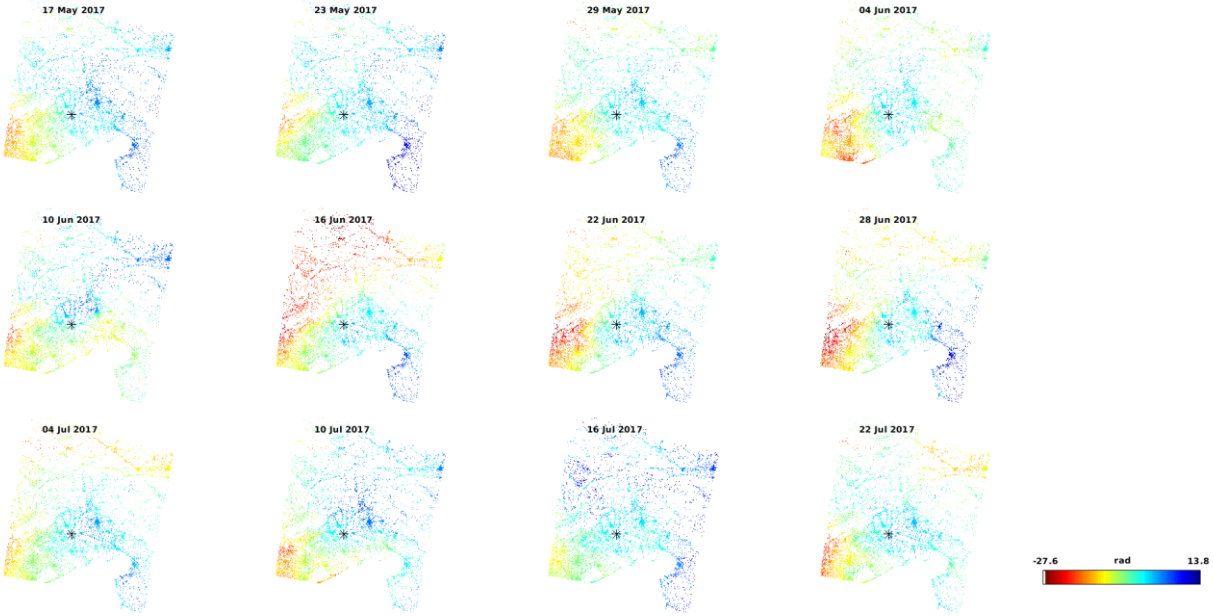

Figure 3.3. Example of unwrapped interferograms for the descending dataset. After the unwrapping operation, no more fringes are visible. The figure shows the datasets after applying the Goldstein filter (window: 64x64 pixels).

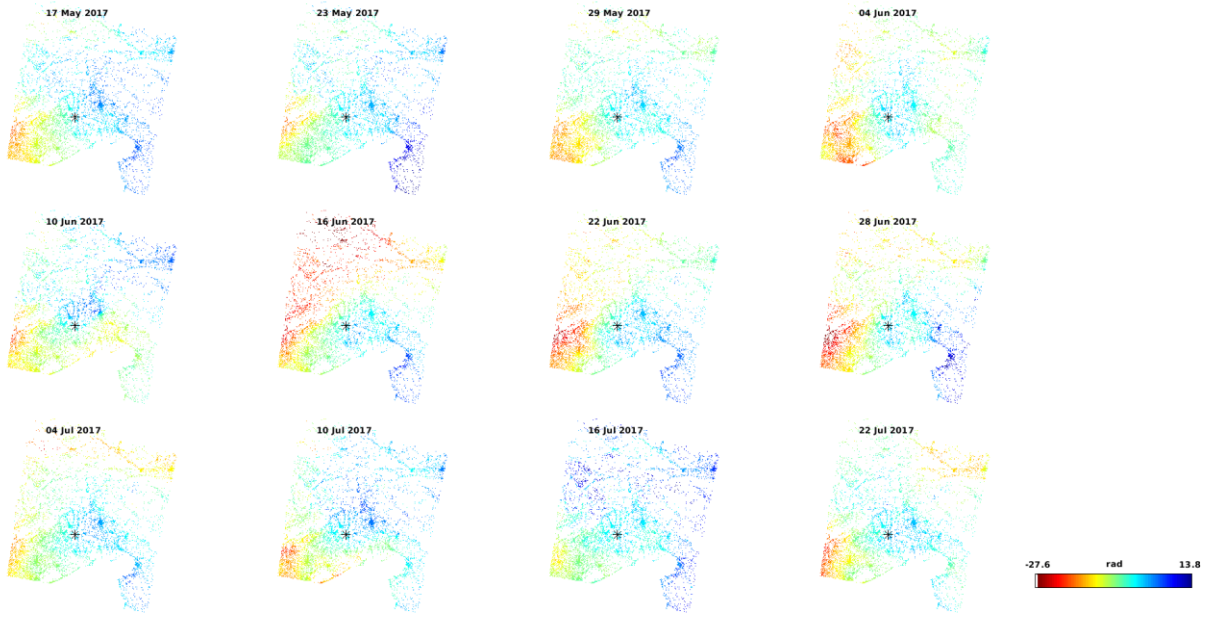

Figure 3.4. Example of unwrapped interferograms for the descending dataset. After the unwrapping operation, no more fringes are visible. The figure shows the datasets after applying the Goldstein filter (window: 32x32 pixels).

Figures 3.5 and 3.6 (A-C) show the preliminary results of the PSI processing for the descending and ascending datasets after the phase-to-displacement conversion of the unwrapped products and the estimation of the linear velocity component. In the velocity maps, the positive (blue) and negative (red) rates indicate a ground motion toward and away from the satellite along LOS, respectively.

As described in Section 2.1.2.2, during step #7, the spatially-correlated look angle error (SCLA), mainly due to the DEM errors, was estimated. Considering our purpose focused on studying the tectonic deformation in the study area, we removed it. For the same reason, we also removed the contributions referred to the satellite orbits through a “deramping tool” on StaMPS. For the removal, the software estimated a linear ramp considering the region of interest. Figures 3.5 and 3.6 (B-D) show the resulting maps for the 100_64 and 100_32 datasets along both orbit tracks.

Observing the descending datasets (Fig. 3.5), we observe a general decrease in velocity after removing the DEM and orbital contributions, especially in the northwestern sector of the study area. Conversely, the rates increase in other areas (e.g., the southeastern sector).

Regarding the ascending maps, the velocity field in Figure 3.6 (A-C) is clearly dominated by the presence of a ramp that masks the signals in the study area. Nevertheless, after removing the DEM errors and the estimated orbital ramp, the maps reveal some deformation patterns on the plain and across the mountain belt. In addition, we also notice the presence of large areas in the northwestern sector, which are characterized by absolute rates higher than 4.5 mm/yr.

Observing the datasets 100_64 and 100_32, we note some discrepancies mainly localized across the mountain belt and the presence of lower rates in the second dataset (100_32; Fig.3.6D).

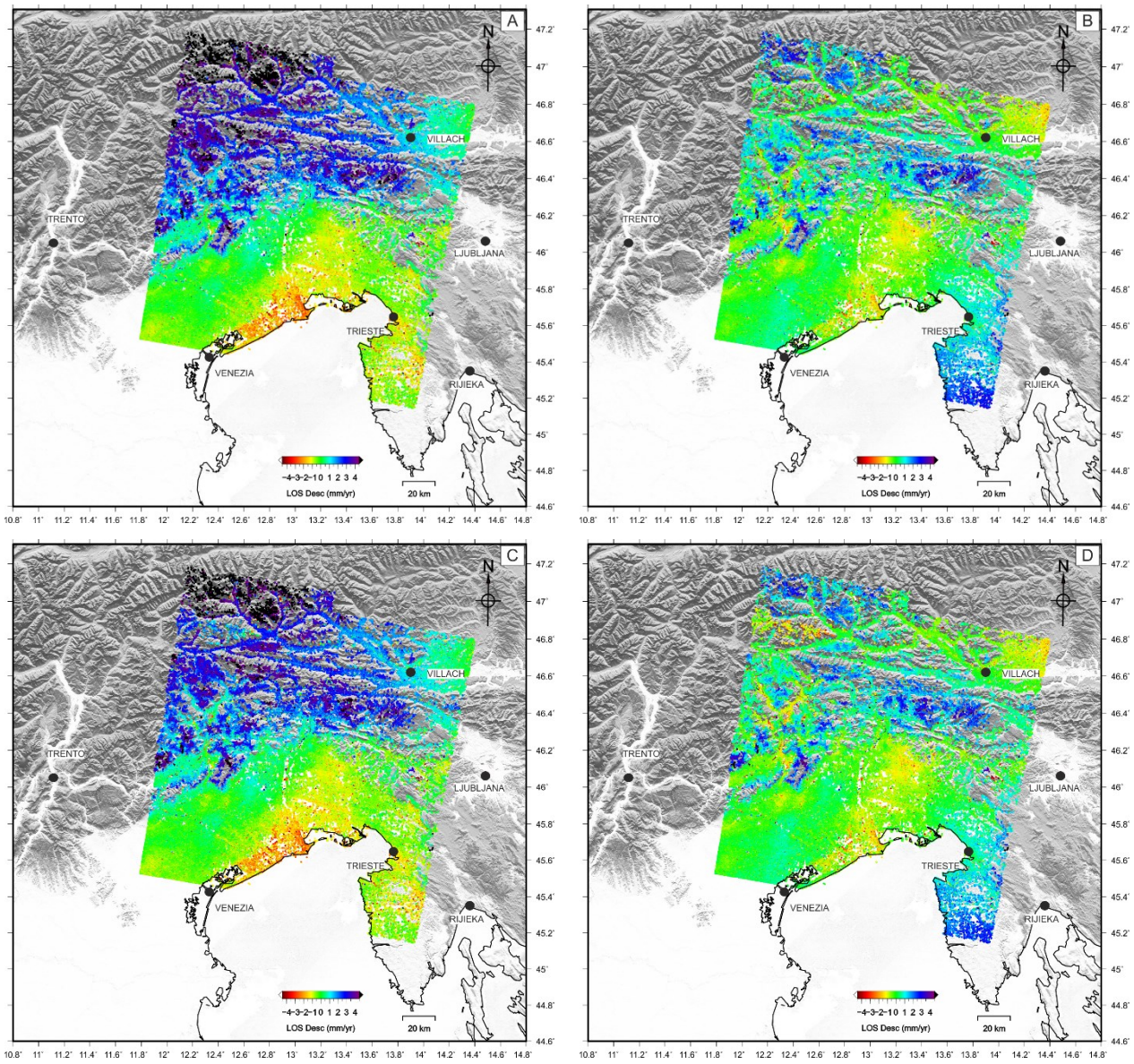

Figure 3.5. LOS mean ground velocity maps for the descending dataset. A) and C) show the mean ground velocity field after the PSI processing tested for Goldstein filter window sizes at 64 and 32, respectively. B) and D) represent the velocity fields in the study area after the removal of DEM error (*d*) and orbital ramp (*o*) for the 100_64 and 100_32 data.

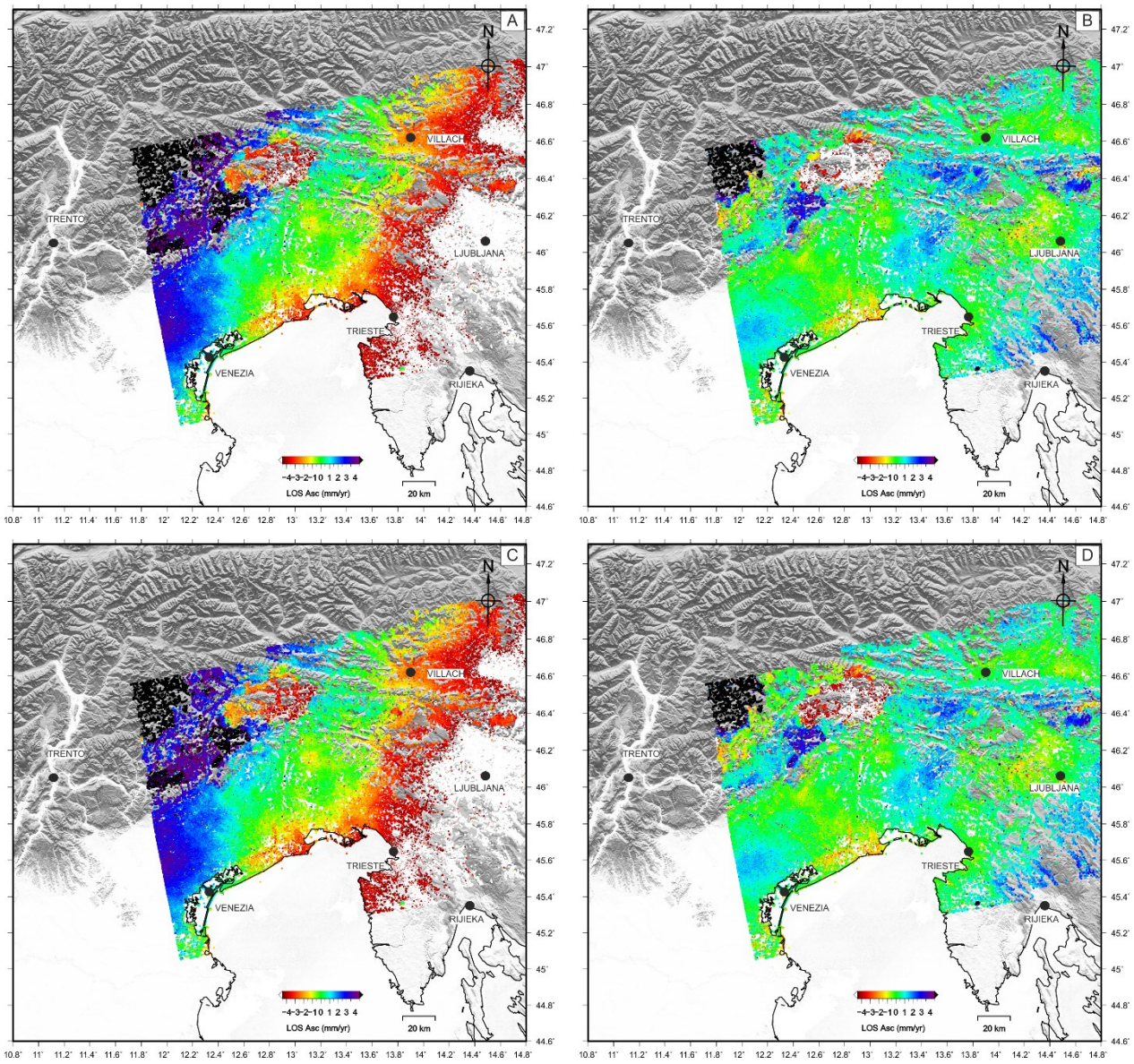

Figure 3.6. LOS mean ground velocity maps for the ascending dataset. A) and C) show the mean ground velocity field after the PSI processing tested for Goldstein filter window sizes at 64 and 32, respectively. B) and D) represent the velocity fields in the study area after the removal of DEM error (*d*) and orbital ramp (*o*) for the 100_64 and 100_32 data.

3.2. Removal of the atmospheric contributions

In addition to DEM errors and orbital ramps, SAR data may contain atmospheric contributions. Indeed, during the propagation of the radar electromagnetic beam through the atmosphere, the delay effect provoked by the different layers may mask the signal.

Hence, in order to isolate the displacement that occurred during the observation period, we applied two different methods: the application of filters in space and time and the linear estimation of the atmosphere correlated with the topography.

Starting from the LOS velocity maps free from DEM errors and orbital ramps, Figures 3.7 and 3.8 show the obtained results for the different LOS datasets after removing the atmospheric components using spatial-temporal filters (A-C) and a linear phase-topography correction (B-D). The linear atmospheric correction enables the estimation and removal of the atmospheric components mainly related to the topography, assuming a uniform troposphere. However, the method does not effectively remove the turbulent and coherent short-scale components (Bekaert *et al.,* 2015). On the other hand, the application of high pass and low pass filters in time and space can mitigate these tropospheric contributions (Ferretti *et al.*, 2001; Berardino *et al.*, 2002; Hooper *et al.*, 2007), even if some limitations can arise in the presence of temporally correlated stratified tropospheric contributions (Doin *et al.*, 2009).

In the descending datasets (Fig. 3.7), we note significant differences in the western-northwestern and southeastern sectors, characterized by positive rates on the A-C maps and negative rates on the B-D maps. Moreover, in the southeastern areas (south of Trieste), we observe a marked transition between negative and positive rates in Figures 3.7 (B-D), which is not visible in Figures 3.7 (A-C).

Conversely, the ascending datasets show fewer differences (Fig. 3.8). Here, we mention the presence of areas characterized by higher rates (absolute values > 4.5 mm/yr) in the northwestern region.

As regards the comparison between 100_64 and 100_32 datasets, we report the same observations we described in Section 3.1 (Fig. 3.5-3.6).

To support our analysis, we also evaluated the velocity standard deviation of the datasets, focusing on the maximum, the mean, and the median values for the different tests (Tables 3.1 and 3.2).

We note that the first approach (*v-dso: velocity minus DEM, orbits, and spatial-temporal filters)* reduces the standard deviation values compared to the latter (*v-dao: velocity minus DEM, orbits, and linear correction*), especially for the descending datasets. Moreover, the 100_64 datasets generally present lower values than the 100_32.

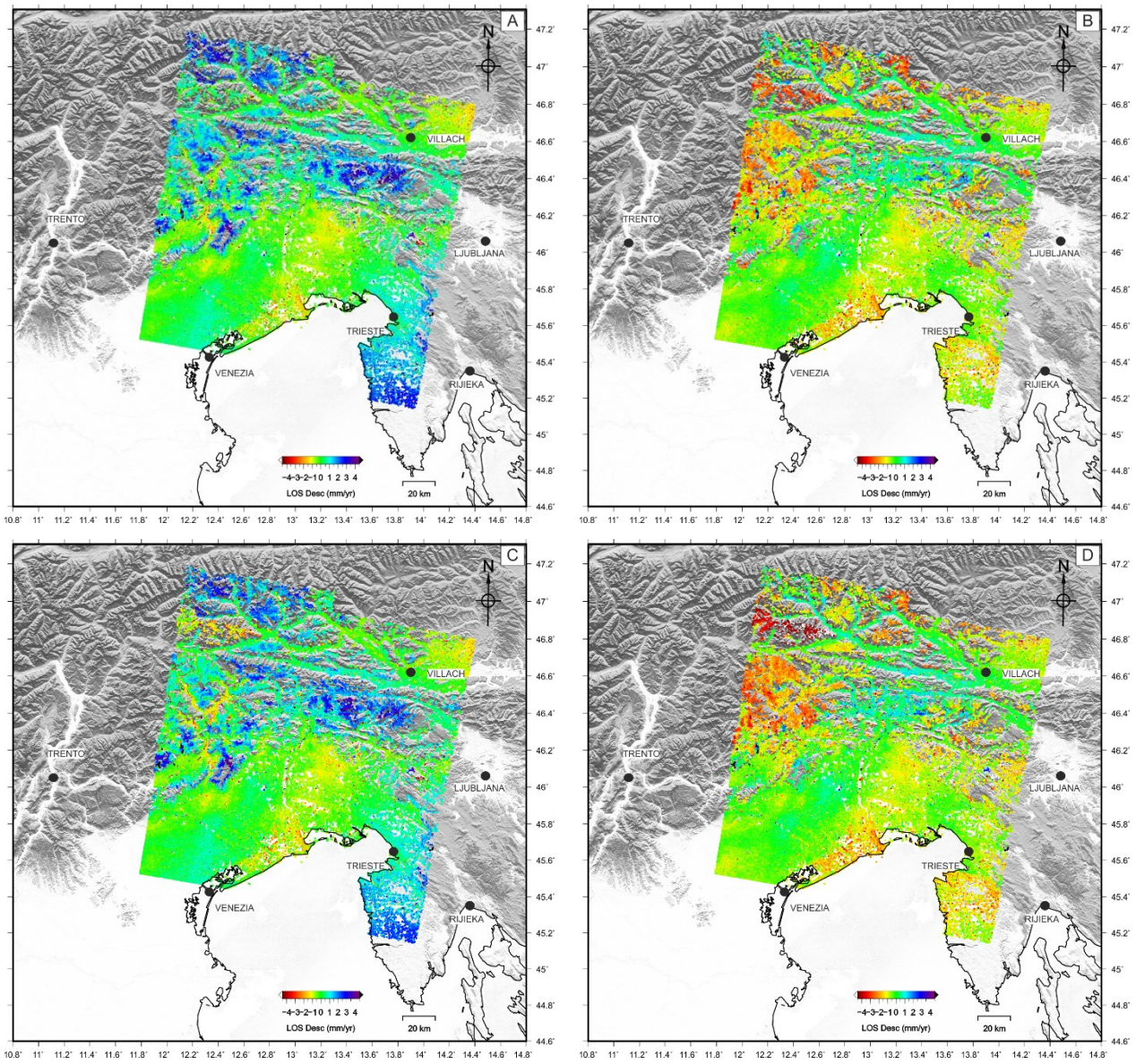

Figure 3.7. Comparison of LOS mean ground velocity maps after the atmospheric correction for the descending datasets. A) and C) show the resulting velocity fields after the application of the spatial and temporal filters (90 days and 400 meters), while B) and D) after the application of the atmospheric linear correction due to the atmosphere-topography correlation. A and B) represent the datasets 100_64, whereas C) and D) the datasets 100_32.

Descending Datasets

Statistics	*Vel_do_64*	*Vel_dao_64*	*Vel_dso_64*	*Vel_do_32*	*Vel_dao_32*	*Vel_dso_32*
Maximum	2.19	1.92	1.76	2.25	1.89	1.82
Mean	0.67	0.62	0.26	0.68	0.62	0.26
Median	0.65	0.62	0.21	0.65	0.62	0.22

Table 3.1. Statistics of the LOS Velocity Standard Deviation. *Vel-do* indicates the datasets after the removal of DEM and orbital ramps. The first approach is named *v-dso,* while the latter *v-dao*.

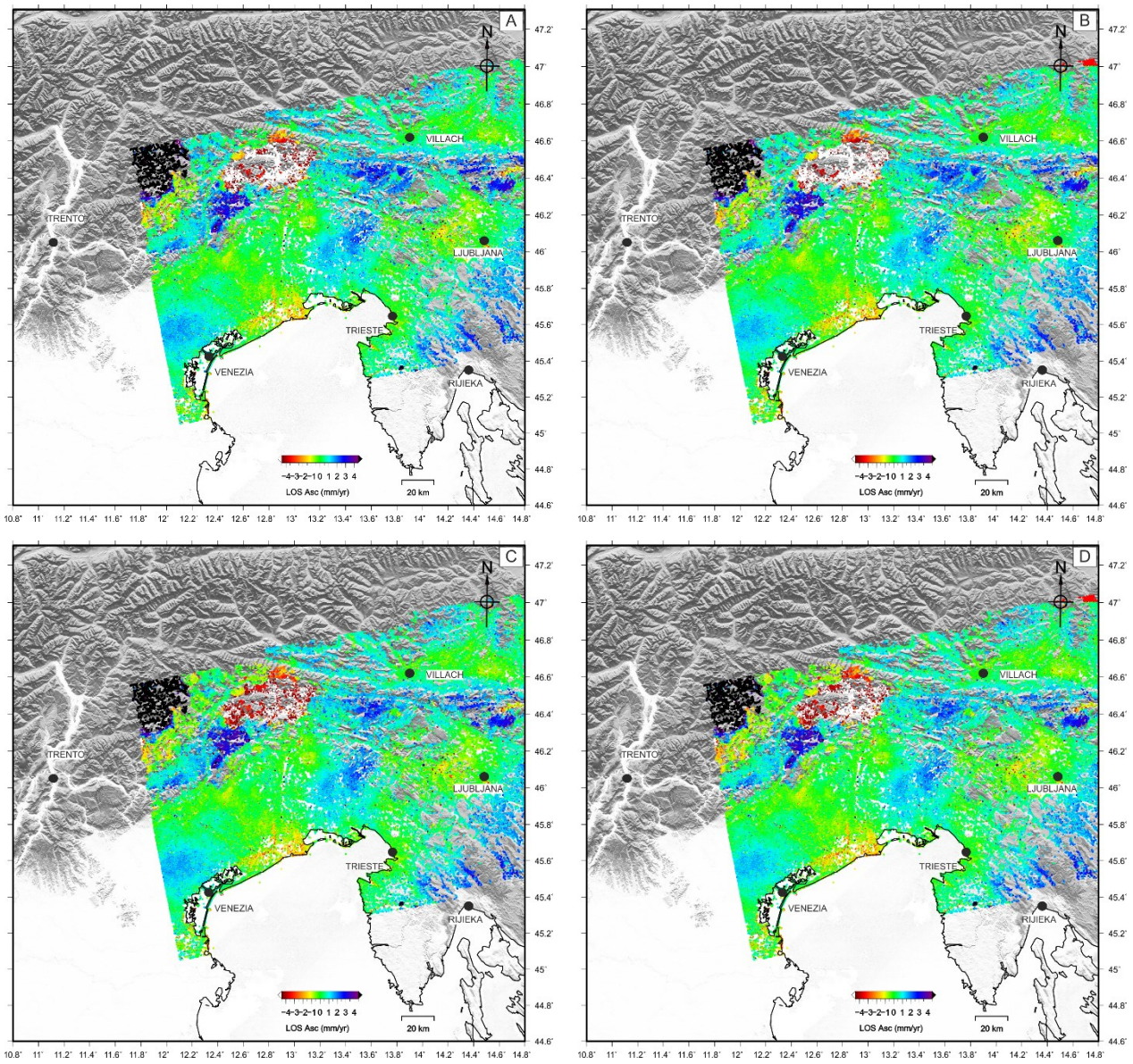

Figure 3.8. Comparison of LOS mean ground velocity maps after the atmospheric correction for the ascending datasets. A) and C) show the resulting velocity fields after the application of the spatial and temporal filters (90 days and 400 meters), while B) and D) after the application of the atmospheric linear correction due to the atmosphere-topography correlation. A and B) represent the datasets 100_64, whereas C) and D) the datasets 100_32

.

Ascending Datasets

Statistics	*Vel_do_64*	*Vel_dao_64*	*Vel_dso_64*	*Vel_do_32*	*Vel_dao_32*	*Vel_dso_32*
Maximum	2.38	2.38	1.49	2.67	2.68	1.80
Mean	0.86	0.86	0.25	0.86	0.86	0.25
Median	0.85	0.85	0.22	0.85	0.85	0.22

Table 3.2. Statistics of the LOS Velocity Standard Deviation. *Vel-do* indicates the datasets after the removal of DEM and orbital ramps. The first approach is named *v-dso,* while the latter *v-dao*

3.3. Post-processing operations: removal of PSs based on height and velocity

After the PSI processing was carried out through StaMPS, we adopted some strategies to obtain a final stable solution.

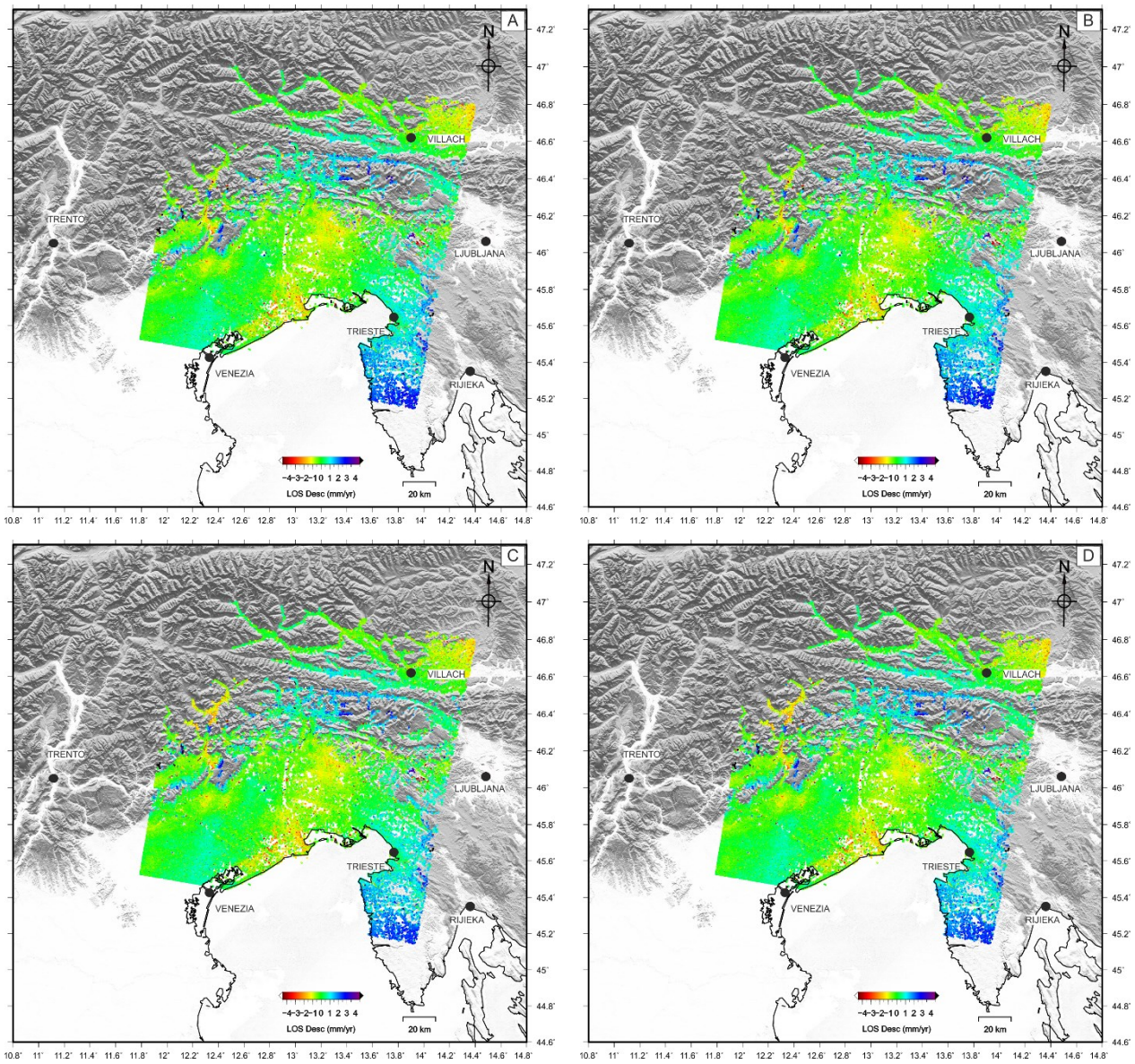

Figure 3.9. Post-processing operations by removing PSs based on height and velocity for the descending datasets. The maps show the LOS mean ground displacement rates for the 100_64 (A-B) and 100_32 datasets (C-D) after the removal of PSs based on height (A-C) and based on height and velocity (B-D).

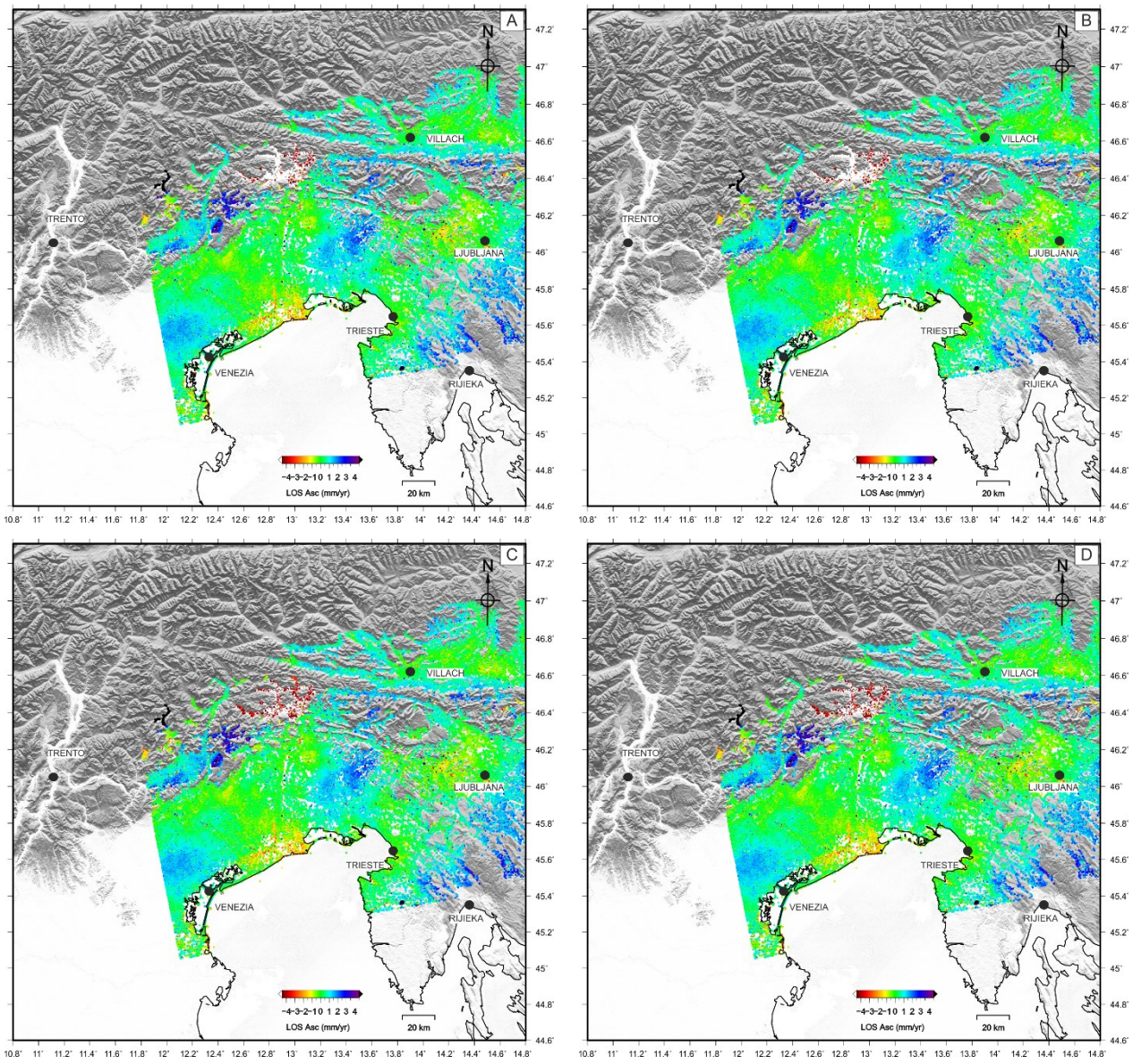

Figure 3.10. Post-processing operations by removing PSs based on height and velocity for the ascending datasets. The maps show the LOS mean ground displacement rates for the 100_64 (A-B) and 100_32 datasets (C-D) after the removal of PSs based on height (A-C) and based on height and velocity (B-D).

Considering the atmospheric effects and the correlation with topography, we removed PSs characterized by a difference in height higher than 1000 meters with respect to the reference point in the study area. The conservative approach enabled the removal of PSs potentially affected by residual atmospheric contributions, mainly in mountainous areas. As observed in Figures 3.9 and 3.10 (A-C), some zones in the north-northwestern sector of the study area, also characterized by higher velocity rates, have been eliminated.

Since we noted some differences between 100_64 and 100_32 datasets obtained by changing the Goldstein filter parameter, we decided to remove PSs based on velocity values. Specifically, we removed PSs having an absolute difference in velocity between datasets higher than 1 mm/yr, as

explained in Section 2.1.2.3. In this case, we report no evident changes in the resulting maps in Figures 3.9 and 3.10 (B-D) due to the removal of most of the affected PSs in the previous step.
In the ascending dataset (Fig. 3.10), we note the presence of two areas in the northern and northwestern sectors of the region characterized by higher rates than the adjacent pixels. The possible explanation of these anomalous deformation patterns might be related to some errors that occurred during the PSI processing.
Hence, in these areas, we removed the PSs having a significant velocity difference compared to the adjacent PSs (absolute mean rates > 5 mm/yr) (Fig. 3.10). Finally, to improve the data quality, we removed PSs with a coherence lower than 0.6.

3.4. Calibration tests for LOS datasets

After the filtering and the PSs removal, we obtained two datasets along both orbit tracks (ascending and descending) characterized by different Goldstein filter parameters (windows 32x32 and 64x64 pixels).
Since InSAR data are relative measurements, we used the GNSS LOS velocities to calibrate the InSAR data. The procedure enables the integration and comparison between GNSS and InSAR data referring to the same reference system and allows the removal of residual atmospheric and orbital effects at a larger scale.
Firstly, we projected the GNSS 3D velocity vectors along the LOS direction for both tracks. Then, given a search radius from each GNSS station, we calculated the mean ground velocities and the standard deviation of all the PSs in the selected area. In particular, we used radii at 200, 400, 600, and 800 meters. We then selected the GNSS stations for the calibration by using the criteria we explained in Chapter 2.2.1. We report the selection of GNSS stations in Appendix A and B.
After the GNSS selection, we ran 16 tests for each orbit track by considering different Goldstein filter parameters, search radii, and calibration models. We then compared the results based on statistics. Indeed, the standard deviations calculated on the differences between the calibrated InSAR products at the GNSS locations and the GNSS data, as well as the correlation coefficients, have been used as quality parameters (Tables 3.3 and 3.4).

Descending Datasets

	Tests	*Number of PSs*	*Mean*	*Median*	*Standard Deviation*	*Correlation Coefficient*
Linear	32-L-200	50	0	0.02	0.64	0.77
	32-L-400	51	0	0.04	0.65	0.77
	32-L-600	51	0	0.13	0.64	0.77
	32-L-800	51	-0.01	0.13	0.64	0.77

	64-L-200	50	0	0.06	0.6	0.8
	64-L-400	51	0	0.09	0.63	0.79
	64-L-600	51	0	0.12	0.59	0.8
	64-L-800	51	0	0.11	0.6	0.8
Quadratic	32-Q-200	50	0.36	0.46	0.59	0.82
	32-Q-400	51	0.38	0.47	0.60	0.82
	32-Q-600	51	0.36	0.46	0.58	0.83
	32-Q-800	51	0.35	0.46	0.58	0.83
	64-Q-200	50	0.26	0.35	0.58	0.83
	64-Q-400	51	0.27	0.38	0.59	0.82
	64-Q-600	51	0.25	0.36	0.56	0.83
	64-Q-800	51	0.23	0.39	0.56	0.83

Table 3.3. Statistics of the descending datasets. The table reports the statistics (mean, median, standard deviation, and correlation coefficient) of the 32 tests obtained after calibration. The combinations are based on the Goldstein filter window size (32x32 and 64x64 pixels), the search radius used for calibration (200, 400, 600, and 800 meters), and the calibration error model (linear and quadratic).

Ascending Datasets

	Tests	*Number of PSs*	*Mean*	*Median*	*Standard Deviation*	*Correlation Coefficient*
Linear	32-L-200	52	0	0.13	0.82	0.53
	32-L-400	52	0	0.02	0.79	0.53
	32-L-600	52	-0.01	0.07	0.79	0.51
	32-L-800	52	0	0.10	0.8	0.49
	64-L-200	52	0	0.11	0.8	0.54
	64-L-400	52	0	0.01	0.78	0.54
	64-L-600	52	0	0.06	0.78	0.53
	64-L-800	52	0	0.05	0.78	0.51
Quadratic	32-Q-200	52	0.23	0.18	0.72	0.68
	32-Q-400	52	0.2	0.11	0.69	0.68
	32-Q-600	52	0.24	0.19	0.68	0.68
	32-Q-800	52	0.23	0.19	0.68	0.67
	64-Q-200	52	0.1	0	0.72	0.67
	64-Q-400	52	0.1	0.03	0.69	0.67
	64-Q-600	52	0.12	0.08	0.68	0.67
	64-Q-800	52	0.12	0.06	0.68	0.66

Table 3.4. Statistics of the ascending datasets. The tables report the statistics (mean, median, standard deviation, and correlation coefficient) of the 32 tests obtained after calibration. The combinations are based on the Goldstein filter window size (32x32 and 64x64 pixels), the search radius used for calibration (200, 400, 600, and 800 meters), and the calibration error model (linear and quadratic).

Comparing the Goldstein filter window size parameters, we note that the standard deviations and the correlation coefficients of residuals generally improve by using a larger window (64x64 pixels) (Tables 3.3 and 3.4). Similarly, we observe an increase in the standard deviations and a decrease in correlation coefficients for datasets having a 600 meters radius. Finally, by comparing the calibrated LOS datasets, we observe a significant improvement in the standard deviations and correlation coefficients using a quadratic calibration model. Moreover, we also report an increase in the mean and median differences

Considering a low standard deviation and a high correlation coefficient of residuals, we finally selected as the best solution the LOS datasets having a quadratic calibration error model, a search radius of 600 meters, and a Goldstein filter window size of 64.

3.5. LOS Velocity maps before and after the calibration and GNSS comparison

The interferometric processing of Sentinel-1 SAR images generated LOS mean ground velocity maps, as shown in Figure 3.11 (A-B), for the ascending and descending orbit tracks. The post-processing operations and following tests yielded calibrated LOS velocity maps (Fig. 3.11 C-D).

The estimation and the removal of an offset and a 2-D quadratic ramp have revealed several signals in the study area. Specifically, we observe an area characterized by negative rates in both datasets on the Venetian-Friulian plain and along the coasts. Conversely, the northern sector shows positive velocities, especially on the descending dataset (Fig. 3.11D). In other areas, such as around Udine, the rates are characterized by opposite signs in both LOS datasets.

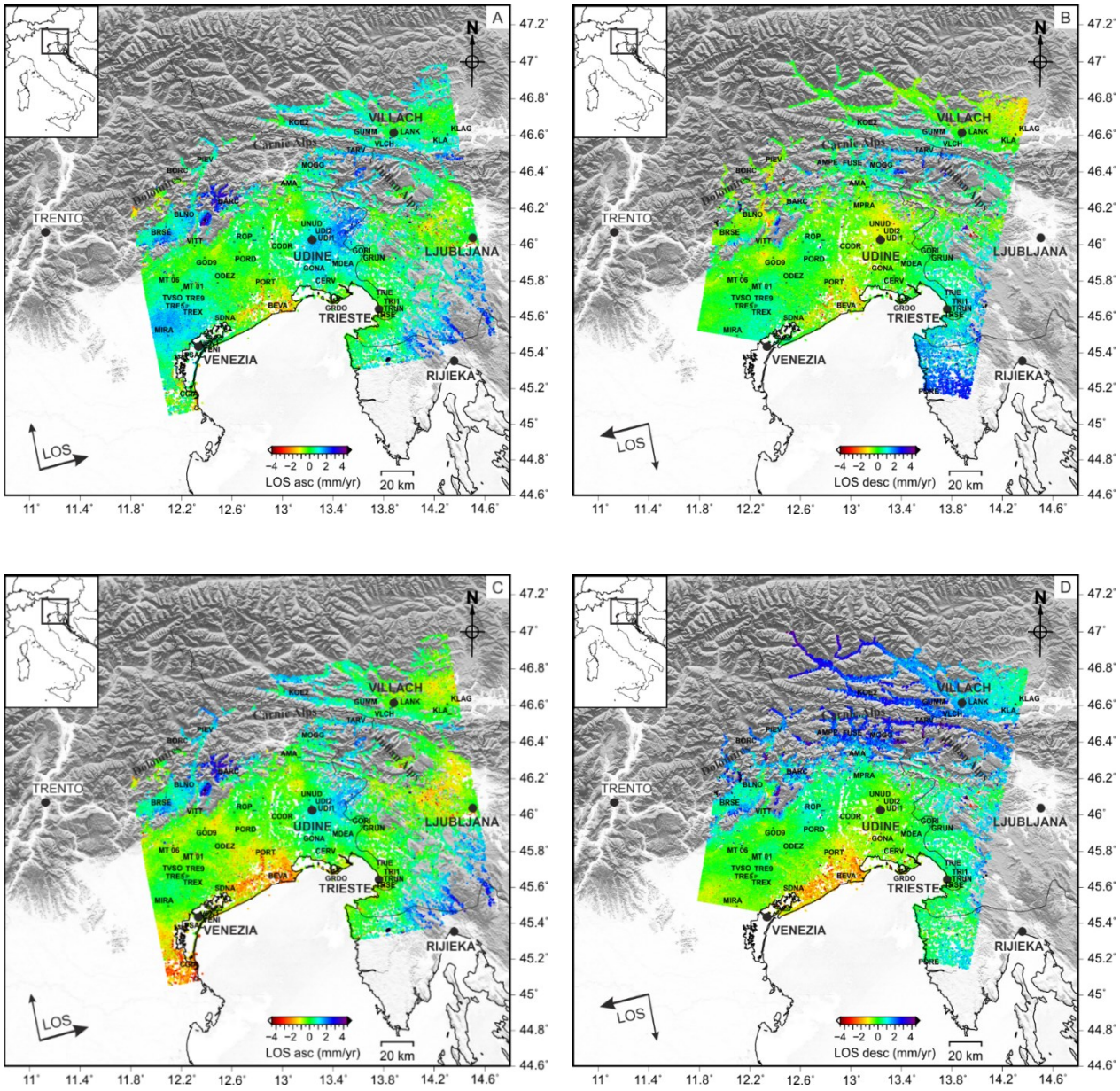

Figure 3.11. LOS Velocity maps. The LOS mean ground deformation maps before (A-B) and after the calibration (C-D) for the ascending (A-C) and descending (B-D) tracks. According to StaMPS software, positive and negative signals indicate movement toward and away from the satellite.

Regarding the comparison between InSAR and GNSS velocities, the standard deviations of the resulting solutions are 0.68 and 0.57 mm/yr for the ascending and descending datasets, respectively, with a mean value of ~ 0.6 mm/yr. The correlation plots (Fig. 3.12) also confirm the good agreement and the positive correlation between the geodetic data.

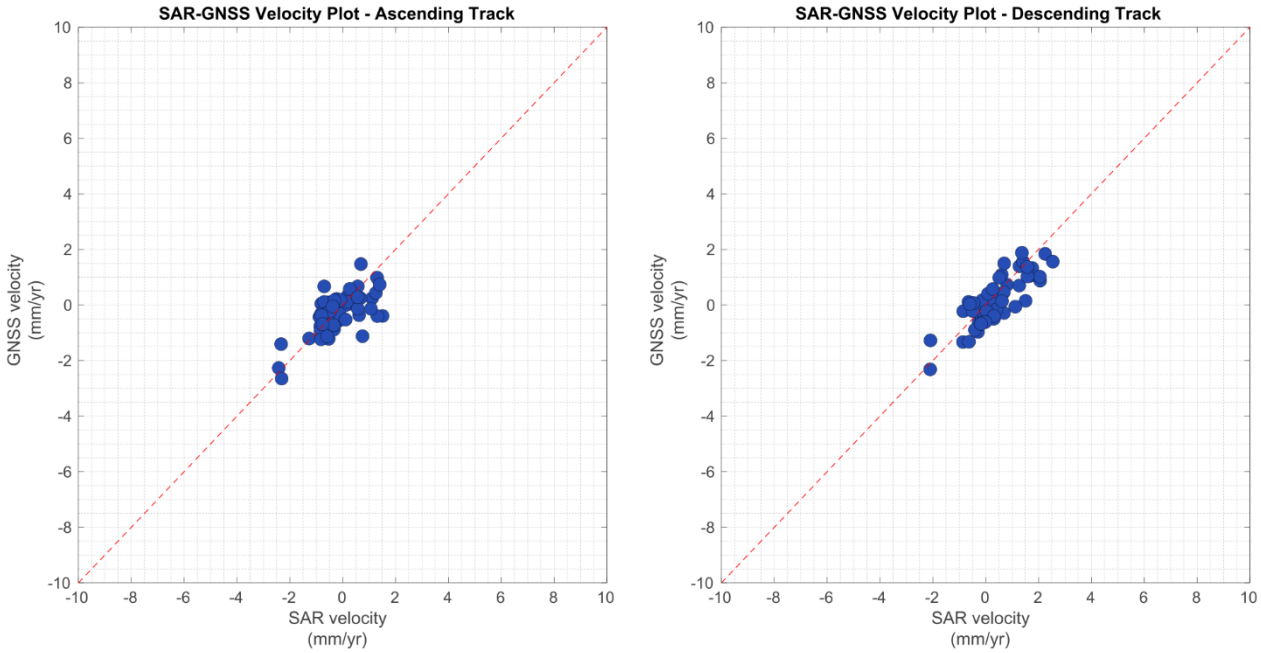

Figure 3.12. InSAR-GNSS LOS velocity plots show the correlation between geodetic data after the calibration.

3.6. East-west and Vertical velocity maps and GNSS comparison

In order to improve the observation and interpretation of the geodetic data, we combined the ascending and descending datasets in a regular grid of 100x100 meters by obtaining the east-west and vertical components of the velocity field of the study area. Figures 3.13 (A-B) show the resulting InSAR velocity maps together with the GNSS velocities along east-west and vertical directions.

Based on the E-W velocity map (Fig. 3.13A), we report a general eastward ground motion that increases northeastward by reaching ~1-2 mm/yr. A positive signal characterizes the Venetian-Friulian plain, especially in the northern sector, although in the southeastern corner of the region, we record displacement rates of 0.5-1 mm/yr in the opposite direction. A westward deformation is also detected in the Dolomites area, with average values of 1-2 mm/yr, reaching locally up to 2 mm/yr.

The northern Friuli, the Austrian area, and the eastern Slovenian sector show E-ward velocities at rates of ~1-2 mm/yr, whereas the southeastern sector of the study area presents rates of 0.5-1 mm/yr (Fig. 3.13A).

Finally, the area east of Udine, across the Italy-Slovenia border, is characterized by a negative signal on the ascending map and a positive signal on the descending map (Fig. 3.11 C-D), implying a westward ground deformation with values of 0.5-1 mm/yr (Fig. 3.13A).

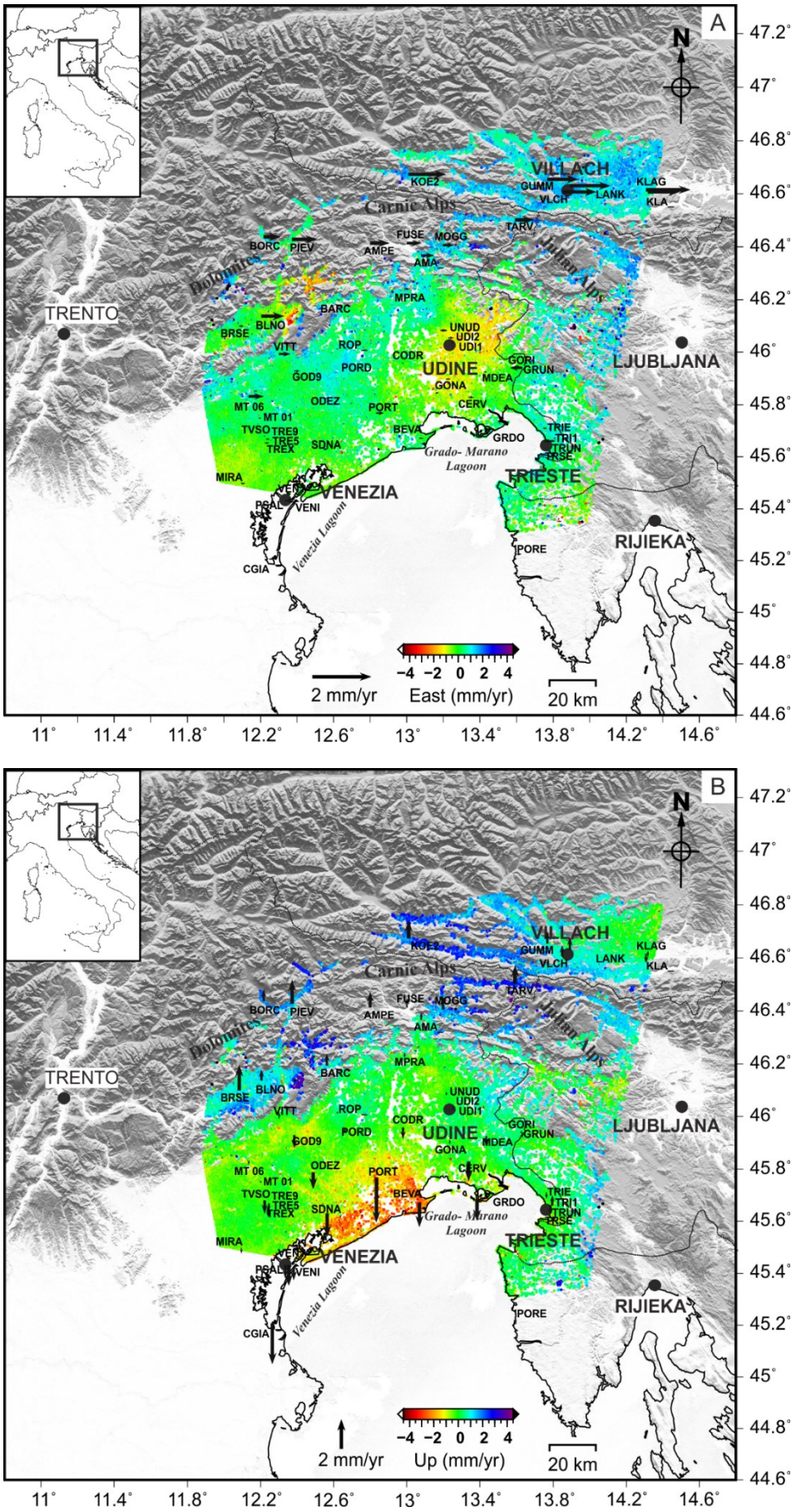

Figure 3.13. East-west (A) and Vertical (B) velocity maps.

Regarding the vertical velocities (Fig. 3.13B), the Venetian-Friulian plain and the coasts are mainly affected by subsidence, with negative rates of 0.5-3 mm/yr. In particular, we observe negative vertical velocity values of 2-3 mm/yr between the Venice and the Grado-Marano Lagoon that decrease toward the inland. In particular, on the western plain, we note the presence of subsidence along the major rivers and close to the mountain belt with mean rates of 0.5-1 mm/yr.

The southeastern coasts present slower subsidence rates, which decrease eastward and inland (< 1 mm/yr). However, strong local signals with subsidence rates higher than 4 mm/yr can be detected along the coasts, especially around harbors and industrial areas.

The vertical displacement rates increase northward across the Alpine belt (Fig. 3.13B). We estimate an uplift rate of ~1-2 mm/yr, reaching locally up to > 3 mm/yr in the northwestern sector of the study area, between the Dolomites and the Carnic Alps. Moving eastward, we observe positive vertical rates higher than 2 mm/yr on the northeastern Friulian sector and southern Austria, decreasing southward (Italy-Slovenia border) and eastward (i.e., Austria and Slovenia) with values up to 0.5-1 mm/yr (Fig. 3.13B). Finally, we observe subsidence with rates of ~ 1 mm/yr affecting the Slovenian area (W of Ljubliana) and the Austrian region (E of Villach), whereas the southeastern sector is characterized by an uplift rate of 0.5-1 mm/yr.

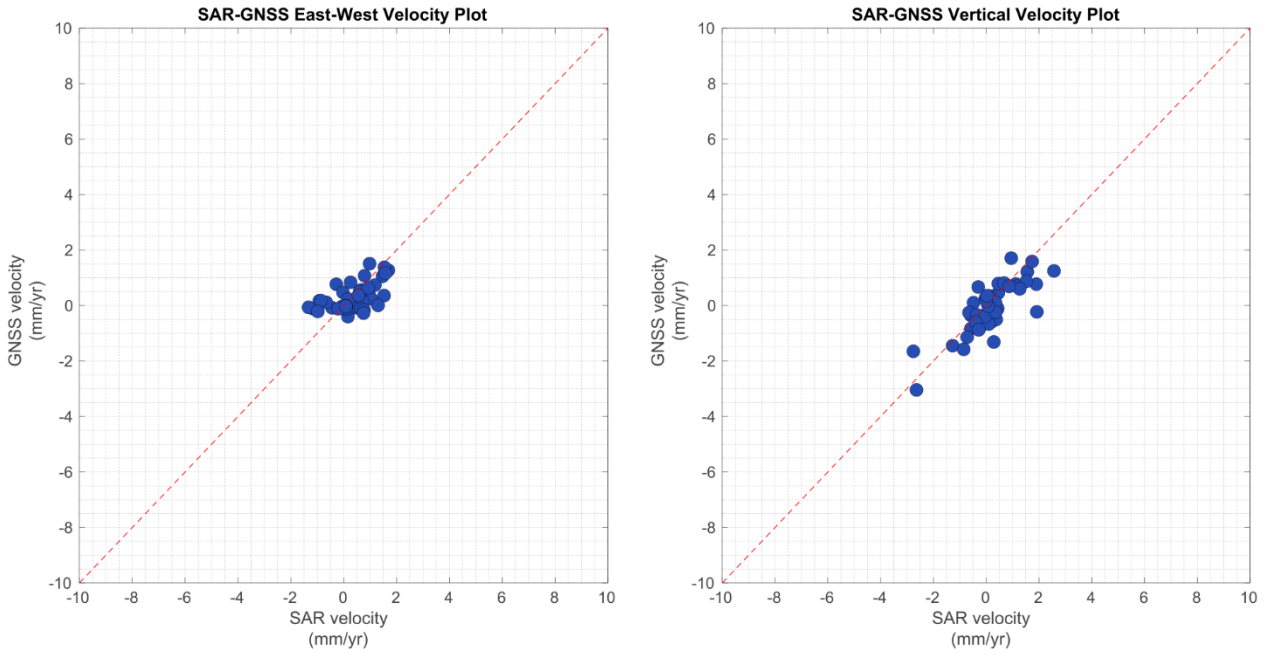

Figure 3.14. InSAR-GNSS velocity plots showing the correlation between geodetic data on the east-west and vertical components.

We also compared the InSAR-GNSS velocity after the decomposition, as shown in Figure 3.14. Here again, we notice a good agreement between the geodetic data, also confirmed by the statistics (Table 3.5). In this case, the standard deviation values reach 0.61 and 0.62 mm/yr for the vertical

and the east-west velocity maps, which are comparable with the standard deviations of the LOS datasets.

	Vertical	East-west
N° of GNSS	43	43
Mean	0.27	0.11
Median	0.30	0.19
Standard Deviation	0.61	0.62
Correlation coefficient	0.80	0.54

Table 3.5. Statistics of InSAR-GNSS velocities for the vertical and east-west components.

3.7. Velocity profiles

Given the GNSS-calibrated Sentinel-1 InSAR products, we traced three velocity profiles to better analyze the spatial pattern of the detected ground deformations over the study area, mainly focusing on the tectonic aspects.

Considering the present-day tectonic setting of Northeastern Italy, the region presents SSE-verging thrusts in the western area, S-verging and strike-slip faulting in the central sector, and NW-SE-trending strike-slip faults in the eastern sector. Our profiles cross these three sectors, allowing the correlation between the detected signals and the geological structures. In addition, we plotted the 2000-2017 instrumental seismicity along these sections to further improve the analysis of the recent activity of the tectonic structures together with the geodetic (InSAR and GNSS) data.

3.7.1. Alpine system in the western sector

The westernmost NNW-SSE-trending section (Fig. 3.15) crosses the alpine thrusts (Dolomites) and the Venetian plain from north to south. Since the vertical displacement rates may be considered as the prevailing signals in the area, we plotted along this section only the vertical component.

Starting from the south, the littorals and the southern plain show negative vertical velocity of 1-3 mm/yr, with a minimum located around the ERAC GNSS station. Moving northward, the velocity trend increases, reaching values of ± 1mm/yr close to the MT01 GNSS site.

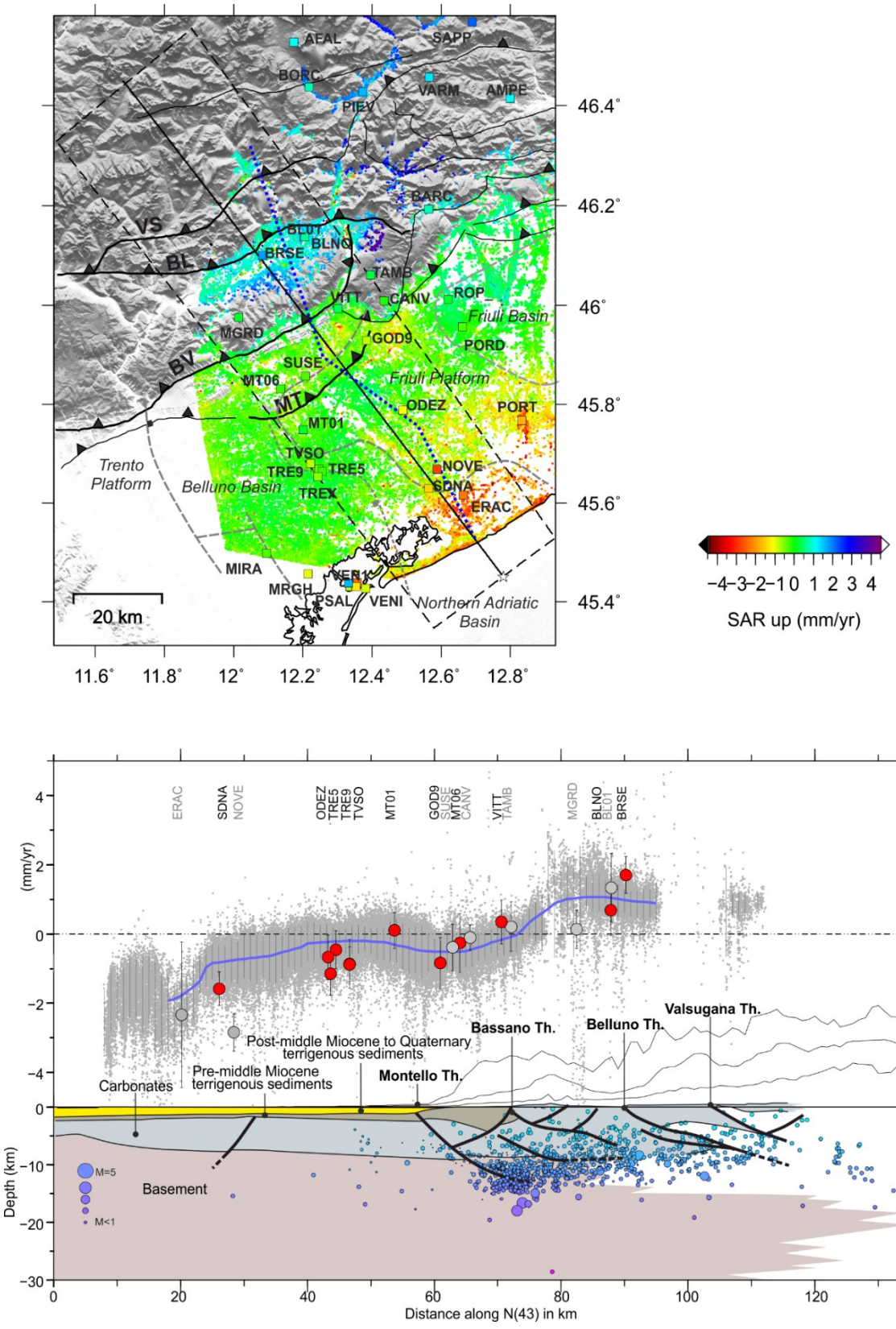

Figure 3.15. Vertical profile across the Alpine system (Dolomites). Top: the map shows the vertical velocity values for each PS, while the colored squares indicate the vertical velocity of the GNSS stations, according to the InSAR multicolor scale on the right (blue = uplift; red = subsidence). The grey dashed lines define the borders between platforms and basins, whereas the grey dotted lines separate the Belluno from the Northern Adriatic basin. The black lines represent the main tectonic structures in the area, while the blue dotted line represents the trace of the geological section reported

below. The profile (black line) with a buffer of 20 km (black dashed lines) is 140 km long, and the white star indicates the starting point. Bottom: the plot shows the vertical SAR velocities (grey dots) where the blue line indicates the median value. The circles with relative uncertainties represent the vertical velocities of GNSS stations; specifically, the grey ones have not been used during the calibration. The topographic profile, the geological section, and the seismicity complete the plot. Specifically, the geological section is modified from Fantoni and Franciosi (2010).

A similar trend is also detected by GNSS data, which show initial negative values and a progressive positive trend in the vertical velocity. The first 50-60 km of the profile are also characterized by the absence of recent seismicity, as shown in Figure 3.15. Considering the geological section modified from Fantoni and Franciosi (2010), the southern area presents thick post-middle Miocene to Quaternary terrigenous units, whose width decreases northward.

After the stable sector, we observe a positive velocity gradient of about 1 mm/yr in the mountain region between the VITT station and the Belluno Valley (BLNO–BL01 GNSS stations). Observing the seismicity, we note the presence of significant clusters characterized by moderate-small earthquakes with a hypocentral depth of 10-15 km deep. The recent seismic activity is concentrated on the deeper portions of the main thrusts, especially the Montello, Bassano-Valdobbiadene, and Belluno Thrusts.

3.7.2. Alpine system and Dinaric systems in the central sector

Regarding the central sector of the study area, we traced an NNE-SSW-oriented velocity profile based on the geological profile of Merlini *et al.* (2002) to estimate the gradient across the Julian Alps and Dinarides. Given the presence of thrusts and strike-slip faults, we analyzed both velocity profiles in the east-west and vertical directions.

Starting from the Friulian coasts, we observe negative vertical rates of 1-3 mm/yr, which rapidly increase, moving 20 km northward along the profile (rates > -1mm/yr) (Fig. 3.16). A gradual positive vertical trend is then detected, reaching a stable area between Udine and JOAN GNSS station, close to the Julian Alps. Here, the GNSS data show an excellent agreement with InSAR measurements (Fig. 3.16). According to the geological section, we report the presence of compressible Miocene-Quaternary terrigenous deposits over thick carbonatic units of the Friulian platform in the plain (south of the JOAN GNSS site). Furthermore, the area presents low seismicity, mainly characterized by small events at depths of 5-15 km.

Moving to the mountain belt, our InSAR measurements show an increase in vertical velocity toward Tarvisio (TARV), recording an uplift up to 2.3 mm/yr within 35 km along the profile, then followed by a velocity decrease (mean rates up to 1 mm/yr) toward Austria.

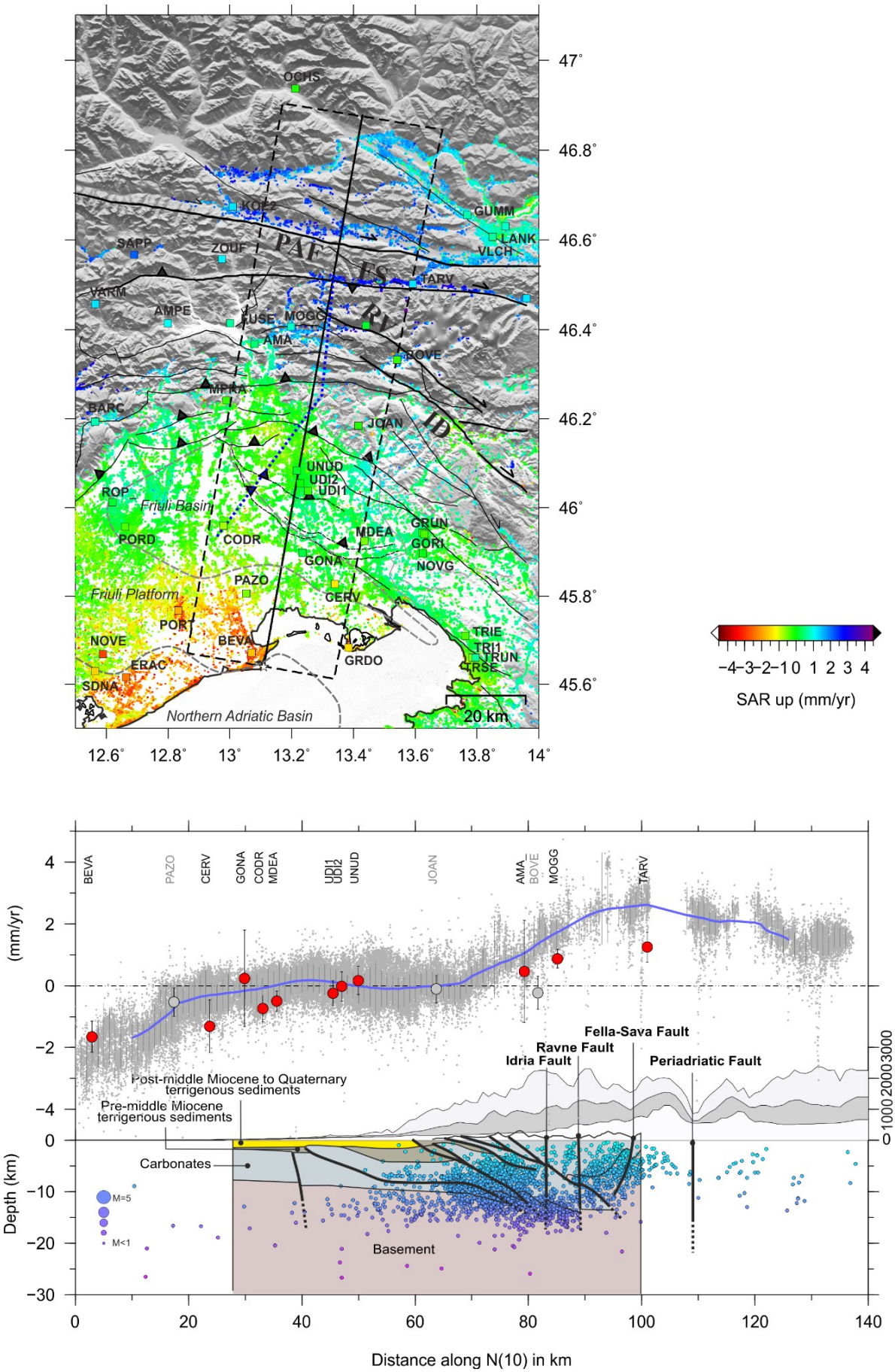

Figure 3.16. Vertical profile across the Alpine (Julian Alps) and Dinaric system. Top: the map shows the vertical velocity values for each PS, while the colored squares indicate the east-west velocity of the GNSS stations, according to the

InSAR multicolor scale on the right (blue = uplift; red = subsidence). The grey dashed lines define the borders between platforms and basins, whereas the black lines represent the main tectonic structures in the area. The blue dotted line represents the trace of the geological section reported below. The profile (black line) with a buffer of 20 km (black dashed lines) is 140 km long, and the white star indicates the starting point. Bottom: the plot shows the vertical SAR velocities (grey dots) where the blue line indicates the median value. The circles with relative uncertainties represent the vertical velocities of GNSS stations; specifically, the grey ones have not been used during the calibration. The topographic profile, the geological section, and the seismicity complete the plot. Specifically, the geological section is modified from Merlini *et al.* (2002).

The positive vertical gradient appears steeper than the one estimated by the GNSS stations, reaching rates of about 1 mm/yr at the Tarvisio site (i.e., TARV). Here, the interaction between the Alpine and Dinaric systems is more evident due to the presence of several south-verging thrusts and sub-vertical parallel strike-slip faults, such as the Idrija and Ravne faults. The location of these tectonic structures corresponds with the positive velocity gradient, as observed in Figure 3.16. Regarding seismic activity, we observe two clusters at depths of 5-15 km, characterized by small events. The former, distributed between the carbonates and the basement, is localized near the deeper portions of the front thrusts. On the other hand, the latter, characterized by fewer events and shallower hypocentral depths, mainly corresponds with the aforementioned Dinaric structures and the strike-slip Fella-Sava fault.

Analyzing the horizontal profile (Fig. 3.17), a westward movement dominates the southern section, starting from a stable area along the coasts (mean velocity of 0 mm/yr) until Udine, reaching 1 mm/yr. Despite the vertical profile, no clear westward trend may be estimated from GNSS velocities, which indicate a stable area. After Udine, we report a velocity increase (eastward motion), reaching about 1 mm/yr around Tarvisio (TARV GNSS station). In this case, a positive gradient is also observed by GNSS stations, despite the lower rates (< 1 mm/yr). However, even on the east-west velocity profile, the detected positive (eastward) gradient is located in correspondence with the main tectonic structures of the areas.

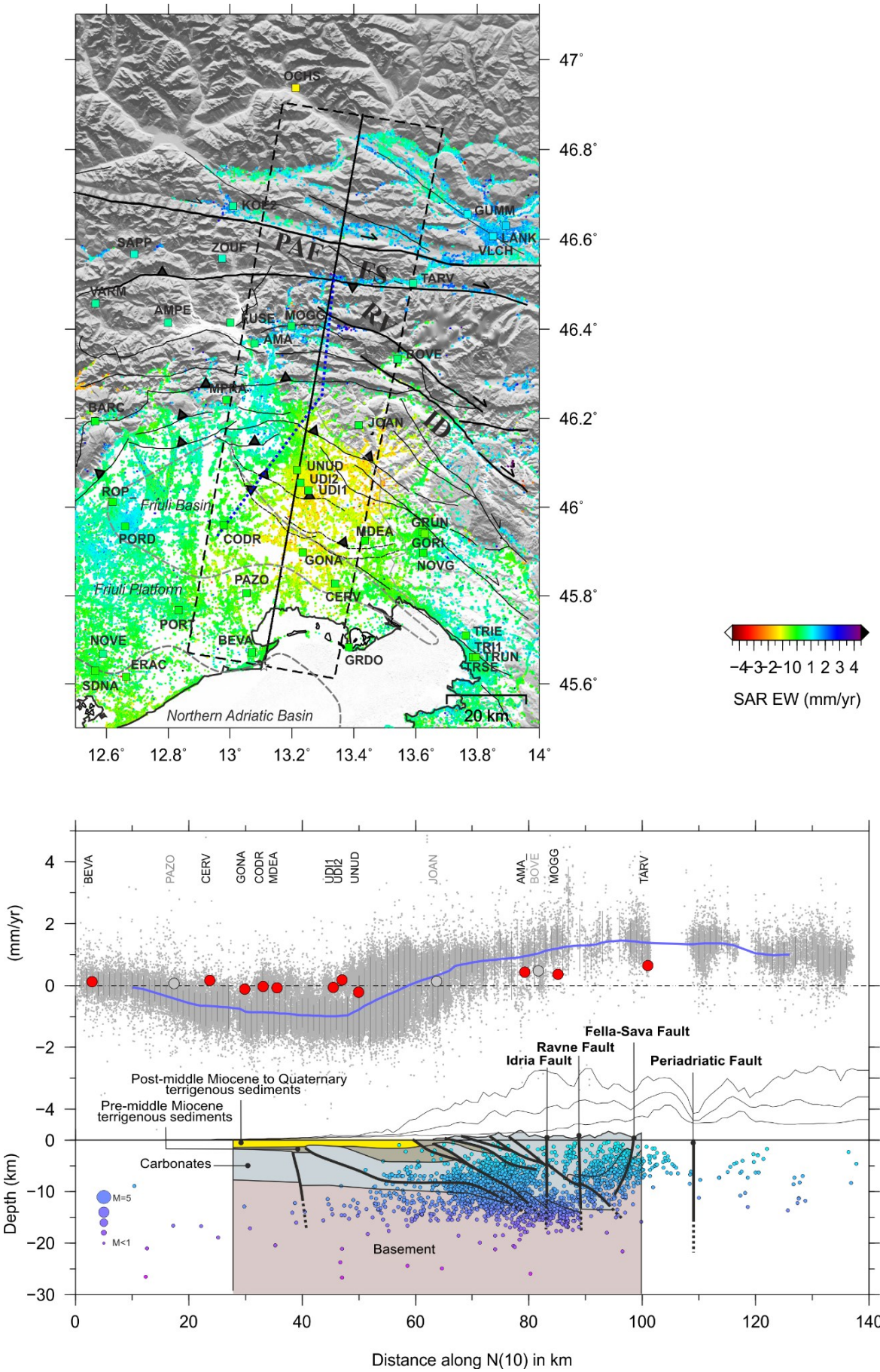
OCHS
KOZ2
GUMM
LANK
VLCH
SAPP
ZOUF
PAF
FS
RI
ID
TARV
VARM
AMPE
USE
MOGG
AMA
BOVE
MPRA
BARC
JOAN
UNUD
UDI2
UDI1
ROP
Friuli Basin
PORD
CODR
MDEA
GRUN
GORI
NOVG
GONA
PAZO
Friuli Platform
CERV
PORT
NOVE
BEVA
GRDO
TRIE
TRI1
TRUN
ERAC
TRSE
SDNA
Northern Adriatic Basin
20 km
47˚
46.8˚
46.6˚
46.4˚
46.2˚
46˚
45.8˚
45.6˚
12.6˚
12.8˚
13˚
13.2˚
13.4˚
13.6˚
13.8˚
14˚
−4 −3 −2 −1 0 1 2 3 4
SAR EW (mm/yr)

BEVA
PAZO
CERV
GONA
CODR
MDEA
UDI1
UDI2
UNUD
JOAN
AMA
BOVE
MOGG
TARV
(mm/yr)
4
2
0
−2
−4
Fella-Sava Fault
Ravne Fault
Idria Fault
Periadriatic Fault
Post-middle Miocene to Quaternary terrigenous sediments
Pre-middle Miocene terrigenous sediments
Carbonates
Basement
M=5
M<1
Depth (km)
0
−10
−20
−30
Topography (m)
1000
2000
3000
0
20
40
60
80
100
120
140
Distance along N(10) in km

Figure 3.17. East-west profile across the Alpine (Julian Alps) and Dinaric system. Top: the map shows the east-west velocity values for each PS, while the colored squares indicate the east-west velocity of the GNSS stations, according to the InSAR multicolor scale on the right (red = westward; blue = eastward displacement). The grey dashed lines define the borders between platforms and basins, whereas the black lines represent the main tectonic structures in the area. The blue dotted line represents the trace of the geological section reported below. The profile (black line) with a buffer of 20 km (black dashed lines) is 140 km long, and the white star indicates the starting point. Bottom: the plot shows the east-west SAR velocities (grey dots) where the blue line indicates the median value. The circles with relative uncertainties represent the east-west velocities of GNSS stations; specifically, the grey ones have not been used during the calibration. The topographic profile, the geological section, and the seismicity complete the plot. Specifically, the geological section is modified from Merlini *et al.* (2002).

3.7.3. Dinaric system in the eastern sector

Based on the trace of Moulin *et al.* (2016), the third section crosses the dextral sub-parallel faults NW-SE trending, which belonged to the Dinaric system (e.g., Bechtold *et al.*, 2009; Serpelloni *et al.*, 2016; Atanackov *et al.,* 2021).

Similar to the previous section, we analyzed the vertical and east-west velocity components considering the presence of NW-SE transcurrent and transpressional structures.

Starting from the vertical profile (Fig. 3.18), we observe a gradual increase in velocity from the Grado-Marano Lagoon (mean rate >-1 mm/yr) toward the inland, reaching rates lower than 1 mm/yr near the NOVG GNSS station. On the other hand, we notice a positive velocity gradient (eastward motion) in the east-west velocity profile (Fig. 3.19), except for a weak westward signal confined between MDEA and NOVG stations due to the strong effect of the deformation pattern recorded near Udine. GNSS data are in good agreement with InSAR measurements. As regards the seismicity, few small events are localized between the crystalline basement and the carbonate units. We also observe the presence of some buried thrusts and strike-slip faults located on the Friulian plain.

Between Raša and Idrija faults, on the vertical profile (Fig. 3.18), we record an uplift, reaching ~ 1 mm/yr on the Predjama fault and ~ 0 mm/yr close to the Idrija location. Concerning the east-west profile, we note a positive gradient of 1 mm/yr (eastward motion), especially between Predjama and Ravne faults (Fig. 3.19). The cluster of seismicity is localized at depths of 10-15 km, interesting the deeper portions of the strike-slip faults in the area. Specifically, we observe a concentration of seismic activity around the Ravne fault.

After the IDRI station, the velocity increases, implying an eastward movement, reaching values up to 1.5 mm/yr in correspondence with the RADO station, gradually decreasing northward (~ 1 mm/yr) (Fig. 3.19). Similarly, on the vertical profile (Fig. 3.18), a positive vertical gradient of about 1.5 mm/yr is recorded within approximately 35 km along the profile, decreasing toward the Austrian valley of Villach (~ 0 mm/yr). Despite the lower estimated rates, even the GNSS data delineate similar trends in vertical and east-west velocity moving north-northeastward. The seismic data shows a small cluster near the Fella-Sava fault at depths of 5-10 km.

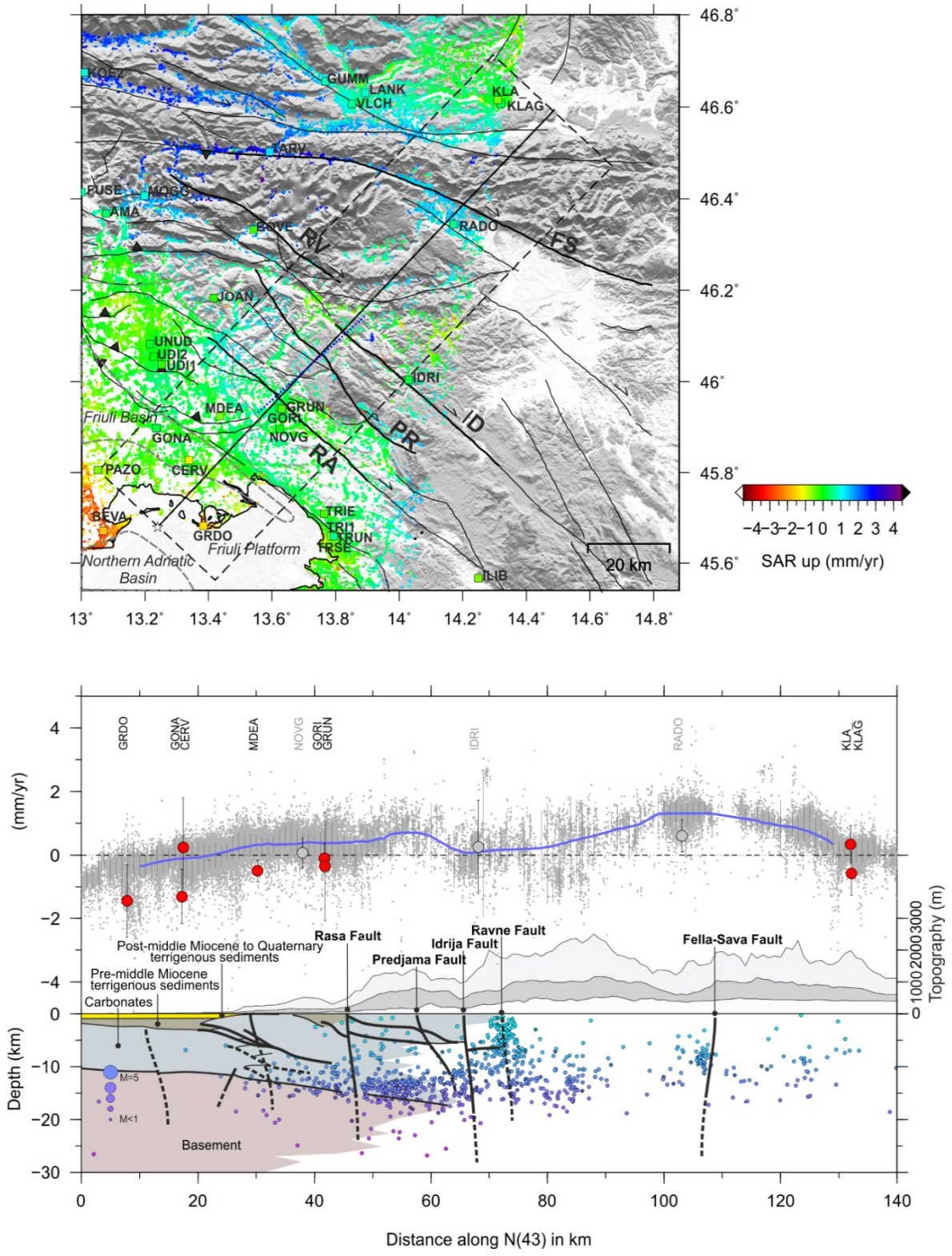

Figure 3.18. Vertical profile across the Dinaric system. Top: the map shows the vertical velocity values for each PS, while the colored squares indicate the vertical velocity of the GNSS stations, according to the InSAR multicolor scale on the right (blue = uplift; red = subsidence). The grey dashed lines define the borders between platforms and basins, whereas the black lines represent the main tectonic structures in the area. The blue dotted line represents the trace of the geological section reported below. The profile (black line) with a buffer of 20 km (black dashed lines) is 140 km long, and the white star indicates the starting point. Bottom: the plot shows the vertical InSAR velocities (grey dots) where the

blue line indicates the median value. The circles with relative uncertainties represent the vertical velocities of GNSS stations; specifically, the grey ones have not been used during the calibration. The topographic profile, the geological section, and the seismicity complete the plot. Specifically, the geological section is modified from Moulin *et al.* (2016).

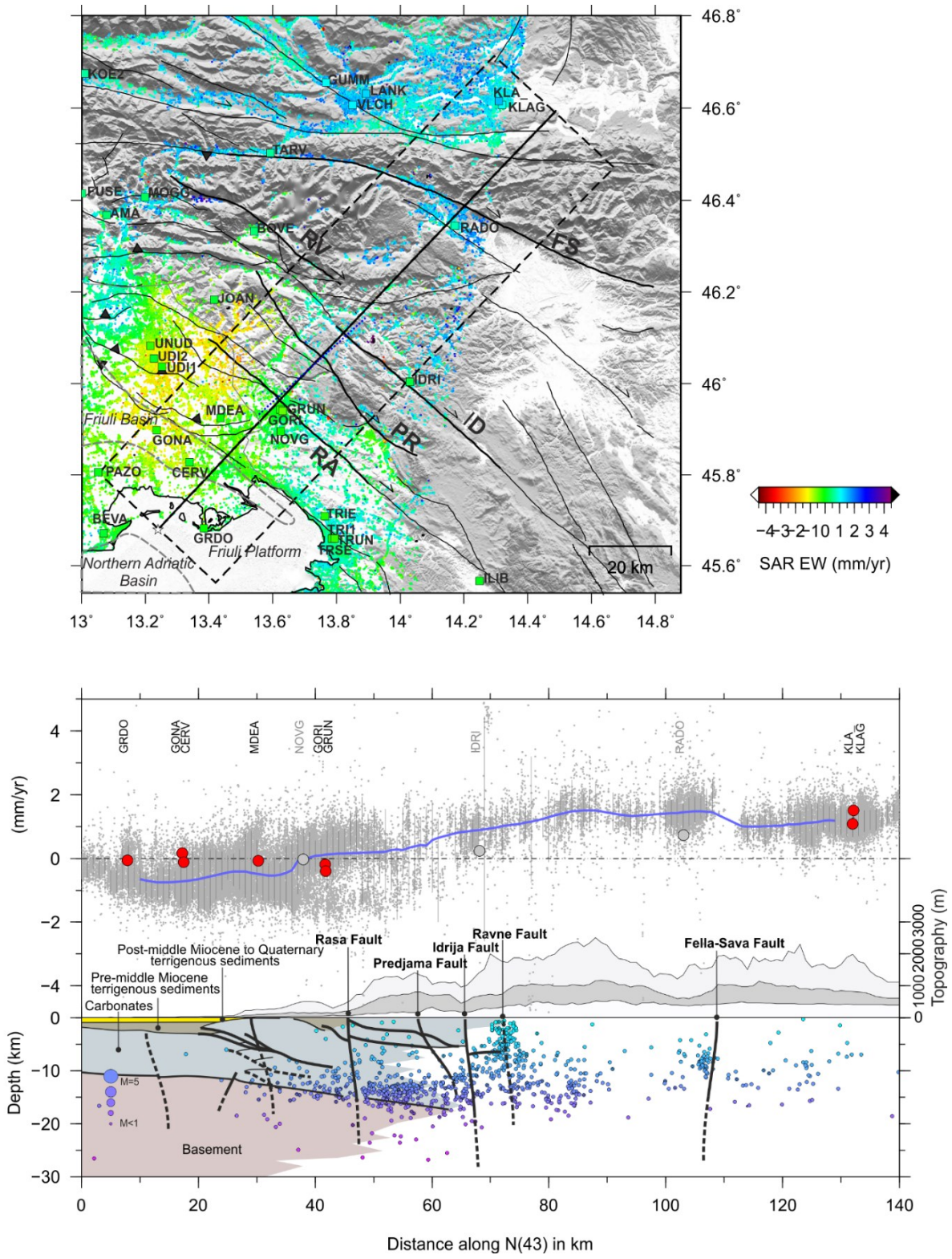

Figure 3.19. East-west profile across the Dinaric system. Top: the map shows the east-west velocity values for each PS, while the colored squares indicate the east-west velocity of the GNSS stations, according to the InSAR multicolor

scale on the right (red = westward; blue = eastward displacement). The grey dashed lines define the borders between platforms and basins, whereas the black lines represent the main tectonic structures in the area. The blue dotted line represents the trace of the geological section reported below. The profile (black line) with a buffer of 20 km (black dashed lines) is 140 km long, and the white star indicates the starting point. Bottom: the plot shows the east-west InSAR velocities (grey dots) where the blue line indicates the median value. The circles with relative uncertainties represent the east-west velocities of GNSS stations; specifically, the grey ones have not been used during the calibration. The topographic profile, the geological section, and the seismicity complete the plot. Specifically, the geological section is modified from Moulin *et al*. (2016).

3.8. Modeling of the fault in the Alpine system

Once we analyzed the sections, we computed an inversion based on a two-dimensional model to extract the geometrical and kinematic parameters of the causative source, as explained in Section 2.3. In particular, we selected the first profile, crossing the Dolomites in the eastern sector, where a clear tectonic signal is visible and may be attributed to a single fault. Conversely, in the profiles located in the central and eastern sectors, it is not possible to distinguish and isolate the single contribution among the different tectonic structures because of the complexity of the tectonic context. Hence, we sampled the InSAR datasets with the method explained in Section 2.3.1 to obtain about 3300 final points (N_p) (Table 3.6).

	Alpine thrust						
	T_p	Div_{lon}	Div_{lat}	N_{crit}	N_p	R	*Final points*
Ascending	69810	10	10	698	3300	33%	3375
Descending	73965	10	10	740	3300	33%	3429

Table 3.6. Sampling parameters.

Before the inversion, we defined the weight of the InSAR datasets, given the median GNSS direction of the horizontal velocities and the direction of the LOS. We attributed the maximum weight (1) in the case of GNSS-LOS alignment and the minimum weight (0) for GNSS-Heading alignment.

	Alpine thrust			
	Median GNSS direction	*Median SAR Heading angle*	*Median SAR LOS angle*	*Weight*
Ascending	144°	349.13°	79.13°	0.28
Descending	144°	189.93°	279.93°	0.51

Table 3.7. Weight definition for InSAR datasets with respect to the median GNSS direction.

In the present work, we fixed the length and width of the fault at 1500 km to simulate an infinite rectangular plane. We defined the strike based on the geological and seismic data (i.e., Fantoni and Franciosi, 2010; DISS Working Group, 2021) together with the seismicity and focal mechanism. Regarding the mid-point of the upper portion of the fault, we strictly defined the range of the X and Y coordinates in meters with respect to the reference point. Based on the seismological data, we defined the depth range between 3 to 20 km within the seismogenic layer. Finally, the slip rates along dip and strike were left free to vary.

Thus, after importing the geodetic data and defining the source parameters, we ran several tests by fixing the dip angle. The tests have been then evaluated based on the Weighted Residuals Sum of Squares (WRSS) of GNSS and SAR data

$$WRSS = (obs - mod)^T * C^{-1} * (obs - mod) \quad (3.1)$$

Where obs and mod are the observed and modeled geodetic data whereas C^{-1} is the inverse of the covariance matrix.

In Table 3.8, we report the resulting WRSS values obtained by varying the dip angle, namely at 15, 20, 25, 30, and 35 degrees, assuming “Andersonian” inverse faults (Anderson *et al.*, 1905).

	WRSS		
Dip (°)	*WRSS_GPS*	*WRSS_ASC*	*WRSS_DSC*
15	257.7718	35136.14	54031.59
20	273.8449	34915.55	53788.3
25	300.5898	34446.02	53316.27
30	337.7375	33752.96	52727.77
35	386.3534	32743.35	52016.01

Table 3.8. WRSS of the geodetic datasets and dip angle values.

We observe that an increase in the dip angle corresponds to a general increase of the GNSS WRSS and a decrease of the InSAR WRSS and vice versa.

Thus, we plotted the WRSS of GNSS and both InSAR datasets, calculated the mid-point (barycenter), and then extracted the correspondent dip angle to minimize the residuals, as shown in Figure 3.20.

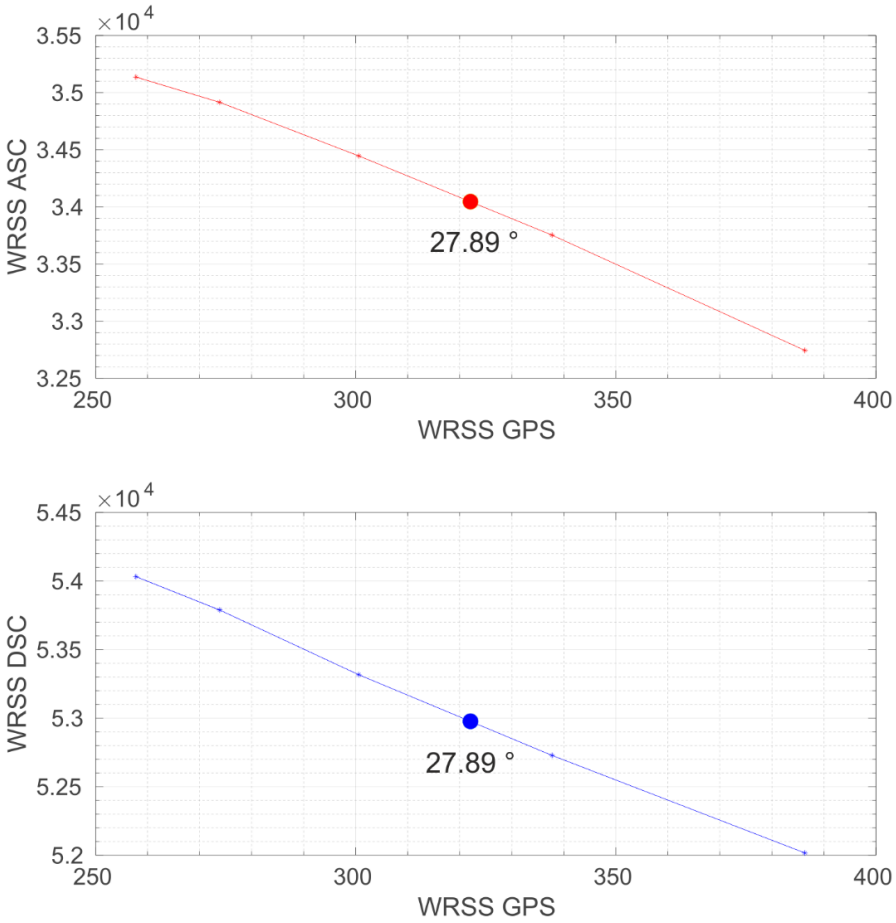

Figure 3.20. Correlation plot between WRSS GNSS and InSAR datasets (ascending and descending tracks). The barycenter corresponds to the dip angle value of 27.89°

We ran another test by fixing the dip angle with the extracted value (27.89 °) and evaluated the final results. Table 3.9 reports the resulting parameters and the corresponding WRSS values, whereas Figure 3.21 shows the comparison between the observed and the modeled data provided by the geodetic datasets.

Source Parameters

Lenght	*Width*	*Depth*	*Dip*	*Strike*	*X*	*Y*	*Strike Slip*	*Dip Slip*
km	*km*	*km*	°	°	°	°	*mm/yr*	*mm/yr*
1500	1500	5,334	27.89	62	12.00	45.96	-0.4	2.01

WRSS GNSS	*WRSS ASC*	*WRSS DSC*
322.18	34067.99	52982.38

Table 3.9. Source parameters of the fault after the inversion and WRSS values.

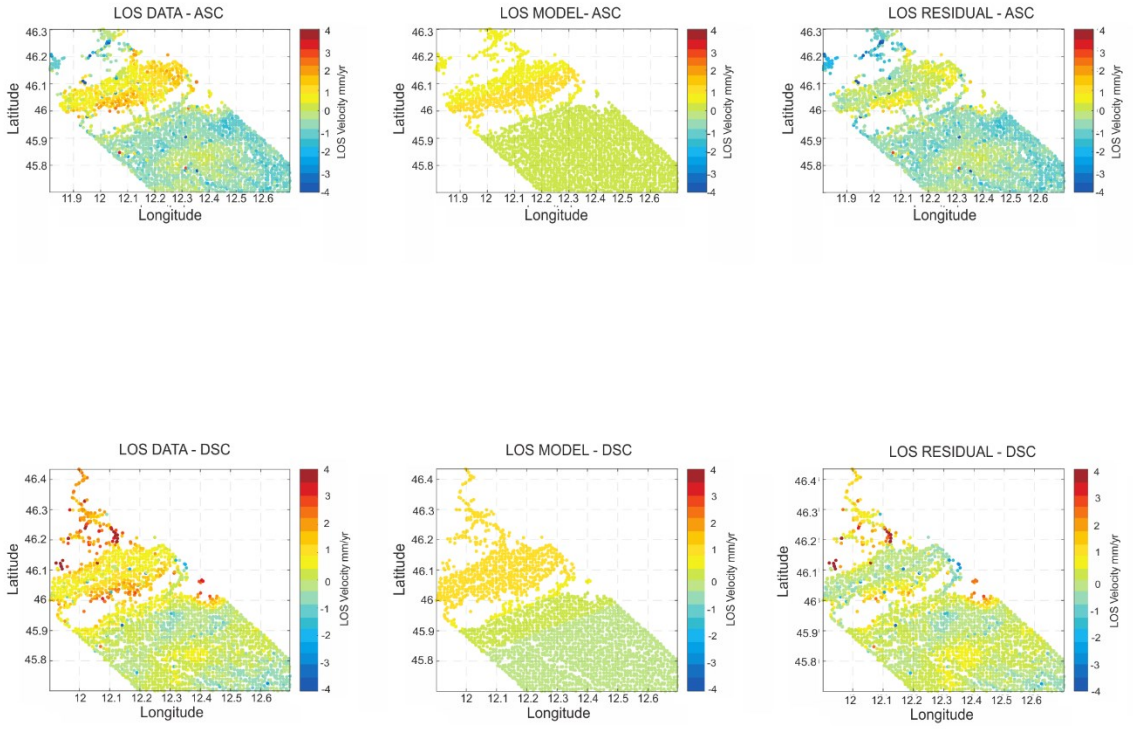

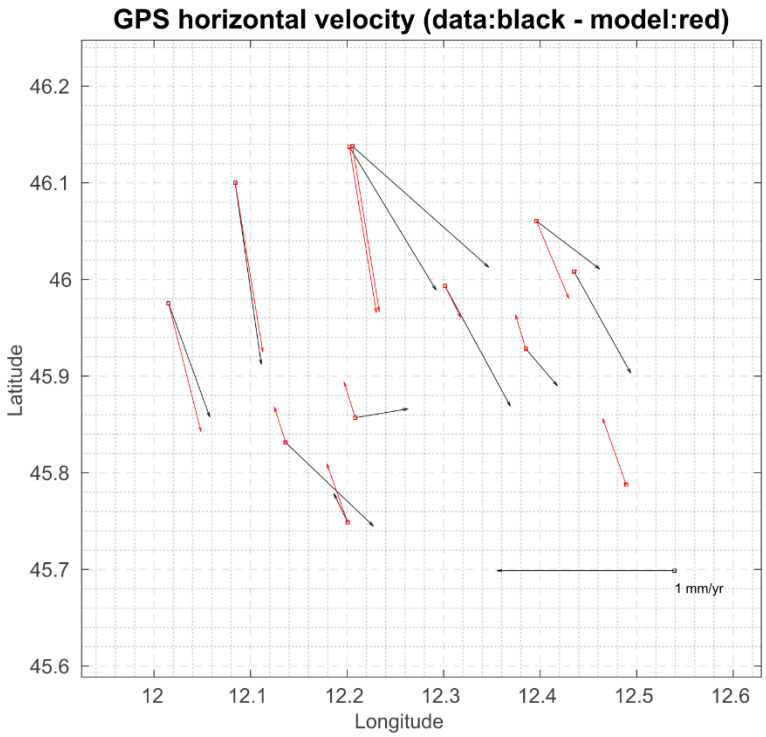

Figure 3.21. Observed and modeled geodetic data after the inversion. Top: Observed, modeled, and residual data referring to the ascending and descending datasets. Bottom: Comparison between the observed and modeled horizontal velocities for GNSS data.

In Figure 3.21, we notice that the modeled data present a similar spatial pattern along the profile with respect to the observed LOS velocities, except for some discrepancies due to local signals. Regarding the GNSS data, we observe a good agreement between observed and modeled data in the northern and southern stations, whereas the central GNSS stations present a poor fit (Fig. 2.1). The rectangular fault plane is characterized by a strike of 62° and a dip angle of 27.89°. The mid-point is located at 12.00°E and 45.96°N at 5.334 km deep. The amount of slip along the dip and strike directions is ~2 mm/yr and -0.4 mm/yr, indicating inverse kinematics with a small sinistral strike-slip component (Table 3.9). We also report the geodetic data WRSS values to confirm the previous analysis.

We finally added the model fault plane to the profile across the Alpine system (Fig. 3.22). On the map, the red line shows the strike of the fault, which is comparable to the strike of the Bassano-Valdobbiadene thrust. As regards the velocity profile, the red segment and the point indicate the geometry of the fault segment and the location of the mid-point with the relative depth, which corresponds to the deeper portion of the Bassano-Valdobbiadene thrust. Comparing the observed and modeled velocity along the profile, we note a good fit of the positive vertical gradient between the Bassano-Valdobbiadene and the Belluno thrusts. Moving southward, we observe a misfit between the modeled and the observed velocity.

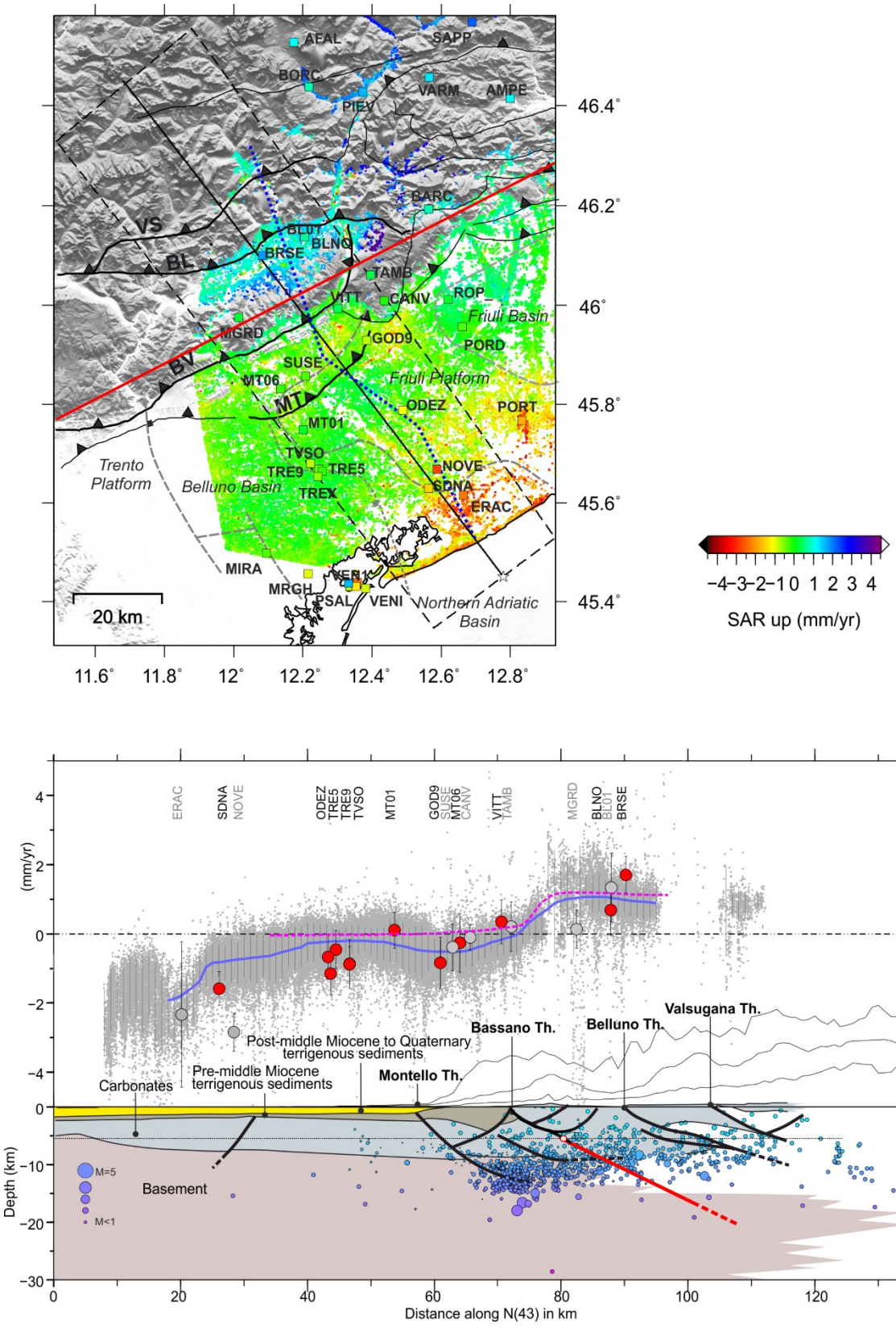

Figure 3.22. Alpine system velocity profile with the resulting fault (red line) after the inversion. In the velocity profile, the blue and the dashed magenta lines indicate the observed and modeled vertical velocity, respectively.

4. DISCUSSION

4.1. Mean Ground Velocity Maps

The calibrated LOS mean ground velocity maps present different signals.

Compared to the study of Farolfi *et al.* (2019a), which focused on the estimation of the subsidence in the Po plain at a regional scale by using InSAR images acquired by the ENVISAT satellites in the period 2004-2010, we observe the presence of a negative pattern with comparable rates (> -2 mm/yr) in the northern Venice Lagoon area, especially in the ascending dataset (Fig. 4.1 A-C).

Even Anderlini *et al.* (2020) employed ENVISAT data to investigate the easternmost Veneto region. Here, the LOS measurements show positive rates of 2-3 mm/yr across the Dolomites (i.e., Belluno valley) that decrease toward the coasts, reaching negative velocity (1-2 mm/yr) (Fig. 4.2 A-B). Our measurements show similar deformation patterns in the northern and southern regions, but the estimated LOS displacement rates are lower (Fig. 4.2 C-D).

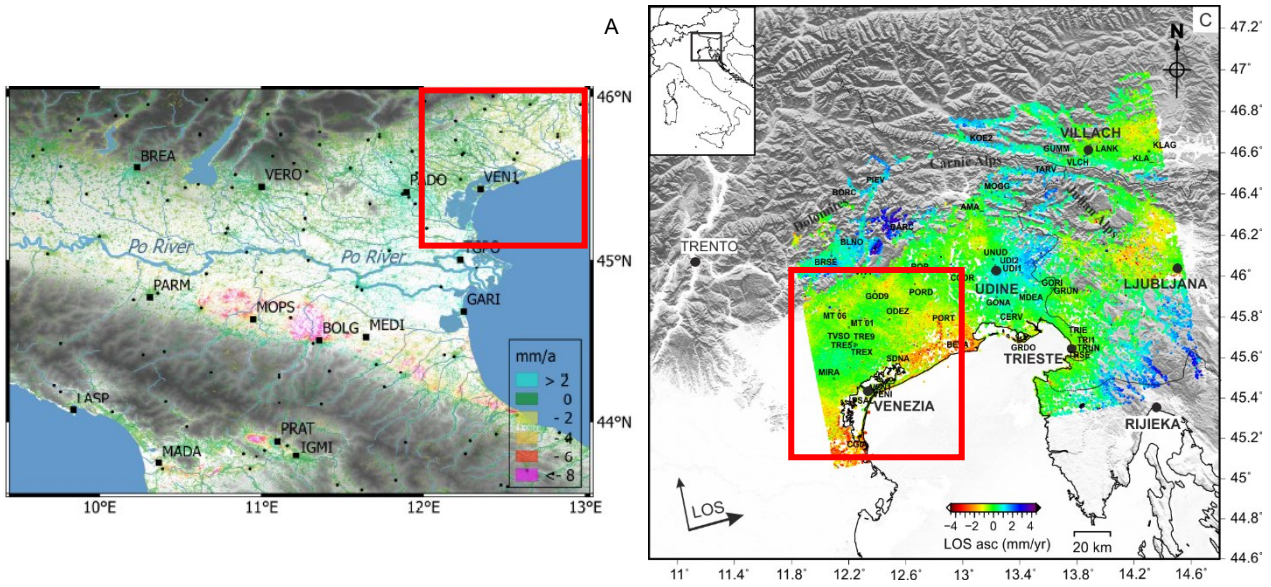

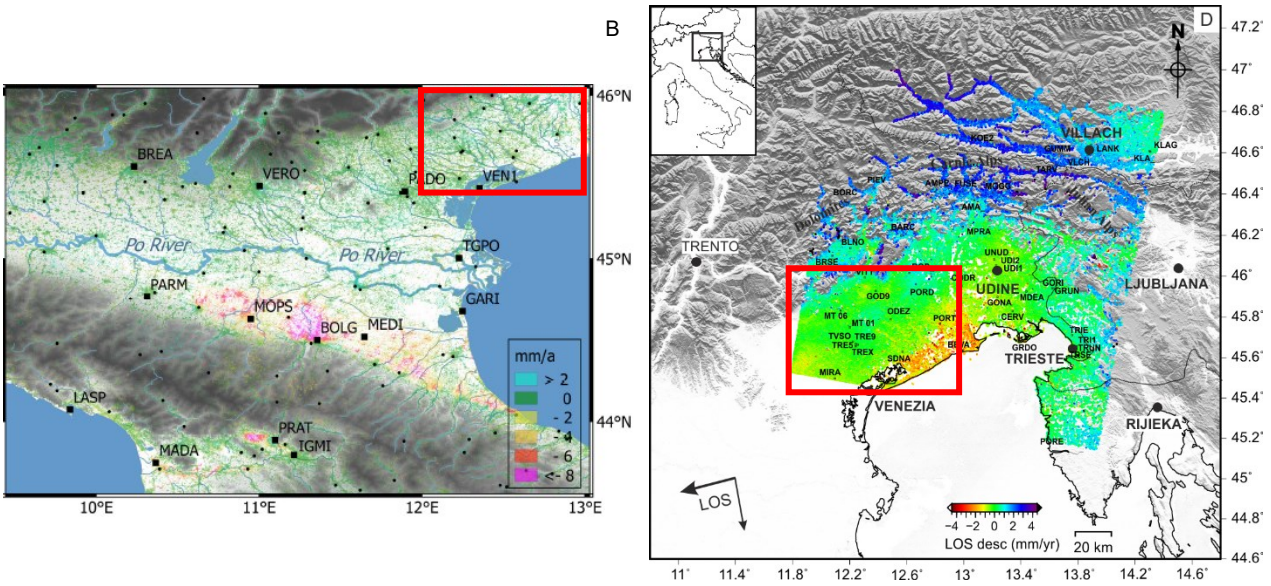

Figure 4.1. Comparison between LOS velocity maps. A) Ascending LOS dataset obtained after the PSI processing of ENVISAT data (Farolfi *et al.*, 2019a). The black points represent the GNSS permanent stations. B) Descending LOS dataset obtained after the PSI processing of ENVISAT data (Farolfi *et al.,* 2019a). C) Ascending LOS dataset obtained after the PSI processing of Sentinel-1 in the present study. D) Descending LOS dataset obtained after the PSI processing of Sentinel-1 in the present study. The black arrows indicate the east-west velocity of the GNSS stations. According to the legend, the positive and negative values indicate a surface motion toward and away from the satellite along the Line-Of-Sight. The red rectangles indicate the common areas.

To better compare and evaluate the detected patterns in the study area, we exploited the results obtained after the decomposition along the vertical and east-west directions.

Starting with the InSAR-GNSS velocity comparison, we observe a good agreement based on statistics (Table 3.5) and the correlation plots, especially for the vertical component (Fig. 3.14). The differences in rates observed for some sites (see Appendix C and D) might be related to the linear estimation of the velocity for InSAR data without considering the seasonal contributions, as done for the GNSS measurements (see Section 2.2.1). Thus, to better evaluate these discrepancies, further analysis should be conducted to estimate the InSAR velocities, considering all the signals within the time series in each site.

Concerning the east-west velocity map, we observe a general eastward motion of the study area with rates that generally increase toward NNE (Fig. 4.3B). Indeed, the northeastern sector between Italy and Austria shows eastward rates of 1-2 mm/yr, in agreement with the GNSS measurements (e.g., Serpelloni *et al.,* 2016; Fig. 4.3A).

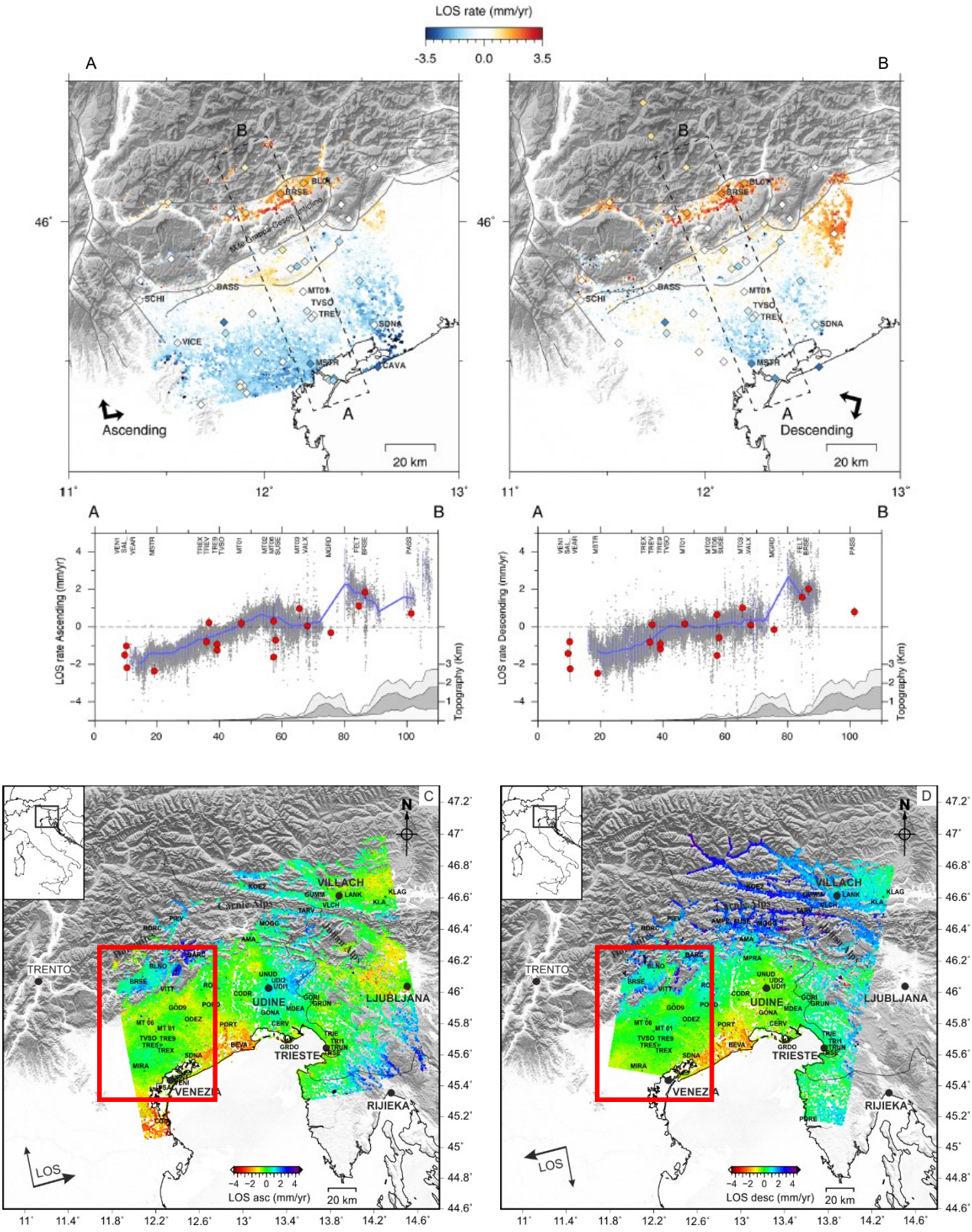

Figure 4.2. Comparison between LOS velocity maps. A) Ascending LOS dataset obtained after the PSI processing of ENVISAT data (Anderlini *et al.,* 2020). The colored diamonds indicate the GNSS velocities projected along the LOS direction. Bottom panel: LOS velocity profiles with InSAR (grey dots) and GNSS data (red points with relative uncertainties). The blue line indicates the median values of the InSAR measurements, whereas the light bars represent the data dispersion in each bin (every 1 km). B) Descending LOS dataset obtained after the PSI processing of ENVISAT

data (Anderlini *et al.*, 2020). C) Ascending LOS dataset obtained after the PSI processing of Sentinel-1 in the present study. The black arrows indicate the east-west velocity of the GNSS stations. D) Descending LOS dataset obtained after the PSI processing of Sentinel-1 in the present study.
According to the legend, the positive and negative values indicate a surface motion toward and away from the satellite along the Line-Of-Sight. The red rectangles indicate the common areas.

A significant pattern may be observed around Udine, characterized by negative (westward) rates of about 1 mm/yr (Fig. 4.3B). Considering the GNSS data, we note some discrepancies, especially for the sites of UDI1, UDI2, GONA, and CERV (see Appendix C-D), whose rates mainly indicate the presence of a stable area. In Serpelloni *et al.* (2016), observing the horizontal velocity field in an Adria-fixed reference frame derived from GNSS data, the area around Udine seems to move slightly westward (Fig. 4.3A). By consulting the newest European Ground Motion Service (EGMS) (https://egms.land.copernicus.eu/) provided by the Copernicus Land Monitoring Service, the MT-InSAR measurements based on Sentinel-1 data within the period 2016-2020 in the area show a westward motion with rates that are comparable to the estimated rates in our study (< 1 mm/yr).
Concerning other horizontal signals, we observe a westward motion of the area east of the Belluno Valley (i.e., BLNO GNSS site) across the Dolomites between Veneto and Friuli Venezia Giulia Region (Fig. 4.3B). A similar pattern can also be detected in the EGMS service, with rates of 2-3 mm/yr, in agreement with our study. Conversely, another detected pattern around Pordenone, which moves eastward with rates of ~ 1 mm/yr, is not identified by the ESGM service or by the GNSS data (i.e., PORD GNSS station).
Regarding the vertical component, the southern regions are characterized by negative velocities, which increase toward the mountain belt, reaching rates of 1-2 mm/yr (Fig. 3.13B).
Based on the results, we observe diffuse subsidence along the coasts and the Venetian-Friulian plain. The northern sector of the Venice Lagoon to the Grado-Marano Lagoon is characterized by subsidence rates of 1-3 mm/yr, locally reaching values even higher than 4 mm/yr, as also observed in other studies (Brambati *et al.*, 2003; Teatini *et al.*, 2005; Tosi *et al.*, 2010; Bock *et al.,* 2012; Farolfi *et al.,* 2019a). Specifically, the higher rates have been recorded around the Tagliamento River delta, along the coasts of the northern Venice province (i.e., Caorle-Bibbione), around the city of Eraclea, and Portogruaro in the hinterland (Fig. 4.4B). The subsidence rates decrease toward the hinterland, reaching stable areas (±0.5 mm/yr). Along the rivers and near the Prealps (i.e., between MT06 and GOD9 GNSS stations), the areas subside with mean rates of ~1 mm/yr, with local values up to 2 mm/yr.

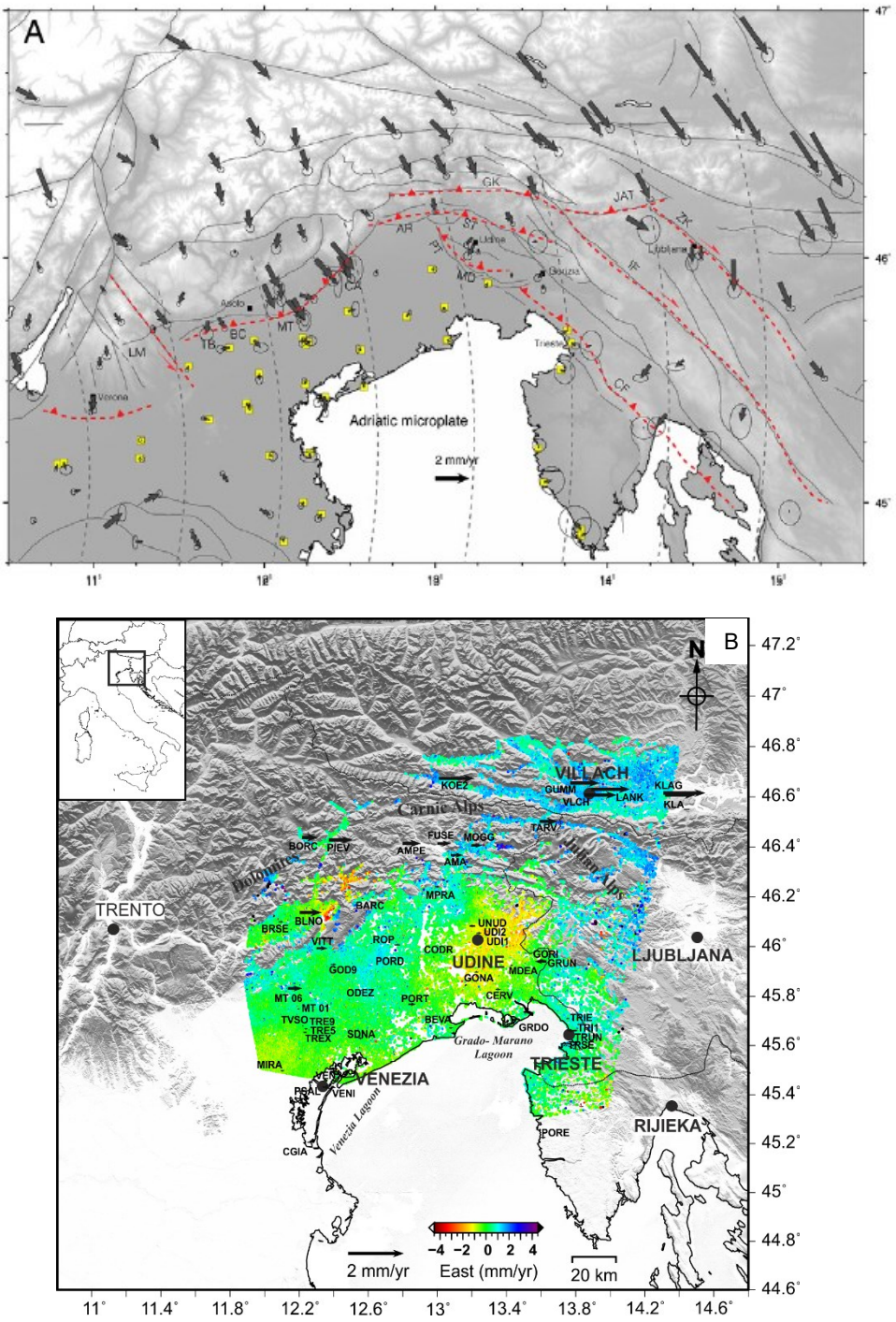

Figure 4.3. Comparison between horizontal velocity maps. A) GNSS velocities in an Adria-fixed reference frame. The black arrows indicate the GNSS horizontal velocities with 95% confidence error ellipses. The yellow squares indicate GNSS stations used to define the reference frame whereas the red dashed lines indicate the tectonic structures (Serpelloni *et al.,* 2016). B) East-west velocity map obtained after the PSI processing in the present study. The black arrows indicate the east-west velocity of the GNSS stations. The positive and negative velocities indicate eastward and westward motions, respectively.

On the other hand, around the Grado-Marano Lagoon, the subsidence rates decrease eastward and toward the hinterland. Specifically, the east side of the Tagliamento River (i.e., BEVA GNSS station) is characterized by subsidence rates of ~ 1-4 mm/yr, while the coastal area (i.e., Trieste Province, Slovenia, and Croatia) and the mainland subside slower (< -1 mm/yr) (Fig. 3.13B). However, even in these zones, local signals can be observed in the harbor and industrial areas with rates higher than -5 mm/yr (i.e., Trieste, Muggia, Kopen). Our data confirm the measurements estimated by Da Lio and Tosi (2018), which focused on land subsidence in Friuli Venezia Giulia coasts using MT-InSAR data.

Several investigations were conducted in the southern sector of the study area by using geodetic data, different methods for the MT-InSAR processing, and different satellites, especially C-band satellites such as ERS1/2 and ENVISAT. By comparing their works with our study, we note that similar deformation patterns can be observed with almost comparable rates, as previously reported. Nevertheless, we note that the mean surface displacement rates derived by the processing of Sentinel-1 data during the 2015-2019 interval in the present work are lower than the rates measured with ERS1/2 (period 1992-2002) and ENVISAT (2003-2007/2010) in Teatini *et al*. (2005), Tosi *et al.* (2010) and Da Lio and Tosi study (2018).

For example, the study of Teatini *et al.* (2005) integrated different methods (i.e., spirit leveling, Differential Global Positioning Systems) with the Interferometric Synthetic Aperture (InSAR) and Interferometric Point Target Analysis (IPTA) approaches applied to ERS-1/2 SAR images. Their results reveal downward movements of 2.5-5.5 mm/yr in the plain and coastal areas located east of Treviso (Fig. 4.4A), whereas our measurements show lower rates in the same areas (2-3 mm/yr) (Fig. 4.4B). However, we note a similar pattern NNE of Treviso, showing an uplift of 0.5-1.5 mm/yr in Teatini *et al.* (2005; Fig. 4.4A) and <1 mm/yr in our data (Fig. 4.4B).

Considering the same area, the study of Tosi *et al*. (2010) compared the ERS1/2 and the ENVISAT datasets by observing some differences, such as the increment in subsidence rates in the San Donà, Portogruaro, and Carole zones. In these areas, we estimate slower negative velocities instead of the higher rates identified by Tosi *et al.* (2010) in the ENVISAT dataset (Fig. 4.5A). For example, around San Donà and Portogruaro, we detect mean subsidence rates of 1-2 mm/yr and > 3 mm/yr, while, according to Tosi *et al.* (2010), the estimated velocities reach values higher than 3 and 5 mm/yr respectively (Fig. 4.5).

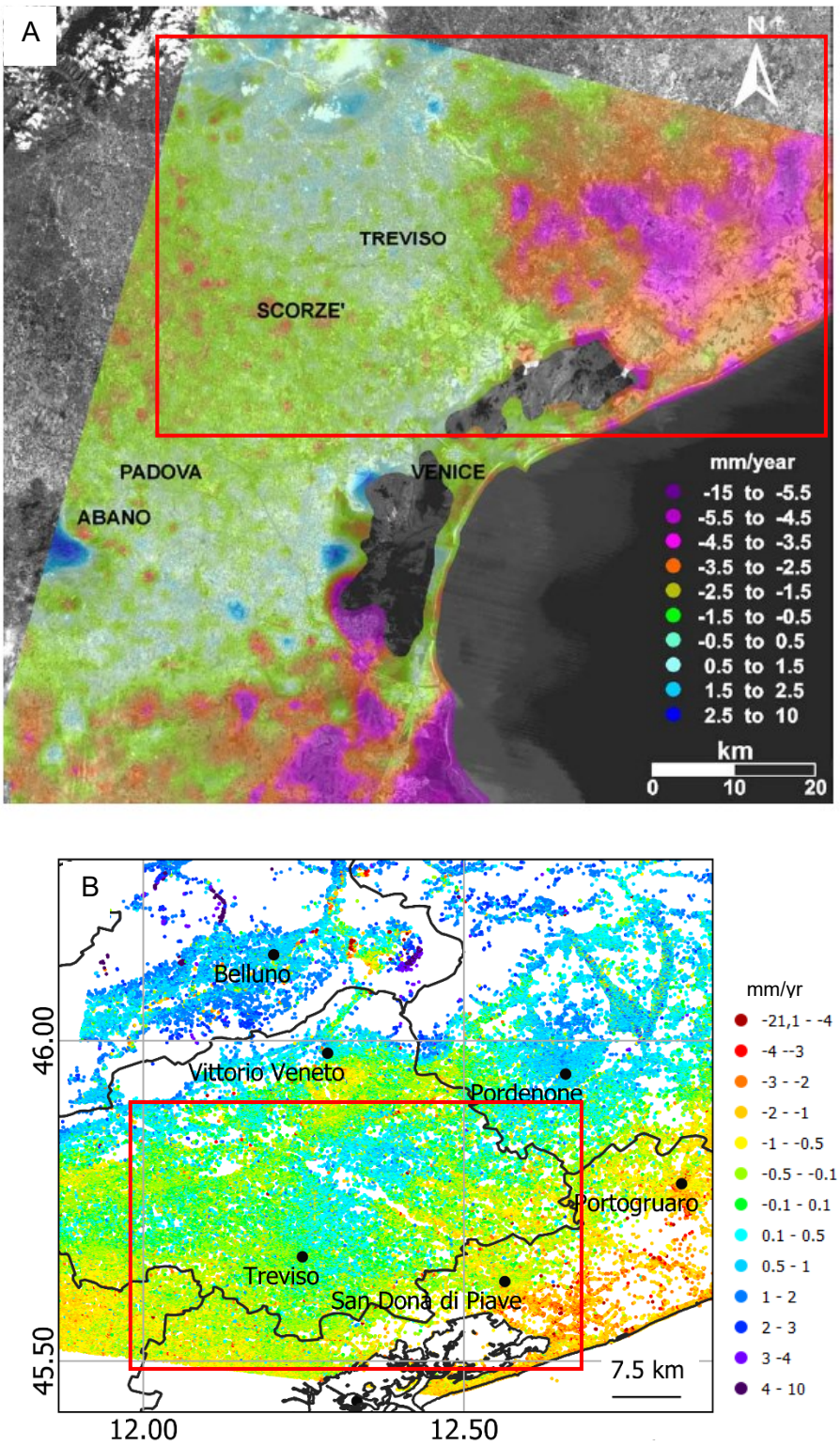

Figure 4.4. Comparison between horizontal velocity maps in the Venice plain and lagoon. A) Vertical velocity map obtained after the ERS1/2 data processing in the 1992-2000 period (Teatini *et al.,* 2005). B) Vertical velocity map obtained after the Sentinel-1 data processing in the present study. The red rectangles indicate the common areas in the two datasets. The positive and negative velocities indicate upward and downward motions, respectively.

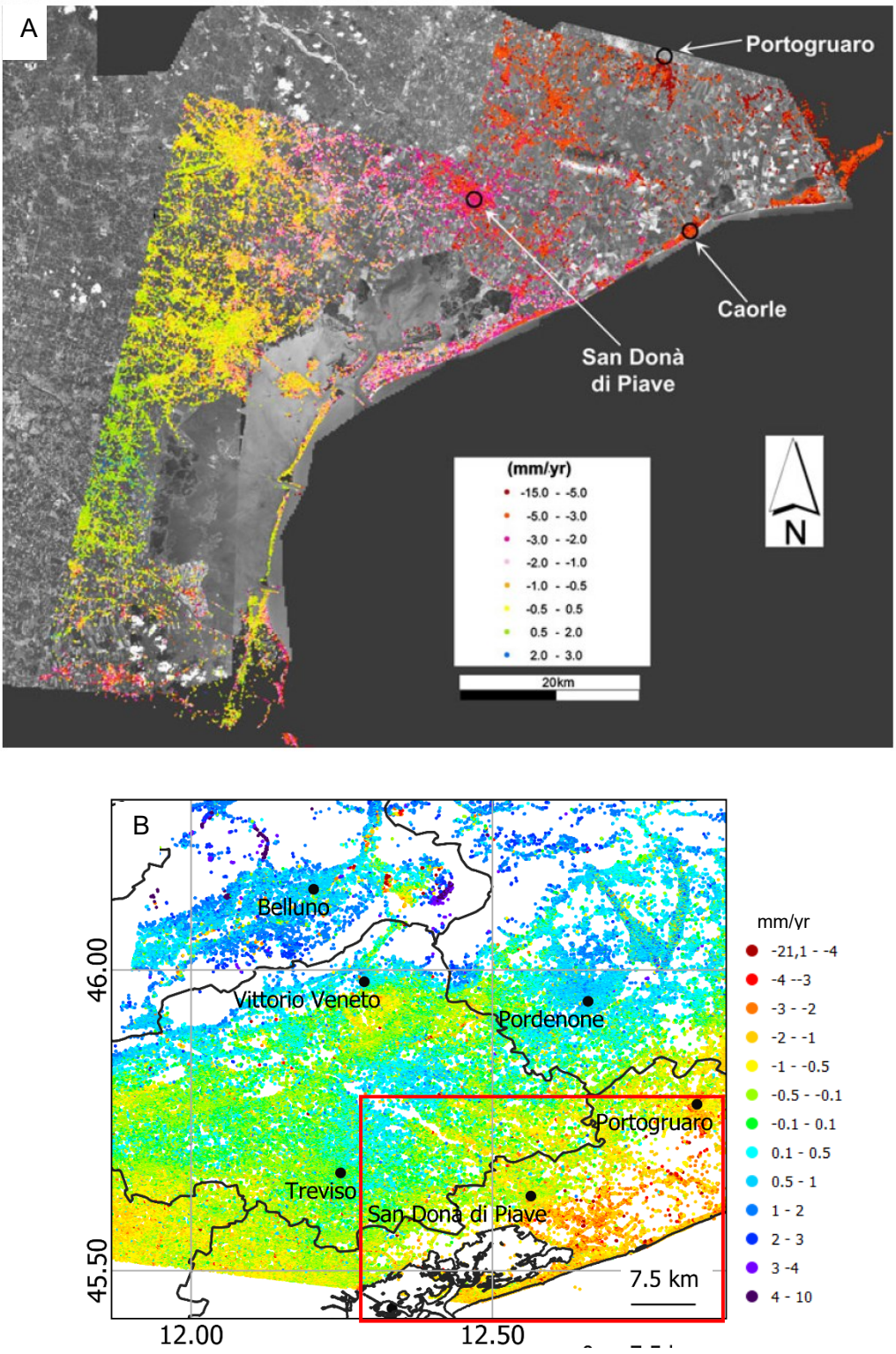

Figure 4.5. Comparison between horizontal velocity maps in the Venice lagoon. A) Vertical velocity map obtained after the ENVISAT data processing in the 2003-2007 period (Tosi *et al.*, 2010). B) Vertical velocity map obtained after the Sentinel-1 data processing in the present study. The red rectangles indicate the common areas in the two datasets. The positive and negative velocities indicate upward and downward motions, respectively.

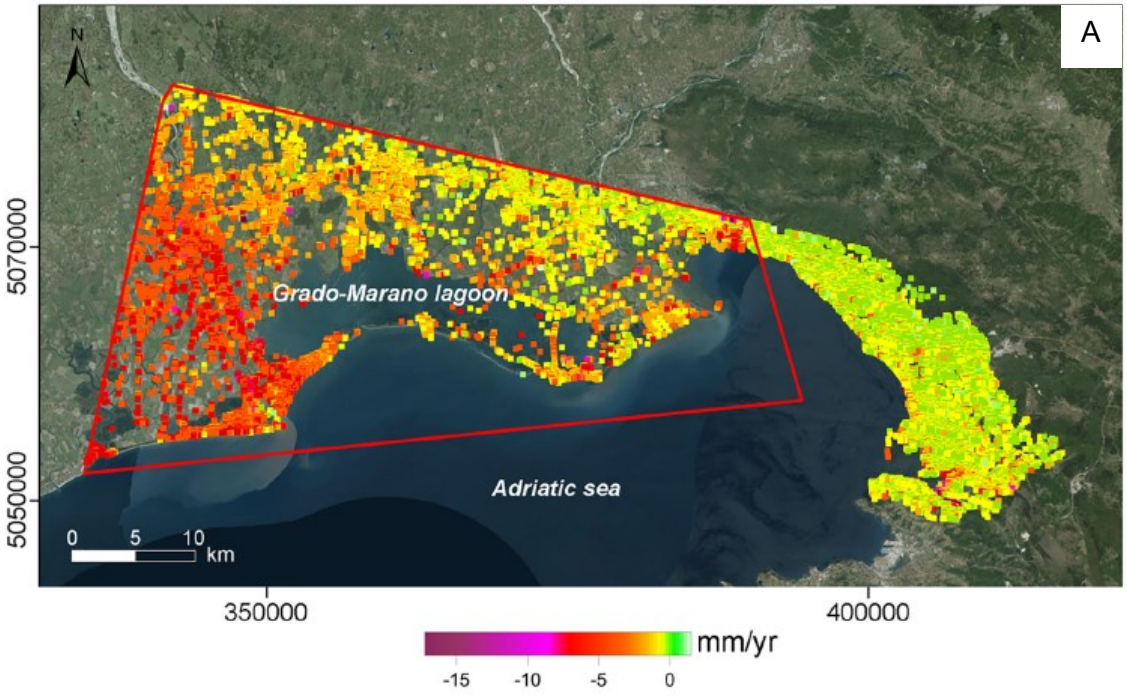
A
N
Grado-Marano lagoon
Adriatic sea
0 5 10
km
5070000
5050000
350000
400000
mm/yr
-15 -10 -5 0

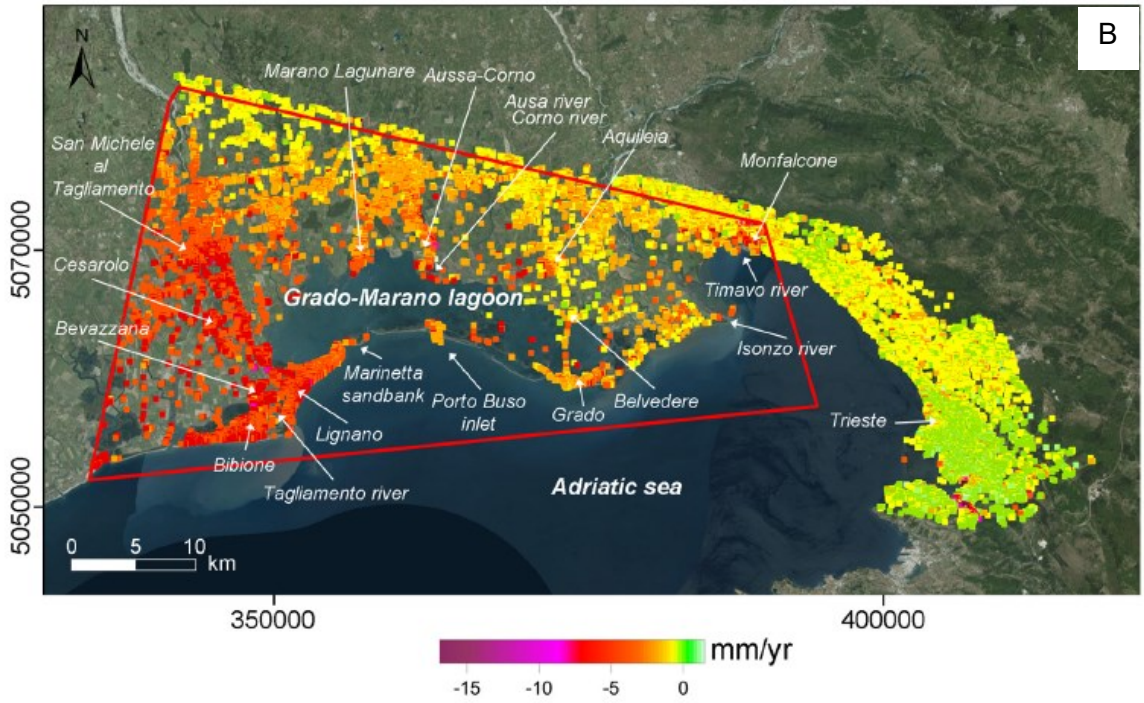
B
N
Marano Lagunare
Aussa-Corno
Ausa river
Corno river
Aquileia
Monfalcone
San Michele al Tagliamento
Cesarolo
Grado-Marano lagoon
Timavo river
Bevazzana
Isonzo river
Marinetta sandbank
Porto Buso inlet
Grado
Belvedere
Trieste
Lignano
Bibione
Tagliamento river
Adriatic sea
0 5 10
km
5070000
5050000
350000
400000
mm/yr
-15 -10 -5 0

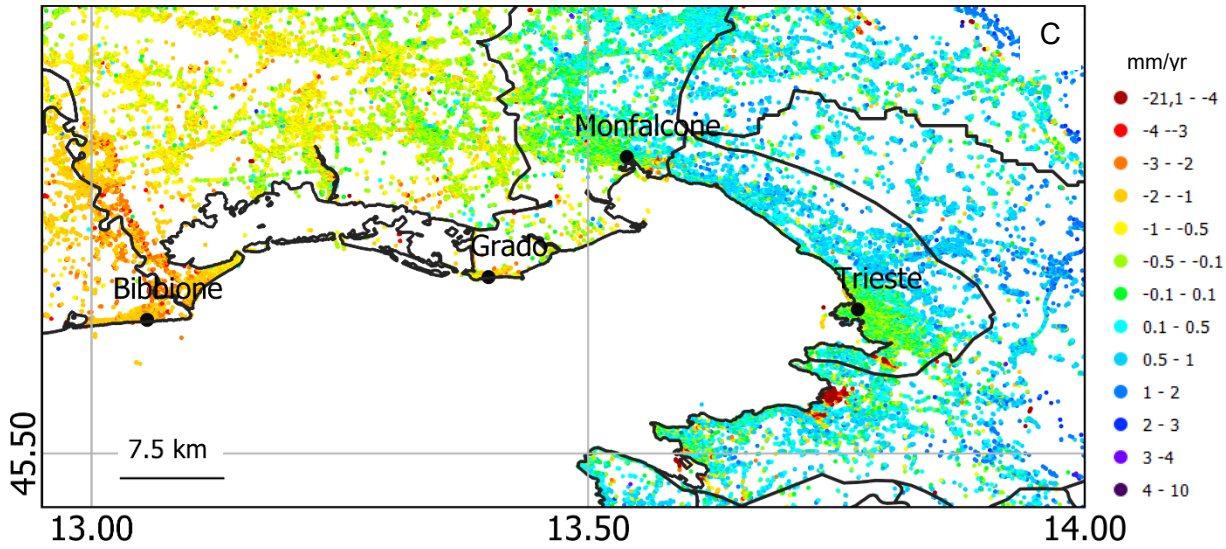

Figure 4.6. Comparison between horizontal velocity maps. A) Vertical velocity map obtained after the ERS1/2 data processing in the 1992-2000 period (Da Lio and Tosi, 2018). B) Vertical velocity map obtained after the ENVISAT data processing in the 2003-2010 period (Da Lio and Tosi, 2018). C) Vertical velocity map obtained after the Sentinel-1 data processing in the present study. The positive and negative velocities indicate upward and downward motions, respectively.

Regarding the Grado-Marano Lagoon, the estimated rates in our study are lower than the study of Da Lio and Tosi (2018), which used ERS1/2 and ENVISAT data. For example, the subsidence rates recorded along Tagliamento River (i.e., Bibbione) are higher than 5 mm/yr (Fig. 4.6 A-B). In contrast, our measurements show slower subsidence in the area (rates ~ 2-4 mm/yr) (Fig. 4.6C).

The comparison with different datasets and approaches reveals differences in rates at the local-intermediate scale. A possible explanation deals with the use of different Multi-Temporal Interferometric techniques (i.e., PSInSAR, IPTA, SBAS, StaMPS) and the different strategies adopted for calibrating and correcting datasets with GNSS data. Da Lio and Tosi (2018) also observed that the rate differences might depend on the calibration procedures and the models used. Specifically, based on our tests, we observe that GNSS stations must be chosen carefully by considering the characteristics of the GNSS time series, the spatial coverture of InSAR data around each site, and the spatial variability (see Section 2.2). Furthermore, it is essential to have many stations homogenously distributed over the area of interest to better estimate the residual orbital and atmospheric contributions and the satellite reference.

The differences may even be attributed to the effects of time-variable phenomena, whose rates may vary during the different observation periods. Comparing the ERS1/2 and ENVISAT datasets in the study of Da Lio and Tosi (2018), we observe that the latter (Fig. 4.6B) show higher subsidence rates than the velocity map obtained by ERS1/2 data (Fig. 4.6A), especially on the Grado-Marano Lagoon

and in the areas north of Trieste. Based on this consideration, even some changes in velocity between InSAR and GNSS data (i.e., BEVA, CERV sites) might be explained (Fig. 3.13B). Assuming a steady interseismic deformation in this contest, these effects in the southern region might be attributed to other phenomena potentially unrelated to tectonics (see Section 4.3).

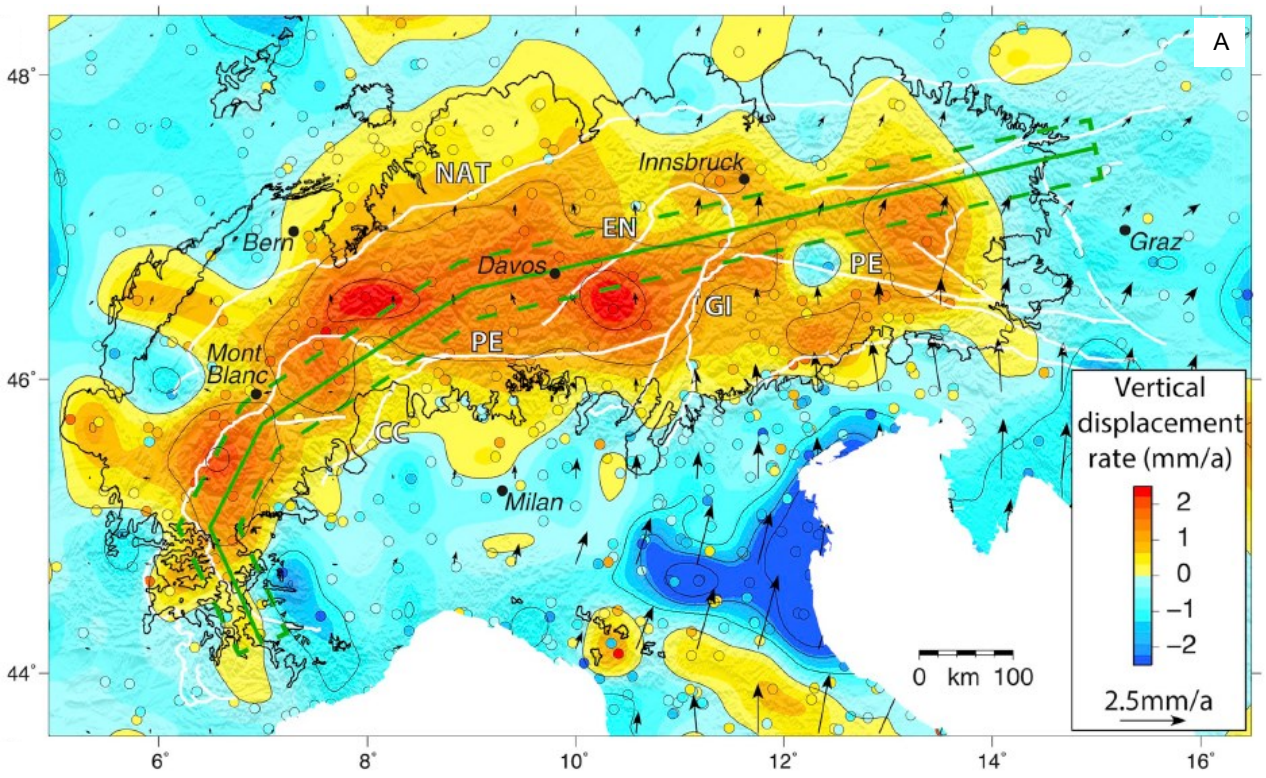

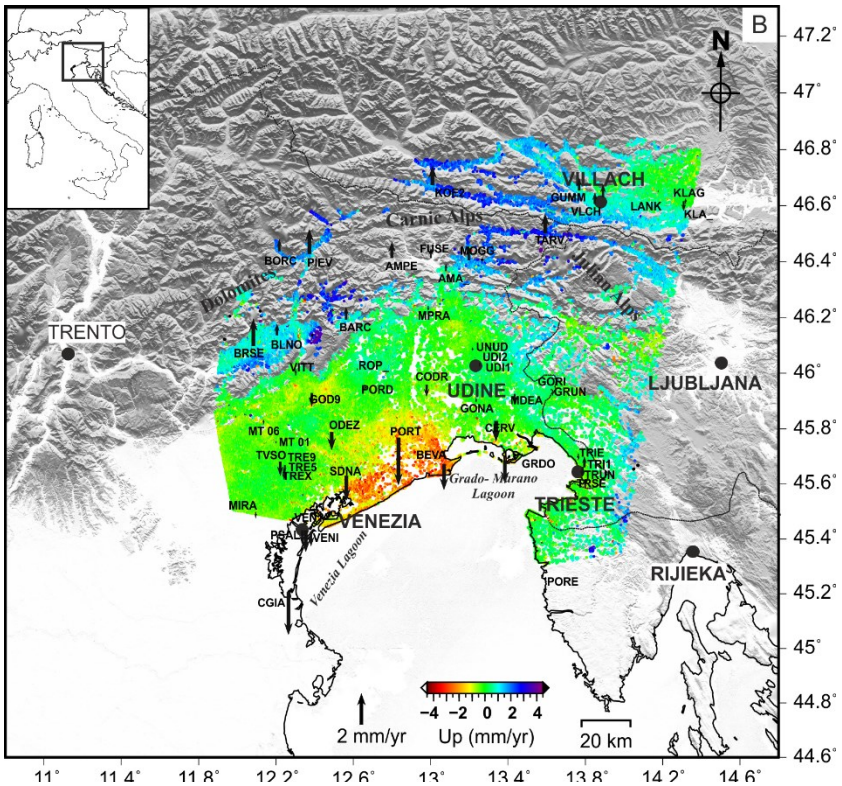

Figure 4.7. Comparison between vertical velocity maps. A) Vertical velocity maps based on the interpolation of GNSS stations (circles). The thin black lines indicate the isolines at 1 mm/yr intervals, whereas the black arrows show the horizontal velocity field as from the model by Serpelloni *et al.* (2016) (Sternai *et al.,* 2019). B) Vertical velocity map obtained after the Sentinel-1 data processing in the present study. The black arrows indicate the vertical velocity of the GNSS stations. The positive and negative velocities indicate upward and downward motions, respectively.

Concerning the northern sector of the study area, the vertical rates increase northward, as confirmed by other geodetic studies (Serpelloni *et al*., 2016; Sternai *et al.,* 2019; Anderlini *et al*., 2020). Toward the Belluno valley, the uplift records rates of ~1 mm/yr (Fig. 4.7B and 4.8B), as also estimated by Sternai *et al.* (2019) (Fig. 4.7A). On the other hand, for Anderlini *et al.* (2020), the rates are higher (~2 mm/yr) (Fig. 4.8A). In our measurements, these velocities are recorded in an area east of the Belluno Valley, between the Dolomites and Carnic Alps (> 2 mm/yr) (Fig. 4.7B).

We observe an increase in vertical velocities in the central sector up to 2 mm/yr, especially in northeastern Friuli and southern Austria (Fig. 4.7B). The GNSS stations also record the uplift but with lower rates (~ 1 mm/yr) (see Appendix C-D), as also reported in Sternai *et al.* (2019) (Fig. 4.7A). On the other hand, we observe a gradual decrease in rates southward (i.e., Italy-Slovenia border) and eastward (i.e., Austria and Slovenia, across the Julian Alps), which is in agreement with the study of Sternai *et al.* (2019) (Fig. 4.7).

The mean ground velocity maps obtained after the InSAR and GNSS data processing enable the detection, estimation, and analysis of the deformation patterns induced by natural and anthropogenic phenomena. However, considering the aim of the present study, in the following section, we will analyze and discuss the detected signals correlated to the tectonic activity of the Alpine-Dinaric systems. Furthermore, we will also report some examples of other deformation signals we observed in our study in Section 4.3.

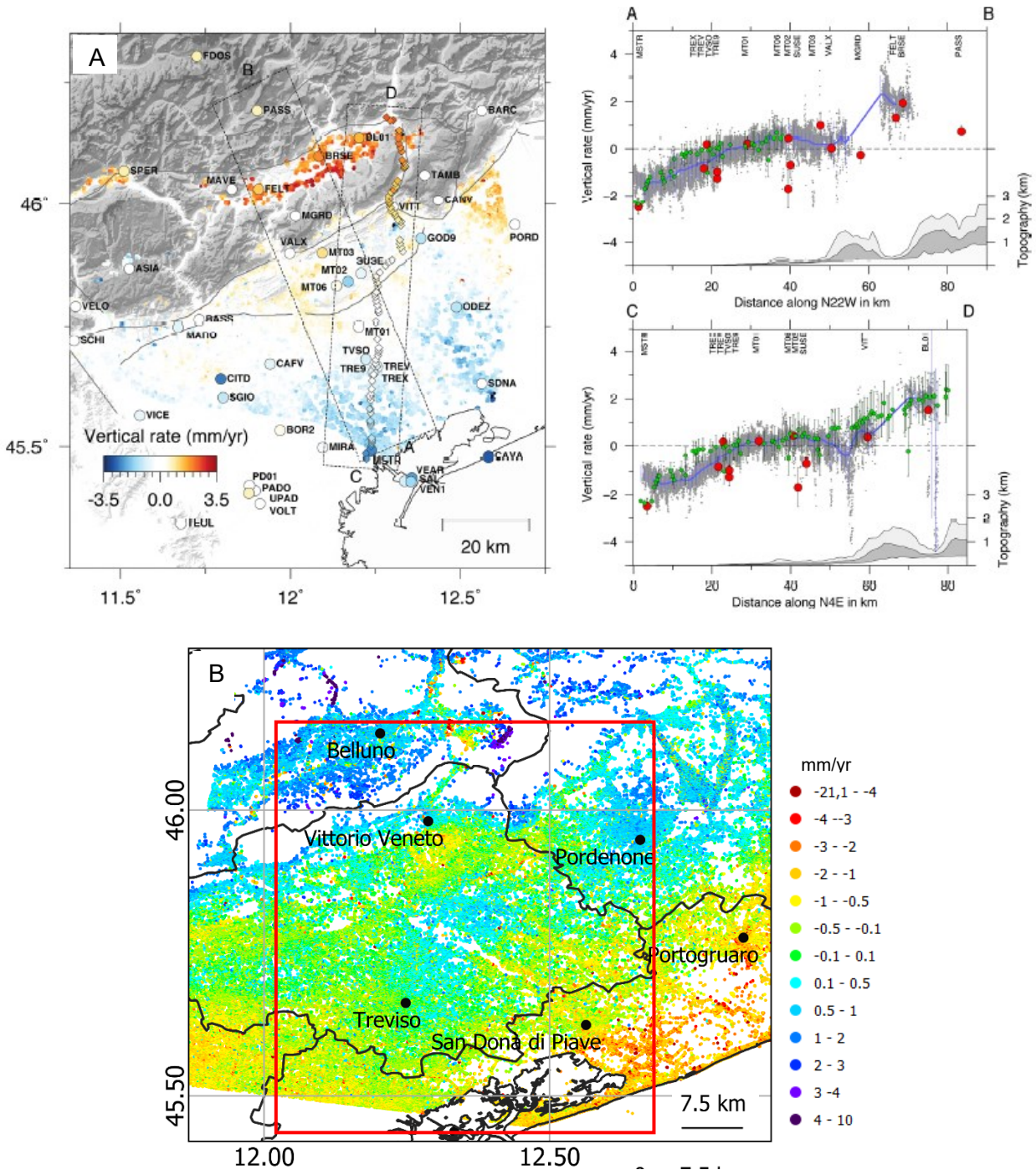

Figure 4.8. Comparison between vertical velocity maps in the easternmost sector of the Veneto region. A) Vertical velocity map obtained after the processing of ENVISAT data, GNSS data (circles), and leveling (diamonds) data. The plots on the right show the vertical profiles along the two traces, A-B and C-D (Anderlini *et al.,* 2020). B) Vertical velocity map obtained after processing Sentinel-1 images in the present study. The red rectangles indicate the common areas in the two datasets. The positive and negative velocities indicate upward and downward motions, respectively.

4.2. Tectonic Signals

Based on geological, seismological, and geodetic investigations, many studies focused on the estimation of the seismogenic potential of the study area through the modeling and the resulting interseismic coupling maps (e.g., Barba *et al.*, 2013; Cheloni *et al.*, 2014; Serpelloni *et al.*, 2016). Indeed, interseismic coupling plays a crucial role in the evaluation of the seismic hazard by defining the aseismic (i.e., creeping behavior) or seismic behavior (i.e., a locked fault that can generate earthquakes) of the active tectonic structures (e.g., Avouac *et al.,* 2015).

In our area, many studies suggest the presence of northward-dipping thrusts, locked above ~10 km depth and characterized by low slip rates (e.g., D'Agostino *et al.*, 2005; Cheloni *et al.*, 2014; Serpelloni *et al.*, 2016). Tectonic structures, such as the thrusts located in the Veneto-Friuli region, are mostly locked (i.e., Cheloni *et al.*, 2014; Serpelloni *et al.*, 2016), whereas for others (e.g., Montello-Cansiglio thrust system) an aseismic creep have been suggested (Barba *et al.*, 2013; Serpelloni *et al.*, 2016) (Fig. 4.9).

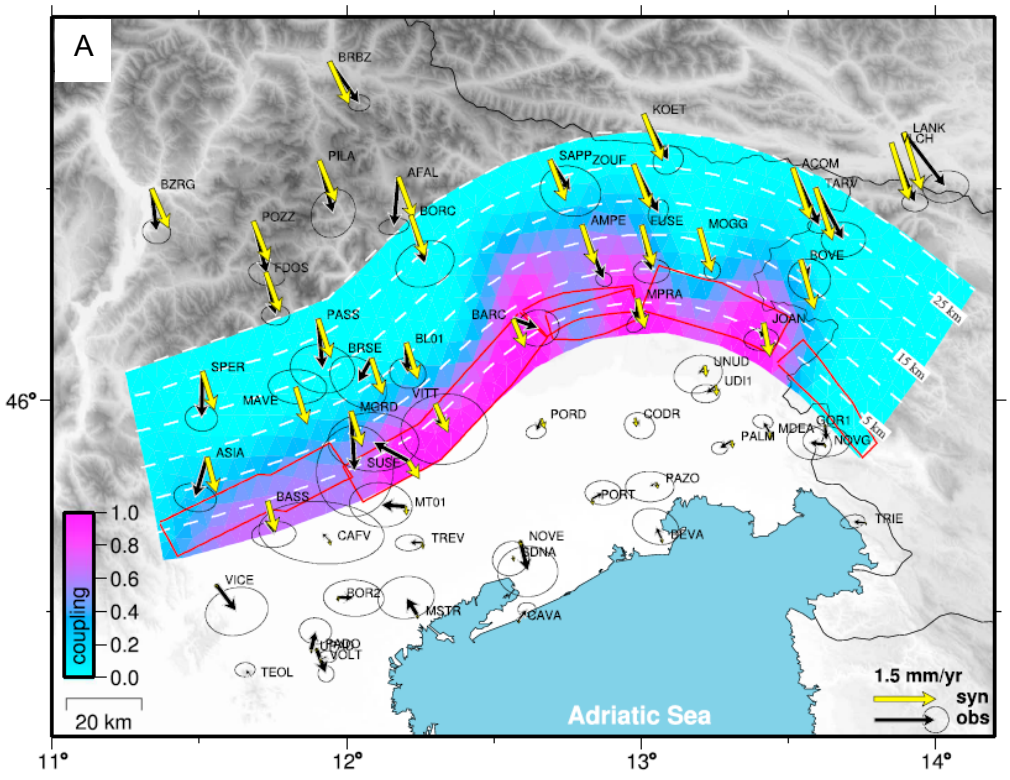

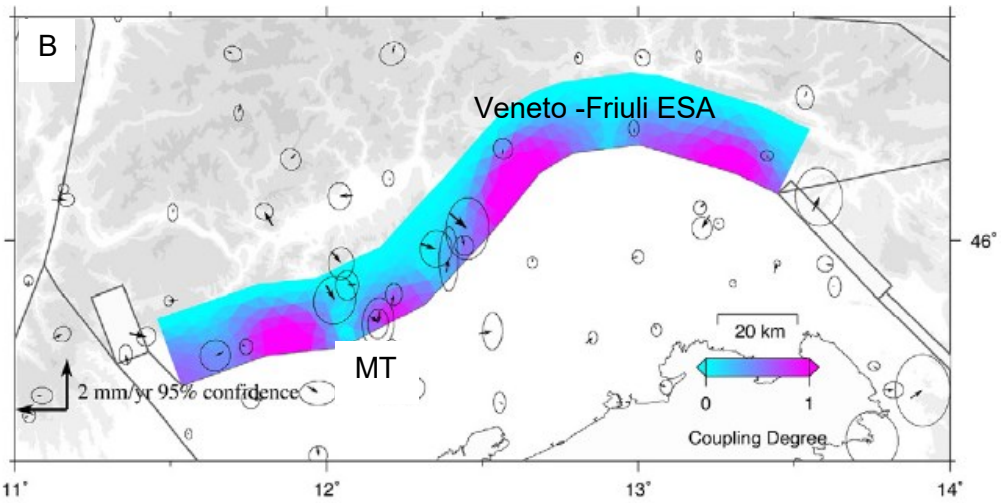

Figure 4.9. Interseismic coupling based on the GNSS velocity field, between 1 (fully coupled) to 0 (fully uncoupled). A) The arrows indicate the observed (black) and predicted (yellow arrows) horizontal GNSS velocities (error ellipses at 95% C.I.). White dashed lines show the fault isodepths, spaced every 5 km, whereas the red boxes define the seismogenic sources (From Cheloni *et al.*, 2014). B) The arrows indicate the GNSS horizontal velocity field with related errors (ellipses). (From Serpelloni *et al.*, 2016). MT: Montello thrust system. ESA: Eastern Southern Alps.

To confirm or argue the interseismic slip along the active structures in our area, we traced three different profiles, comparing seismicity, tectonic structures, and geodetic data.

In the western sector of the study area, we traced an NNW-SSE-trending profile by plotting the vertical component of InSAR and GNSS data, the seismicity, and the geological section modified from Fantoni and Franciosi (2010) (Fig. 4.10B).

The subsidence rates (1-3 mm/yr) recorded by InSAR and GNSS measurements along the Venetian coasts and southern plain areas and the absence of seismicity suggest that non-tectonic geological phenomena affect these areas (see Section 4.3 for a discussion on this topic).

Moving northward, the positive velocity gradient of 1 mm/yr across the mountain belt between the VITT GNSS station and the Belluno valley is not correlated to the topographic profile, implying a negligible effect of the extra phase contributions, such as the atmosphere (i.e., stratified troposphere), after the correction that we applied (e.g., Liu *et al.*, 2018). Thus, we suggest that the gradient is related to the activity of the Alpine thrusts. Specifically, based on the geological and seismic information, we suggest that the surface displacement occurs as a consequence of the motion of the deeper segment of the Bassano-Valdobbiadene thrust, within the seismogenic layer (maximum depth 10-15 km), during the observation period 2015-2019 (Fig. 4.10B).

Although the activity of the Bassano-Valdobbiadene thrust is debated based on a lack of geological, geomorphological, and seismic evidence (Galadini *et al.*, 2005; Burrato *et al.*, 2008), recent studies suggest a seismogenic potential of the fault based on the results of interseismic fault model inversion (Barba *et al.*, 2013; Anderlini *et al.*, 2020).

A similar trend in the vertical profile can be observed in the study of Anderlini *et al.* (2020), showing a rapid decrease moving seaward and a positive gradient toward the Belluno valley (Fig. 4.10A).

Regarding the negative velocity near the coasts, the subsidence rates are almost comparable, except for the minimum we observe in our profile (Fig. 4.10B). The difference can be explained by the different orientations of the profiles and the lack of data between SDNA and CAVA stations (Fig. 4.8A; profile A-B). Another difference is the steeper positive velocity gradient, reaching a mean rate up to 2 mm/yr with respect to 1 mm/yr, as shown in Figure 4.10B. Despite these differences due to the profile orientation, different InSAR datasets, and processing steps, both studies reveal the presence of tectonic activity potentially related to the Bassano-Valdobbiadene thrust.

Based on the results after the inversion of the geodetic data, we found a fault plane whose position and geometry correspond to the Bassano-Valdobbiandene thrust (Fig. 4.10B). In particular, we obtained a locking depth of 5.3 km and dip and strike-slip rates of ~2 mm/yr and -0.4 mm/yr, respectively, suggesting inverse kinematics with a small sinistral strike-slip component (Table 3.9). After the inversion of InSAR, GNSS, and leveling data, Anderlini *et al.* (2020) report a comparable slip rate for the Bassano-Valdobbiadene thrust (~ 2 mm/yr) but with a deeper locking depth (~9 km deep (Fig. 4.10). Even the dip angle values differ since Anderlini *et al.* (2020) fixed the dip at 22 and 25°. In contrast, we selected the dip angle at 27.89° (see Section 3.8). In this case, besides the different datasets, the use of a more articulated fault model (e.g., ramp-flat geometry) that includes the Montello thrust may explain the variances between the two studies.

Indeed, considering the misfit between the observed and modeled velocities in GNSS (Fig. 3.21 in Section 3.8) and InSAR data (Fig. 4.10B), our single-fault model cannot fully explain the presence of signals located south of the Bassano-Valdobbiadene thrust. Hence, we suggest that the southern deformations could be attributed to the presence of the Montello thrust (Fig. 4.10B).

The Montello thrust represents another important tectonic structure. According to geological, geomorphological, and geodetic evidence, the uplift rate is estimated between 0.4-1 mm/yr with a slip rate of 0.47-1.56 mm/yr (Galadini *et al.*, 2005; Benedetti *et al.*, 2000; Barba *et al.*, 2013; Danesi *et al.*, 2015; Anderlini *et al.*, 2020; DISS Working Group, 2021). Furthermore, the Montello thrust is characterized by a low coupling, suggesting an aseismically release of strain (Barba *et al.*, 2013; Serpelloni *et al.*, 2016; Anderlini *et al.*, 2020). In our case, a weak signal might be attributed to the activity of Montello thrust, as testified by the misfit between the observed and modeled geodetic velocities. Still, it cannot be clearly defined because of the low rates in the area.

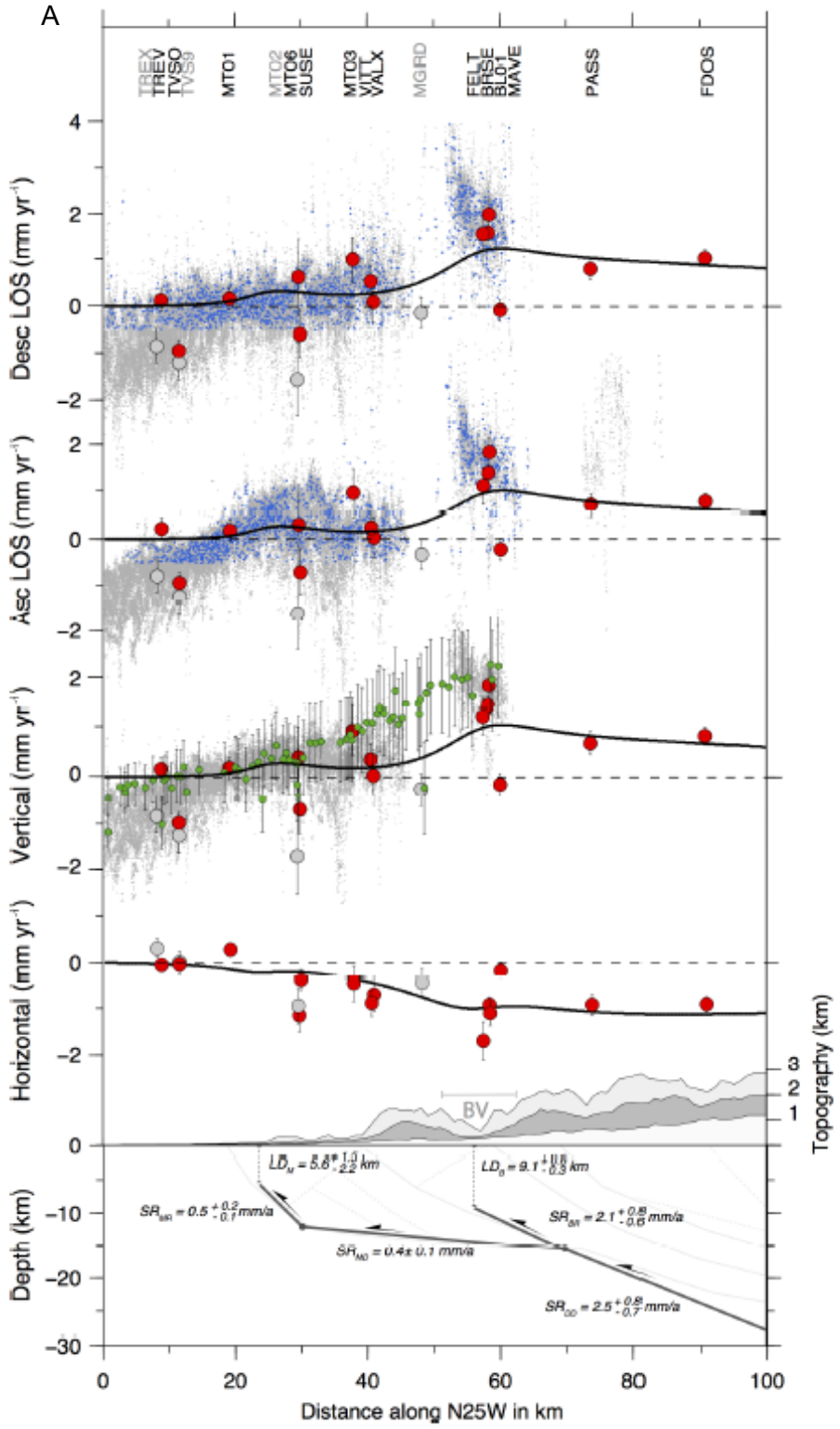
A
TREX
TREV
TVSO
TVS9
MT01
MT02
MT06
SUSE
MT03
VTLX
VALX
MGRD
FELT
BRSE
BL01
MAVE
PASS
FDOS
Desc LOS (mm yr⁻¹)
Asc LOS (mm yr⁻¹)
Vertical (mm yr⁻¹)
Horizontal (mm yr⁻¹)
Topography (km)
BV
Depth (km)
Distance along N25W in km

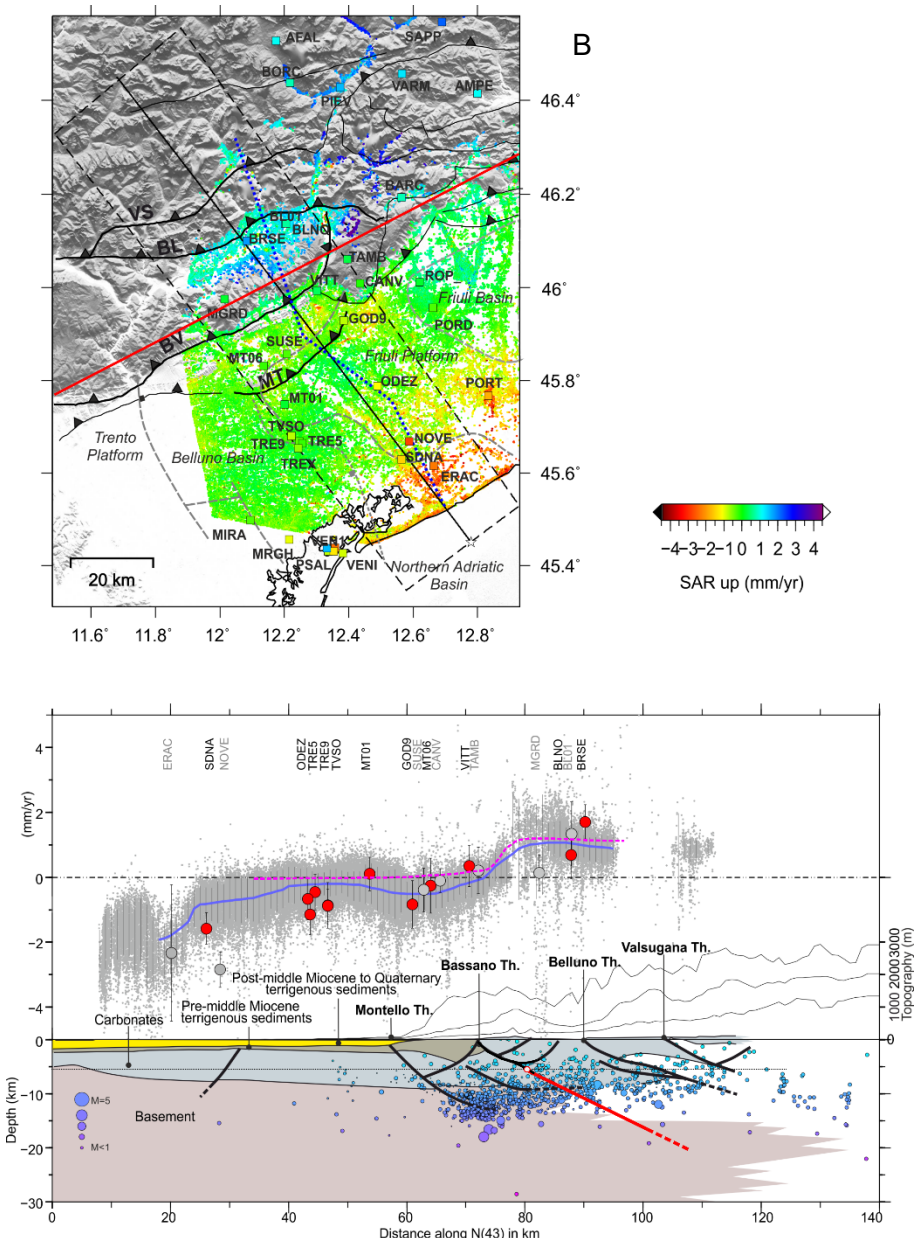

Figure 4.10. Comparison between the vertical velocity profiles of the Alpine system in the eastern sector. A) Cross sections across the A-B profile in Fig. 4.8A. The black line indicates the modeled velocities for the descending, ascending, vertical, and horizontal datasets. Grey dots represent the InSAR data, the blue dots the subsampled InSAR data, the red and grey dots the GNSS velocities, whereas the green points indicate the leveling data.
The bottom panel shows the optimal fault geometry with the estimated locking depths and dip-slip rates. BV: Belluno valley (From Anderlini *et al.*, 2020). B) Vertical profile across the Alpine system (Dolomites) obtained in our study. The red line indicates the modeled fault source after the inversion. In the velocity profile, the blue and the dashed magenta lines indicate the observed and modeled vertical velocity, respectively.

Hence, based on our measurements and results, we indicate the Bassano-Valdobbiadene thrust as the main responsible for the interseismic signal detected in the western sector of the study area, showing a positive velocity gradient of ~1 mm/yr. However, we cannot exclude the secondary effects

of the Montello thrust, located southward with respect to the Bassano-Valdobbiadene tectonic structure.

Moving to the central sector of the study area, across the Carnic and Julian Alps, we traced and analyzed the vertical and horizontal velocity profiles.

The Friulian coasts are mainly affected by subsidence with variable rates, within 20 km along the profile, without any significant east-westward movements (Fig. 4.11). As done for the western sector, we will discuss these rates in Section 4.3.

The vertical rates then increase until reaching the foothills of the Julian Alps (i.e., JOAN GNSS stations), where the area is stable (Fig. 4.11), as confirmed by the GNSS data. The low uplift rates detected close to the thrusts near Udine also agree with the estimated rates in the study of Viscolani *et al.* (2020).

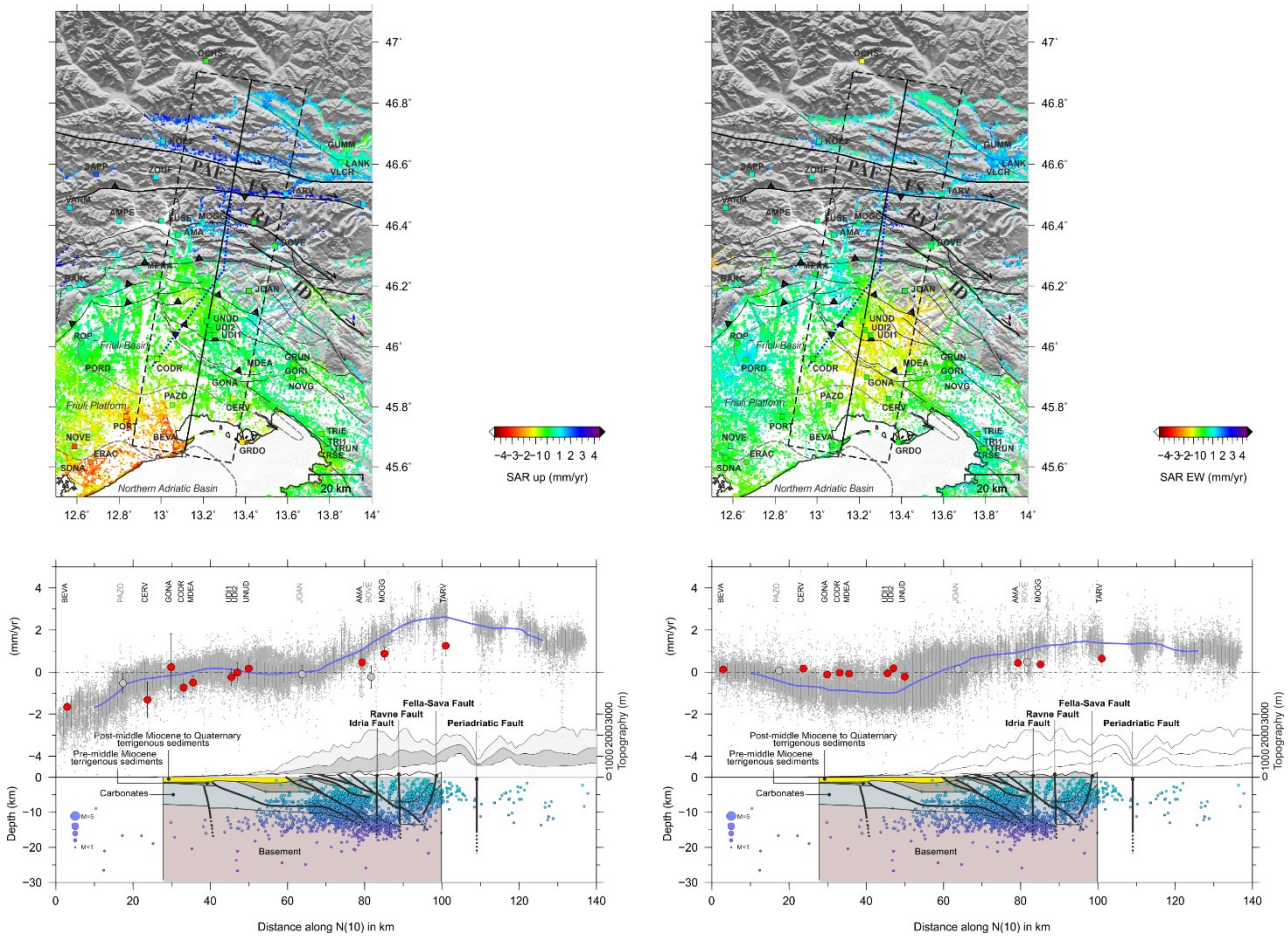

Figure 4.11. Vertical (left) and east-west (right) velocity profiles across the Alpine (Julian Alps) and Dinaric system (see Result 3.7.2).

North of the JOAN site, we observe a velocity gradient up to 2 mm/yr across the Carnic-Julian Alps, which gradually decreases toward Austria (~ 1mm/yr). In this case, we cannot observe a good agreement with GNSS data because of a positive vertical gradient of 1 mm/yr (i.e., TARV and MOGG

sites) (Fig. 4.11). The difference in rates might be attributed to the potential atmospheric residuals due to the strong topography in the area (Delacourt *et al.*, 1998; Doin *et al.*, 2009). However, considering both geodetic datasets, the positive gradient is accommodated within ~40 km along the profile between JOAN and TARV, which corresponds to the Alpine belt. Here, based on the geological and seismic information, several active tectonic structures (i.e., south-verging thrusts) are present (Fig. 4.11).

Regarding the horizontal profile, we note that the Friulian plain (south of Udine) is moving westward. In contrast, the northern sector is characterized by an eastward motion that reaches about 1 mm/yr around Tarvisio, followed by a slight decrease toward Austria (Fig. 4.11). The transition zone is located within 30-40km along the profile, between Udine and MOGG GNSS sites. Although GNSS data do not identify these patterns, other InSAR measurements detected these signals. As mentioned in Section 4.2, ESGM service detected a westward motion, showing similar patterns with comparable rates. Considering the presence of active thrusts and the termination of the Dinaric strike-slip faults, such as Idrija, Predjama, and Rasa faults in the area, we hypothesize a potential correlation between the deformation pattern and the tectonic structures (i.e., buried thrusts, transcurrent and transpressive faults) in the area.

The interaction between the Alpine and Dinaric systems is more evident in this sector because of the presence of several south-verging thrusts and sub-vertical parallel strike-slip faults, such as Idrija, Ravne, and Fella-Sava faults, where also the seismicity is localized. Furthermore, the area presents a high seismic hazard due to several seismogenic faults, which are mostly locked (e.g., Burrato *et al.*, 2008; Cheloni *et al.*, 2014; Serpelloni *et al.*, 2016).

For that reason, it is essential to mention the destructive seismic sequence that hit the Friuli region in 1976-1977 (Aoudia *et al.*, 2000; Pondrelli *et al.*, 2001; Poli *et al.*, 2002; Carulli and Slejko, 2005). According to recent studies, the event was attributed to the activation of the Susan-Tricesimo thrust with the potential contribution of the transpressive faults (i.e., Predjama fault), which played an essential role during the mainshock (6th May 1976; Mw 6.5) and the foreshock (15th September 1976; Mw 6.0) (Poli and Zanferrari, 2018; Patricelli *et al.*, 2022). The evidence suggests a complex interaction between the two tectonic systems, indicating the need for further investigations in these regions characterized by a high seismogenic potential (Cheloni *et al.*, 2014; Serpelloni *et al.*, 2016). Even the presence of the Fella-Sava fault, a 150-km long active dextral strike-slip fault with an estimated slip rate of ~1 mm/yr, should be taken into account since it may play a significant role in the study area (Vrabec *et al.*, 2006; Serpelloni *et al.*, 2016; Atanackov *et al.*, 2021).

In summary, based on our results, the measurements reveal the eastward and upward motion of the southeastern Alps (i.e., Carnic-Julian Alps), which is accommodated by the active Alpine and Dinaric thrusts and strike-slip faults. Furthermore, we also observe a westward motion of the Friulian plain, potentially related to the effects induced by the termination of the Dinaric transcurrent faults.

However, further analysis (e.g., multi-fault inversion) should be conducted to constrain the geodetic rates and seismogenic potential in the area.

The easternmost sector is characterized by dextral sub-parallel faults NW-SE trending, which belong to the Dinaric system (e.g., Bechtold *et al.*, 2009; Serpelloni *et al.*, 2016; Atanackov *et al.*, 2021).

No significant gradient is detected in the vertical profile until Gorizia (e.g., GORI GNSS site; Fig. 4.12), except for a weak rate increase from the coast to the inner areas. Conversely, an eastward motion can be observed, except for a westward signal due to the deformation pattern located around Udine and potentially related to blind thrusts and transcurrent faults, as previously explained (Fig. 4.12).

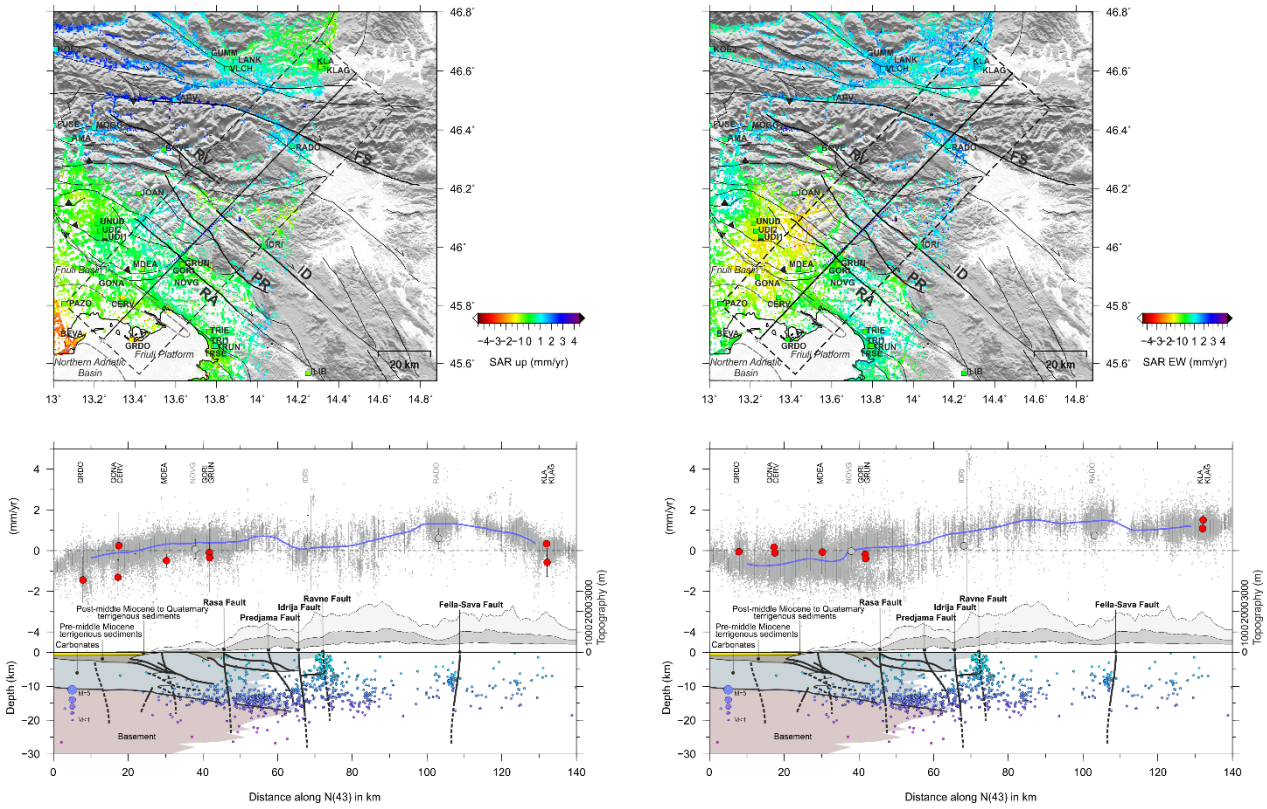

Figure 4.12. Vertical (left) and east-west (right) velocity profiles across the Dinaric system (see Result 3.7.3).

Between the Raša and Idrija faults, the uplift of ~ 1 mm/yr and the positive gradient of 1 mm/yr with a change in the trend around the Predjama fault might suggest a correlation with these Dinaric structures, as shown in the geological profile (Fig. 4.12). We also note the presence of seismicity, which is concentrated on the basement-carbonatic platform transition (10-15 km deep).

According to the literature, the subparallel dextral strike-slip faults are active, and their slip rates have been estimated by exploiting multi-disciplinary investigations. For example, Moulin *et al.* (2016) used ^{36}Cl cosmic ray exposure dating to extract the mean slip rates over the last 255 kyr of 1.30 ± 0.20, 1.15 ± 0.15, and 1.45 ± 0.25 mm/yr for Raša, Predjama, and Idrija faults respectively. On the

other hand, in the Slovenian database of active faults based on geologic, paleoseismic, geodynamic, geophysical, geodetic, and seismological data, the recent work of Atanackov *et al.* (2021) reports slip rates of 0.7, 0.7, and 1 mm/yr for the same structures. These tectonic structures are currently being investigated to better define their characteristics (geometry and kinematics) and their seismogenic potential. Indeed, despite their low rates, these active dextral transcurrent-transpressive tectonic structures characterized by complex geometries are capable of moderate/strong earthquakes, as the 1998 Mw 5.6 and 2004 Mw 5.2 Bovec-Krn earthquakes (NW Slovenia) (Kastelic *et al.*, 2008; Kastelic and Carafa, 2012; Vičič *et al.*, 2019; Atanackov *et al.*, 2021; Grützner *et al.*, 2021). Although it is not possible to discriminate the contribution of every single structure, the signals detected in our profile suggest the activity of these transcurrent and transpressive structures. Furthermore, we have to consider the complex geometry of the Dinaric strike-slip faults, composed of several segments (e.g., Atanackov *et al.,* 2021), which may move differently (i.e., aseismic and seismic). For example, the signal observed on the eastern border of the map (Fig. 4.12) might suggest the aseismic behavior of one or more segments of the Predjama fault. Hence, even in this case, multi-fault models might help evaluate the tectonic signals in relation to the strike-slip faults in the areas.

In the proximity of the Ravne fault, no significant signals are detected on the velocity profiles. The Ravne fault was the source of the 1998 Mw 5.6 Krn-Bovec earthquake and the recent 2004 Mw 5.2 Bovec event (Bajc *et al.*, 2001; Kastelic *et al.*, 2008), which was also recorded by the seismicity in the 2000-2017 time interval. Thus, the recent and historical seismicity in the area confirms its seismogenic potential. Based on these considerations, we suggest that the presence of a locked fault and the strain release during the 2004 event might explain the absence of tectonic signals on the velocity profiles around the Ravne fault.

In the northeastern sector, the detected vertical uplift of 1 mm/yr and the eastward motion might be related to the structures across the Carnic and Julian Alps (Fig. 4.12). However, the orientation of the profile and the lack of PSs, especially in the easternmost sector, may bias the analysis and interpretation of the potential tectonic signals. For example, in the proximity of the Fella-Sava fault, the east-west velocity profile suggests a sinistral transcurrent regime, which does not agree with its kinematics (e.g., Merlini *et al.*, 2002). However, the previous profile traced perpendicularly to the tectonic structure shows no apparent horizontal motion (Fig. 4.11). Concerning the vertical profile, the uplift across the mountain belt (Fig. 4.12) might also be attributed to other tectonic structures, such as the strike-slip faults in Austria.

Even in this case, our measurements reveal tectonic signals that may be accommodated by the Dinaric structures, especially between Raša and Idrija. Predjama fault may partially move aseismically, whereas Ravne fault may be locked.

In conclusion, the three profiles derived from the geodetic data in the present work represent an example of the signals detected in the study area in response to active tectonics, even in the case

of low rates. Further investigations must be conducted to define and constrain the faults' geometrical characteristics and improve the knowledge about their seismogenic potential for seismic hazard assessment by estimating locking depths and slip rates through modeling.

4.3. Non-tectonic signals

The present study aims to estimate the surface deformation in Northeast Italy and correlate the detected signals to the active tectonic structures. Therefore, we adopted several strategies to obtain the velocity field for interseismic deformation analysis.

Nevertheless, after processing and analyzing the maps and the velocity profiles, we noted the presence of other signals potentially unrelated to the active tectonics in the study area, such as the active subsidence in the southern region.

Hence, in this section, we want to discuss the deformation patterns at a regional scale related to the subsidence and present some examples dealing with local geological phenomena.

Observing the vertical map (Fig. 3.13B), active subsidence affects the Adriatic coasts and the Venetian-Friulian plain with variable rates. Specifically, we observe that the highest rates are recorded between the Northern Venice Lagoon and the Grado-Marano Lagoon, decreasing toward the inland.

Considering the profile in the western sector of the study area (Fig. 4.10), we detect an abrupt decrease in velocity near San Donà di Piave (i.e., SDNA GNSS sites), reaching a mean value of ~ -2.5 mm/yr. Compared with the geological section, this visible jump on the vertical profile corresponds to the Friuli Platform-Northern Adriatic Basin transition. The presence of the basin and the characteristics of the sedimentary deposits strongly influence the subsidence. That would explain the lower vertical velocities (> -1 mm/yr) recorded in the Grado-Marano Lagoon (Fig. 4.11 and 4.12) in the eastern sector of the study area, where no significant basins are present.

Several studies demonstrated that the subsidence in the study area is a consequence of the combination of different causes that act differently in time and space. Specifically, the reasons may be attributed to the consolidation of compressible sediments due to natural processes or in response to surface loading, tectonics, fluid extractions, seasonal fluctuation of aquifers, and human activities (Brambati *et al.*, 2003; Teatini *et al.*, 2005, 2012; Carbognin *et al.*, 2009; Tosi *et al.*, 2009, 2010). If we consider the study area, we note a correlation between the distribution and the deep base of pre-Quaternary deposits with respect to the land subsidence. Meso-Cenozoic carbonates and Pliocene sediments may affect the area differently, inducing variable subsidence rates (Tosi *et al.*, 2009; Da Lio and Tosi, 2018). Indeed, higher subsidence rates have been recorded in the Venetian-Friulian plain, covering the Belluno-Northern Adriatic basin, where a thick succession of Pliocene deposits is present (Fig. 4.10).

Even the thickness of Quaternary deposits and their differential compaction due to their lithological characteristics may have an impact on subsidence rates, as reported in other studies focused on the estimation of the land subsidence in Venice Lagoon (Brambati *et al.*, 2003; Tosi *et al.*, 2009, 2010) and Friuli-Venezia Giulia coastal plain (Da Lio and Tosi, 2018). The northern and southern Venice Lagoon is mainly composed of clay sediments, which are more compressible than sandy deposits located, for example, in the central sector of Venice Lagoon, implying differential subsidence rates (Fig. 4.13; Tosi *et al.*, 2009).

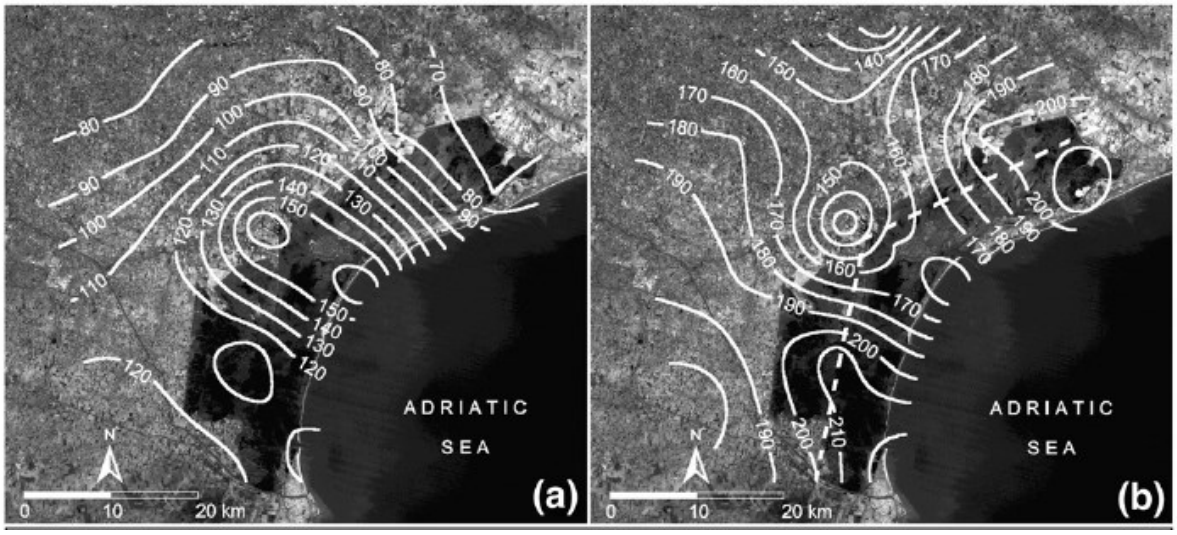

Figure 4.13. Cumulative thicknesses (m) of the (a) sandy and (b) clayey deposits in the upper 400 m of the Venice sedimentary sequence. (From Tosi *et al.*, 2009).

Finally, especially along the coasts, the variability in land subsidence may be explained by the effects of the Holocene coastal progradation and the relative deposition of recent sediments (i.e., marine-lagoon and alluvial deposits) (Tosi *et al.*, 2009). Indeed, according to Da Lio and Tosi (2018), the subsidence of the Grado-Marano Lagoon area is mainly dominated by the bedrock settings and the Holocene deposits (Fig. 4.14).

Locally, some areas report higher subsidence rates (>3 mm/yr), such as Portogruaro, Caorle, Eraclea, and Cavallino littoral areas, as observed in Figure 4.15. Here, one of the leading causes of subsidence may be related to the extraction of fluids (geothermal water and groundwater) at 500 meters and shallow depths (< 300 m) (Tosi *et al.*, 2009). The loading effects due to the industrial areas and urbanization have further increased the subsidence rates in the last decades. The case of Portogruaro is an example of land subsidence where the high rates are related to the consolidation of Holocene lagoon and alluvial deposits mainly due to urbanization and the extractions of fluids (Fig. 4.15; Floris *et al.*, 2019).

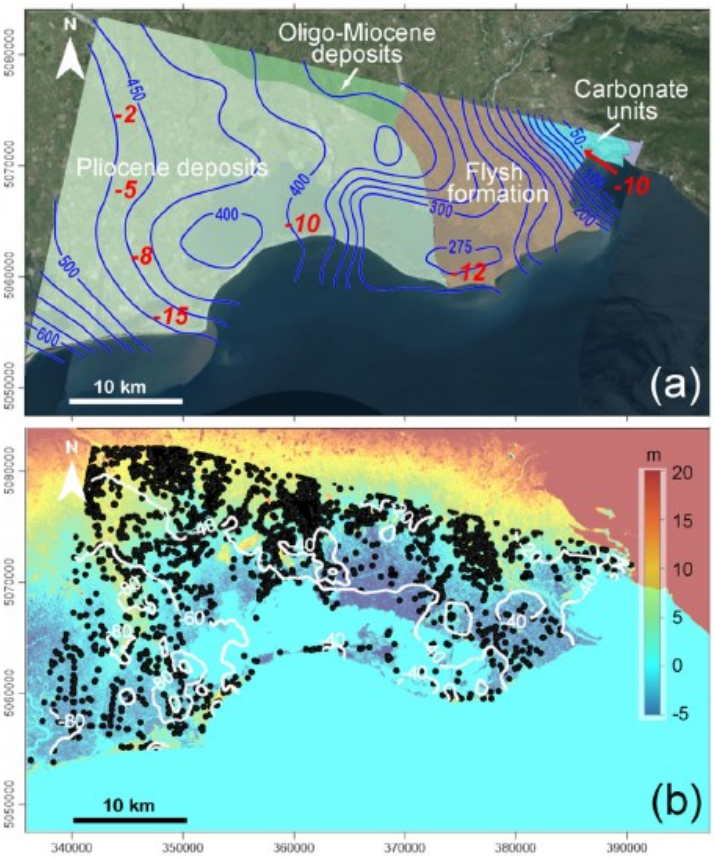

Figure 4.14. Geological setting of the area. A) Pre-Quaternary deposits and isodepths of the Quaternary base. Red numbers refer to the approximate thickness (m) of Holocene deposits. B) Elevation map with the cumulative land subsidence in the 1992–2010 time interval (white contour lines). Black dots refer to the groundwater well positions. (From Da Lio and Tosi, 2018).

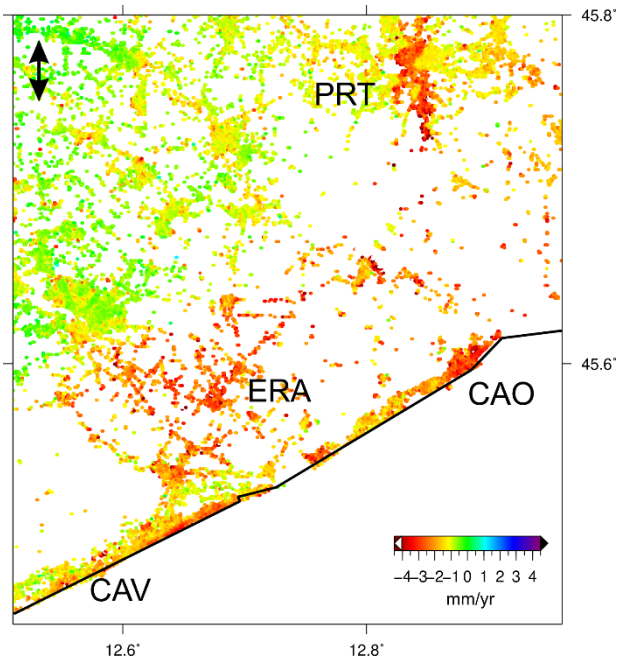

Figure 4.15. Subsidence rates in the northern Venice Lagoon. The map shows the subsidence (red color) and the stable areas (green color) in the area of interest. Portogruaro is characterized by a peculiar deformation pattern that correlates with the distribution of the alluvial deposits. PRT: Portogruaro; ERA: Eraclea; CAO: Caorle; CAV: Cavallino.

Locally, we also note some strong subsidence signals in correspondence of infrastructures and industrial areas, such as in the case of Pieve d'Alpago and Muggia. North of Santa Croce Lake, the industrial area of Pieve D'Alpago (BL), called "*Le Paludi*" (a.k.a. *Marshes*), subsides at 6-10 mm/yr, reaching even higher rates (Fig. 4.16). On the other hand, the industrial area of Muggia (TS) presents subsidence rates of 3-4 mm/yr, with rates up to 8 mm/yr. In both cases, the surface loading caused by the infrastructures and human activities might have strongly affected the subsidence in these areas during the observation period (2015-2019).

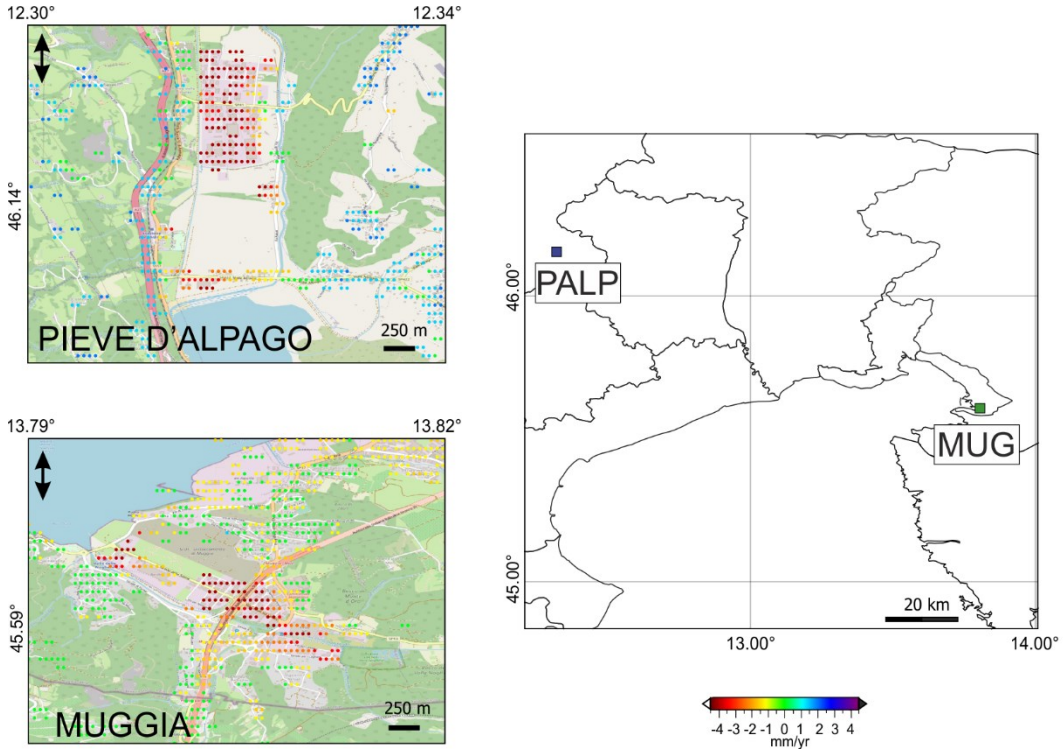

Figure 4.16. Vertical velocity in the proximity of industrial areas. The maps show the estimated rates in Pieve d'Alpago and Muggia, which are characterized by high negative vertical velocities (> 4 mm/yr).

Among other phenomena that induce surface displacements and may be detected by geodetic data, we must mention landslides and slope instabilities. Indeed, the potential of geodetic data has been successfully exploited for detecting and estimating these phenomena (e.g., Colesanti and Wasowki, 2006; Notti *et al.*, 2015; Balbi *et al.*, 2021). However, these methods also present some limitations that should be considered in these investigations. For InSAR data, the land cover (i.e., the presence of vegetated areas or snow coverture) strongly affects the PSs detection, limiting the spatial density of the measurements (e.g., Colesanti and Wasowki, 2006). Even the slope inclination and the orientation with respect to the SAR viewing angle may influence the measurements since the SAR

satellite can detect the displacement along its 1D Line-OF-Sight direction (e.g., Colesanti and Wasowki, 2006). Another limit is due to the velocity of the geological phenomenon because, with MT-InSAR methods, only the slower landslides (rates <1.6 m/yr) can be identified, especially in the case of the slide and flows-type phenomena (Cruden and Varnes, 1996).

Here, we report two examples of surface displacements related to landslides and slope instabilities obtained after the PSI processing in the present work.

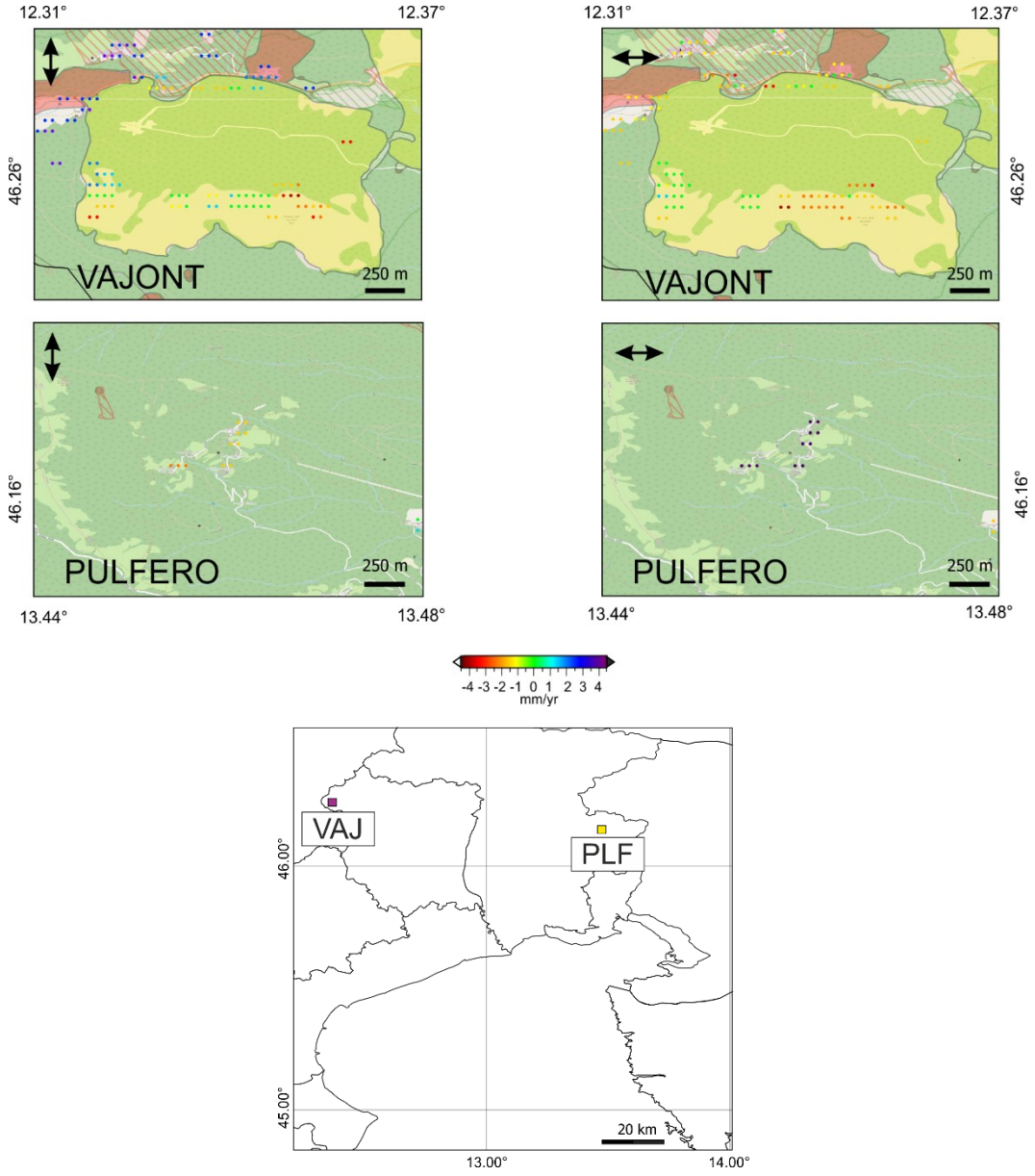

Figure 4.17. Example of surface displacements induced by potential slope instabilities in Vajont and Pulfero areas. The maps on the left report the vertical displacement (red: downward; blue: upward), whereas on the right, we can observe the horizontal ground motion of the area of interest (red: westward; blue: eastward). The yellow area defines the Vajont landslides, according to IFFI ("Inventario dei Fenomeni Franosi"; https://idrogeo.isprambiente.it/app/) by ISPRA. VAJ: Vajont; PLF: Pulfero.

Based on our measurements, we observe some movements in the Vajont area (Fig. 4.17). The site is well-known because of the destructive landslides on 9th October 1963, when a mass of 270-300 million m^3 collapsed into the reservoir, causing the generation of a wave that destroyed Longarone and the other villages (e.g., Barla and Paronuzzi, 2013).

Observing the velocity field, we detect some PSs located in a non-vegetated area within the landslide boundaries (Fig. 4.17; yellow area), estimating a downward and westward movement of ~ 2 mm/yr that increases westward. Even the EGMS service (see https://egms.land.copernicus.eu/) provides comparable measurements, showing a displacement that occurred during the observation period. Although we did not deepen our analysis by correlating our measurements with geological and geomorphological information, these data may be exploited in future investigations and studies.

Regardless, our study enables us to estimate the rates of a well-known landslide and identify new potential phenomena. For example, near Pulfero (UD), we observe a small area that is moving downward (rates of 1.5-2 mm/yr) and eastward rates (4-7 mm/yr) (Fig. 4.17). Although the landslide is not present in the official catalog (IFFI: "Inventario dei Fenomeni Franosi"; https://idrogeo.isprambiente.it/app/), thanks to geodetic data and geomorphological investigations, the phenomenon has been detected, as also described in the Master Thesis of Muro (2022).

In summary, our study reveals significant deformation signals at a regional scale by confirming the correlation between subsidence and the geological setting of the study area. Our measurements also allow the detection of some non-tectonic phenomena at a small scale, dealing with human activities and slope instabilities. However, further analysis (e.g., time series analysis) could improve the understanding of these geological phenomena by estimating the rates, defining the affected areas, and promoting actions for environmental, industrial, and cultural heritage safeguarding.

5. CONCLUSIONS

In this study, we estimated the surface velocity field after the PSI processing of Sentinel-1 images during the 2015-2019 period, the application of post-processing operation for the refinement of the measurements, and the calibration with GNSS data. We focused on 1) the estimation of the interseismic deformation, 2) the detection and analysis of the deformation patterns and their rates, and finally, 3) the correlation between the signals and the active tectonic structures in Northeast Italy.
Firstly, we estimated the velocity field after the StaMPS processing, the additional post-processing operations, and the calibration with GNSS data. We ran several tests to obtain reliable solutions, mainly working on removing the atmospheric and orbital contributions by using filters and calibration models. Finally, we obtained LOS, vertical and east-west velocity maps showing the interseismic deformation in the area of interest during the 2015-2019 observation period.
Based on these products, we observed several patterns, especially on the vertical and east-west velocity maps, which are mostly in agreement with GNSS data and previous geodetic studies (e.g., Tosi *et al.*, 2009; 2010; Serpelloni *et al.*, 2016; Da Lio and Tosi, 2018; Farolfi *et al.*, 2019a; Sternai *et al.*, 2019; Anderlini *et al.*, 2020). Our measurements confirmed the positive vertical gradients of ~1 mm/yr detected across the Dolomites, the Julian Alps, and Dinarides. On the other hand, we estimated vertical velocities up to 2 mm/yr across the Carnic Alps, which resulted in being higher than previous measurements (e.g., Serpelloni *et al.*, 2016; Sternai *et al.*, 2019; see Section 4.2).
The east-west velocity maps showed a general eastward motion of the region, which increased northeastward with rates of 1-2 mm/yr, as also observed by previous studies (e.g., Serpelloni *et al.*, 2016). However, we observed a westward motion of the Friulian plain (< 1 mm/yr) in the Udine area. Considering the tectonic setting of the area, we related these signals to the activity of Alpine and Dinaric thrust and fault systems.
To deepen our analyses and to better correlate the signals with the active tectonics, we used three velocity profiles across the Alps (western sector), the Dinarides (eastern sector), and the central region, characterized by the interaction of these two systems.
In the western sector, i.e., in the Dolomites sector, we observed a significant positive vertical gradient of 1 mm/yr. Comparing the geodetic measurements with the geological and seismic information, we suggested the Bassano-Valdobbiadene thrust as the main responsible for the interseismic signal detected in the area. The inversion we ran under the assumption of a single rectangular finite plane fault suggested a locking depth located at 5.3 km depth and a slip rate of ~2 mm/yr. Nevertheless, observing the poor fit of some GNSS stations located south of the Bassano-Valdobbiadene thrust, we also suggested the Montello thrust's secondary contribution, as confirmed by previous studies (Barba et al., 2013; Serpelloni et al., 2016; Anderlini et al., 2020).
Concerning the central sector, we noted a positive vertical gradient up to 2 mm/yr across the Carnic Alps, which overestimated the GNSS measurements. We also observed an eastward movement of

the northern sector and a westward motion of the Friulian plain. Based on the velocity gradients, the seismicity, and the geological setting, we suggested that the tectonic signals were accommodated by the faults (i.e., thrusts and strike-slip faults) in the area, even if it was not possible to discriminate the contribution of every single structure. Moreover, we suggested that the westward signal in the southern sector was related to the presence of transcurrent and transpressive systems together with buried thrusts.

The velocity profiles in the eastern sector of the study area showed an uplift of about 1 mm/yr and an eastward motion of 0.5-1 mm/yr between the Raša and Idrija faults. Considering the presence of several sub-parallel, vertical, strike-slip faults, the tectonic signals might not be attributed to a single structure. However, observing the velocity gradients in correspondence to the Predjama fault and a local velocity deformation pattern, we might suggest that some segments of the Predjama fault were moving aseismically. We also suggested that the Ravne fault could be locked, based on the absence of evident velocity gradients in the structure's proximity, together with the recent seismicity and the 2004 event.

In addition, our measurements showed multiple non-tectonic signals, such as the subsidence along the coasts and on the Venetian-Friulian plain. In particular, we observed a correlation between higher subsidence rates in the northern Venice Lagoon and the transition between the Friuli platform and the Belluno-Northern Adriatic basin, with subsidence rates of 2-3 mm/yr. Conversely, the eastern coasts presented lower subsidence rates (> -1 mm/yr).

In general, our study revealed significant deformation signals at a regional scale by confirming the correlation between subsidence and the geological setting of the study area, as also described in other MT-InSAR and GNSS studies (e.g., Brambati *et al.*, 2003; Teatini *et al.*, 2005; Tosi *et al.*, 2009, 2010; Da Lio and Tosi, 2018; Farolfi *et al.*, 2019a). We also reported some examples showing local surface deformation patterns related to human activities (i.e., surface loading) and slope instabilities.

In conclusion, our study demonstrates that MT-InSAR and GNSS data can be extremely useful for estimating surface deformation in response to active tectonics, even in areas characterized by low deformation rates, such as Northeast Italy. Moreover, the following approach may also provide information about non-tectonic phenomena, even at the local scale, like subsidence, surface displacements related to human activities, and slope instabilities.

Different approaches and strategies improved the final results, as demonstrated by the good agreement with other independent measurements, like the GNSS data.

However, further improvements, such as the integrated PSI-SBAS method and the employment of combined approaches for estimating and removing the atmospheric effects, might enhance the data quality and coverture, especially in non-urban areas. The time-series analysis should also be considered to re-estimate the InSAR velocities and evaluate the time-variable phenomena. In general, further studies should be conducted to define and constrain the geometrical characteristics

of the faults and improve the knowledge about their seismogenic potential for hazard purposes (i.e., estimation of locking depths and slip rates).

Additional investigations might also deepen the understanding of differential subsidence and slope instabilities in the study area for environmental, industrial, and cultural heritage safeguarding actions.

APPENDIX A

lon	lat	Ve	Vn	Se	Sn	Vu	Su	site	t1	t2	days
12.1745	46.5271	0.359	-1.02	0.116	0.065	1.051	0.379	AFAL_GPS	2004.731	2020.127	1554
13.0795	46.3679	0.427	-1.064	0.162	0.357	0.454	1.651	AMA__GPS	2016.69	2020.127	1120
12.799	46.4147	0.647	-1.32	0.023	0.057	1.01	0.296	AMPE_GPS	1999.401	2020.13	1675
12.5636	46.1931	0.052	-0.589	0.067	0.105	0.775	0.48	BARC_GPS	2007.429	2020.13	1678
13.0694	45.6719	0.122	0.076	0.04	0.076	-1.65	0.496	BEVA_GPS	2008.037	2020.13	1670
12.2025	46.137	0.488	-0.805	0.095	0.19	1.333	0.987	BL01_GPS	2012.892	2018.93	706
12.2057	46.1377	0.767	-0.68	0.084	0.134	0.69	0.735	BLNO_GPS	2012.102	2020.127	1682
12.2181	46.4372	0.565	-0.949	0.084	0.113	0.771	0.571	BORC_GPS	2009.226	2020.127	1643
13.5421	46.3326	0.474	-0.736	0.076	0.127	-0.23	0.532	BOVE_GPS	2006.999	2015.5452	131
12.0841	46.1	0.147	-1.021	0.079	0.143	1.707	0.525	BRSE_GPS	2008.786	2020.13	1649
12.435	46.0083	0.32	-0.572	0.108	0.193	-0.104	0.361	CANV_GPS	2004.384	2020.127	1653
12.5827	45.4794	0.163	0.509	0.041	0.089	-3.066	0.61	CAVA_GPS	2001.544	2011.166	
13.3391	45.8279	0.17	-0.153	0.061	0.141	-1.314	0.856	CERV_GPS	2013.481	2020.127	1684
12.2655	45.2065	-0.112	-0.242	0.076	0.1	-2.762	0.649	CGIA_GPS	2010.963	2020.127	1518
12.9791	45.9585	-0.028	0.064	0.032	0.067	-0.744	0.435	CODR_GPS	2007.333	2020.127	1640
12.6638	45.6155	-0.133	-0.464	0.179	0.36	-2.337	2.101	ERAC_GPS	2017.415	2020.127	615
13.0011	46.4142	0.478	-1.059	0.042	0.084	0.601	0.463	FUSE_GPS	2007.692	2020.127	1720
12.385	45.9284	0.178	-0.208	0.059	0.142	-0.835	0.736	GOD9_GPS	2012.053	2019.873	1501
13.2352	45.8976	-0.122	0.118	0.104	0.239	0.238	1.56	GONA_GPS	2016.69	2020.13	1146
13.6238	45.9433	-0.192	-0.029	0.042	0.085	-0.107	0.457	GORI_GPS	2007.429	2020.13	1719
13.3844	45.6828	-0.065	0.952	0.082	0.167	-1.448	1.142	GRDO_GPS	2015.196	2020.127	1463
13.631	45.9398	-0.402	-0.127	0.172	0.298	-0.351	1.708	GRUN_GPS	2016.693	2020.13	1147
13.768	46.6556	1.053	-1.547	0.085	0.151	0.792	0.655	GUMM_GPS	2011.081	2020.124	1684
12.3849	46.7162	0.296	-1.997	0.08	0.143	1.183	0.782	HELM_GPS	2012.706	2020.13	1367
14.0298	46.0037	0.236	-0.061	0.172	0.242	0.255	1.469	IDRI_GPS	2014.927	2015.5452	136
14.2483	45.5672	0.041	-0.224	0.136	0.098	-0.53	0.494	ILIB_GPS	2006.999	2015.5452	135
13.4161	46.184	0.133	-0.532	0.035	0.066	-0.107	0.442	JOAN_GPS	2007.489	2020.127	1647
14.3193	46.6069	1.075	-1.52	0.059	0.111	0.34	0.588	KLAG_GPS	2008.444	2018.747	1289
14.3092	46.6153	1.508	-2.058	0.234	0.514	-0.587	0.683	KLA__GPS	2011.081	2020.124	1554
13.0094	46.6742	1.272	-1.085	0.086	0.193	1.213	0.631	KOE2_GPS	2008.187	2017.881	956
13.0093	46.6742	0.644	-1.777	0.124	0.228	0.92	0.893	KOET_GPS	2001.415	2008.184	
13.8928	46.6307	1.377	-1.463	0.066	0.107	0.81	0.536	LANK_GPS	2006.999	2018.747	1290
13.4356	45.9245	-0.081	0.19	0.032	0.052	-0.504	0.335	MDEA_GPS	2003.064	2020.127	1516
12.0151	45.9753	0.232	-0.639	0.051	0.148	0.137	0.549	MGRD_GPS	2009.692	2020.13	1507
12.0954	45.4976	0.115	0.254	0.065	0.122	-0.354	0.75	MIRA_GPS	2012.466	2020.127	1427
13.1983	46.4067	0.358	-1.016	0.027	0.064	0.872	0.305	MOGG_GPS	1999.404	2019.966	1644
12.9877	46.2408	0.154	-0.593	0.034	0.076	-0.272	0.327	MPRA_GPS	2002.604	2020.127	1732
12.2149	45.4561	-1.006	0.147	0.255	0.441	-1.08	2.973	MRGH_GPS	2016.173	2018.086	603
12.2386	45.4904	-0.297	0.196	0.065	0.157	-2.699	0.82	MSTR_GPS	2007.889	2014.634	
12.2006	45.7487	-0.077	0.161	0.036	0.085	0.102	0.517	MT01_GPS	2009.218	2020.116	1740
12.1364	45.8313	0.494	-0.47	0.059	0.178	-0.257	0.849	MT06_GPS	2012.053	2020.13	1668
12.5884	45.6684	0.587	-0.178	0.103	0.138	-2.847	0.544	NOVE_GPS	2009.401	2020.127	1615
13.6247	45.8963	-0.031	-0.081	0.037	0.094	0.06	0.473	NOVG_GPS	2006.999	2015.5452	134

13.2121	46.9371	-1.288	-4.958	0.104	0.18	-0.136	0.671	OCHS_GPS	2011.081	2020.124	1694
12.4891	45.7878	-0.011	0.011	0.043	0.099	-1.141	0.622	ODEZ_GPS	2011.168	2020.127	1616
13.921	45.2385	-2.219	-1.525	0.418	0.576	5.651	3.694	PAGS_GPS	2006.001	2007.541	
13.0526	45.8057	0.067	-0.123	0.036	0.078	-0.526	0.47	PAZO_GPS	2007.93	2019.9	1388
12.3733	46.4278	0.837	-1.236	0.141	0.224	1.587	1.165	PIEV_GPS	2014.916	2020.127	1322
13.3076	45.9046	-0.083	-0.073	0.028	0.064	0.258	0.42	PLMN_GPS	1999.497	2012.881	
13.4419	46.4091	0.47	-1.148	0.164	0.33	0.145	1.361	PMNT_GPS	2015.571	2020.127	1384
12.5162	46.0245	-0.937	-0.87	0.322	0.551	9.416	3.191	PN01_GPS	2008.302	2010.355	
13.6039	45.2507	0.816	0.671	0.241	0.457	2.001	3.586	POGS_GPS	2006.001	2007.541	
12.6612	45.9568	0.005	0.176	0.029	0.065	-0.347	0.318	PORD_GPS	2002.001	2020.13	1719
13.595	45.226	0.195	0.213	0.11	0.125	-0.289	0.642	PORE_GPS	2011.045	2020.127	1730
12.8331	45.7674	0.239	0.313	0.032	0.069	-3.042	0.474	PORT_GPS	2007.527	2020.127	1706
12.3365	45.4307	0.264	0.059	0.07	0.141	-0.873	0.945	PSAL_GPS	2014.393	2020.127	1635
14.1716	46.3438	0.735	-1.435	0.062	0.096	0.599	0.506	RADO_GPS	2006.999	2015.5452	133
14.3462	45.3658	-0.056	-0.439	0.11	0.162	-0.648	0.726	RIJE_GPS	2011.045	2018.999	1353
12.62	46.0118	-0.033	-0.639	0.161	0.295	0.113	1.615	ROP__GPS	2016.69	2020.13	1151
12.6898	46.5674	0.84	-1.243	0.074	0.125	2.154	0.572	SAPP_GPS	2009.136	2020.113	1510
12.5642	45.6298	-0.137	-0.016	0.045	0.086	-1.579	0.484	SDNA_GPS	2007.486	2020.127	1696
12.2913	45.23	-2.629	-1.889	0.14	0.154	-4.666	0.691	SFEL_GPS	2001.544	2011.166	
12.425	46.7457	1.02	-0.727	0.078	0.175	-2.315	0.657	SILL_GPS	2011.081	2020.102	1623
12.166	45.4907	0.131	0.301	0.307	0.718	-2.944	4.583	SPIN_GPS	2018.856	2020.127	369
12.2085	45.857	0.297	0.05	0.058	0.148	-0.392	0.671	SUSE_GPS	2011.138	2020.127	1649
12.3961	46.0605	0.356	-0.27	0.082	0.196	0.213	0.707	TAMB_GPS	2011.681	2020.127	1356
13.5926	46.5024	0.64	-1.675	0.044	0.109	1.247	0.486	TARV_GPS	2007.429	2020.13	1663
12.2463	45.6683	-0.091	-0.066	0.04	0.085	-0.45	0.551	TRE5_GPS	2008.042	2017.999	1032
12.2217	45.6798	-0.009	0.027	0.053	0.11	-0.868	0.706	TRE9_GPS	2012.053	2020.127	1615
12.4547	45.4677	2.237	-1.36	0.291	0.407	-9.301	1.703	TREP_GPS	2004.187	2008.072	
12.2565	45.6639	0.015	-0.061	0.058	0.114	-0.287	0.815	TREV_GPS	2004.332	2011.166	
12.2432	45.6532	-0.119	0.211	0.052	0.103	-0.67	0.644	TREX_GPS	2011.174	2020.127	1536
13.7878	45.6606	0.145	0.087	0.051	0.062	-0.334	0.364	TRI1_GPS	2003.39	2019.475	1167
13.7635	45.7098	-0.121	0.045	0.048	0.053	-0.389	0.322	TRIE_GPS	2003.105	2020.13	1648
13.7861	45.6603	-0.168	0.115	0.204	0.319	-0.605	1.809	TRSE_GPS	2016.966	2020.13	1065
13.7947	45.6603	-0.273	0.134	0.216	0.289	0.667	1.631	TRUN_GPS	2016.69	2020.13	1139
12.2217	45.6798	-0.02	-0.039	0.041	0.081	-0.873	0.505	TVSO_GPS	2008.649	2020.127	1488
13.253	46.0375	-0.066	-0.125	0.029	0.061	-0.241	0.399	UDI1_GPS	2006.256	2020.127	1617
13.2277	46.0552	0.174	0.102	0.047	0.09	-0.022	0.47	UDI2_GPS	2008.327	2020.13	1711
13.253	46.0372	0.021	0.43	0.099	0.221	-5.319	1.412	UDIN_GPS	2002.448	2006.678	
13.5297	45.4389	-1.576	0.954	0.318	0.62	1.298	4.603	UMGS_GPS	2006.001	2007.256	
13.2165	46.0831	-0.212	-0.18	0.039	0.074	0.168	0.461	UNUD_GPS	2006.182	2020.127	1651
12.8897	45.9931	-3.014	1.881	0.789	0.386	-0.706	1.626	VALV_GPS	2016.463	2020.127	685
12.5653	46.4571	0.676	-1.214	0.083	0.148	1.209	0.824	VARM_GPS	2012.589	2020.102	1112
12.3339	45.4375	-0.935	-1.294	0.138	0.292	-0.726	1.639	VE01_GPS	2007.851	2011.182	
12.8331	45.7674	0.021	0.682	0.115	0.301	-1.855	2.137	VE02_GPS	2008.551	2011.19	
12.3578	45.4379	0.105	0.395	0.111	0.201	-2.497	1.398	VEAR_GPS	2006.16	2010.716	
12.3541	45.4306	-0.004	-0.307	0.039	0.137	-1.377	0.532	VEN1_GPS	2009.807	2020.13	1750
12.332	45.437	0.643	-0.656	0.09	0.229	1.567	0.93	VENE_GPS	2001.086	2007.563	
12.3823	45.4261	-0.163	0.049	0.106	0.188	-0.915	1.213	VENI_GPS	2015.24	2020.127	1169
12.4211	45.4421	-2.288	3.574	0.143	0.31	-6.121	1.513	VINE_GPS	2012.053	2015.785	68
12.3014	45.9933	0.368	-0.676	0.067	0.133	0.351	0.639	VITT_GPS	2011.185	2020.127	1645

13.8505	46.607	1.164	-1.641	0.036	0.058	0.692	0.351	VLCH_GPS	2001.001	2018.999	1040
12.9736	46.5572	0.86	-1.217	0.039	0.076	1.16	0.336	ZOUF_GPS	2002.448	2020.13	1732

Table A1. Selection of GNSS data based on criteria #1 and #2. The red lines indicate the excluded sites due to the termination of the data acquisition before 2015. Grey lines indicate the GNSS data that have been excluded because of the length of their time series (< 2.5 years, namely 913 days) within the observation period 2015-2019.

APPENDIX B

	Ascending Dataset							
	Search Radius							
	200		400		600		800	
Stations	*St.dev*	*PS*	*St.dev*	*PS*	*St.dev*	*PS*	*St.dev*	*PS*
AMA_	0.12	10	0.27	36	0.53	69	0.64	102
BARC	0.2	5	0.2	16	0.2	24	0.41	28
BEVA	0.58	7	0.44	13	0.54	22	0.49	38
BLNO	0.17	11	0.2	44	0.24	91	0.33	140
BORC	0.16	11	0.25	28	0.28	38	0.3	48
BRSE	0.22	7	0.17	31	0.25	56	0.35	100
CANV	0	1	0.88	5	1	16	0.86	25
CERV	0.21	14	0.37	43	0.3	85	0.36	145
CGIA	0.51	7	0.56	23	0.55	36	0.64	69
CODR	0.25	12	0.26	50	0.28	103	0.25	166
GOD9	0.56	13	0.36	43	0.29	92	0.29	139
GONA	0.06	12	0.21	48	0.22	96	0.21	153
GORI	0.15	11	0.17	53	0.18	97	0.2	179
GRDO	0.43	7	0.61	29	0.51	60	0.49	92
GRUN	0.18	6	0.18	38	0.22	92	0.25	169
GUMM	0.74	6	0.68	19	0.61	25	0.58	43
KLAG	0.16	10	0.35	28	0.31	83	0.26	152
KLA_	0.15	14	0.17	49	0.17	113	0.18	200
KOE2	0.39	6	0.33	19	0.4	45	0.35	82
LANK	0.25	11	0.36	36	0.33	74	0.29	126
MDEA	0.37	3	0.77	10	0.72	15	0.51	31
MIRA	0.15	13	0.3	48	0.28	83	0.53	124
MOGG	0.31	8	0.31	35	0.38	59	0.4	84
MPRA			0.15	3	0.58	10	0.48	28
MT01	0.2	8	0.32	28	0.46	56	0.4	82
MT06	1.87	4	1.15	11	0.84	21	0.65	39
NOVE	0	1	0.76	3	0.66	7	0.71	19
ODEZ	0.18	13	0.49	49	0.42	97	0.42	171
PAZO	0	1	0.14	3	0.29	6	0.42	17

PIEV	0.21	12	0.17	30	0.27	62	0.42	105
PORD	0.11	10	0.28	49	0.29	100	0.3	174
PORT	0.62	14	0.5	38	0.49	68	0.54	141
PSAL	0.17	8	0.23	28	0.21	75	0.27	143
ROP_	0.1	13	0.21	51	0.26	98	0.28	152
SDNA	0.21	14	0.26	45	0.25	86	0.32	149
SUSE	0.94	3	0.94	3	0.97	4	0.69	9
TAMB							0.57	3
TARV	0.31	7	0.4	24	0.52	49	0.48	79
TRE5	0.12	13	0.16	48	0.21	114	0.23	198
TRE9	0.21	11	0.25	47	0.21	103	0.22	188
TREX	0.11	13	0.18	50	0.19	109	0.2	183
TRI1	0.08	12	0.13	42	0.24	99	0.28	167
TRIE	0.27	8	0.39	21	0.31	42	0.31	62
TRSE	0.13	14	0.15	39	0.22	98	0.27	177
TRUN	0.21	13	0.2	43	0.25	87	0.29	159
TVSO	0.21	11	0.25	47	0.21	103	0.22	188
UDI1	0.27	12	0.19	49	0.29	91	0.3	152
UDI2	0.13	13	0.17	49	0.2	111	0.25	195
UNUD	0.29	13	0.25	49	0.24	97	0.24	161
VEN1	0.13	9	0.22	32	0.36	62	0.38	103
VENI	0.29	5	0.34	20	0.38	47	0.35	63
VITT	0.19	11	0.2	41	0.25	84	0.31	142
VLCH	0.27	13	0.21	51	0.24	107	0.24	189
10° Perc		4.5		9.6		19		28
Threshold PS		5		10		19		28

Table B2.1. Selection of GNSS data based on criteria #3 and #4 for the ascending dataset. The table reports, for each GNSS site and search radius, the number of PSs (*PS*) and the standard deviation of their velocities (*St.dev*). The last two lines report the values of the 10th percentile computed on the PS column and the final threshold. Considering each radius separately, the station is highlighted in case of a standard deviation higher than 1 mm/yr and/or a number of PSs lower than the given threshold. The GNSS site (red lines) is excluded if the entire line is highlighted (criteria #3 and #4 not accomplished for all the radii).

	Descending Dataset							
	Search Radius							
	200		400		600		800	
Stations	*St.dev*	*PS*	*St.dev*	*PS*	*St.dev*	*PS*	*St.dev*	*PS*
AMA_	0.27	10	0.65	36	0.68	68	0.75	104
AMPE	0.44	12	0.42	32	0.38	47	0.37	60
BARC	0.14	7	0.46	14	0.5	22	0.6	28
BEVA	0.49	7	0.44	17	0.44	25	0.51	44
BLNO	0.09	11	0.19	44	0.19	81	0.29	128
BORC	0.25	11	0.65	29	0.57	40	0.51	53
BRSE	0.27	9	0.37	30	0.4	61	0.48	105
CANV	0	1	0.34	4	0.36	9	0.64	15
CERV	0.19	12	0.24	39	0.42	85	0.34	139
CODR	0.3	12	0.2	49	0.18	103	0.19	162
FUSE			0.55	3	0.7	24	0.78	53
GOD9	0.32	14	0.27	44	0.23	86	0.23	130
GONA	0.12	11	0.25	48	0.26	93	0.26	147
GORI	0.07	11	0.16	48	0.21	96	0.21	172
GRDO	0.58	8	0.4	28	0.37	57	0.39	95
GRUN	0.29	7	0.46	37	0.35	91	0.32	159
GUMM	0.62	8	0.55	17	0.77	24	0.66	43
KLAG	0.27	9	0.26	29	0.25	84	0.29	140
KLA_	0.13	12	0.17	49	0.19	108	0.21	204
KOE2	0.34	6	0.4	25	0.37	56	0.36	90
LANK	0.24	10	0.33	32	0.33	74	0.33	123
MDEA	0.72	4	0.55	9	0.53	12	0.41	29
MIRA	0.18	13	0.31	47	0.32	81	0.36	125
MOGG	0.46	10	0.28	32	0.5	59	0.57	89
MPRA	0	1	0.21	3	0.87	18	0.78	32
MT01	0.22	9	0.21	35	0.21	57	0.23	86
MT06	1.01	5	0.61	18	0.54	32	0.48	44
NOVE	0.08	2	0.08	2	0.78	9	0.55	21
OCHS	0.37	2	0.29	4	0.33	6	0.25	22
ODEZ	0.13	14	0.53	51	0.43	109	0.41	178
PAZO			0	1	0.57	2	0.44	12
PIEV	0.12	10	0.19	33	0.24	69	0.26	114
PORD	0.14	11	0.25	50	0.25	95	0.33	178

PORE	0.35	8	0.4	36	0.47	64	0.44	104
PORT	0.48	11	0.53	31	0.64	80	0.67	147
ROP_	0.19	14	0.19	51	0.2	97	0.23	152
SDNA	0.12	15	0.27	46	0.26	90	0.28	154
SUSE	0.08	2	0.07	2	0.15	5	0.28	10
TAMB			0	1	0.13	2	0.14	2
TARV	0.26	8	0.27	25	0.68	46	0.57	74
TRE5	0.1	11	0.21	50	0.19	114	0.18	202
TRE9	0.06	8	0.18	50	0.24	103	0.21	184
TREX	0.14	12	0.18	49	0.24	112	0.23	195
TRI1	0.3	11	0.36	39	0.32	95	0.31	174
TRIE	0.71	10	0.56	21	0.49	37	0.43	58
TRSE	0.28	14	0.23	41	0.3	98	0.28	174
TRUN	0.18	14	0.25	46	0.25	87	0.33	158
TVSO	0.06	8	0.18	50	0.24	103	0.21	184
UDI1	0.1	14	0.12	47	0.15	91	0.18	155
UDI2	0.12	14	0.13	47	0.14	107	0.19	189
UNUD	0.16	13	0.16	46	0.16	93	0.22	166
VITT	0.32	12	0.32	42	0.32	94	0.31	161
VLCH	0.16	14	0.23	48	0.26	105	0.25	189
10° Perc		2.6		3.6		10.8		25.6
Threshold PS		3		4		11		26

Table B2.2. Selection of GNSS data based on criteria #3 and #4 for the descending dataset. The table reports, for each GNSS site and each search radius, the number of PSs (*PS*) and the standard deviation of their velocities (*St.dev*). The last two lines report the values of the 10th percentile computed on the PS column and the final threshold. Considering each radius separately, the station is highlighted in case of a standard deviation higher than 1 mm/yr and/or a number of PSs lower than the given threshold. The GNSS site (red lines) is excluded if the entire line is highlighted (criteria #3 and #4 not accomplished for all the radii).

APPENDIX C

Ascending Dataset

SAR	*GNSS*	*Site*
-0.23	0.220876	AMA_
0.57	0.670475	BARC
-2.33	-1.40681	BEVA
1.11	0.242639	BLNO
1.26	0.438641	BORC
0.69	1.47364	BRSE
0.75	-1.12291	CERV
-2.42	-2.26712	CGIA
-0.19	-0.58967	CODR
-0.85	-0.77202	GOD9
0.67	0.249155	GONA
0.24	0.040392	GORI
-1.27	-1.20556	GRDO
0.11	-0.00607	GRUN
-0.54	0.091817	GUMM
-0.46	-0.3081	KLAG
-0.53	-1.21725	KLA_
0.18	0.320482	KOE2
-0.49	-0.12636	LANK
0.62	-0.36559	MDEA
-0.27	-0.38658	MIRA
0.27	0.581086	MOGG
-0.7	0.110241	MT01
-0.88	-0.42707	MT06
-0.84	-0.94435	ODEZ
1.3	0.984391	PIEV
-0.81	-0.30627	PORD
-2.31	-2.64877	PORT
-0.33	-0.8819	PSAL
-0.09	0.178528	ROP_
-0.82	-1.2343	SDNA

Descending Dataset

SAR	*GNSS*	*Site*
0.81	0.729259	AMA_
1.76	1.3311	AMPE
1.27	0.699478	BARC
-2.09	-1.27477	BEVA
0.61	1.09025	BLNO
1.69	1.05208	BORC
0.7	1.49681	BRSE
-0.29	-0.96846	CERV
-0.27	-0.62006	CODR
2.06	0.87719	FUSE
-0.15	-0.5111	GOD9
-0.65	0.112245	GONA
0.41	-0.19025	GORI
-0.86	-1.3314	GRDO
0.31	-0.49731	GRUN
1.28	1.39389	GUMM
0.51	0.983527	KLAG
0.69	0.460579	KLA_
2.25	1.84124	KOE2
1.41	1.56731	LANK
0.05	-0.48075	MDEA
-0.85	-0.22492	MIRA
2.05	1.02022	MOGG
1.12	-0.06219	MPRA
-0.12	0.01161	MT01
-0.13	0.171694	MT06
-0.41	-0.89755	ODEZ
1.37	1.88123	PIEV
0.69	-0.28886	PORD
0.41	-0.16196	PORE
-2.1	-2.31683	PORT

1.4	0.73673	TARV	0.62	0.137813	ROP_
-0.12	-0.32601	TRE5	-0.63	-1.3219	SDNA
-0.34	-0.73276	TRE9	2.54	1.55987	TARV
0.11	-0.52576	TREX	-0.05	-0.39609	TRE5
-0.73	-0.3576	TRI1	-0.18	-0.67483	TRE9
-0.49	-0.22783	TRIE	-0.09	-0.61325	TREX
-0.8	-0.37161	TRSE	0.03	-0.21551	TRI1
-0.7	0.66983	TRUN	0.31	-0.39664	TRIE
-0.34	-0.72454	TVSO	-0.01	-0.61142	TRSE
1.07	-0.13722	UDI1	0.09	0.408172	TRUN
0.57	-0.13309	UDI2	-0.18	-0.67838	TVSO
0.57	0.27993	UNUD	-0.49	-0.22072	UDI1
-0.59	-1.12777	VEN1	-0.46	0.070854	UDI2
-0.76	-0.68902	VENI	-0.6	0.033997	UNUD
-0.32	0.16683	VITT	0.27	0.57593	VITT
-0.38	-0.05202	VLCH	1.57	1.37496	VLCH

Table C1. Comparison between the InSAR and GNSS velocities for the descending and ascending datasets after the calibration. The sites highlighted in yellow present an absolute InSAR-GNSS velocity difference higher than 1 mm/yr.

APPENDIX D

East-west Dataset			Vertical Dataset		
SAR	*GNSS*	*Site*	*SAR*	*GNSS*	*Site*
0.95	0.427	AMA_	0.46	0.454	AMA_
0.57	0.052	BARC	1.12	0.775	BARC
0.18	0.122	BEVA	-2.76	-1.65	BEVA
-0.28	0.767	BLNO	1.18	0.69	BLNO
0.66	0.565	BORC	1.9	0.771	BORC
0.16	0.147	BRSE	0.95	1.707	BRSE
-0.92	0.17	CERV	0.29	-1.314	CERV
-0.05	-0.028	CODR	-0.26	-0.744	CODR
0.58	0.178	GOD9	-0.58	-0.835	GOD9
-1.14	-0.122	GONA	0	0.238	GONA
0.13	-0.192	GORI	0.44	-0.107	GORI
0.37	-0.065	GRDO	-1.27	-1.448	GRDO
0.16	-0.402	GRUN	0.3	-0.351	GRUN
1.47	1.053	GUMM	0.46	0.792	GUMM
0.79	1.075	KLAG	0.13	0.34	KLAG
0.98	1.508	KLA_	0.2	-0.587	KLA_
1.69	1.272	KOE2	1.56	1.213	KOE2
1.54	1.377	LANK	0.68	0.81	LANK
-0.44	-0.081	MDEA	0.38	-0.504	MDEA
-0.66	0.115	MIRA	-0.58	-0.354	MIRA
1.53	0.358	MOGG	1.52	0.872	MOGG
0.43	-0.077	MT01	-0.48	0.102	MT01
0.6	0.494	MT06	-0.65	-0.257	MT06
0.32	-0.011	ODEZ	-0.72	-1.141	ODEZ
0.26	0.837	PIEV	1.74	1.587	PIEV
1.3	0.005	PORD	-0.05	-0.347	PORD
0.17	0.239	PORT	-2.64	-3.042	PORT
0.63	-0.033	ROP_	0.35	0.113	ROP_
0.09	-0.137	SDNA	-0.85	-1.579	SDNA
0.93	0.64	TARV	2.57	1.247	TARV
0.02	-0.091	TRE5	-0.06	-0.45	TRE5

0.08	-0.009	TRE9	-0.28	-0.868	TRE9
-0.21	-0.119	TREX	0.1	-0.67	TREX
0.73	0.145	TRI1	-0.35	-0.334	TRI1
0.66	-0.121	TRIE	-0.03	-0.389	TRIE
0.77	-0.168	TRSE	-0.4	-0.605	TRSE
0.75	-0.273	TRUN	-0.3	0.667	TRUN
0.08	-0.02	TVSO	-0.28	-0.873	TVSO
-1.33	-0.066	UDI1	0.36	-0.241	UDI1
-0.86	0.174	UDI2	0.08	-0.022	UDI2
-0.98	-0.212	UNUD	0	0.168	UNUD
0.56	0.368	VITT	0.03	0.351	VITT
1.58	1.164	VLCH	0.87	0.692	VLCH

Table D1. Comparison between the InSAR and GNSS velocities for the vertical and east-west datasets. The sites highlighted in yellow present an absolute InSAR-GNSS velocity difference higher than 1 mm/yr.

ACKNOWLEDGEMENTS

The Sentinel-1A and 1B data used in the present study were accessed through the Alaska Service Facility (ASF; https://search.asf.alaska.edu/). We are grateful to all public and private institutions and companies that make GPS data freely available for scientific applications, in particular: the EPN-EUREF network, Leica-ITALPOS, Topcon-NETGEO, ASI-GEODAF, INGV-RING, InOGS-FREDNET, Rete "Antonio Marussi" in Friuli Venezia Giulia, STPOS and TPOS in Trentino-Alto Adige and Regione Veneto, the ARPAV-Belluno, the SIGNAL in Slovenia and APOS in Austria.
Most of the figures have been created using the Generic Mapping Tools (GMT) software (Wessel *et al.,* 2019) and CorelDRAW Graphics Suite.

I would like to express my deepest appreciation to Prof. Lorenzo Bonini for his constant support, his great availability, and for encouraging me during these challenging years. I'm also extremely grateful to my co-supervisor, Dr. Giuseppe Pezzo, for believing in me, giving me the opportunity to deepen my knowledge of InSAR data, and for involving me in his projects.

I am very thankful to Dott. Mimmo Palano (INGV) and Prof. Giovanni Toscani (UNIPV) for their constructive comments and valuable suggestions during the revision of my thesis.

I am deeply indebted to Dr. John Peter Merryman Boncori (DTU) for generously providing knowledge and expertise and for taking good care of me in Denmark during the pandemic.

My gratitude goes to Dr. Enrico Serpelloni and Dr. Letizia Anderlini (INGV) for their help, availability, and useful suggestions about GNSS data and modeling.

I would like to extend my sincere thanks to Dr. Giuliana Rossi (OGS) for our interesting discussions and the opportunities she gave me.

I am grateful to Dr. David Zuliani and Dr. Paolo Fabris for hosting me at the Seismological Research Centre of OGS and for introducing me to the world of GNSS data.

I am also thankful to Dr. Lavinia Tunini and Dr. Andrea Magrin (OGS) for their feedback and support.

During these years, I faced many challenging moments in my life that profoundly changed me. Therefore, I am deeply thankful to all the people who strongly supported and believed in me, even when I felt lost.

Firstly, I thank my family for their constant presence and great support during these years, especially my mom, my brother Alessandro with Giada, and my aunt Anna Paola.
I want to thank my friends for encouraging me and for the beautiful experiences we shared, physically and virtually. Among all, I mention my “sister” Caterina, Francesco, Marco, Elisa, Gaia, Roberta, and Federico.

From the bottom of my heart, I thank Michele for your pep talks, your lovely and caring presence, and above all, your endless patience.

Finally, special thanks goes to my father Tullio, my role model, that continues to inspire me. I miss your wise suggestions, your unshakable certainties, and our long conversations.

REFERENCES

Ab Latip, A.S., Matori, A., Aobpaet, A. and Din, A.H.M. (2015) 'Monitoring of offshore platform deformation with Stanford Method of Persistent Scatterer (StaMPS)', *International Conference on Space Science and Communication, IconSpace*, 2015-September, pp. 79–83. doi:10.1109/IconSpace.2015.7283785.

Anderlini, L., Serpelloni, E., Tolomei, C., Marco De Martini, P., Pezzo, G., Gualandi, A. and Spada, G. (2020) 'New insights into active tectonics and seismogenic potential of the Italian Southern Alps from vertical geodetic velocities', *Solid Earth*, 11(5), pp. 1681–1698. doi:10.5194/se-11-1681-2020.

Anderson, E. M. (1905) 'The dynamics of faulting', *Transactions of the Edinburgh Geological Society,* 8, 387-402.

Anselmi, M., Govoni, A., De Gori, P. and Chiarabba, C. (2011) 'Seismicity and velocity structures along the south-Alpine thrust front of the Venetian Alps (NE-Italy)', *Tectonophysics*, 513(1–4), pp. 37–48. doi:10.1016/j.tecto.2011.09.023.

Anzidei, M., Boschi, E., Cannelli, V., Devoti, R., Esposito, A., Galvani, A., Melini, D., Pietrantonio, G., Riguzzi, F., Sepe, V., *et al.* (2009) 'Coseismic deformation of the destructive April 6, 2009 L'Aquila earthquake (central Italy) from GPS data', *Geophysical Research Letters*, 36(17), pp. 3–7. doi:10.1029/2009GL039145.

Aoudia, A., Saraò, A., Bukchin, B. and Suhadolc, P. (2000) 'The 1976 Friuli (NE Italy) Thrust Faulting Earthquake: A Reappraisal 23 Years Later', *Geophysical Research Letters*, 27(4), pp. 577–580.

Aslan, G., Foumelis, M., Raucoules, D., De Michele, M., Bernardie, S. and Cakir, Z. (2020) 'Landslide mapping and monitoring using persistent scatterer interferometry (PSI) technique in the French Alps', *Remote Sensing*, 12(8),1305. doi:10.3390/RS12081305.

Atanackov, J., Jamšek Rupnik, P., Jež, J., Celarc, B., Novak, M., Milanič, B., Markelj, A., Bavec, M. and Kastelic, V. (2021) 'Database of Active Faults in Slovenia: Compiling a New Active Fault Database at the Junction Between the Alps, the Dinarides and the Pannonian Basin Tectonic Domains', *Frontiers in Earth Science*, 9(May), pp. 1–21. doi:10.3389/feart.2021.604388.

Atzori, S., Hunstad, I., Chini, M., Salvi, S., Tolomei, C., Bignami, C., Stramondo, S., Trasatti, E., Antonioli, A. and Boschi, E. (2009) 'Finite fault inversion of DInSAR coseismic displacement of the 2009 L'Aquila earthquake (central Italy)', *Geophysical Research Letters*, 36(15), pp. 1–6. doi:10.1029/2009GL039293.

Avouac, J.P. (2015) 'From Geodetic Imaging of Seismic and Aseismic Fault Slip to Dynamic

Modeling of the Seismic Cycle', *Annual Review of Earth and Planetary Sciences*, 43(1), pp. 233–271. doi:10.1146/annurev-earth-060614-105302.

Bagnardi, M. and Hooper, A. (2018) 'Inversion of Surface Deformation Data for Rapid Estimates of Source Parameters and Uncertainties: A Bayesian Approach', *Geochemistry, Geophysics, Geosystems*, 19(7), pp. 2194–2211. doi:10.1029/2018GC007585.

Bajc, J., Aoudia, A., Saraò, A. and Suhadolc, P. (2001) 'The 1998 Bovec-Krn mountain (Slovenia) earthquake sequence', *Geophysical Research Letters*, 28(9), pp. 1839–1842.

Balbi, E., Terrone, M., Faccini, F., Scafidi, D., Barani, S., Tosi, S., Crispini, L., Cianfarra, P., Poggi, F. and Ferretti, G. (2021) 'Persistent Scatterer Interferometry and Statistical Analysis of Time-Series for Landslide Monitoring: Application to Santo Stefano d'Aveto (Liguria, NW Italy)', *Remote Sensing.*, 13, 3348. doi:10.3390/rs13173348

Bamler, R. and Hartl, P. (1998) 'Synthetic aperture radar interferometry', *Inverse Problems*, 14(4), pp. R1–R54.

Barba, S., Finocchio, D., Sikdar, E. and Burrato, P. (2013) 'Modelling the interseismic deformation of a thrust system: Seismogenic potential of the Southern Alps', *Terra Nova*, 25(3), pp. 221–227. doi:10.1111/ter.12026.

Barbot, S., Hamiel, Y. and Fialko, Y. (2008) 'Space geodetic investigation of the coseismic and postseismic deformation due to the 2003 Mw7.2 Altai earthquake: Implications for the local lithospheric rheology', *Journal of Geophysical Research: Solid Earth*, 113(3), pp. 1–15. doi:10.1029/2007JB005063.

Barbot, S., Fialko, Y. and Bock, Y. (2009) 'Postseismic deformation due to the Mw 6.0 2004 Parkfield earthquake: Stress-driven creep on a fault with spatially variable rate-and-state friction parameters', *Journal of Geophysical Research: Solid Earth*, 114(7), pp. 1–26. doi:10.1029/2008JB005748.

Barla, G. and Paronuzzi, P. (2013) 'The 1963 Vajont Landslide: 50th Anniversary', *Rock Mechanics and Rock Engineering,* 46(6), pp. 1267–1270. doi:10.1007/s00603-013-0483-7.

Battaglia, M., Murray, M.H., Serpelloni, E. and Bürgmann, R. (2004) 'The Adriatic region: An independent microplate within the Africa-Eurasia collision zone', *Geophysical Research Letters*, 31(9), pp. 10–13. doi:10.1029/2004GL019723.

Beccaro, L., Tolomei, C., Gianardi, R., Sepe, V., Bisson, M., Colini, L., De Ritis, R. and Spinetti, C. (2021) 'Multitemporal and multisensor InSAR analysis for ground displacement field assessment at Ischia volcanic island (Italy)', *Remote Sensing*, 13(21). doi:10.3390/rs13214253.

Bechor, N.B.D. and Zebker, H.A. (2006) 'Measuring two-dimensional movements using a single InSAR pair', *Geophysical Research Letters*, 33(16), pp. 1–5. doi:10.1029/2006GL026883.

Bechtold, M., Battaglia, M., Tanner, D.C. and Zuliani, D. (2009) 'Constraints on the active tectonics of the Friuli/NW Slovenia area from CGPS measurements and three-dimensional kinematic modeling', *Journal of Geophysical Research*, 114(B3), p. B03408. doi:10.1029/2008JB005638.

Bekaert, D.P.S., Walters, R.J., Wright, T.J., Hooper, A.J. and Parker, D.J. (2015) 'Statistical comparison of InSAR tropospheric correction techniques', *Remote Sensing of Environment*, 170, pp. 40–47. doi:10.1016/j.rse.2015.08.035.

Benedetti, L., Tapponnier, P., King, G. C., Meyer, B. and Manighetti, I. (2000) 'Growth folding and active thrusting in the Montello region, Veneto, northern Italy', *Journal of Geophysical Research: Solid Earth*, 105(B1), pp. 739-766.

Berardino, P., Fornaro, G., Lanari, R. and Sansosti, E. (2002) 'A new algorithm for surface deformation monitoring based on small baseline differential SAR interferograms', *IEEE Transactions on Geoscience and Remote Sensing*, *40*(11), 2375-2383. doi: 10.1109/TGRS.2002.803792

Biggs, J., Wright, T., Lu, Z. and Parsons, B. (2007) 'Multi-interferogram method for measuring interseismic deformation: Denali Fault, Alaska', *Geophysical Journal International*, 170(3), pp. 1165–1179. doi:10.1111/j.1365-246X.2007.03415.x.

Blanco-Sanchez, P., Mallorquí, J.J., Duque, S. and Monells, D., (2008) 'The coherent pixels technique (CPT): an advanced DInSAR technique for nonlinear deformation monitoring', *Pure and Applied Geophysics,* 165 (6), 1167–1193. doi: 10.1007/978-3-7643-8907-9_10

Blewitt, G., and Lavallée, D. (2002), 'Effect of annual signals on geodetic velocity', *Journal of Geophysical Research: Solid Earth*, 107(B7), 2145, doi:10.1029/2001JB000570.

Blom, R. and Elachi, C. (1981) 'Spaceborne and Airborne Imaging Radar Observations of Sand Dunes', *Journal of Geophysical Research ,* 86(B4), pp. 3061–3073. doi:10.1029/JB086iB04p03061.

Bock, Y., Wdowinski, S., Ferretti, A., Novali, F. and Fumagalli, A. (2012) 'Recent subsidence of the Venice Lagoon from continuous GPS and interferometric synthetic aperture radar', *Geochemistry, Geophysics, Geosystems*, 13(3), pp. 1–13. doi:10.1029/2011GC003976.

Bosellini, A., Masetti, D., and Sarti, M. (1981) 'A Jurassic "Tongue of the ocean" infilled with oolitic sands: The Belluno trough, Venetian Alps, Italy', *Marine Geology*, 44(1-2), p. 59–95, doi:10.1016/0025-3227(81)90113-4.

Brambati, A., Carbognin, L., Quaia, T., Teatini, P. and Tosi, L. (2003) 'The Lagoon of Venice: geological setting, evolution and land subsidence', *Episodes Journal of International Geoscience*, 26(3), pp. 264-268. doi:10.18814/epiiugs/2003/v26i3/020.

Bressan, G., Bragato, P.L. and Venturini, C. (2003) 'Stress and strain tensors based on focal mechanisms in the seismotectonic framework of the Friuli-Venezia Giulia Region (Northeastern

Italy)', *Bulletin of the Seismological Society of America*, 93(3), pp. 1280–1297. doi:10.1785/0120020058.

Bressan, G., Ponton, M., Rossi, G. and Urban, S. (2016) 'Spatial organization of seismicity and fracture pattern in NE Italy and W Slovenia', *Journal of Seismology*, 20(2), pp. 511–534. doi:10.1007/s10950-015-9541-9.

Bressan, G., Barnaba, C., Bragato, P., Ponton, M. and Restivo, A. (2018) 'Revised seismotectonic model of NE Italy and W Slovenia based on focal mechanism inversion', *Journal of Seismology*, 22(6), pp. 1563–1578. doi:10.1007/s10950-018-9785-2.

Bürgmann, R., Rosen, P.A. and Fielding, E.J. (2000) 'Synthetic Aperture Radar Interferometry to measure Earth's surface topography and its deformation', *Annual Review of Earth and Planetary Sciences*, 28, pp. 169–209.

Bürgmann, R. and Thatcher, W. (2013) 'Space geodesy: A revolution in crustal deformation measurements of tectonic processes', *M. E Bickford (Ed.), The web of geological sciences: Advances, impacts and interactions GSA spec. Pap.,* 500, pp. 397– 430.

Burrato, P., Poli, M.E., Vannoli, P., Zanferrari, A., Basili, R. and Galadini, F. (2008) 'Sources of Mw 5 + earthquakes in northeastern Italy and western Slovenia : An updated view based on geological and seismological evidence', *Tectonophysics*, 453, pp. 157–176. doi:10.1016/j.tecto.2007.07.009.

Busetti, A., Calligaris, C., Forte, E., Areggi, G., Mocnik, A. and Zini, L. (2020) 'Non-invasive methodological approach to detect and characterize high-risk sinkholes in urban cover evaporite karst: Integrated reflection seismics, PS-INSAR, leveling, 3D-GPR and ancillary data. A NE Italian case study', *Remote Sensing*, 12(22), pp. 1–28. doi:10.3390/rs12223814.

Carbognin, L., Teatini, P., Tomasin, A. and Tosi, L. (2009) 'Global change and relative sea level rise at Venice: What impact in term of flooding', *Climate Dynamics*, 35(6), pp. 1055–1063. doi:10.1007/s00382-009-0617-5.

Carulli, G.B. and Slejko, D. (2005) 'The 1976 Friuli, Italy, Earthquake', *Giornale di Geologia Applicata*, 1, pp. 147–156. doi:10.1474/GGA.2005-01.0-15.0015.

Castellarin, A. and Cantelli, L. (2000) 'Neo-Alpine evolution of the Southern Eastern Alps', *Journal of Geodynamics*, 30(1–2), pp. 251–274. doi:10.1016/S0264-3707(99)00036-8.

Cattin, R. and Avouac, J.P. (2000) 'Modeling moutain building and the seismic cycle in the Hymalaya of Nepal', *Journal of Geophysical Research*, 105(B6), pp. 13389–13407. doi:10.1029/2000JB900032

Chan, Y.K. and Koo, V.C. (2008) 'An Introduction to Synthetic Aperture Radar (SAR)', *Progress In Electromagnetics Research B*, 2, pp. 27–60.

Chaussard, E., Johnson, C.W., Fattahi, H. and Bürgmann, R. (2016) 'Potential and limits of InSAR to characterize interseismic deformation independently of GPS data: Application to the southern San Andreas Fault system', *Geochemistry Geophysics Geosystems*, 17, pp. 1214–1229. doi:10.1002/2015GC006246.

Cheloni, D., D'Agostino, N. and Selvaggi, G. (2014) 'Interseismic coupling, seismic potential, and earthquake recurrence on the southern front of the Eastern Alps (NE Italy)', *Journal of Geophysical Research: Solid Earth*, 119(5), pp. 4448–4468. doi:10.1002/2014JB010954.

Cheloni, D., De Novellis, V., Albano, M., Antonioli, A., Anzidei, M., Atzori, S., Avallone, A., Bignami, C., Bonano, M., Calcaterra, S., *et al.* (2017) 'Geodetic model of the 2016 Central Italy earthquake sequence inferred from InSAR and GPS data', *Geophysical Research Letters*, 44(13), pp. 6778–6787. doi:10.1002/2017GL073580.

Chen, C.W. and Zebker, H.A. (2002) 'Phase unwrapping for large SAR interferograms: Statistical segmentation and generalized network models', *IEEE Transactions on Geoscience and Remote Sensing*, 40(8), pp. 1709–1719. doi:10.1109/TGRS.2002.802453.

Colesanti, C. and Wasowki, J. (2006) 'Investigating landslides with space-borne Synthetic Aperture Radar (SAR) Interferometry', *Engineering Geology*, 88, pp. 173–199. doi: 10.1016/j.enggeo.2006.09.013

Costantini, M., Falco, S., Malvarosa, F. and Minati, F., (2008) 'A new method for identification and analysis of persistent scatterers in series of SAR images', *Proceedings IEEE Int. Geoscience and Remote Sensing Symp. (IGARSS).*

Crosetto, M., Crippa, B. and Biescas, E., (2005) 'Early detection and in-depth analysis of deformation phenomena by radar interferometry', *Engineering Geology*, 79, pp. 81–91. doi:10.1016/j.enggeo.2004.10.016

Crosetto, M., Biescas, E., Duro, J., Closa, J. and Arnaud, A., (2008) 'Generation of advanced ERS and Envisat interferometric SAR products using the stable point network technique' *Photogrammetric Engineering & Remote Sensing,* 74 (4), 443–450. doi:10.14358/PERS.74.4.443

Crosetto, M., Monserrat, O., Jungner, A., and Crippa, B. (2009) 'Persistent scatterer interferometry: Potential and limits', *Proceedings of the 2009 ISPRS Workshop on High-Resolution Earth Imaging for Geospatial Information, Hannover, Germany* (Vol. 25).

Crosetto, M., Monserrat, O., Cuevas-González, M., Devanthéry, N. and Crippa, B. (2016) 'Persistent Scatterer Interferometry: A review', *ISPRS Journal of Photogrammetry and Remote Sensing*, 115, pp. 78–89. doi:10.1016/j.isprsjprs.2015.10.011.

Cruden, D. M. and Varnes, D. J. (1996) 'Landslides: investigation and mitigation. Chapter 3-

Landslide types and processes', *Transportation research board special report*, 247.

Curran, P.J. (1988) 'The semivariogram in remote sensing: An introduction', *Remote Sensing of Environment*, 24(3), pp. 493–507. doi:10.1016/0034-4257(88)90021-1.

D'Agostino, N., Cheloni, D., Mantenuto, S., Selvaggi, G., Michelini, A. and Zuliani, D. (2005) 'Strain accumulation in the southern Alps (NE Italy) and deformation at the northeastern boundary of Adria observed by CGPS measurements', *Geophysical Research Letters*, 32(19), pp. 1–4. doi:10.1029/2005GL024266.

Da Lio, C. and Tosi, L. (2018) 'Science of the Total Environment Land subsidence in the Friuli Venezia Giulia coastal plain, Italy : 1992 – 2010 results from SAR-based interferometry', *Science of the Total Environment*, 633, pp. 752–764. doi:10.1016/j.scitotenv.2018.03.244.

Danesi, S., Pondrelli, S., Salimbeni, S., Cavaliere, A., Serpelloni, E., Danecek, P., Lovati, S. and Massa, M. (2015) 'Active deformation and seismicity in the Southern Alps (Italy): The Montello hill as a case study', *Tectonophysics*, 653, pp. 95–108. doi:10.1016/j.tecto.2015.03.028.

Decriem, J., Árnadóttir, T., Hooper, A., Geirsson, H., Sigmundsson, F., Keiding, M., Ófeigsson, B.G., Hreinsdóttir, S., Einarsson, P., LaFemina, P., Bennett, R.A. (2010) 'The 2008 May 29 earthquake doublet in SW Iceland', *Geophysical Journal International*, 181(2), pp. 1128–1146. doi:10.1111/j.1365-246X.2010.04565.x

Delacourt, C., Briole, P. and Achache, J. (1998) 'Tropospheric corrections of SAR interferograms with strong topography. Application to Etna', *Geophysical Research Letters*, 25(15), pp. 2849–2852. doi:10.1029/98GL02112.

Delouis, B., Nocquet, J.M. and Vallée, M. (2010) 'Slip distribution of the February 27, 2010 Mw = 8.8 Maule Earthquake, central Chile, from static and high-rate GPS, InSAR, and broadband teleseismic data', *Geophysical Research Letters*, 37(17), pp. 1–7. doi:10.1029/2010GL043899.

Del Soldato, M., Farolfi, G., Rosi, A., Raspini, F. and Casagli, N. (2018) 'Subsidence evolution of the Firenze-Prato-Pistoia plain (Central Italy) combining PSI and GNSS data', *Remote Sensing*, 10(7), pp. 1–19. doi:10.3390/rs10071146.

Del Soldato, M., Confuorto, P., Bianchini, S., Sbarra, P. and Casagli, N. (2021) 'Review of works combining GNSS and insar in Europe', *Remote Sensing*, 13(9). doi:10.3390/rs13091684.

Devanthéry, N., Crosetto, M., Monserrat, O., Cuevas-González, M. and Crippa, B. (2014) 'An approach to persistent scatterer interferometry', *Remote Sensing*., 6 (7), 6662– 6679. doi: 10.3390/rs6076662

Devoti, R., Zuliani, D., Braitenberg, C., Fabris, P. and Grillo, B. (2015) 'Hydrologically induced slope deformations detected by GPS and clinometric surveys in the Cansiglio Plateau, southern Alps',

Earth and Planetary Science Letters, 419, pp. 134–142. doi:10.1016/j.epsl.2015.03.023.

Devoti, R., D'Agostino, N., Serpelloni, E., Pietrantonio, G., Riguzzi, F., Avallone, A., Cavaliere, A., Cheloni, D., Cecere, G., D'Ambrosio, C., Falco, L., Selvaggi, G., Métois, M., Esposito, A., Sepe, V., Galvani, A. and Anzidei, M. (2017) 'A combined velocity field of the Mediterranean region', *Annals of Geophysics*, 60(2), 0215.

De Zan, F. and Guarnieri, A.M. (2006) 'TOPSAR: Terrain observation by progressive scans', *IEEE Transactions on Geoscience and Remote Sensing*, 44(9), pp. 2352–2360. doi:10.1109/TGRS.2006.873853.

Ding, X. L., Li, Z. W., Zhu, J. J., Feng, G. C. and Long, J. P. (2008) 'Atmospheric effects on InSAR measurements and their mitigation', *Sensors*, *8*(9), pp. 5426-5448. doi:10.3390/s8095426.

DISS Working Group (2021) 'Database of Individual Seismogenic Sources (DISS), Version 3.3.0: A compilation of potential sources for earthquakes larger than M 5.5 in Italy and surrounding areas', *Istituto Nazionale di Geofisica e Vulcanologia (INGV)*. doi:10.13127/diss3.3.0

Doglioni, C. and Bosellini, A. (1987) 'Eoalpine and mesoalpine tectonics in the Southern Alps', *Geologische Rundschau*, 76(3), pp. 735–754. doi:10.1007/BF01821061.

Doin, M.P., Lasserre, C., Peltzer, G., Cavalié, O. and Doubre, C. (2009) 'Corrections of stratified tropospheric delays in SAR interferometry: Validation with global atmospheric models', *Journal of Applied Geophysics*, 69(1), pp. 35–50. doi:10.1016/j.jappgeo.2009.03.010.

Dudczyk, J. and Kawalec, A. (2014) 'Optimizing the minimum cost flow algorithm for the phase unwrapping process in SAR radar', *Bulletin of the Polish Academy of Sciences Technical Sciences*, 62(3). doi:10.2478/bpasts-2014-0055.

Dumont, Q., Cayol, V. and Froger, J.L. (2021) 'Mitigating bias in inversion of InSAR data resulting from radar viewing geometries', *Geophysical Journal International*, 227(1), pp. 483–495. doi:10.1093/gji/ggab229.

Duro, J., Inglada, J., Closa, J., Adam, N., and Arnaud, A. (2003) 'High resolution differential interferometry using time series of ERS and ENVISAT SAR data', *FRINGE 2003 workshop* , 550, pp. 72.

Fantoni, R. and Franciosi, R. (2008) 'Geological sections crossing Po Plain and Adriatic foreland', *Rendiconti online della Società Geologica Italiana*, *3*, pp. 365-366.

Fantoni, R. and Franciosi, R. (2010) 'Tectono-sedimentary setting of the Po Plain and Adriatic foreland', *Rendiconti Lincei*, 21, pp. 197–209. doi:10.1007/s12210-010-0102-4.

Farolfi, G., Bianchini, S. and Casagli, N. (2019a) 'Integration of GNSS and Satellite InSAR Data:

Derivation of Fine-Scale Vertical Surface Motion Maps of Po Plain, Northern Apennines, and Southern Alps, Italy', *IEEE Transactions on Geoscience and Remote Sensing*, 57(1), pp. 319–328. doi:10.1109/TGRS.2018.2854371.

Farolfi, G., Del Soldato, M., Bianchini, S. and Casagli, N. (2019b) 'A procedure to use GNSS data to calibrate satellite PSI data for the study of subsidence: an example from the north-western Adriatic coast (Italy)', *European Journal of Remote Sensing*, 52(sup4), pp. 54–63. doi:10.1080/22797254.2019.1663710.

Feng, G., Ding, X., Li, Z., Mi, J., Zhang, L. and Omura, M. (2012) 'Calibration of an Insar-derived coseimic deformation map associated with the 2011 Mw-9.0 Tohoku-Oki earthquake', *IEEE Geoscience and Remote Sensing Letters*, 9(2), pp. 302–306. doi:10.1109/LGRS.2011.2168191.

Ferretti, A., Prati, C. and Rocca, F. (2000) 'Nonlinear subsidence rate estimation using permanent scatterers in differential SAR interferometry', *IEEE Transactions on Geoscience and Remote Sensing*, 38(5), pp. 2202–2212. doi:10.1109/36.868878.

Ferretti, A., Prati, C. and Rocca, F. (2001) 'Permanent Scatters in SAR Interferometry', *IEEE Transactions on Geoscience and Remote Sensing*, 39(1), pp. 8–20. doi:10.1109/36.898661.

Ferretti, A., Fumagalli, A., Novali, F., Prati, C., Rocca, F., and Rucci, A. (2011) 'A new algorithm for processing interferometric data-stacks: SqueeSAR', *IEEE Transactions on Geoscience and Remote Sensing*, *49*(9), pp. 3460-3470. doi: 10.1109/TGRS.2011.2124465.

Fialko, Y. (2006) 'Interseismic strain accumulation and the earthquake potential on the southern San Andreas fault system', *Nature*, 441(7096), pp. 968–971. doi:10.1038/nature04797.

Floris, M., Fontana, A., Tessari, G. and Mulè, M. (2019) 'Subsidence zonation through satellite interferometry in coastal plain environments of NE Italy: A possible tool for geological and geomorphological mapping in Urban Areas', *Remote Sensing*, 11, 165. doi:10.3390/rs11020165.

Foumelis, M., Blasco, J.M.D., Desnos, Y.L., Engdahl, M., Fernández, D., Veci, L., Lu, J. and Wong, C. (2018) 'ESA SNAP - StaMPS integrated processing for Sentinel-1 persistent scatterer interferometry', *International Geoscience and Remote Sensing Symposium (IGARSS)*, 2018-July(1), pp. 1364–1367. doi:10.1109/IGARSS.2018.8519545.

Gabriel, A.K., Goldstein, R.M. and Zebker, H.A. (1989) 'Mapping small elevation changes over large areas: differential radar interferometry', *Journal of Geophysical Research*, 94(B7), pp. 9183–9191. doi:10.1029/JB094iB07p09183.

Galadini, F., Poli, M.E. and Zanferrari, A. (2005) 'Seismogenic sources potentially responsible for earthquakes with M ≥ 6 in the eastern Southern Alps (Thiene-Udine sector, NE Italy)', *Geophysical Journal International*, 161(3), pp. 739–762. doi:10.1111/j.1365-246X.2005.02571.x.

Galetto, F., Hooper, A., Bagnardi, M. and Acocella, V. (2020) 'The 2008 Eruptive Unrest at Cerro Azul Volcano (Galápagos) Revealed by InSAR Data and a Novel Method for Geodetic Modelling', *Journal of Geophysical Research: Solid Earth*, 125(2), pp. 1–20. doi:10.1029/2019JB018521.

Galvani, A., Anzidei, M., Devoti, R., Esposito, A., Pietrantonio, G., Pisani, A. R., Riguzzi, F. and Serpelloni, E. (2012) 'The interseismic velocity field of the Central Apennine from a dense GPS network', *Annals of Geophysics*, 55(5), pp. 1039–1049. doi:10.4401/ag-5634.

Gama, F.F., Mura, J.C., Paradella, W.R. and De Oliveira, C.G. (2020) 'Deformations prior to the Brumadinho dam collapse revealed by Sentinel-1 InSAR data using SBAS and PSI techniques', *Remote Sensing*, 12(21), pp. 1–22. doi:10.3390/rs12213664.

Giuliani, R., Anzidei, M., Bonci, L., Calcaterra, S., D'Agostino, N., Mattone, M., Pietrantonio, G., Riguzzi, F. and Selvaggi, G. (2007) 'Co-seismic displacements associated to the Molise (Southern Italy) earthquake sequence of October-November 2002 inferred from GPS measurements', *Tectonophysics*, 432(1–4), pp. 21–35. doi:10.1016/j.tecto.2006.11.005.

Goel, K. and Adam, N. (2014), 'A distributed scatterer interferometry approach for precision monitoring of known surface deformation phenomena', *IEEE Transactions on Geoscience and Remote Sensing,* 52 (9), 5454–5468.doi: 10.1109/TGRS.2013.2289370

Goldstein, R.M., Zebker, H.A. and Werner, C.L. (1988) 'Satellite radar interferometry: Two-dimensional phase unwrapping', *Radio Science*, 23(4), pp. 713–720. doi:10.1029/RS023i004p00713.

Goldstein, R.M. (1995) 'Atmospheric limitations to repeat-track radar interferometry been unduly disturbed during the time between', *Geophysical Research Letters*, 22(18), pp. 2517–2520.

Goldstein, R.M. and Werner, C.L. (1998) 'Radar interferogram filtering for geophysical applications', *Geophysical Research Letters*, 25(21), pp. 4035–4038. doi:10.1029/1998GL900033.

Gonzalez-Ortega, A., Fialko, Y., Sandwell, D., Nava-Pichardo, F.A., Fletche, J., Gonzalez-Garcia, J., Lipovsky, B., Floyd, M. and Funning, G. (2014) 'El Mayor-Cucapah (Mw 7.2) earthquake: Early near-field postseismic deformation from InSAR and GPS observations', *Journal of Geophysical Research : Solid Earth*, 119, pp. 1482–1497. doi:10.1002/2013JB010193.

Grandin, R., Doin, M.P., Bollinger, L., Pinel-Puysségur, B., Ducret, G., Jolivet, R. and Sapkota, S.N. (2012) 'Long-term growth of the Himalaya inferred from interseismic InSAR measurement', *Geology*, 40(12), pp. 1059–1062. doi:10.1130/G33154.1.

Gray, A.L., Mattar, K.E. and Sofko, G. (2000) 'Influence of Ionospheric Electron Density Fluctuations on Satellite Radar Interferometry', *Geophysical Research Letters*, 27(10), pp. 1451–1454. doi:10.1029/2000GL000016.

Grützner, C., Aschenbrenner, S., Jamšek Rupnik, P., Reicherter, K., Saifelislam, N., Vičič, B., Vrabec, M., Welte, J. and Ustaszewski, K. (2021) 'Holocene surface-rupturing earthquakes on the Dinaric Fault System, western Slovenia', *Solid Earth*, 12(10), pp. 2211–2234. doi:10.5194/se-12-2211-2021.

Hanssen, R.F. (2001) 'Radar Interferometry: Data Interpretation and Error Analysis', *Edited by K.A. Publishers*. doi:10.1007/0-306-47633-9.

Hastings, W. K., (1970) 'Monte Carlo sampling methods using Markov chains and their applications', *Biometrika*, 57(1), pp. 97–109. doi: 10.1093/biomet/57.1.97

Hein, A. (2004) 'Processing of SAR data: fundamentals, signal processing, interferometry', *Springer-Verlag*. doi:10.1007/978-3-662-09457-0.

Henriquet, M., Peyret, M., Dominguez, S., Barreca, G., Monaco, C. and Mazzotti, S. (2022) 'Present-day surface deformation of Sicily derived from Sentinel-1 InSAR time-series', *Journal of Geophysical Research: Solid Earth*, 127(3). doi:10.1029/2021jb023071.

Herring, T.A., King, R.W., Mcclusky, S.C. and Sciences, P. (2015) 'Introduction to GAMIT / GLOBK', *Analysis*, pp. 1–50.

Hetland, E. A., Musé, P., Simons, M., Lin, Y. N., Agram, P. S. and DiCaprio, C. J. (2012) 'Multiscale InSAR time series (MInTS) analysis of surface deformation', *Journal of Geophysical Research: Solid Earth*, *117*(B2). doi: 10.1029/2011JB008731

Hofmann-Wellenhof B., Lichtenegger H. and Wasle E. (2008) 'GNSS: global navigation satellite systems: GPS, Glonass, Galileo, and more', *Springer*, New York

Hooper, A., Zebker, H., Segall, P. and Kampes, B. (2004) 'A new method for measuring deformation on volcanoes and other natural terrains using InSAR persistent scatterers', *Geophysical Research Letters*, 31(23), pp. 1–5. doi:10.1029/2004GL021737.

Hooper, A., Segall, P. and Zebker, H. (2007) 'Persistent scatterer interferometric synthetic aperture radar for crustal deformation analysis, with application to Volcán Alcedo, Galápagos', *Journal of Geophysical Research*, 112, pp. 1–21. doi:10.1029/2006JB004763.

Hooper, A. and Zebker, H. A. (2007). 'Phase unwrapping in three dimensions with application to InSAR time series', *JOSA A*, *24*(9), 2737-2747. doi:10.1364/JOSAA.24.002737

Hooper, A., Bekaert, D., Spaans, K. and Arikan, M. (2012) 'Recent advances in SAR interferometry time series analysis for measuring crustal deformation', *Tectonophysics*, 514–517, pp. 1–13. doi:10.1016/j.tecto.2011.10.013.

Hussain, E., Hooper, A., Wright, T.J., Walters, R.J. and Bekaert, D.P.S. (2016) 'Interseismic strain accumulation across the central North Anatolian Fault from iteratively unwrapped InSAR measurements', *Journal of Geophysical Research: Solid Earth*, 121(12), pp. 9000–9019. doi:10.1002/2016JB013108.

Iinuma, T., Ohzono, M., Ohta, Y. and Miura, S. (2011) 'Coseismic slip distribution of the 2011 off the Pacific coast of Tohoku Earthquake (M 9.0) estimated based on GPS data-Was the asperity in Miyagi-oki ruptured?', *Earth, Planets and Space*, 63(7), pp. 643–648. doi:10.5047/eps.2011.06.013.

Kampes, B. M. (2006) 'Radar interferometry (Vol. 12)', *Dordrecht, The Netherlands: Springer*.

Karimzadeh, S., Cakir, Z., Osmanoğlu, B., Schmalzle, G., Miyajima, M., Amiraslanzadeh, R. and Djamour, Y. (2013) 'Interseismic strain accumulation across the North Tabriz Fault (NW Iran) deduced from InSAR time series', *Journal of Geodynamics*, 66(February), pp. 53–58. doi:10.1016/j.jog.2013.02.003.

Kastelic, V., Vrabec, M., Cunningham, D. and Gosar, A. (2008) 'Neo-Alpine structural evolution and present-day tectonic activity of the eastern Southern Alps: The case of the Ravne Fault, NW Slovenia', *Journal of Structural Geology*, 30(8), pp. 963–975. doi:10.1016/j.jsg.2008.03.009.

Kastelic, V. and Carafa, M.M.C.C. (2012) 'Fault slip rates for the active External Dinarides thrust-and-fold belt', *Tectonics*, 31(3). doi:10.1029/2011TC003022.

Klemm, H., Quseimi, I., Novali, F., Ferretti, A. and Tamburini, A. (2010) 'Monitoring horizontal and vertical surface deformation over a hydrocarbon reservoir by PSInSAR', *First Break*, 28(5), pp. 29–37. doi:10.3997/1365-2397.2010014.

Komac, M., Holley, R., Mahapatra, P., Van der Marel, H. and Bavec, M. (2015) 'Coupling of GPS/GNSS and radar interferometric data for a 3D surface displacement monitoring of landslides', *Landslides*, 12(2), pp. 241–257. doi:10.1007/s10346-014-0482-0.

Lanari, R., Mora, O., Manunta, M., Mallorquí, J.J., Berardino, P. and Sansosti, E. (2004) 'A small-baseline approach for investigating deformations on full-resolution differential SAR interferograms', *IEEE Transactions on Geoscience and Remote Sensing*, 42(7), pp. 1377–1386. doi:10.1109/TGRS.2004.828196.

Le Pichon, X., Francheteau, J. and Bonnin, J. (2013) 'Plate tectonics (Vol. 6)', *Elsevier*.

Li, Y. (2021) 'Analysis of GAMIT/GLOBK in high-precision GNSS data processing for crustal deformation', *Earthquake Research Advances*, 1(3), p. 100028. doi:10.1016/j.eqrea.2021.100028.

Liang, C., Agram, P., Simons, M. and Fielding, E. J. (2019) 'Ionospheric correction of InSAR time series analysis of C-band Sentinel-1 TOPS data', *IEEE Transactions on Geoscience and Remote Sensing*, 57(9), pp. 6755–6773. doi:10.1109/TGRS.2019.2908494.

Lin, Y. N., Simons, M., Hetland, E. A., Muse, P., and DiCaprio, C. (2010) 'A multiscale approach to estimating topographically correlated propagation delays in radar interferograms', *Geochemistry, Geophysics, Geosystems*, 11(9), pp. 1-17. doi:10.1029/2010GC003228.

Lisowski, M., Prescott, W.H., Savage, J.C. and Johnston, M.J. (1990) 'Geodetic estimate of coseismic slip during the 1989 Loma Prieta, California, earthquake', *Geophysical Research Letters*, 17(9), pp. 1437–1440.

Liu, C., Ji, L., Zhu, L. and Zhao, C. (2018) 'InSAR-Constrained Interseismic Deformation and Potential Seismogenic Asperities on the Altyn Tagh', *Remote Sensing*, 10. doi:10.3390/rs10060943.

Lohman, R.B. and Simons, M. (2005) 'Some thoughts on the use of InSAR data to constrain models of surface deformation: Noise structure and data downsampling', *Geochemistry, Geophysics, Geosystems*, 6(1). doi:10.1029/2004GC000841.

López-Quiroz, P., Doin, M.P., Tupin, F., Briole, P. and Nicolas, J.M. (2009) 'Time series analysis of Mexico City subsidence constrained by radar interferometry', *Journal of Applied Geophysics*, 69 (1), 1–15.doi: 10.1016/j.jappgeo.2009.02.006

Lv, X., Yazici, B., Zeghal, M., Bennett, V. and Abdoun, T. (2014) 'Joint-scatterer processing for time-series InSAR'*, IEEE Transactions on Geoscience and Remote Sensing,* 52 (11), 7205–7221.doi: 10.1109/TGRS.2014.2309346

Maître, H. (2008) Processing of synthetic aperture radar images, *John Wiley & Sons*. doi:10.1002/9780470611111.

Malenovský, Z., Rott, H., Cihlar, J., Schaepman, M. E., García-Santos, G., Fernandes, R. and Berger, M. (2012) 'Sentinels for science: Potential of Sentinel-1,-2, and-3 missions for scientific observations of ocean, cryosphere, and land', *Remote Sensing of environment*, *120*, pp. 91-101. doi: 10.1016/j.rse.2011.09.026

Masetti, D., Fantoni, R., Romano, R., Sartorio, D. and Trevisani, E. (2012) 'Tectonostratigraphic evolution of the Jurassic extensional basins of the eastern southern Alps and Adriatic foreland based on an integrated study of surface and subsurface data', *AAPG Bulletin*, 96(11), pp. 2065–2089. doi:10.1306/03091211087.

Massonnet, D., Rossi, M., Carmona, C., Adragna, F., Peltzer, G., Feigl, K. and Rabautet, T. (1993) 'The displacement field of the Landers earthquake mapped by rada interferometry', *Nature*, 364(July), pp. 138–142.

Massonnet, D. and Feigl, K.L. (1998) 'Radar interferometry and its application to changes in the earth's surface', *Reviews of Geophysics*, 36(4), pp. 441–500. doi:10.1029/97RG03139.

Mehrabi, H., Voosoghi, B., Motagh, M. and Hanssen, R.F. (2019) 'Three-Dimensional Displacement

Fields from InSAR through Tikhonov Regularization and Least-Squares Variance Component Estimation', *Journal of Surveying Engineering*, 145(4), p. 04019011. doi:10.1061/(asce)su.1943-5428.0000289.

Mellere, D., Stefani, C., and Angevine, C. (2000) 'Polyphase tectonics through subsidence analysis: the Oligo-Miocene Venetian and Friuli Basin, north-east Italy', *Basin research*, *12*(2), pp. 159-182.

Merlini, S., Doglioni, C., Fantoni, R. and Ponton, M. (2002) 'Analisi strutturale lungo un profilo geologico tra la linea Fella-Sava e l'avampaese adriatico (Friuli Venezia Giulia-Italia)', *Memorie della Società Geologica Italiana*, 57, pp. 293–300.

Mora, O., Mallorqui, J.J. and Broquetas, A., (2003) 'Linear and nonlinear terrain deformation maps from a reduced set of interferometric SAR images', *IEEE Transactions on Geoscience and Remote Sensing,* 41 (10), 2243–2253.

Moulin, A., Benedetti, L., Rizza, M., Jamšek Rupnik, P., Gosar, A., Bourlès, D., Keddadouche, K., Aumaître, G., Arnold, M., Guillou, V., *et al.* (2016) 'The Dinaric fault system: Large-scale structure, rates of slip, and Plio-Pleistocene evolution of the transpressive northeastern boundary of the Adria microplate', *Tectonics*, 35(10), pp. 2258–2292. doi:10.1002/2016TC004188.

Moya, L., Yamazaki, F., Liu, W. and Chiba, T. (2017) 'Calculation of coseismic displacement from lidar data in the 2016 Kumamoto, Japan, earthquake', *Natural Hazards and Earth System Sciences*, *17*(1), 143-156 . doi:10.5194/nhess-2016-315.

Muro, F. (2022), 'Applicazione di interferometria radar satellitare per il monitoraggio dei fenomeni franosi in Friuli Venezia Giulia – Caso studio: Comune di Pulfero (UD)" – University of Trieste [unpublished Master Thesis]

Nicolich, R., Della Vedova, B., Giustiniani, M. and Fantoni, R. (2004) 'Carta del sottosuolo della Pianura Friulana', *Regione Autonoma Friuli Venezia–Giulia. Direzione Centrale Ambiente e Lavori pubblici. Servizio Geologico*

Notti, D., Calò, F., Cigna, F., Manunta, M., Herrera, G., Berti, M., Meisina, C., Tapete, D. and Zucca, F. (2015) 'A User-Oriented Methodology for DInSAR Time Series Analysis and Interpretation: Landslides and Subsidence Case Studies', *Pure and Applied Geophysics*, 172(11), pp. 3081–3105. doi:10.1007/s00024-015-1071-4.

Okada, Y. (1985) 'Surface deformation due to shear and tensile faults in a half-space', *International Journal of Rock Mechanics and Mining Sciences Geomechanics Abstracts*, 75(4), pp. 1135–1154. doi:10.1016/0148-9062(86)90674-1.

Osmanoğlu, B., Dixon, T.H., Wdowinski, S., Cabral-Cano, E. and Jiang, Y. (2011) 'Mexico City subsidence observed with persistent scatterer InSAR', *International Journal of Applied Earth*

Observation and Geoinformation, 13(1), pp. 1–12. doi:10.1016/j.jag.2010.05.009.

Ozawa, T., Fujita, E. and Ueda, H. (2016) 'Crustal deformation associated with the 2016 Kumamoto Earthquake and its effect on the magma system of Aso volcano', *Earth, Planets and Space*, 68(1), p. 186. doi:10.1186/s40623-016-0563-5.

Patricelli, G., Poli, M.E. and Cheloni, D. (2022) 'Structural Complexity and Seismogenesis: The Role of the Transpressive Structures in the 1976 Friuli Earthquakes (Eastern Southern Alps, NE Italy)', *Geosciences*, 12(227). doi:/doi.org/10.3390/ geosciences12060227.

Perissin, D. and Wang, T. (2012) 'Repeat-pass SAR interferometry with partially coherent targets', *IEEE Transactions on Geoscience and Remote Sensing,* 50 (1), 271–280.doi: 10.1109/TGRS.2011.2160644

Perski, Z., Hanssen, R., Wojcik, A. and Wojciechowski, T. (2009) 'InSAR analyses of terrain deformation near the Wieliczka Salt Mine, Poland', *Engineering Geology*, *106*(1-2), 58-67. doi:10.1016/j.enggeo.2009.02.014

Pezzo, G., Tolomei, C., Atzori, S., Salvi, S., Shabanian, E., Bellier, O. and Farbod, Y. (2012) 'New kinematic constraints of the western Doruneh fault, northeastern Iran, from interseismic deformation analysis', *Geophysical Journal International*, 190(1), pp. 622–628. doi:10.1111/j.1365-246X.2012.05509.x.

Pezzo, G., Boncori, J.P.M., Tolomei, C., Salvi, S., Atzori, S., Antonioli, A., Trasatti, E., Novali, F., Serpelloni, E., Candela, L., *et al.* (2013) 'Coseismic deformation and source modeling of the May 2012 Emilia (Northern Italy) earthquakes', *Seismological Research Letters*, 84(4), pp. 645–655. doi:10.1785/0220120171.

Pezzo, G., Merryman Boncori, J.P., Visini, F., Carafa, M.M.C., Devoti, R., Atzori, S., Kastelic, V., Berardino, P., Fornaro, G., Riguzzi, F., *et al.* (2015), *Interseismic ground velocities of the Central Apennines from GPS and SAR measurements and their contribution to seismic hazard modelling : preliminary results of the ESA CHARMING project*, *Miscellanea INGV*.

Pezzo, G., Palano, M., Tolomei, C., Gori, P. De, Calcaterra, S., Gambino, P. and Chiarabba, C. (2020a) 'Flank sliding: A valve and a sentinel for paroxysmal eruptions and magma ascent at Mount Etna, Italy', *Geology*, 48(11), pp. 1077–1082. doi:10.1130/G47656.1.

Pezzo, G., Petracchini, L., Devoti, R., Maffucci, R., Anderlini, L., Antoncecchi, I., Billi, A., Carminati, E., Ciccone, F., Cuffaro, M., *et al.* (2020b) 'Active Fold-Thrust Belt to Foreland Transition in Northern Adria, Italy, Tracked by Seismic Reflection Profiles and GPS Offshore Data', *Tectonics*, 39(11), pp. 1–21. doi:10.1029/2020TC006425.

Placer, L., Vrabec, M. and Celarc, B. (2010) 'The bases for understanding of the NW Dinarides and

Istria Peninsula tectonics', *Geologija*, 53(1), pp. 55–86. doi:10.5474/geologija.2010.005.

Polcari, M., Albano, M., Montuori, A., Bignami, C., Tolomei, C., Pezzo, G., Falcone, S., Piana, C. La, Doumaz, F., Salvi, S., *et al.* (2018) 'InSAR monitoring of Italian coastline revealing natural and anthropogenic ground deformation phenomena and future perspectives', *Sustainability (Switzerland)*, 10(9), pp. 4–7. doi:10.3390/su10093152.

Poli, M. E., Peruzza, L., Rebez, A., Renner, G., Slejko, D. and Zanferrari, A. (2002) 'New seismotectonic evidence from the analysis of the 1976-1977 and 1977-1999 seismicity in Friuli (NE Italy)', *Bollettino di Geofisica Teorica ed Applicatal*, *43*(1-2), pp. 53-78.

Poli, M.E. and Zanferrari, A. (2018) 'The seismogenic sources of the 1976 Friuli earthquakes: A new seismotectonic model for the Friuli area', *Bollettino di Geofisica Teorica ed Applicata*, 59(4), pp. 463–480. doi:10.4430/bgta0209.

Pondrelli, S., Ekström, G. and Morelli, A. (2001) 'Seismotectonic re-evaluation of the 1976 Friuli, Italy seismic sequence', *Journal of Seismology*, 5(1), pp. 73–83. doi:10.1023/A:1009822018837.

Prats-Iraola, P., Marotti, L., Wollstadt, S. and Scheiber, R. (2010) 'TOPS interferometry with TerraSAR-X', *Proceedings of the European Conference on Synthetic Aperture Radar, EUSAR*, 50(8), pp. 44–47.

Reid, H. F. (1910), 'Permanent displacements of the ground, in the California earthquake of April 18, 1906', *Report of the State Earthquake Investigation Commission*, *2*, 16-28.

Rollins, C., Barbot, S. and Avouac, J.P. (2015) 'Postseismic Deformation Following the 2010 M = 7.2 El Mayor-Cucapah Earthquake: Observations, Kinematic Inversions, and Dynamic Models', *Pure and Applied Geophysics*, 172(5), pp. 1305–1358. doi:10.1007/s00024-014-1005-6.

Rosen, P.A., Hensley, S., Joughin, I.R., Li, F.K., Madsen, S.N., Rodriguez, E. and Goldstein, R.M. (2000) 'Synthetic aperture radar interferometry', *Proceedings of the IEEE*, 88(3), p. 50. doi:10.1088/0266-5611/14/4/001.

Rossi, G., Zuliani, D. and Fabris, P. (2016) 'Tectonophysics Long-term GNSS measurements from the northern Adria microplate reveal fault-induced fluid mobilization', *Tectonophysics*, 690, pp. 142–159. doi:10.1016/j.tecto.2016.04.031.

Rossi, G., Fabris, P. and Zuliani, D. (2018) 'Overpressure and Fluid Diffusion Causing Non-hydrological Transient GNSS Displacements', *Pure and Applied Geophysics*, 175(5), pp. 1869–1888. doi:10.1007/s00024-017-1712-x.

Rossi, G., Pastorutti, A., Nagy, I., Braitenberg, C. and Parolai, S. (2021) 'Recurrence of Fault Valve Behavior in a Continental Collision Area: Evidence From Tilt/Strain Measurements in Northern Adria', *Frontiers in Earth Science*, 9(June). doi:10.3389/feart.2021.641416.

Rovida, A., Locati, M., Camassi, R., Lolli, B. and Gasperini, P. (2020) 'The Italian earthquake catalogue CPTI15', *Bulletin of Earthquake Engineering*, 18(7), pp. 2953–2984. doi:10.1007/s10518-020-00818-y.

Ryder, I., Parsons, B., Wright, T.J. and Funning, G.J. (2007) 'Post-seismic motion following the 1997 Manyi (Tibet) earthquake: InSAR observations and modelling', *Geophysical Journal International*, 169(3), pp. 1009–1027. doi:10.1111/j.1365-246X.2006.03312.x.

Savage, J.C. and Burford, R.O. (1973) 'Geodetic Determination of Relative Plate Motion in Central California', *Journal of Geophysical Research*, 78(5), pp. 832–845. doi:10.1029/JB078i005p00832

Savage, J.C. and Prescott, W.H. (1978) 'Asthenosphere readjustment and the earthquake cycle', *Journal of Geophysical Research: Solid Earth*, 83(B7), pp. 3369–3376. doi:10.1029/JB083iB07p03369.

Savage, J.C. (1983) 'A dislocation model of strain accumulation and release at a subduction zone', *Journal of Geophysical Research*, 88, pp. 4984–4996. doi:10.1029/JB088iB06p04984

Schmidt, D. A. and Bürgmann, R. (2003) 'Time-dependent land uplift and subsidence in the Santa Clara valley, California, from a large interferometric synthetic aperture radar data set', *Journal of Geophysical Research: Solid Earth*, *108*(B9). doi:10.1029/2002JB002267

Seeber, G. *(*2003*)* *'*Satellite Geodesy', *Walter de Gruyter*.

Segall, P. (2010) 'Earthquake and Volcano Deformation', *Princeton University Press*.

Serpelloni, E., Casula, G., Galvani, A., Anzidei, M. and Baldi, P. (2006) 'Data analysis of permanent GPS networks in Italy and surrounding regions: Application of a distributed processing approach', *Annals of Geophysics*, 49(4–5), pp. 897–928. doi:10.4401/ag-4410

Serpelloni, E., Anderlini, L., Avallone, A., Cannelli, V., Cavaliere, A., Cheloni, D., D'Ambrosio, C., D'Anastasio, E., Esposito, A., Pietrantonio, G., *et al.* (2012) 'GPS observations of coseismic deformation following the May 20 and 29, 2012, Emilia seismic events (northern Italy): Data, analysis and preliminary models', *Annals of Geophysics*, 55(4), pp. 759–766. doi:10.4401/ag-6168.

Serpelloni, E., Faccenna, C., Spada, G., Dong, D. and Williams, S.D.P. (2013) 'Vertical GPS ground motion rates in the Euro-Mediterranean region: New evidence of velocity gradients at different spatial scales along the Nubia-Eurasia plate boundary', *Journal of Geophysical Research: Solid Earth*, 118(11), pp. 6003–6024. doi:10.1002/2013JB010102.

Serpelloni, E., Vannucci, G., Anderlini, L. and Bennett, R.A. (2016) 'Kinematics, seismotectonics and seismic potential of the eastern sector of the European Alps from GPS and seismic deformation data', *Tectonophysics*, 688, pp. 157–181. doi:10.1016/j.tecto.2016.09.026.

Serpelloni, E., Pintori, F., Gualandi, A., Scoccimarro, E., Cavaliere, A., Anderlini, L., Belardinelli, M.E. and Todesco, M. (2018) 'Journal of Geophysical Research : Solid Earth Hydrologically Induced Karst Deformation : Insights From GPS Measurements in the Adria-Eurasia Plate Boundary Zone Journal of Geophysical Research : Solid Earth', 123(5), pp. 4413–4430. doi:10.1002/2017JB015252.

Shen, Z.K. and Liu, Z. (2020) 'Integration of GPS and InSAR Data for Resolving 3-Dimensional Crustal Deformation', *Earth and Space Science*, 7(4), pp. 1–17. doi:10.1029/2019EA001036.

Skolnik, M. I., (2009) 'Introduction to Radar System', *Ed. Tata McGraw-Hill (third ed.),* pp.790

Sternai, P., Sue, C., Husson, L., Serpelloni, E., Becker, T.W., Willett, S.D., Faccenna, C., Di Giulio, A., Spada, G., Jolivet, L., *et al.* (2019) 'Present-day uplift of the European Alps: Evaluating mechanisms and models of their relative contributions', *Earth-Science Reviews*, 190(January), pp. 589–604. doi:10.1016/j.earscirev.2019.01.005.

Stocchi, P., Spada, G. and Cianetti, S. (2005) 'Isostatic rebound following the Alpine deglaciation: Impact on the sea level variations and vertical movements in the Mediterranean region', *Geophysical Journal International*, 162(1), pp. 137–147. doi:10.1111/j.1365-246X.2005.02653.x.

Stramondo, S., Tesauro, M., Briole, P., Sansosti, E., Salvi, S., Lanari, R., Anzidei, M., Baldi, P., Fornaro, G., Avallone, A., *et al.* (1999) 'The September 26, 1997 Colfiorito, Italy, earthquakes: Modeled coseismic surface displacement from SAR interferometry and GPS', *Geophysical Research Letters*, 26(7), pp. 883–886. doi:10.1029/1999GL900141.

Teatini, P., Tosi, L., Strozzi, T., Carbognin, L., Wegmüller, U. and Rizzetto, F. (2005) 'Mapping regional land displacements in the Venice coastland by an integrated monitoring system'. *Remote Sensing of Environment*, 98(4), 403-413.

Teatini, P., Tosi, L., Strozzi, T., Carbognin, L., Cecconi, G., Rosselli, R. and Libardo, S. (2012) 'Resolving land subsidence within the Venice Lagoon by persistent scatterer SAR interferometry', *Physics and Chemistry of the Earth*, 40–41, pp. 72–79. doi:10.1016/j.pce.2010.01.002.

Thatcher, W. (1979) 'Systematic inversion of geodetic data in central California', *Journal of Geophysical Research: Solid Earth*, 84(B5), pp. 2283–2295. doi:10.1029/JB084iB05p02283.

Tong, X., Sandwell, D.T. and Smith-Konter, B. (2013) 'High-resolution interseismic velocity data along the San Andreas Fault from GPS and InSAR', *Journal of Geophysical Research: Solid Earth*, 118(1), pp. 369–389. doi:10.1029/2012JB009442.

Torres, R., Snoeij, P., Geudtner, D., Bibby, D., Davidson, M., Attema, E., Potin, P. Rommen, B., Floury, N., Brown, M., *et al.* (2012) 'GMES Sentinel-1 mission', *Remote sensing of environment*, *120*, pp. 9-24. doi: 10.1016/j.rse.2011.05.028

Toscani, G., Marchesini, A., Barbieri, C., Di Giulio, A., Fantoni, R., Mancin, N. and Zanferrari, A.

(2016) ‘The friulian-venetian basin I: Architecture and sediment flux into a shared foreland basin’, *Italian Journal of Geosciences*, 135(3), pp. 444–459. doi:10.3301/IJG.2015.35.

Tosi, L., Teatini, P., Carbognin, L. and Brancolini, G. (2009) ‘Using high resolution data to reveal depth-dependent mechanisms that drive land subsidence: The Venice coast, Italy’, *Tectonophysics*, 474(1–2), pp. 271–284. doi:10.1016/j.tecto.2009.02.026.

Tosi, L., Teatini, P., Strozzi, T., Carbognin, L., Brancolini, G. and Rizzetto, F. (2010) ‘Ground surface dynamics in the northern Adriatic coastland over the last two decades’, *Rendiconti Lincei*, 21(1), pp. 115–129. doi:10.1007/s12210-010-0084-2.

Tosi, L., Teatini, P. and Strozzi, T. (2013) ‘Natural versus anthropogenic subsidence of Venice’, S*cientific reports*, *3*(1), pp. 1–9. doi:10.1038/srep02710.

Vajedian, S., Motagh, M., Mousavi, Z., Motaghi, K., Fielding, E.J., Akbari, B., Wetzel, H.U. and Darabi, A. (2018) ‘Coseismic deformation field of the Mw 7.3 12 November 2017 Sarpol-e Zahab (Iran) earthquake: A decoupling horizon in the Northern Zagros Mountains inferred from InSAR observations’, *Remote Sensing*, 10(10). doi:10.3390/rs10101589.

Van Leijen, F. (2014), ‘Persistent Scatterer Interferometry based on geodetic estimation theory (Doctoral dissertation)’, *TU Delft, Delft University of Technology*.

Vecchio, A., Anzidei, M., Serpelloni, E. and Florindo, F. (2019) ‘Natural variability and vertical land motion contributions in the Mediterranean sea-level records over the last two centuries and projections for 2100’, *Water (Switzerland)*, 11(7). doi:10.3390/w11071480.

Vergne, J., Cattin, R. and Avouac, J.P. (2001) ‘On the use of dislocations to model interseismic strain and stress build-up at intracontinental thrust faults’, *Geophysical Journal International*, 147(1), pp. 155–162. doi:10.1046/j.1365-246X.2001.00524.x.

Vičič, B., Aoudia, A., Javed, F., Foroutan, M. and Costa, G. (2019). Geometry and mechanics of the active fault system in western Slovenia. *Geophysical Journal International*, 217(3), 1755-1766. doi:10.1093/gji/ggz118.

Virk, A.S., Singh, A. and Mittal, S.K. (2018) ‘Journal of Remote Sensing & GIS Advanced MT-InSAR Landslide Monitoring : Methods and Trends’, *Journal of Remote Sensing and GIS*, 7(1), pp. 1–6. doi:10.4172/2469-4134.1000225.

Viscolani, A., Grützner, C., Diercks, M., Reicherter, K. and Ustaszewski, K. (2020) ‘Late quaternary tectonic activity of the Udine-Buttrio thrust, Friulian plain, NE Italy’, *Geosciences (Switzerland)*, 10(2), pp. 1–24. doi:10.3390/geosciences10020084.

Vrabec, M. and Fodor, L. (2006) ‘Late cenozoic tectonics of Slovenia: structural styles at the Northeastern corner of the Adriatic microplate’, *The Adria Microplate: GPS Geodesy, Tectonics and*

Hazards, pp. 151-168*, Springer, Dordrecht.* doi: 10.1007/1-4020-4235-3_10

Vrabec, M., Prešeren, P.P. and Stopar, B. (2006) 'GPS study (1996-2002) of active deformation along the Periadriatic fault system in northeastern Slovenia: Tectonic model', *Geologica Carpathica*, 57(1), pp. 57–65.

Walters, R.J., Holley, R.J., Parsons, B. and Wright, T.J. (2011) 'Interseismic strain accumulation across the North Anatolian Fault from Envisat InSAR measurements', *Geophysical Research Letters*, 38(5), pp. 1–5. doi:10.1029/2010GL046443.

Wang, K., Wells, R., Mazzotti, S. and Hyndman, R.D. (2003) 'A revised dislocation model of interseismic deformation of the Cascadia subduction zone', *Journal of Geophysical Research: Solid Earth,* 108, pp. 1–13. doi:10.1029/2001JB001227.

Wang, H. and Wright, T.J. (2012) 'Satellite geodetic imaging reveals internal deformation of western Tibet', *Geophysical Research Letters*, *39*(7), pp. 1–5. doi:10.1029/2012GL051222.

Wdowinski, S., Bock, Y., Zhang, J., Fang, P. and Genrich, J. (1997) 'Southern California Permanent GPS Geodetic Array: Spatial filtering of daily positions for estimating coseismic and postseismic displacements induced by the 1992 Landers earthquake', *Geophysics*, 102, pp. 18057–18070.

Weiss, J.R., Walters, R.J., Morishita, Y., Wright, T.J., Lazecky, M., Wang, H., Hussain, E., Hooper, A.J., Elliott, J.R., Rollins, C., *et al.* (2020) 'High-Resolution Surface Velocities and Strain for Anatolia From Sentinel-1 InSAR and GNSS Data', *Geophysical Research Letters*, 47(17). doi:10.1029/2020GL087376.

Wells, D.L. and Coopersmith, K.J. (1994) 'New Empirical Relationships among Magnitude , Rupture Length , Rupture Width , Rupture Area , and Surface Displacement', *Bulletin of the Seismological Society of America*, 84(4), pp. 974–1002.

Wen, Y., Xiao, Z., He, P., Zang, J., Liu, Y. and Xu, C. (2021) 'Source Characteristics of the 2020 Mw 7.4 Oaxaca, Mexico, Earthquake Estimated from GPS, InSAR, and Teleseismic Waveforms', *Seismological Research Letters*, 92(3), pp. 1900–1912. doi:10.1785/0220200313.

Werner, C., Wegmuller, U., Strozzi, T. and Wiesmann, A. (2003) 'Interferometric point target analysis for deformation mapping', *IGARSS 2003. 2003 IEEE International Geoscience and Remote Sensing Symposium. Proceedings (IEEE Cat. No. 03CH37477), 7,* pp. 4362-4364.

Wessel, P., Luis, J. F., Uieda, L., Scharroo, R., Wobbe, F., Smith, W. H. F. and Tian, D. (2019) 'The Generic Mapping Tools version 6', *Geochemistry, Geophysics, Geosystems*, 20, pp. 5556–5564. doi:10.1029/2019GC008515

Wright, T., Parsons, B., & Fielding, E. (2001) 'Measurement of interseismic strain accumulation across the North Anatolian Fault by satellite radar interferometry', *Geophysical Research Letters*, *28*(10), 2117-2120.

Wright, T.J., Lu, Z. and Wicks, C. (2003) 'Source model for the Mw 6.7, 23 October 2002, Nenana Mountain Earthquake (Alaska) from InSAR', *Geophysical Research Letters*, 30(18), pp. 30–33. doi:10.1029/2003GL018014.

Yang, C., Han, B., Zhao, C., Du, J., Zhang, D. and Zhu, S. (2019) 'Co- and post-seismic deformation mechanisms of the MW 7.3 Iran earthquake (2017) revealed by Sentinel-1 InSAR observations', *Remote Sensing*, 11(4), pp. 1–17. doi:10.3390/rs11040418.

Zebker, H.A. and Rosen, P. (1994) 'On the derivation of coseismic displacement fields using differential radar interferometry: The Landers earthquake', *International Geoscience and Remote Sensing Symposium (IGARSS)*, 1, pp. 286–288. doi:10.1109/igarss.1994.399105.

Zebker, A., Rosen, P.A. and Hensley, S. (1997) 'Atmospheric effects in interferometric synthetic aperture radar surface deformation and topographic maps', *Journal of Geophysical Research*, 102, pp. 7547–7563.

Zeng, Y. and Shen, Z.K. (2014) 'Fault network modeling of crustal deformation in California constrained using GPS and geologic observations', *Tectonophysics*, 612–613, pp. 1–17. doi:10.1016/j.tecto.2013.11.030.

Žibret, G., Komac, M. and Jemec, M. (2012) 'PSInSAR displacements related to soil creep and rainfall intensities in the Alpine foreland of western Slovenia', *Geomorphology*, 175–176, pp. 107–114. doi:10.1016/j.geomorph.2012.07.002.